Joint PP and PS Wave Analysis for Lithology and Fluid Prediction

Jinghua Zhang

Thesis submitted in the fulfilment of
the requirements for the degree of
Doctor of Philosophy

School of Geosciences
University of Edinburgh
2007

Declaration

I declare that this thesis has been composed solely by myself and that it has not been submitted, either in whole or in part, in any previous application for a degree. Except where otherwise acknowledged, the work presented is entirely my own.

Jinghua Zhang

March, 2007

Abstract

In recent years, multicomponent seismology has gained wide acceptance in the oil industry as a useful tool for improving both seismic imaging and reservoir characterization. However, the anticipated breakthrough of multicomponent seismic into a mainstream technology is still to be realized. One of the bottlenecks lies in the interpretation and analysis of multicomponent seismic data: there is a still lack of understanding of how to link the multicomponent seismic information to rock properties directly. In this thesis, I tackle this problem through a joint inversion of multicomponent PP and PS-seismic data in order to facilitate the direct comparison of seismic information with rock properties.

I first study some basic problems related to joint inversion, such as correlation of the PP- and PS-data, estimation of the V_p/V_s ratio and PP- and PS-AVO responses. I develop the algorithms and workflow for evaluating the merit of PP- and PS- joint inversion, test the workflow through numerical modeling and apply them to field data. Furthermore, I study the frequency-dependent behaviours of the PP- and PS-waves in thin-layered sand reservoirs containing different fluids in order to gain a more fundamental understanding of the wave behaviours during fluid substitution.

For event registration between PP- and PS-wave data, a new approach is investigated by reflection moveout analysis. This approach is based on matching the P-wave stacking velocity at zero-offset time T_{p0} obtained from PP-wave data with the P-wave stacking velocity at zero-offset time T_{c0} obtained from Converted PS-wave data. The tests on synthetic and real data show that the offset-to-depth ratio must be at least 1.5 to resolve the squared stacking velocity ratio accurately with errors less than 1%. The method is valid for multi-layered isotropic media.

Joint PP- and PS-wave AVO inversion based on weighted stacking techniques has provided the potential to determine elastic parameters such as V_P/V_S ratio, P- and S-wave impedance, and Lamè moduli from prestack seismic data and therefore to infer the subsurface lithology and fluid content. Some rock properties can be preferable to others in reservoir description due to specific geological and geophysical conditions, for example, thin-layer tuning and weak P-impedance contrast. It is necessary to evaluate the merits of different approaches and to understand the limitation of different elastic parameters using synthetics based on wireline logs. In this thesis, I use the Aki-Richards approximations with no limitation on the extent of the angle bands. This overcomes problems related to the class II AVO anomalies common in the study area, the Ordos basin, China. The investigation of the offset-dependent tuning effect shows an adverse effect on both the PP- and PS-wave AVO response.

Standard AVO analysis based on Gassmann fluid substitution is frequency independent and ignores attenuation and dispersion. However, high attenuation related to gas reservoirs has been observed on both VSP and seismic data for many years. Previous modeling work has suggested that the fluid-related dispersion may have a pronounced effect on the AVO behaviour at the interface. Here, I address the issues of whether or not such signatures from the simple single layer models persist into the more complicated multi-thin layer cases, and whether it is possible to detect such effects in seismic physical modeling and field data. By contrast to the low-frequency effect previously demonstrated for class III AVO response, I conclude that in the case of Class I AVO response, the presence of gas will induce a high-frequency bright spot. Tuning does indeed make the analysis difficult, but the effect of dispersion can still be observed.

Acknowledgements

After working in PetroChina for nine years, I moved to Edinburgh for my PhD study. I am very grateful for having Professor Xiang-Yang Li and Dr Roger Scrutton as my supervisors. Their deep insight of academic and industry demands have guided me to achieve the goal of this PhD research.

I sincerely thank Xiang-Yang for teaching me a lot in multicomponent seismic and generally how to approach scientific problems and write an academic paper. I especially appreciate his review and correction of this thesis. Thanks are also to Roger for his guidance in the thesis planning and English correction.

I sincerely thank Dr Enru Liu for his supervision, particularly in rock physics. I also benefit a lot from his in-depth academic knowledge of spectral decomposition. I must thank Dr Mark Chapman for sharing his deep knowledge in frequency dependent AVO, I am also grateful for his review and correction of the parts of the thesis.

Dr Hengchang Dai gives me the guidance and a big help in programming and converted wave processing. Our numerous discussions enlighten me through this PhD research. I also thank Guangpin Li for his help in programming, Helena Jack David Kerridge, David Booth for the administration work, and Brian Bainbridge, Ruth Addinall, Steve Love for the computer administration.

I thank all the guys who study together with me at EAP, Baerbel Traub, Fabio Mancini, Sonja Maultzsch, Lifeng Wang, Andy Dobson, and Zhongping Qian for the wonderful seminars and parties. I especially thank my friend, classmate and flatmate Isabel Varela, for the all happy time we share together.

I thank PetroChina for permission to show the data, and I also thank the EAP sponsors: BG, BGP, BP, Chevron, ConocoPhillips, CNPC, ENI-Agip, ExxonMobil, GX Technology, Kerr-McGee, Landmark, Marathon, Norsk Hydro, PDVSA, Shell, Schlumberger, Total, Veritas.

Last but not least, I would like to thank my husband Xianbin for his support and love, his delicious cooking and care when I was sick in hospital. I would also thank my father, for his encouraging poems, mother and two big sisters for their patience. I want to thank our family friends Taohua Li, Zhou Ying, Qiangyi Li, and Zhang Juan for all help they have given us throughout these years.

Contents

Declaration iii

Abstract v

Acknowledgements vii

Contents ix

Mathematical convention and notations xv

List of Figures xxi

List of Tables xxvii

Chapter 1: Introduction 1

1.1 Motivation 1

1.2 Objective and outline of the thesis 3

1.3 Datasets and software used in this thesis 5

Chapter 2: Overview of multicomponent seismic 7

2.1 History of multicomponent seismic 7

2.2 The applications of multicomponent data: A review 8

2.3 A practical work flow 14

Chapter 3: Ordos multicomponent data processing 17

3.1 Introduction 17

3.2 The study area 18

3.3 Data acquisition and characterization 21

3.4 Data processing 26

3.4.1 Static correction 29

3.4.2 ACCP and CCP binning for PS-wave data 33

3.4.3 Non-hyperbolic moveout analysis 35

3.4.4 Diodic effect 38

3.4.5 Pre-stack Kirchhoff time migration 40

3.5 Conclusion 44

Chapter 4: PP- and PS-wave event correlation by PS-wave moveout analysis 47

4.1 Introduction 47

4.1.1 Post-stack data event correlation 48

4.1.2 Pre-stack data event registration 49

4.2 Method 50

4.3 Model study 55

4.3.1 Double scanning semblance analysis 55

4.3.2 Sensitivity analysis of γ_{iso} for different offset depth ratio 60

4.3.3 Determination of γ_0 69

4.4 Application to the Ordos data 70

4.5 Discussion and conclusion 76

Chapter 5: AVO theory and PP-data analysis 77

5.1 Introduction 77

5.2 AVO class definition 78

5.3 Lithology and fluid effect on rock properties 80

5.3.1 Gassmann fluid substitution 80

5.3.2 Fluid effect on rock properties from laboratory data 87
5.3.3 Lithology and fluid effect on rock properties from log data 96
5.4 PP-wave AVO analysis 100
5.4.1 Intercept and gradient analysis 100
5.4.2 Well and seismic data analysis 101
5.5 Pitfalls in PP-wave AVO analysis 112
5.5.1 The reliability of AVO attributes 112
5.5.2 Wavelet variation and NMO stretch effect 113
5.5.3 Prestack amplitude balancing effect 113
5.6 Conclusions 114
Chapter 6: Joint PP- and PS-wave AVO inversion : modelling and data application 115
6.1 Method 115
6.2 Method testing 120
6.2.1 PS-inversion alone 123
6.2.2 PP-inversion alone 130
6.2.3 Joint inversion of PP- and PS-data 135
6.3 Offset-dependent tuning effect on AVO 138
6.4 Data application 147
6.5 Conclusions 159
Chapter 7: Frequency-dependent AVO for fluid detection 161
7.1 Introduction 161
7.2 Theory 164
7.2.1 Dynamic fluid substitution 164

7.2.2 Spectral decomposition technique 166

7.3 Data example 172

7.3.1 Example 1 172

7.3.2 Example 2 183

7.4 Thick-layer model without tuning 188

7.5 Thin-layer model with tuning 197

7.6 Discussion and conclusion 202

Chapter 8: Application of frequency-dependent variations for fluid detection in thin-bedded sands 205

8.1 Introduction 205

8.2 The physical model 206

8.3 Data acquisition and characteristics 208

8.4 Analysis of the 2D fixed-offset data 211

8.4.1 Analysis of amplitude spectra 213

8.4.2 Application of spectral decomposition 218

8.5 Analysis of the 2D Stacked data 227

8.6 Discussion and conclusion 234

Chapter 9: Conclusions 237

9.1 Major conclusions from this thesis 237

9.1.1 Event correlation between PP- and PS-data 237

9.1.2 Sensitivity of elastic parameters to rock properties 238

9.1.3 Elastic parameters estimation from Joint AVO inversion 239

9.1.4 Offset dependent tuning effect on PP- and PS-wave AVO 240

9.1.5 Frequency dependent AVO for fluid detection 240

9.2 Future work recommendation 241

References **243**

Appendix **253**

A: Calculation of the frequency dependent elastic tensor 253

B: Publications 257

Mathematical convention and notations

All the mathematical variables and other abbreviations used in the thesis are explained here. They are arranged in the order of their appearance.

Abbreviations

Symbol	Meaning
PP	Downgoing and upgoing compressional waves
PS or C-wave	Downgoing compressional and upgoing shear waves
AVO	Amplitude versus offset
P-wave	Compressional wave
S-wave	Shear wave
MC	Multi-component
VSP	Vertical seismic profile
4C	Three orthogonally oriented geophones X, Y and Z plus hydrophone for marine acquisition
OBC	Ocean-bottom cable
MEMS	Micro Electric Mechanical System
CWP	Center for Wave Phenomena
CNPC	China National Petroleum Company
CCP	Common conversion point
ACCP	Asymptotic common conversion point
CIP	Common image point
V_p/V_s	P- and S-wave velocity ratio
F-K	Frequency-wavenumber

RMS	Root mean square
DSR	Double square root
NMO	Normal moveout
DMO	Dip moveout
AVA	Amplitude versus angle
CDP	Common depth point
CMP	Common middle point
PSTM	Prestack time migration
PKTM	Prestack kirchhoff time migration
PSDM	Prestack depth migration
INMO	Inverse normal moveout
SC	Semblance coefficient
X/Z	Offset depth ratio
STFT	Short time Fourier transform
CWT	Continuous wavelet transform

Mathematical symbols

Symbol	Meaning
V_p	P-wave velocity
V_s	S-wave velocity
X_p	Approximate conversion position
γ_0	Vertical velocity ratio of P- and S-wave
t_c	Converted wave travel time
t_{p0}	Zero offset PP-wave travel time

t_{c0}	Zero offset PS-wave travel time
V_{c2}	PS-wave stacking velocity
γ_2	Stacking P- and S-velocity ratio
γ_{eff}	Effective velocity ratio
γ_{iso}	Squared P- and PS-stacking velocity ratio
χ_{eff}	PS-wave anisotropic parameter
V_{pk}	Interval P-wave velocity
V_{sk}	Interval S-wave velocity
A	Intercept
B	Gradient
A*B	Product of intercept and gradient
K_{dry}	Effective bulk modulus of dry rock
K_m	Bulk modulus of rock matrix
K_f	Effective bulk modulus of pore fluid
μ_{dry}	Effective shear modulus of dry rock
ϕ	Porosity
ρ_{sat}	Density of saturated rock
S_w	Water saturation
K_w	Bulk modulus of water
K_{hc}	Bulk modulus of hydrocarbon
ρ_m	Density of rock matrix
ρ_w	Density of water
ρ_{hc}	Density of hydrocarbon
β	Biot coefficient
σ_{dry}	Poisson's ratio of dry rock

σ	Poisson's ratio
I_p	P-impedance
I_s	S-impedance
λ	Bulk modulus less two-thirds of the shear modulus
μ	Shear modulus
ρf	Fluid component
ρs	Dry component
θ	Average of P-wave angles of incidence and transmission across the interface
φ	Average of shear-wave angles of reflection and transmission across the interface
$R_{ps}(\theta,\varphi)$	PS-wave reflection coefficient
$R_{pp}(\theta)$	PP-wave reflection coefficient
α	Average V_p across the interface
β	Average V_s across the interface
$\Delta\alpha$	Contrast in V_p across the interface
$\Delta\beta$	Contrast in V_s across the interface
$\Delta\rho$	Contrast in density across the interface
$\Delta\alpha/\alpha$	P-wave velocity reflectivity
$\Delta\beta/\beta$	S-wave velocity reflectivity
$\Delta\rho/\rho$	Density reflectivity
$\Delta\sigma/\sigma$	Pseudo Poisson's ratio reflectivity
ΔF	Fluid factor
$\Delta I_p/I_p$	P-impedance reflectivity
$\Delta I_s/I_s$	S-impedance reflectivity
$\Delta\lambda/\lambda$	λ reflectivity

$\Delta\mu/\mu$	μ reflectivity
W	Scalar for PS-wave in joint AVO inversion
τ	Time scale parameter
ε	Crack density
r	Crack aspect ratio

List of Figures

Figure 2.1: The example from Tommeliten Field for imaging through a gas cloud 10

Figure 2.2: Converted wave image showing improved imaging of Type II Sand relative to the streamer P-wave data 11

Figure 2.3: A relationship between V_p/V_s (Poisson's ratio) and lithology. 13

Figure 2.4: A workflow for joint PP- and PS-data interpretation and inversion 15

Figure 3.1: Study area location and Stratigraphic column map 18

Figure 3.2: A 2D 3C line from Ordos field, onshore China 21

Figure 3.3: I/O's VectorSeis sensor module 22

Figure 3.4: Comparison of various acquisition systems 23

Figure 3.5: Shot example of the amplitude spectra from conventional geophone and digital geophone. 24

Figure 3.6: A shot gather and it's F-K spectrum 25

Figure 3.7: Sample shot gathers and hodogram between X- and Z-components 27

Figure 3.8: The flowchart of PP- and PS-wave data processing. 29

Figure 3.9: Study area terrain and near surface velocity model 30

Figure 3.10: Comparison of the static correction effect on P-wave stacked sections 31

Figure 3.11: PS-wave ray path and common receiver point trajectory 35

Figure 3.12: Comparison between hyperbolic and Non-hyperbolic moveout analysis in ACCP 800 37

Figure 3.13: A schematic diagram showing the diotic effect. 39

Figure 3.14: ACCP gather 1100 after NMO 39

Figure 3.15: Effect of the diodic velocity on the negative and positive offset stacking images 40

Figure 3.16: Kirchhoff PSTM for a scatter point. 41

Figure 3.17: Comparison between ACCP 7433 and CIP 7433. 43

Figure 3.18: PSTM images of PP- and PS-wave 44

Figure 4.1: Residual time for the 1st to 5th reflectors of the model in Table 4.1. 52

Figure 4.2: PS-wave synthetic gather calculated for the model in Table 4.1 56

Figure 4.3: Double-scanning results for V_{c2} and γ_{iso} corresponding to the five events in Table 4.1 57

Figure 4.4: Double-scanning results for V_{c2} and γ_{iso} when offset depth ratio is 1 66

Figure 4.5: Double-scanning results for V_{c2} and γ_{iso} when offset depth ratio is 1.5 62

Figure 4.6: Double-scanning results for V_{c2} and γ_{iso} when offset depth ratio is 2.5 65

Figure 4.7: Time errors of two-parameter PS-wave travel time equation for five events in Figure 4.2 69

Figure 4.8: Correlation of the velocity picks 70

Figure 4.9: Double scanning analysis for V_{c2} and γ_{iso} for the Ordos converted-wave data 71

Figure 4.10: Single-scanning results for V_{c2} and γ_{iso} in the Ordos converted-wave data 73

Figure 4.11: Comparison of V_{p2} spectra obtained from PS-wave moveout data with V_{p2} spectra from PP-wave moveout data. 74

Figure 4.12: Correlation between stacked PP-wave and PS-wave 75

Figure 5.1: AVO classification at the top of gas sand 79

Figure 5.2: A cube of porous rock described by Gassmann theory 81

Figure 5.3: P- and S-wave velocity versus gas saturations from lab data 88

Figure 5.4: The variation of V_p/V_s with the gas saturation at the three different temperature and pressure conditions 90

Figure 5.5: V_p/V_s versus porosity for tight gas sand at the different saturations 92

Figure 5.6: P-impedance versus S-impedance for tight gas sand from lab data 94

Figure 5.7: $\lambda\rho$ versus $\mu\rho$ for tight gas sand from lab data 95

Figure 5.8: ρf versus ρs for tight gas sand from lab data. 96

Figure 5.9: V_p/V_s versus P-impedance from a dipole sonic log 98

Figure 5.10: V_p/V_s versus S-impedance from a dipole sonic log 98

Figure 5.11: $\lambda\rho$ versus $\mu\rho$ from a dipole sonic log. 99

Figure 5.12: ρf versus ρs from a dipole sonic log. 99

Figure 5.13: T5 blocked log curves and petrophysics interpretation. 103

Figure 5.14: Post-stack section across well T5 103

Figure 5.15: AVO synthetics for the wet sand model, gas sand model and CDP gather in the well location 104

Figure 5.16: AVO analysis for the wet sand and gas sand models. 105

Figure 5.17: Wet sand and gas sand V_p and V_s relation from the rock samples measurement 106
Figure 5.18: AVO attribute and fluid factor sections across the well T5 107
Figure 5.19: Crossplot of $\lambda\rho$ versus $\mu\rho$ for the gas layer of the well T5 108
Figure 5.20: The P-wave impedance I_p, by inverting the P-reflectivity 109
Figure 5.21: The S-wave impedance I_s, by inverting the S-reflectivity 109
Figure 5.22: The $\lambda\rho$ section by combining the I_p and I_s inversions 110
Figure 5.23: The $\mu\rho$ section by Is inversions 111
Figure 5.24: A crossplot between $\lambda\rho$ and $\mu\rho$ section 111
Figure 5.25: The interpeted gas zone by the low $\lambda\rho$ values 112
Figure 6.1: A multi-layer model for inversion testing 120
Figure 6.2: Ray tracing paths of both PP-wave and PS-wave 121
Figure 6.3: PP-wave and PS-wave synthetic gathers by Zoeppritz equation 122
Figure 6.4: The linear P- and S-velocity model for comparing the velocity effect on the inversion results 123
Figure 6.5: Ray-traced PS-wave incident angles and reflection angles for the exact model and the smoothed model 124
Figure 6.6: Weight distribution for S-impedance and density reflectivity from PS-wave inversion 126
Figure 6.7: Inverted results from PS-data alone 127
Figure 6.8: PS-wave synthetic gathers by Zoeppritz equation 128
Figure 6.9: Iverted results from PS-data alone at depth from 3100m to 3200m 129
Figure 6.10: Weight distribution for P- and S-impedance reflectivity from PP-wave inversion. 131
Figure 6.11: Full offset data and the muted data. 132
Figure 6.12: Inverted results for the full offset data and the muted data 133
Figure 6.13: S-impedance reflectivity in the absence of gas and in the presence of gas from PP-data alone 135
Figure 6.14: PP-wave and PS-wave synthetic gathers 136
Figure 6.15: Weight W applied to PS-data in joint inversion 136
Figure 6.16: PP alone and joint inversion results with or without noise 137
Figure 6.17: PP synthetic shot gathers for Model 1 140
Figure 6.18: PS-synthetic shot gathers for Model 1 141

Figure 6.19: Effect of Poisson's ratio and tuning on PP-wave for Model 1. 142
Figure 6.20: Effect of Poisson's ratio and tuning on PS-wave for Model 1 144
Figure 6.21: Effect of Poisson's ratio and tuning on PP-wave for Model 2. 145
Figure 6.22 Effect of Poisson's ratio and tuning on PS-wave for Model 2. 146
Figure 6.23 Pseudo Poission's ratio reflectivity of Model 1 and Model 2.....147
Figure 6.24: Blocked logs of the gas well S6.....148
Figure 6.25: Synthetic seismogram of PP-data and PS-data.....150
Figure 6.26: Joint inversions for the elastic impedance. 151
Figure 6.27: $\lambda\rho$ reflectivity from joint impedance inversion and λ reflectivity.....151
Figure 6.28: Common image point gathers at the gas well S6.....153
Figure 6.29: Final migrated image of PP- and PS-data.....153
Figure 6.30: P-impedance reflectivity from PP-data alone and joint inversion.....154
Figure 6.31: model-based inversions for P-impedance.....156
Figure 6.32: S-impedance reflectivity from PP-data alone and joint inversion.....157
Figure 6.33: model-based inversion for S-impedance. 157
Figure 6.34: $\lambda\rho$ from both PP- and joint-inversion.....158
Figure 7.1: Predicted P- and S-velocity and attenuation as a function of non-dimensional frequency $\omega\tau$ under gas and water saturation 165
Figure 7.2: A synthetic seismogram and its short time Fourier transform with Gaussian window function at the different time window.....169
Figure 7.3: The amplitude spectra for the synthetics in Figure 7.2.....170
Figure 7.4: A synthetic seismogram and its wavelet transform with Gaussian wavelet at the different frequency band 171
Figure 7.5: PP stacked sections from example 1, band-passed into low and high frequency sections 173
Figure 7.6: PP-wave reflection coefficients under both water and gas saturation in low and high frequency limit.....174
Figure 7.7: Balanced spectra for PP-wave gas saturation at the different frequency for the different time scale.....176
Figure 7.8: "Difference traces" formed by stacking the synthetic data, performing spectral decomposition, consistent spectral balancing and subtracting the 30 Hz trace from the 15 Hz trace.....178
Figure 7.9: The results of balancing and differencing the sections from Figure 7.5. 179

Figure 7.10: PS-wave reflection coefficients under both water and gas saturation cases in low and high frequency limits 180

Figure 7.11: Balanced spectra for PS-wave gas saturation at the different frequency for the different time scale..... 181

Figure 7.12: Balanced spectra for PS-wave water saturation at the different frequency for the different time scale..... 182

Figure 7.13: PS-wave synthetic for high frequency limit under water saturation.. 183

Figure 7.14: The stack section showing a dim spot from the gas reservoir at 2.25s 184

Figure 7.15: The amplitude spectra from inside (CDP 1000-1020) and outside (CDP800-820) gas reservoir..... 185

Figure 7.16: Iso-frequency sections showing a systematic amplitude increase from 15hz to 30hz 186

Figure 7.17: Frequency-dependent reflection coefficients in the low and high frequency limits for a Class I AVO sand in Table 7.2 189

Figure 7.18: The synthetic seismograms for the thick gas saturation layer in Table 7.2 190

Figure 7.19: Amplitude spectra for the gas and water-saturated thick layers at the offset 2000m.. 191

Figure 7.20: Iso-frequency spectra from 15hz to 40hz for the gas-saturated thick-layer in the low frequency limit case..... 193

Figure 7.21: The picked amplitude values with offset from the gas-saturated iso-frequency spectra at low and high frequency bands..... 196

Figure 7.22: The picked amplitude values with offset from the water-saturated iso-frequency spectra at low and high frequency bands..... 197

Figure 7.23: The parameters for the multi-thin layer model.. 198

Figure 7.24: The synthetic seismograms for the multi-thin layered model with gas saturation in the low frequency limit case and in the dispersion case. 199

Figure 7.25: Amplitude spectra for the gas and water-saturated multi-layered model 200

Figure 7.26: The picked amplitude from the gas-saturated multi-thin layered model. 201

Figure 7.27: The picked amplitude values from the water-saturated multi-thin layered model 202

Figure 8.1: The physical model used in the study..... 208

Figure 8.2: Acquisition geometry of the physical modelling experiment..... 209

Figure 8.3: Illustration of the Class I AVO by pure elastic-wave modelling.....210

Figure 8.4: The 2D fixed-offset data for water-, oil- and gas-saturated model with seven sand layers. 212

Figure 8.5: The amplitude spectra of the reflections from the water bottom for the seven sand-layered model. 214

Figure 8.6: The average amplitude spectra and spectra ratio for the top of the overburden between trace 30 and 80 215

Figure 8.7: The amplitude spectra of the reflections from the thin-layered reservoir for the seven sand-layered model in Figure 8.4 216

Figure 8.8: The average amplitude spectra and spectra ratio for the thin beds between trace 30 and 80 217

Figure 8.9: Instantaneous spectra for seven sand layered models in trace 40.....219

Figure 8.10: Instantaneous spectra for seven sand layered models in trace 60.....220

Figure 8.11: Instantaneous spectra for seven sand layered models in trace 80.....221

Figure 8.12: Instantaneous spectra for seven sand layered models in trace 30.....222

Figure 8.13: Iso-frequency sections for the gas-saturated model with seven sand layers in Figure 8.4. 223

Figure 8.14: Application of the static correction for the water-saturated models in Figures 8.4 and 8.5. 225

Figure 8.15: Instantaneous spectra for the seven sand layered models for the summed fixed-offset traces.....226

Figure 8.16: Stacked sections of the 2D survey for water-, oil- and gas-saturated models with seven sand layers 226

Figure 8.17: The average amplitude spectra and spectra ratio for the thin beds between CDP 120 and 240 in Figure 8.19.....229

Figure 8.18: Comparison of the iso-frequency sections for water- and oil saturated models at 30hz. 231

Figure 8.19: Iso-frequency sections for gas-saturated model.....232

List of Tables

Table 3.1: The acquisition parameters of the line 03585B 23

Table 4.1: Modelling parameters to examine the accuracy of the travel time equations.....51

Table 4.2: The PP-wave stacking velocity calculated by PS-wave moveout analysis. Offset depth ratio is 2. 59

Table 4.3 The PP-wave stacking velocity calculated by PS-wave moveout analysis. Offset depth ratio is 1.5. 68

Table 4.4: The PP-wave stacking velocity calculated by PS-wave moveout analysis. Offset depth ratio is 2.5. 68

Table 4.5: Optimum picked γ^*_{iso} and calculated V^*_{p2} in T_{c0} 68

Table 4.6: Results of double scanning from the Ordos data 74

Table 5.1: P-wave velocity, density data in the Ordos basin 102

Table 6.1: The S-impedance reflectivity for the model and the PS-wave inversion results.....126

Table 6.2: The S-impedance reflectivity and PS-wave inversion results.....130

Table 6.3: The P-impedance reflectivity and PP-wave inversion results.....133

Table 6.4: The S-impedance reflectivity and PP-wave inversion results.....134

Table 6.5: The parameters of Model 1 and Model 2 139

Table 6.6: Impedance, Lamè constants average change in brine and gas sand cases 149

Table 7.1: Parameters used in the computations for Example 1 173

Table 7.2: The elastic parameters used for numerical modelling 188

Table 8.1: The scaling ratio used in the physical modelling study. 207

Table 8.2: The elastic parameters of the seven-sand layer model.....210

Chapter 1: Introduction

1.1 Motivation

In oil & gas exploration, initially, the focus has been on the use of compressional P-waves for studying the subsurface structure. Not until the mid 1980's, did the use of shear waves for investigating rock properties start to emerge (e.g. Crampin, 1985; Alford, 1986; McCormack and Tatham, 1991; Li, 1997; Garotta, 2000; Thomsen, 2002), which leads to the development of multicomponent seismology. Nowadays, multicomponent seismology for the resource exploration has been gained much more acceptance than was the case twenty years ago.

In recent years, multicomponent (MC) seismic data have been used to improve both seismic imaging and reservoir characterization due to the advent of digital sensor technology (Calvert, 2005). By means of shear wave information, which is less affected by the presence of gas, improved imaging beneath shallow gas clouds can be obtained using MC data (Thomsen, 1999; Li *et al.*, 2001). Because P-wave and S- waves sense different rock and pore-fluid properties, joint use of PP- and PS-data can provide better lithology and fluid discrimination. Roche *et al.* (2005) reported the use of converted-wave reflectivity recorded by MEMS sensors for mapping gas production in sand reservoirs, and Mattocks *et al.* (2005) presented examples for characterizing fractures in carbonates.

Despite these various efforts, the anticipated breakthrough of multicomponent seismic into a mainstream science or technology is still to be realized. One of the bottlenecks lies in the interpretation and analysis of multicomponent seismic data, which has not experienced as rapid a progress as the acquisition and processing of MC data. To understand where the gaps lie, the Society of Exploration Geophysicists (SEG) held an investigation in a workshop in 2000, and the results were published in SEG website, which indicates that the only proven applications

are on imaging below gas clouds and imaging targets with low P-wave impedance contrast. Other applications such as lithology delineation, fluid discrimination, fracture characterization and reservoir monitoring still need to be proven. Tatham (2002) believes this is due to a lack of understanding of how to fully exploit these types of data by interpreters. In generally, there is a still lack of understanding on how to link the multicomponent seismic information to rock properties directly.

In this thesis, I tackle this problem through a joint inversion of multicomponent PP and PS-seismic data in order to facilitate the direct comparison of seismic information with rock properties. For this purpose, I study some basic problems related to joint inversion, such as correlation of the PP and PS data, estimation of the V_P/V_S ratio and PP and PS-AVO responses. I write the code for joint PP- and PS-inversion and also develop the workflow to evaluate the merit of PP- and PS-joint inversion, test the workflow through numerical modelling and apply them to field data. Furthermore, I study the frequency-dependent behaviours of the PP- and PS-waves in thin-layered sand reservoirs containing different fluids in order to gain a more fundamental understanding of the wave behaviours during fluid substitution.

One technique that I focus on in MC interpretation is event registration between PP- and PS-wave data. Through the determination of an average, vertical V_P/V_S (or γ_0), PS-wave data are stretched to PP-time. Currently, event registration in practice is mainly based on interpretive and qualitative approaches. Seeking a reliable quantitative method is still necessary (e.g. Gaiser, 1996; Kristiansen *et al.*, 2003; Nickel and Sonneland, 2004).

Joint PP- and PS-wave AVO inversion based on weighted stacking techniques (Goodman, 2002) has been a robust method and provided the potential to determine elastic parameters such as P and S-wave velocity, impedance, Poisson's ratio, and Lamè constants from amplitude variations on the pre-stack seismic data. Some rock properties are more preferable to others in reservoir description due to the specific geology and geophysics conditions, such as thin-layer tuning. It is necessary to

evaluate the merits of different approaches and to understand the limitation of different elastic parameters using synthetics based on wireline logs.

Since Taner *et al.* (1979) reported low frequency shadows underneath the gas reservoir zones, high attenuation related to gas reservoirs has been observed on both VSP and seismic data (e.g. Kan *et al.*, 1983; Klimentos, 1995; Dasios *et al.*, 2001; Castagna *et al.*, 2003). However, standard AVO analysis based on Gassmann fluid substitution is frequency independent and ignores attenuation and dispersion. Based on a number of frequency-dependent models developed in recent years (Hudson *et al.*, 1996; van de Kolk *et al.*, 2001), Chapman (2003) provides a correction to Gassmann and considers the dispersion effect during fluid substitution. Through numerical modelling, Chapman *et al.* (2005) have suggested that the fluid-related dispersion may have a pronounced effect on the AVO behaviour at the interface. However, it is an unclear matter whether or not one can robustly detect such effects in field data or to demonstrate that the signatures from the simple single layer models persist into the more complicated multi-layer cases. In this thesis, these issues and their implications for the use of MC data for characterizing thin-layer reservoirs will be investigated using numerical modelling and seismic physical modelling, as well as field multicomponent data.

1.2 Objective and outline of the thesis

The main objectives of the thesis are to estimate the V_p/V_s ratio quantitatively from multicomponent PP- and PS data for event correlation; to develop a practical multicomponent interpretation and inversion workflow for reservoir description; and to investigate the use of frequency-dependent PP- and PS-AVO for characterizing thin-layered sand reservoirs.

In Chapter 2, I first give a brief review of the acquisition and processing of multicomponent data, then give a detailed description of application of MC data. A

practical workflow for MC interpretation and inversion is explained. It includes prestack time migration for CIP gathers, event registration, pre-conditioning PP- and PS-data, and velocity model building for joint AVO inversion.

Chapter 3 introduces the 3C data from the Ordos basin, North China. The data are acquired by MEMS digital sensors. PP-wave and converted-wave data are processed by the author. The processing flow is described, which aims to apply an amplitude-preserved processing and help noise attenuation.

Chapter 4 reviews the event correlation methodology in literature. A new method is put forward based on a modified converted-wave travel time equation. The accuracy of the modified travel time equation is tested on a five-layer-isotropic model. Event registration is demonstrated on synthetics through converted-wave moveout analysis. Sensitivity analysis of γ_{iso} for different offset/depth ratios is performed. Finally, the method is applied to the Ordos data.

In Chapter 5, the definition of AVO classification is briefly described, and fluid substitution based on Gassmann Equations is reviewed. Through the analysis of the laboratory data and well log data, the sensitivity of the different rock properties to the lithology and fluid is illustrated. PP-wave AVO analysis on well logs and real data shows the difficulty in traditional AVO attribute analysis for the study area; Lamè parameters show an advantage in fluid discrimination over the impedance attributes.

Chapter 6 first reviews the linear least square AVO inversion methods. A joint PP- and PS-AVO inversion algorithm is described by a full use of Aki-Richard equations without cancelling the density term. The method is tested by the synthetic and real data. Compared to the single wave mode inversion, joint inversion improves the accuracy of Shear-impedance. The offset-dependent tuning effect is also investigated, which has an adverse effect on both PP- and PS-AVO.

Chapter 7 extends standard AVO analysis to frequency-dependent AVO and introduces the dynamic fluid substitution concept and spectral decomposition technique. Numerical modelling reveals that there is a shift of the reflection energy towards lower frequency ends for traditional Class III AVO, and towards higher frequencies for Class I AVO, which are observed on field data as well. Comparing the thick-layer model without tuning with the multi-thin-layer model with tuning, I conclude that tuning does indeed make the analysis difficult, but that the effect of dispersion can still be observed.

In Chapter 8, I use eleven-layer and fifteen-layer thin inter-bedded sand/shale physical models to evaluate the frequency dependent variation in different fluid saturations and examine the high frequency effect predicted in Chapter 7. Application of spectral decomposition on both 3D fixed-offset data and 2D stacked data demonstrate that there is a systematic shift of energy to the high frequencies in the gas-saturated case, which does agree with the numerical modelling.

Finally, Chapter 9 summarizes the thesis and discusses some possible future work.

1.3 Datasets and software used in this thesis

The Synthetic seismograms in Chapter 4 for semblance analysis are generated using Seismic Unix (CWP, Colorado School of Mines); PP- and PS-AVO synthetics in Chapter 5 and 6 are generated using AVO modelling (HampsonRussell). Frequency-dependent AVO synthetics in Chapter 7 are generated by ANISEIS (David Taylor).

2D 3C land data from the Ordos basin of north China are processed using the CX-tool (EAP) and ProMAX (Landmark). 2D lines from northeast China are processed using a spectral decomposition technique (EAP).

Eleven-layer and fifteen-layer inter-bedded sand/shale physical models provided by CNPC Key Geophysical Laboratory are used to analyze the frequency dependent variation in the different fluid saturations.

The codes for semblance analysis in Chapter 4 and AVO inversion in Chapter 5 and 6 are written by the author. The events between PP- and PS-wave are correlated using the CX-tool (EAP) and ProMC (HampsonRussell). The post stack inversion in this thesis is by STRATA (HampsonRussell). The frequency-dependent elastic constants are calculated using a FORTRAN code (EAP).

Chapter 2: Overview of multicomponent seismic

2.1 History of multicomponent seismic

In the 75 year history of applying seismic technology in oil and gas industry, use of the compressional wave, or P-wave, has achieved great success with technology advancing from 2D, 3D to time lapse 4D surveys. However, P-wave methods cannot solve every seismic imaging or reservoir description problem. P-wave velocity is a function of density, bulk modulus and shear modulus, and is sensitive to both the medium solids and fluid contents. The effect of the decrease in bulk modulus due to increasing sand porosity is offset by the increase in shear modulus from shale to sand. Shear wave velocity, a function of density and shear modulus of the medium, is insensitive to a rock's fluid content and thus has less ambiguity in differentiating litholgy. Combining both P-wave and S-wave information is beneficial in solving imaging problems caused by gas clouds and small P-wave impedance contrast, and also in lithology and fluid discrimination. Barkved *et al.* (2004) concluded that in areas where conventional seismic techniques are inadequate, multicomponent methods that use information from both compressional and shear waves are reducing exploration risk and improving reservoir management.

The first attempts at S-wave in the exploration and production industry date back to the 1950s and the practical experiments were on land using an S-wave source (Jolly, 1956). Since then, many efforts at improving S-wave sources have been made. These efforts were very useful for improving the understanding of S-waves. However, none of these have seen practical use due to poor signal to noise ratio.

Towards the end of 1980s, use of a P-wave source to generate S-waves has grown rapidly because it has been proved that a downgoing P-wave can generate an upgoing S-wave at reflectors, not seabed, which is fortunate for marine

multicomponent surveys. With the development of measurement systems, land 3C and cable 4C detector systems have been used commercially. In the past seven years, around 200 PS-wave surveys worldwide have been acquired and processed (Gaiser and Strudley, 2005). Recently, a new digital sensor system using micro-electro-mechanical accelerometers (MEMS) has been developed. Compared to the conventional analog geophone array, these sensors can record the full seismic wave field (both pressure and shear waves) with high accuracy and in three dimensions, and provide more fold coverage, better signal to noise ratio, wider bandwidth, and a more accurate amplitude response (Gibson *et al.*, 2003). Although still at early stage of technology adoption, it is believed full-wave seismic increasingly will become the standard within the next several years (Peebler and White, 2005).

Because of the asymmetry of the converted wave raypath from the source to the receiver, the reflection point is no longer the midpoint between the source and receiver as in PP-wave raypaths. Processing of converted wave (PS-wave) data becomes more complicated. The challenges in MC processing include the common conversion point (CCP) position location; adequate NMO corrections for the medium and long offsets since converted energy is mostly contained in the middle-to-far offset traces; and anisotropy effects in residual moveout. Much research work has been done (e.g. Tsvankin and Thomsen, 1994; Zhang, 1996; Thomsen, 1999; Li and Yuan, 2001a, 2001b, 2003), and put into practice successfully (e.g. Nolte *et al.*, 1999; Bagaini *et al.*, 1999 and among others). Now, converted-wave anisotropic prestack depth migration is a focus of technology development to improve resolution and image quality (Dellinger *et al.*, 2002).

2.2 The applications of multicomponent data: A review

Advances in acquisition and processing of MC data have led to the improvement of data quality, which simulates the interpretation and application of these data.

Caldwell (1999), Stewart *et al.* (2003) and Tatham (2006) outline the applications of multicomponent data. The following summarize these potential applications.

Gas cloud imaging

One of the most wide acceptable applications of multicomponent data is gas cloud imaging. Many cases from marine 3C or 4C data (e.g. Thomsen *et al.*, 1997; Caldwell, 1999; Pope *et al.*, 2000; Li *et al.*, 2001; Kommedal *et al.*, 2002; Nahm and Duhon, 2003; Tian *et al.*, 2004; Mancini *et al.*, 2005) have successfully demonstrated the better PS-wave structural sections. Because the shear wave leg of PS-wave is insensitive to saturated fluid, PS-wave reflections are not distorted or attenuated by the presence of the shallow gas. Interpreters can use the traditional interpretation techniques of PP-wave data straightaway in PS-wave data (Caldwell, 1999). Figure 2.1 is one of the earliest examples that showed the usefulness of PS-wave data compared to PP for imaging through a gas cloud, from the Tommeliten field in the Norwegian sector of the North Sea. The PS-wave section demonstrates a useful image beneath the gas chimney, which disrupts the PP-wave section.

Direct Hydrocarbon Indicator

Based on a similar principle to multicomponent data application in gas cloud imaging, direct hydrocarbon identification utilising PS-wave has been used in identifying true or false bright spots shown on the PP-wave. Since there is a dramatic P-wave velocity drop with gas saturation, a strong PP-reflection is observed in processed PP-section, as opposed to no response on PS-section due to the insensitivity of S-wave to gas. A strong response both on PP- and PS-reflection is expected as a lithologic response. Applications have been found in both land and marine data (e.g. De Tomasi, 1996; Caldwell, 1999; Thompson *et al*, 2000; He *et al.*, 2002; Li and Gu, 2004; and Podolak, 2004).

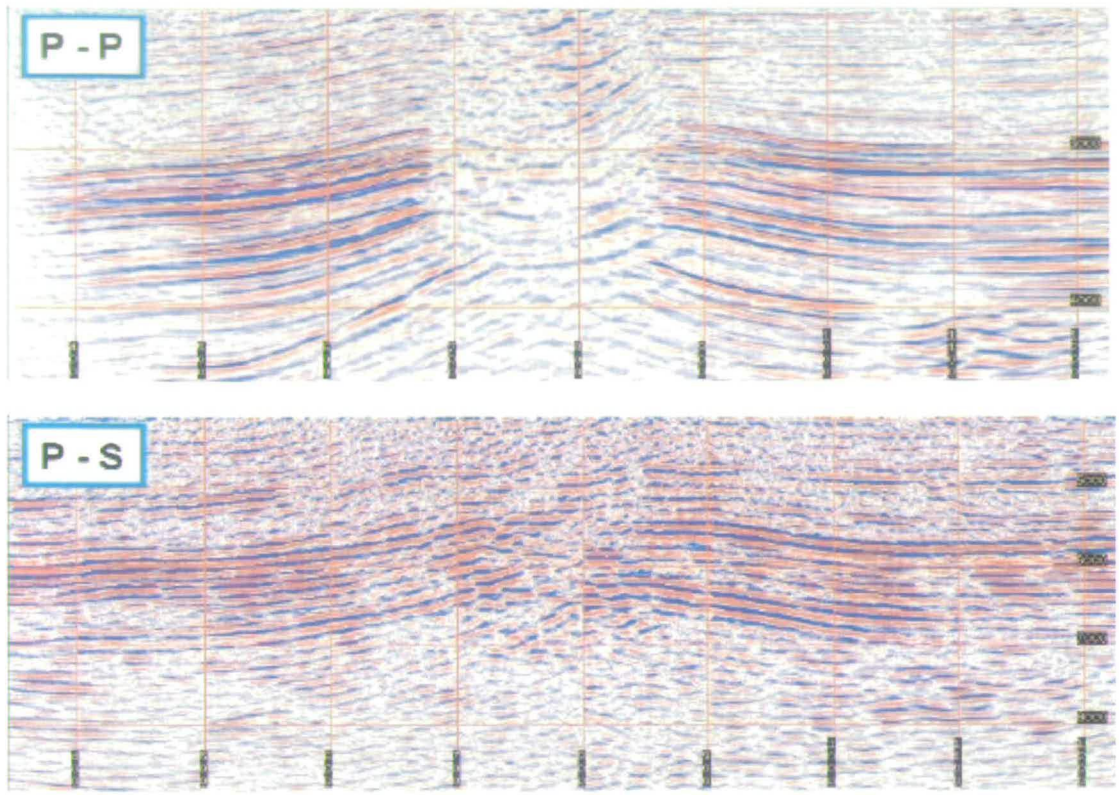

Figure 2.1: This example is from the Tommeliten Field in the Norwegian sector of the North Sea, courtesy of Statoil. It is one of the earliest examples that demonstrated the usefulness of PS-wave data compared to PP for imaging through a gas cloud. Note how the gas chimney disrupts the PP-wave (upper section), while allowing the S-wave (lower section) energy to generate a useful image beneath the gas chimney (Caldwell, 1999.)

Type II sand discrimination

Multicomponent data is also applied to detecting the sand with large S-wave impedance contrast associated with small P-wave impedance contrast (Type II sand). Top reservoir is absent on PP reflection section due to small or no change in P-wave velocity between reservoir and overlaid rocks, whilst strong PS-reflection reveals a clear reservoir top due to a large change in S-wave velocity. Good examples can be found in both marine and land applications (e.g. MacLeod *et al.*, 1999; Probert and Wells, 2000; Stearn and Backhouse, 2001; Stewart *et al.*, 2003; Wei *et al.*, 2003).

As a seismic lithology analysis tool, the Amplitude Versus Offset (AVO) method has been practiced in the petroleum industry for more than 20 years. In recent years, much work has shown a great promise for lithology identification and fluid discrimination using joint PP- and PS-wave AVO interpretation (e.g. Stewart, 1994; Larsen, 1999; Margrave *et al.*, 2001; Goodway, 2002; Gray, 2003). Furthermore, the PS-wave offers another source of information (or constraint) for distinguishing partial gas saturation by utilizing the S-wave impedance, the P- and S-impedance ratio, and density contrasts. Although this still remains to be fully tested, the results are encouraging (Caldwell, 1999).

The application of 3C/4C data in joint AVO analysis is not straightforward and requires correlation between PP- and PS-wave data by the determination of an average, vertical V_p/V_s (or γ_0). Due to the frequency bandwidth and polarity difference between PP- and PS-data, event registration is no easy task and a focus of technology development. Estimating the V_p/V_s ratio is also becoming important in multicomponent processing such as long-period static corrections, CCP-binning, Kirchhoff prestack time migration and prestack depth imaging.

Estimation of the V_p/V_s ratio is also beneficial for reservoir description. V_p/V_s ratio is used as a lithology/fluid indicator based on a relationship between V_p/V_s ratio and lithology and gas saturation (Figure 2.3). For example, Pickett (1963) obtained values of V_p/V_s near 1.9 for limestone, 1.8 for dolomite, and 1.6-1.75 for sandstone. Furthermore, V_p/V_s is sensitive to fluid in sedimentary rocks. V_p/V_s can be 10-20 percent lower for gas saturation compared to liquid saturation (Gardner *et al.*, 1968).

Macleod *et al.* (1999) presented 4C 3D data of the Alba field in the North Sea showing an oil-filled sand where the sonic logs indicate no change in V_p and a large change in V_s. P-wave impedance contrast between the top of the reservoir and the overlying rocks is very small (Figure 2.2), whilst the PS-section clearly shows the top-of-reservoir event. The oil-water contact is visible in both sections.

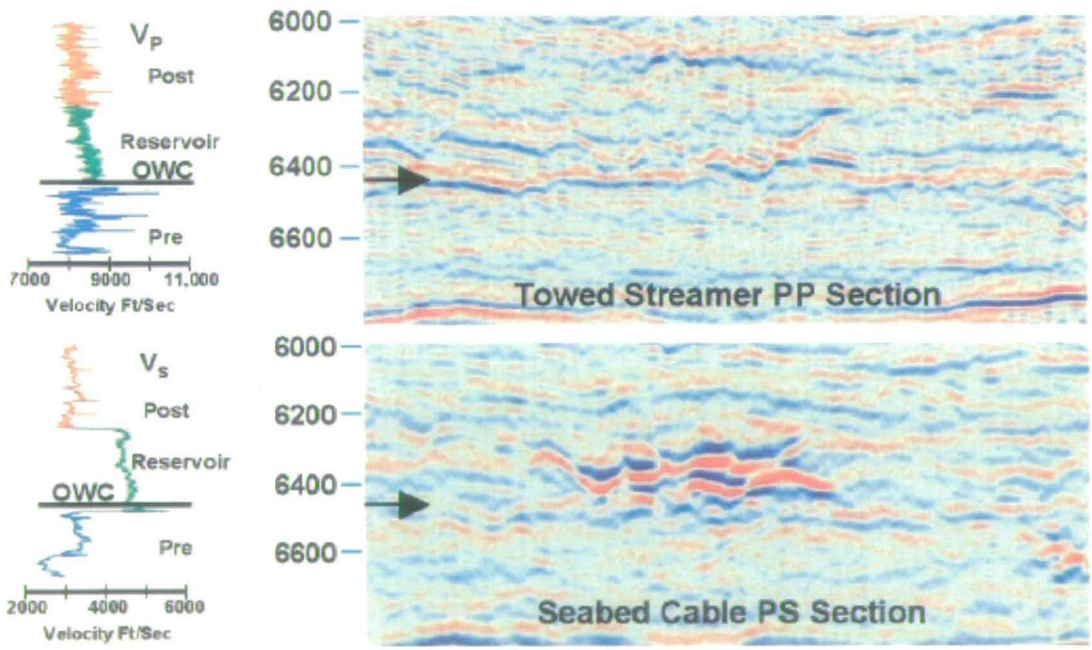

Figure 2.2: Converted-wave image (bottom) showing dramatically improved imaging of Type II Sand relative to the streamer P-wave data (top) (Macleod *et al*, 1999).

Structural and velocity model building for P-wave prestack depth migration

To improve PP-wave imaging degraded by gas clouds, prestack depth migration is necessary. However, it is difficult to build a P-wave velocity model in such case. Dellinger *et al.* (2002) use a PS-wave image as a constraint on the P-wave velocity model. Through careful velocity model building using well logs and the PS-wave image as a structural and velocity model guide, prestack depth migration obtains the improved PP-wave images.

Lithology and fluid prediction

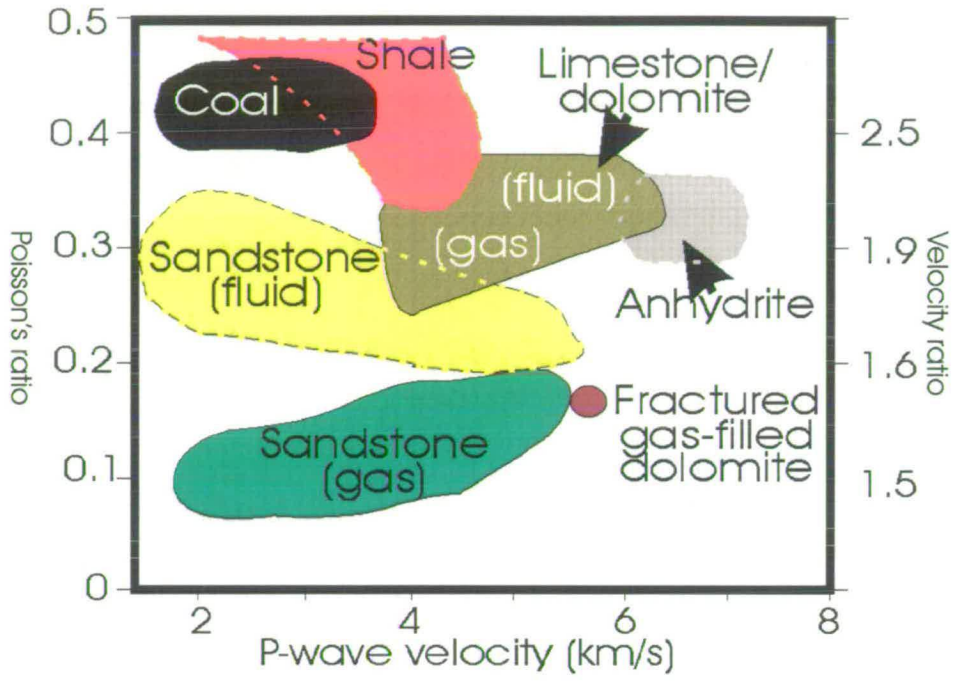

Figure 2.3: A relationship between V_p/V_s (Poisson's ratio) and lithology (Berg, 1997).

Fracture Prediction

Using seismic anisotropy, particularly shear wave splitting, to estimate fracture parameters such as fracture orientation and density from multicomponent data has been a subject of considerable effort (e.g., Li *et al.*, 1995; Gaiser, 1999; Probert *et al.*, 2000; Vetri *et al.*, 2003). Some work (e.g. Li *et al.*, 1996; Guest *et al.*, 1998) has suggested that that gas saturated and oriented fractures may have an effect on anisotropic PS-reflectivity: this is contrast to the isotropic case, where fluid saturation appears to have less impact on S-wave velocity.

Reservoir monitoring

The application to reservoir monitoring is still in its the early stages. Pioneering studies have used time-lapse data to estimate potential variation in fluid pressure (e.g. Spitz *et al.*, 2000; Lewis *et al.*, 2003).

2.3 A practical work flow

Unlike for P-waves, there is no recognised standard workflow for MC interpretation and inversion. The key issues in the workflow include event registration in time, PP- and PS data conditioning for joint inversion, and inversion methodology.

The first step is to consider what type of data should be used in inversion. Seismic amplitude interpretation and inversion have encouraged the need for preserved-amplitude seismic processing. Provided that the migration can restore the amplitude distortions of wave propagation between sources and receivers, it is thus possible to correct some of the problems, such as CDP smear, geometrical spreading loss, source/receiver directivity, by analyzing common-image-point (CIP) gathers rather than CDP gathers. Based in this principle, I have processed the field PP- and PS-wave data using a prestack Kirchhoff time migration approach aiming to obtain amplitude preserved PP/PS-CIP gathers.

Event registration is a focus in MC interpretation. Joint inversion is performed on each data sample. However, it is difficult to correlate PS-data with PP-data sample by sample because of the different frequency contents and uncertainty in phase. A practical way is to match major reflectors and target reservoir layers. I use two approaches for converting PS-data into PP-time. First, I performed PS-wave moveout analysis to obtain γ_0 for major reflectors. Using these γ_0 as a reference, a set of γ_0 can also be obtained from migrated stacked PP- and PS-profiles by interpretive methods. Horizon interpretation was performed through seismic ties to wells. Synthetic data used in well-seismic tie are from well logs. In the case that shear logs are not available, they are needed to build up.

Pre-conditioning on PP- and PS-CIP gathers should be performed before joint inversion, which include frequency matching and amplitude scaling between PP-

and PS-data. For the field data, if polarity in PP- and PS-data is unknown, AVO modeling based on well logs can be used to confirm the polarity in PP- and PS-data.

The wavelet variation (amplitude and phase) from near to far offsets is one of major hindrances in AVO inversion. Phase shifts need to be applied on PP/PS-data to ensure zero-phase for all offsets by tying seismic data to a zero phased synthetic.

Velocity-depth models at well locations are built for ray-tracing and velocity background of inversion. Figure 2.4 shows a workflow I performed for interpretation and inversion of MC data in this thesis.

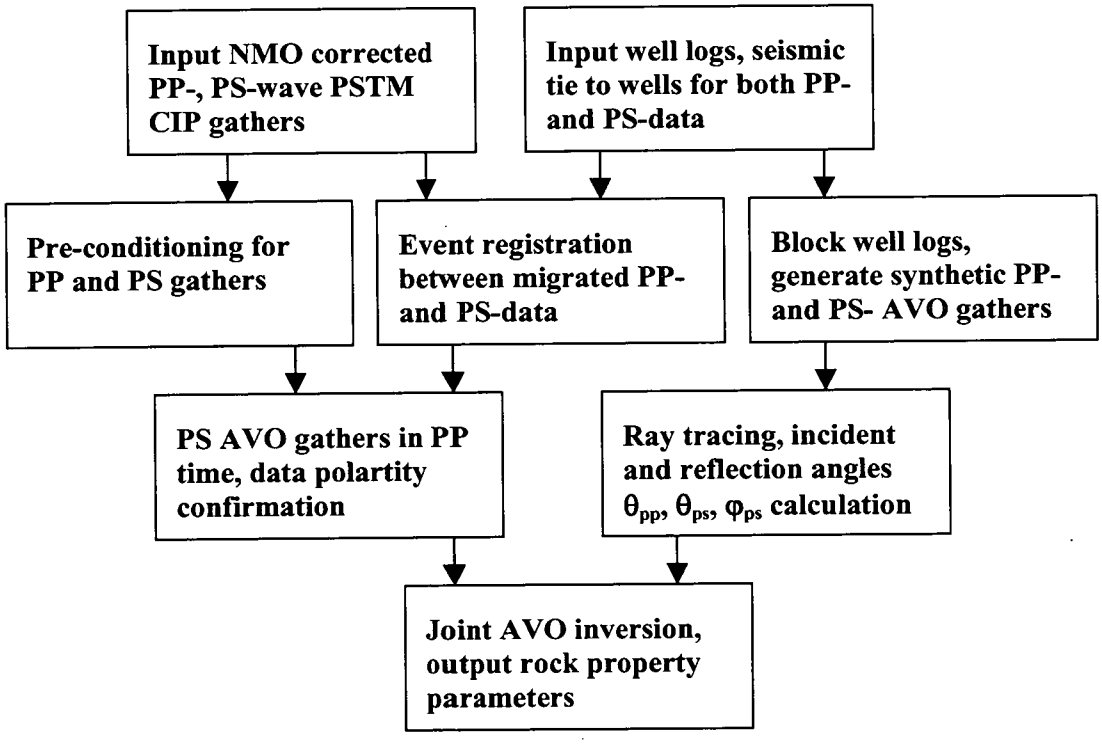

Figure 2.4: A workflow for joint PP- and PS-data interpretation and inversion in the thesis.

Chapter 3: Ordos multicomponent data processing

3.1 Introduction

The lithology changes within the earth can be predicted from the elastic parameter contrasts, which manifest themselves on seismic response as offset/angle dependent reflectivity (AVO/AVA). In order to measure reflectivity reliably, amplitude preserved seismic processing has been encouraged in AVO development. Gray (1997) indicates that interpretation of angle dependent reflectivity on unmigrated records is often hindered by the effects of common-depth-point (CDP) smear, incorrectly specified geometrical spreading loss, source/receiver directivity as well as other factors. Cambois (2000) points out once the data are corrected for propagation effects (spherical divergence, NMO) through prestack migration, the velocity field is raytraced to derive a relationship between offset, arrival time, and incidence angle. Then the desired lithology parameters can be obtained by fitting Zeoppritz approximation equations to the prestack amplitude samples.

3C data of the study area were acquired using a newly-developed digital sensor. Vertical (Z) and horizontal (X) components are processed by the author using a prestack Kirchhoff time (PSTM) migration approach. Since the structure in the study area is generally flat, PSTM is adequate when dealing with simple geologic structure. For complex structure, AVO analysis following prestack depth migration (PSDM) is imperative. Due to the enhanced imaging and accurate reflection point position by PSTM, we can use common-image-point (CIP) PP/PS-gathers from PSTM rather than CDP gathers as input for AVO inversion. Special cares are taken in the process flow, e.g. static correction and ground roll removal. A detailed PS-wave processing flow used in a 2D-3C line of the area is explained.

3.2 The study area

The Ordos basin is located in north China within the Yellow River drainage basin between latitudes 34°00′N to 40°35′N and longitudes 106°50′E to 110°10′E, and covers an area of 250,000 Km^2 (Figure 3.1a). The Palaeozoic and Mesozoic intervals are the main exploration layers. The Paleozoic stratigraphy of the Ordos basin consists of a Cambrian-Ordovician section that is dominantly marine limestone and dolomite, and a Carboniferous-Permian section that varies from shallow marine limestone, sandstone and shale lower in the section to mostly deltaic and fluvial sandstone and mudstone in the higher section.

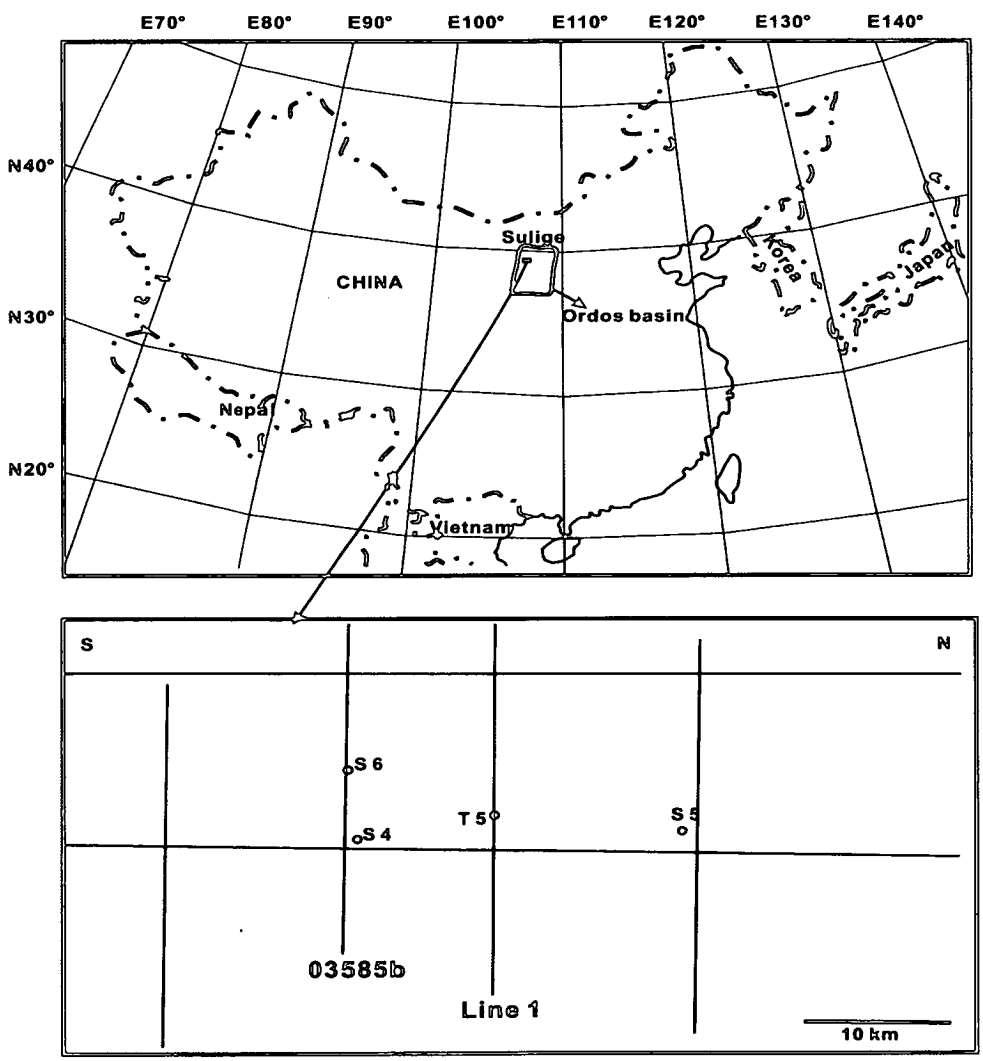

Figure 3.1a: Study area Sulige, Seismic lines and wells location map.

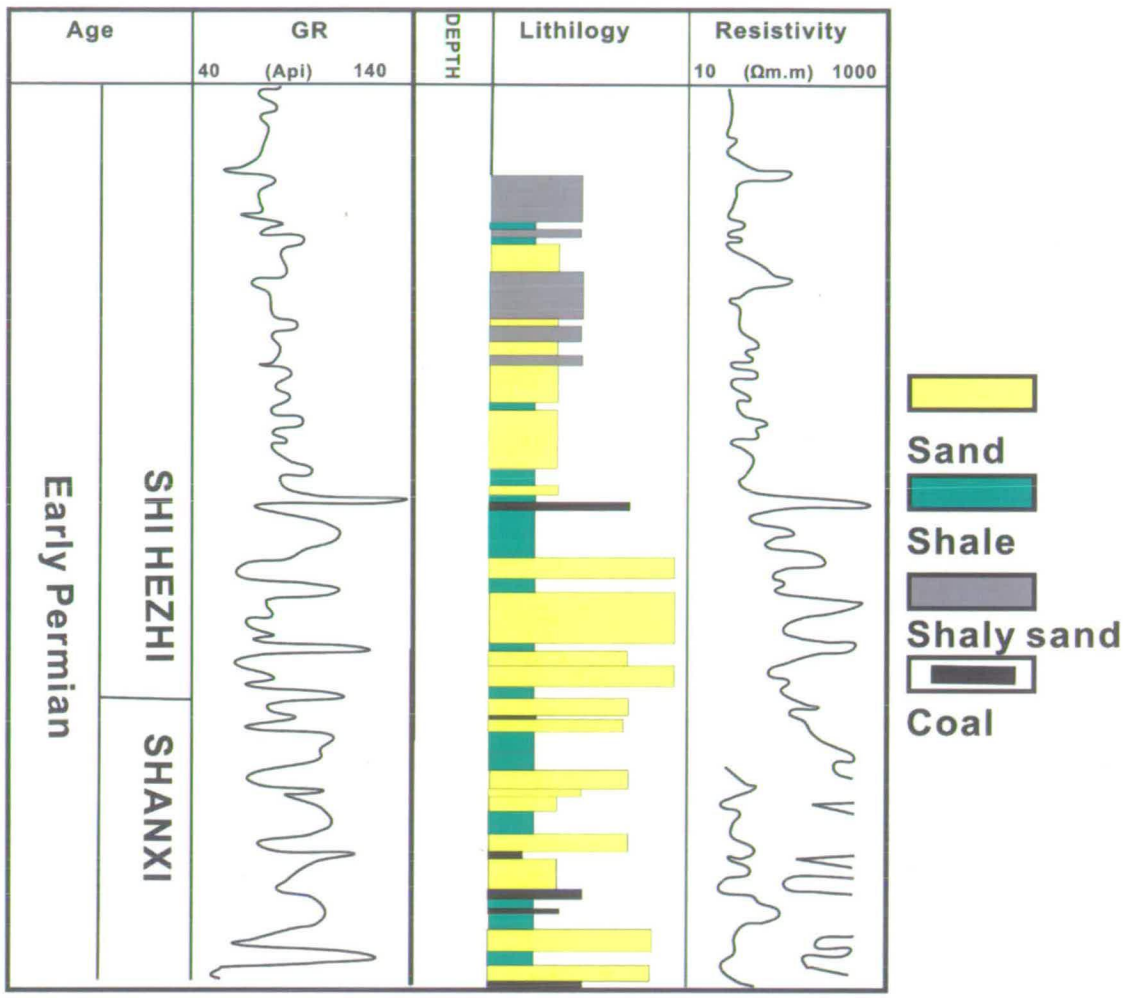

Figure 3.1b: Stratigraphic column of Shihezi and Shanxi formations (adapted from an internal report).

The study area Sulige, situated in the western part of the Ordos basin, was discovered in 2000 and proved as the largest gas field in China. The surface is covered with desert sands, and the thickness of the low velocity near surface layer varies from100m to180m. Reservoirs are dominated by coarse-grained sandstones of the Lower Permian Shihezi and Shanxi formations, especially those of the H8 and S1 units (Figure3.1b). These sands, with an average burial depth of 3200-3500m, were deposited in a braided-river environment. Due to the deep burial depths, primary porosity was reduced significantly; however, secondary dissolution

pores developed, accounting for 80% of the total pore spaces (He *et al.*, 2006). The average porosity of the gas reservoir in the H8 unit is 12%. The gas saturation can be up to 70%.

The S1 unit has a relatively thick (15 to 25 m) sandstone reservoir; the sand contains a high content of quartz. The velocity of the gas sandstone is relatively high (4600 to 4800 m/s) contrasting with the low velocity surrounding mudstone (3500 to 4500 m/s) and coals (2200-2800 m/s). The obvious P-impedance contrast between the sandstone and the surrounding rocks causes the medium to strong amplitude reflections on the P-wave seismic.

In the H8 unit, the gas layer is thin (8 to 12 m). The velocities of the sandstone (3800-4400 m/s) and mudstone (3500-4500 m/s) are quite similar. Because the beds are thin, the weak P-impedance contrast and composite layers make the P-wave reflections very weak. The acquisition, processing and interpretation of multicomponent data aim to obtain a better image and identify the gas reservoirs. Figure 3.2 is a pilot line (Wei *et al.*, 2003) of the study area showing the weak P-wave reflection due to the presence of gas and strong PS-reflection due to the insensitivity of S-wave to gas.

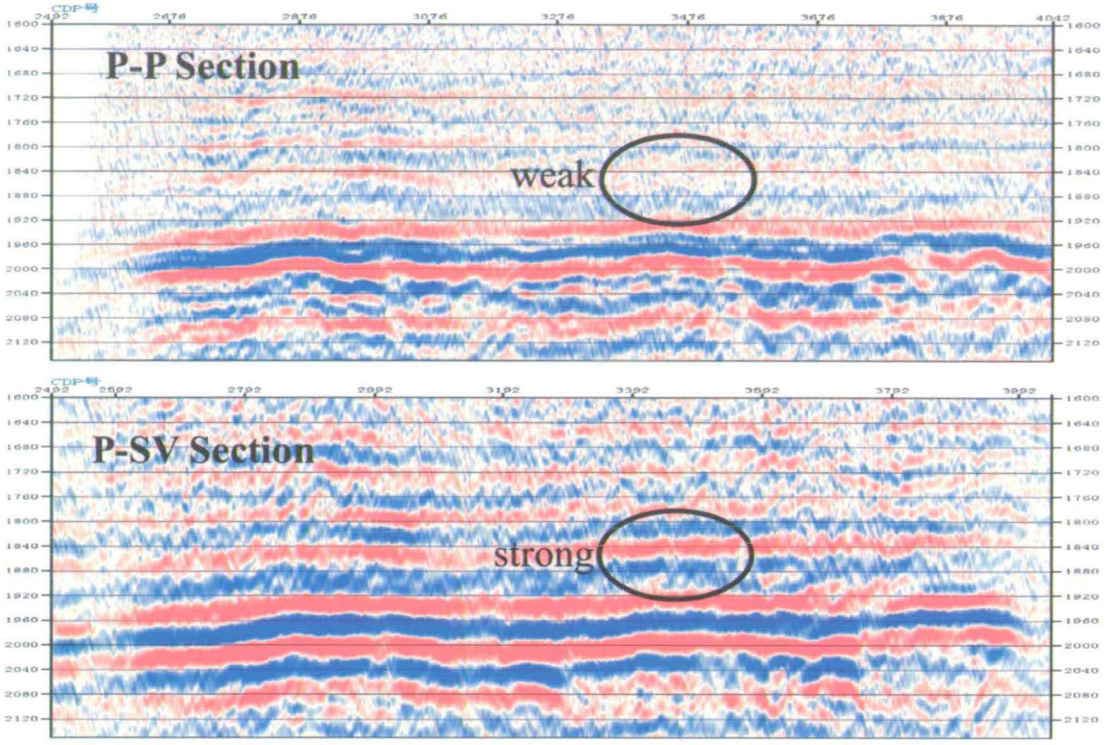

Figure 3.2: A 2D 3C line from Ordos field, onshore China shows weak PP-reflection due to small P-wave impedance contrast caused by gas presence, where strong S-impedance contrast make PS-wave a strong reflection at the top of reservoir (black circle)

3.3 Data acquisition and characterization

The 2D-3C seismic line 03585B is 33km long and is laid near the most productive gas well (S6) in the area. It was acquired (October, 2003) using I/O MEMS digital sensors (VectorSeis), which is the first such development in onshore China. MEMS is an integrated accelerometer (Figure3.3) and has benefits of reduced size and weight, integration of system electronics, and calibrated response sensor-to-sensor. These features make the sensor suitable for economic multicomponent seismic acquisition (Maxwell, 2001).

Figure 3.3: I/O's VectorSeis sensor module. Three of the digital sensors are mounted at right angles to each other in a tubular housing. This housing can be coupled to the ground for multicomponent land seismic recording (Maxwell, 2001).

Figure 3.4 compares different recording systems. Instead of an array of conventional P-wave and 3C receiver sensor, a 3C MEMS sensor is point receiver, which has advantages in direct digital output, excellent vector fidelity, broadband linear phase and amplitude response, low distortion and correction for tilt (Gibson, *et al.*, 2003).

The basic acquisition parameters of the 3C MEMS sensors line 03585B are shown in the Table 3.1. The receiver interval is just 5m, compared to 25m separation in conventional acquisition; maximum offset is almost 7200m, which is about twice the reservoir depth. The acquisition parameters of conventional 3C lines in the area are: source: dynamite; shot interval: 50m; receiver: 3×240 channel; receiver interval: 25m; minimum offset: 175m, maximum offset: 6275m; sample interval: 1ms; record length: 6s.

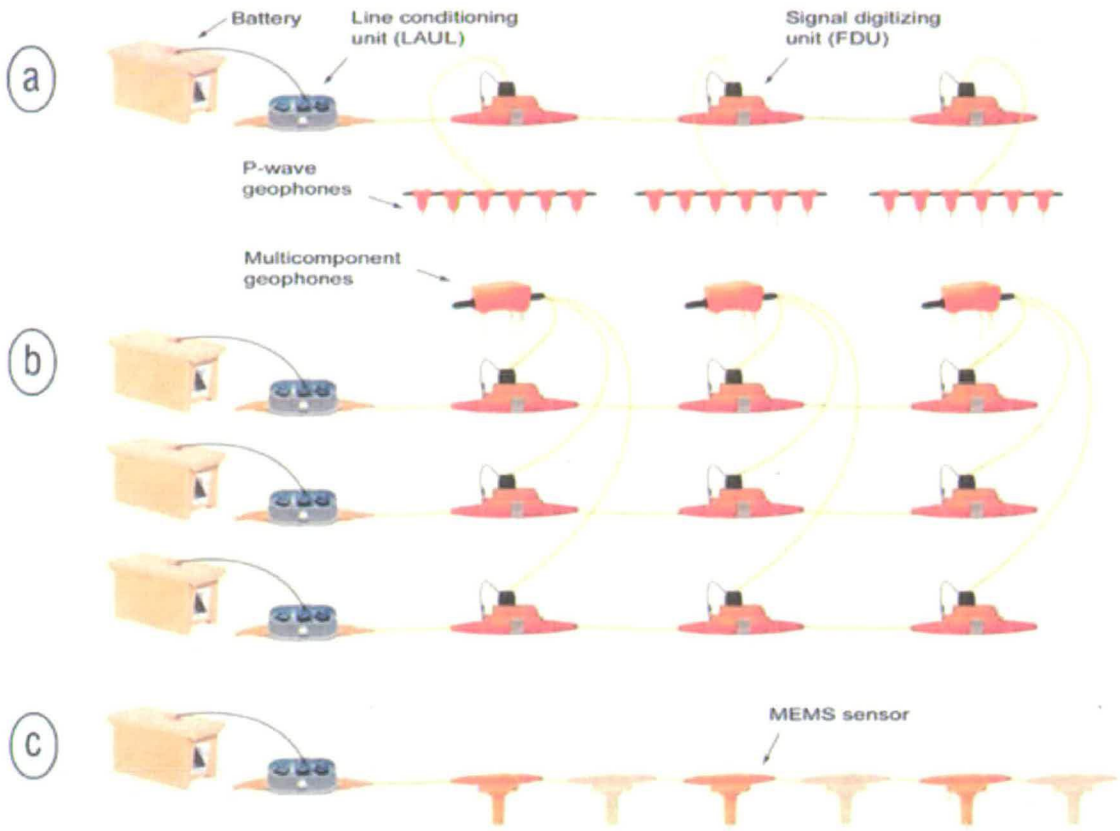

Figure 3.4: Comparison of various acquisition systems. (a) P-wave geophone array with 6 elements, (b) conventional 3C geophones, and (c) MEMS sensor with single cable, less weight and power requirements, easy deployment (Gibson *et al.*, 2003).

Source type	Dynamite
Number of shots	620
Shot interval	40m
Number of receivers	3x2402
Receiver interval	5m
Maximum offset	7197.5m
Sample interval	2ms
Trace length	6s

Table 3.1: The acquisition parameters of line 03585B

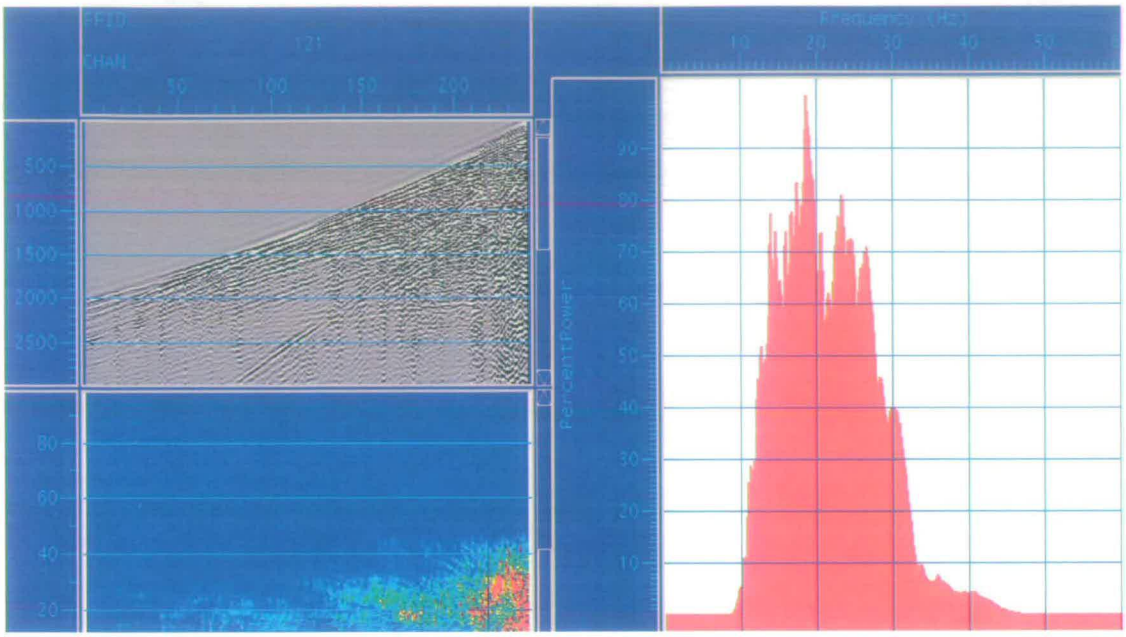

(a) Amplitude Spectrum of a shot gather acquired by conventional 3C geophones. The shot gather (left top), the FX spectrum (left bottom) and the amplitude spectrum (right)

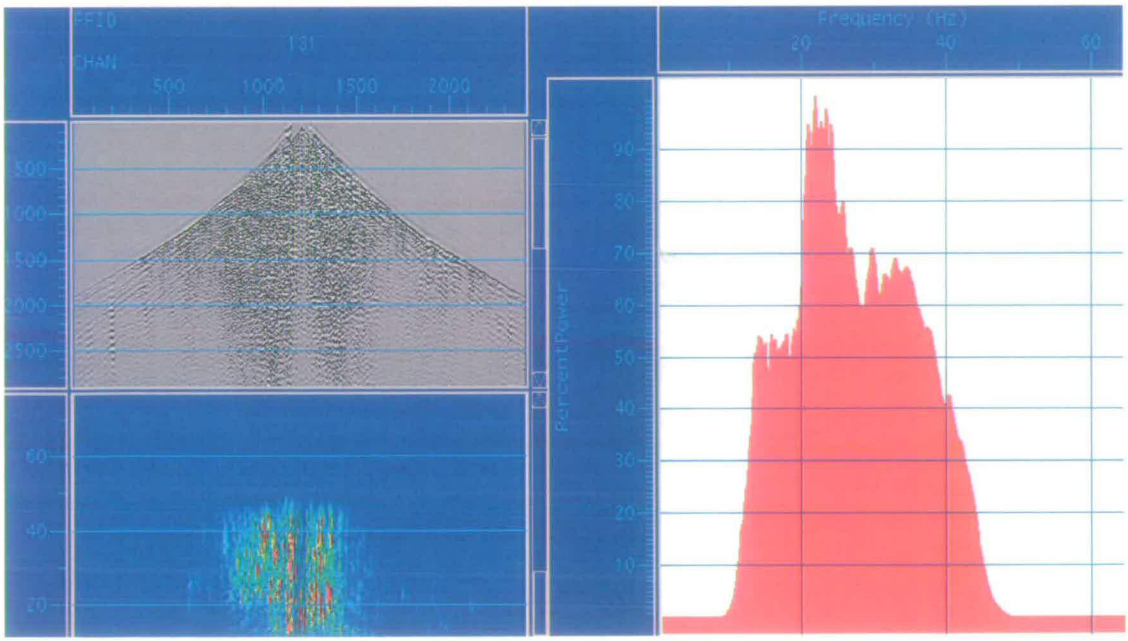

(b) As in (a), but amplitude spectrum of a shot gather from line 03585B acquired by 3C digital geophones.

Figure 3.5: Shot example of the amplitude spectra. (a) Conventional geophone; (b) MEMS geophone. The shot gather by digital geophone has a wider bandwidth.

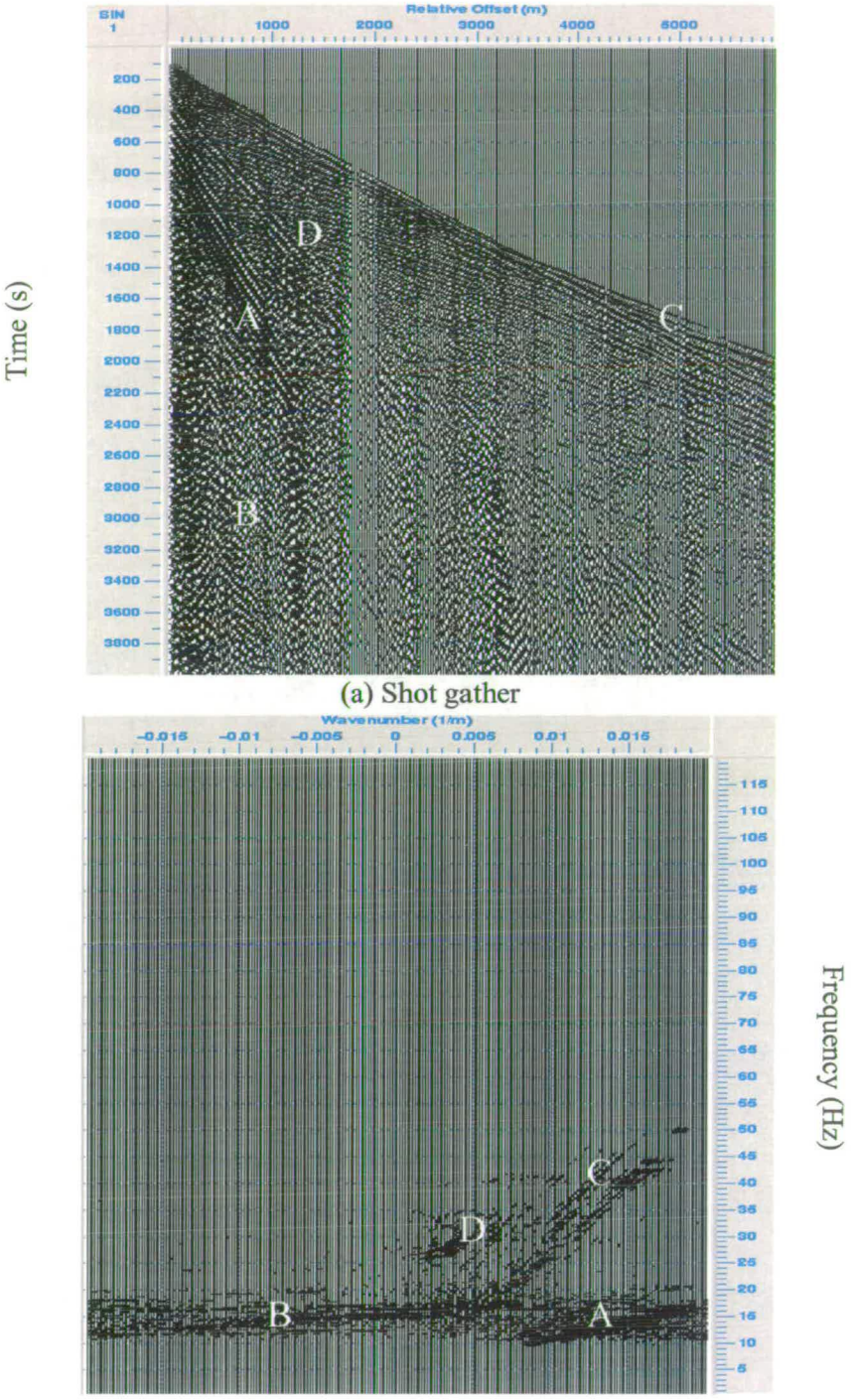

Figure 3.6: A shot gather and it's F-K spectrum. A=ground roll B=ground roll's backscattered component C=refraction waves D=primary reflection.

Figure 3.5 shows the amplitude spectrum of one of PP-wave shot gathers of line 03585B compared with the spectrum of a PP-wave shot gather acquired by conventional 3C geophones. The comparison between the two spectra shows that the data acquired by digital receivers have a wider bandwidth than those acquired by conventional receivers.

Due to the thick (100-180m) low velocity layer near surface, severe ground roll (A in Figure3.6a) is present on shot gathers. The ground roll conceals some reflection energy (D in Figure 3.6a). The refracted is also visible in the early part of the record (C in Figure 3.6a). An F-K analysis shows ground roll has low frequency, low velocity and large energy in the F-K domain (Figure 3.6b).

3.4 Data processing

Due to the presence of a thick low velocity near-surface layer, the direction of wave propagation is nearly vertical when arriving at receivers. Thus the components of PP- and PS-wave separate naturally. The vertical Z-component consists mainly of PP-wave signals, whilst the horizontal X-component contains mainly PS-wave signals (Figure 3.7). The hodogram between X- and Z-components shows particle motion at near offsets is vertically and inclines to horizontaldirection at far offsets. The preprocessing sequence included static correction, trace muting and bad trace editing, true amplitude recovery, surface consistent amplitude correction, band-pass filtering, and F-K filtering. The whole processing flowchart is shown in Figure 3.8.

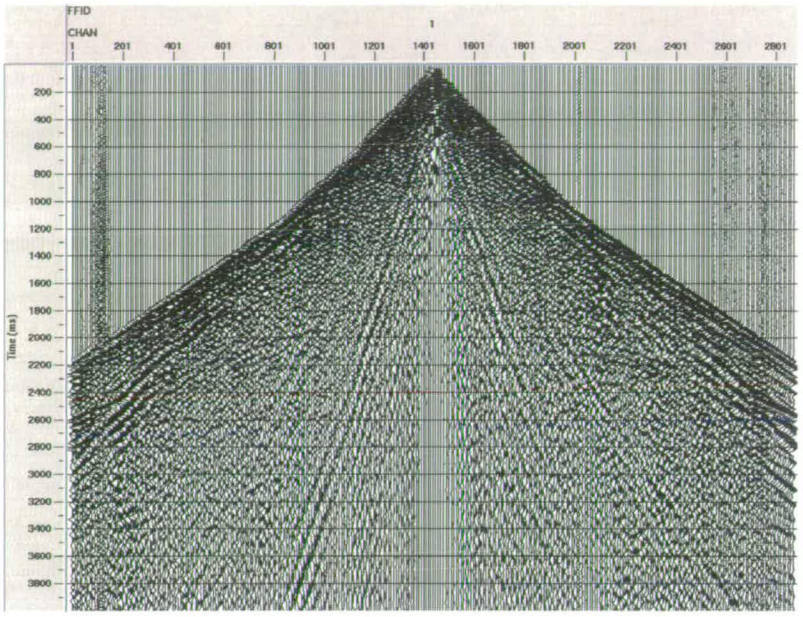

(a) Vertical Z-component

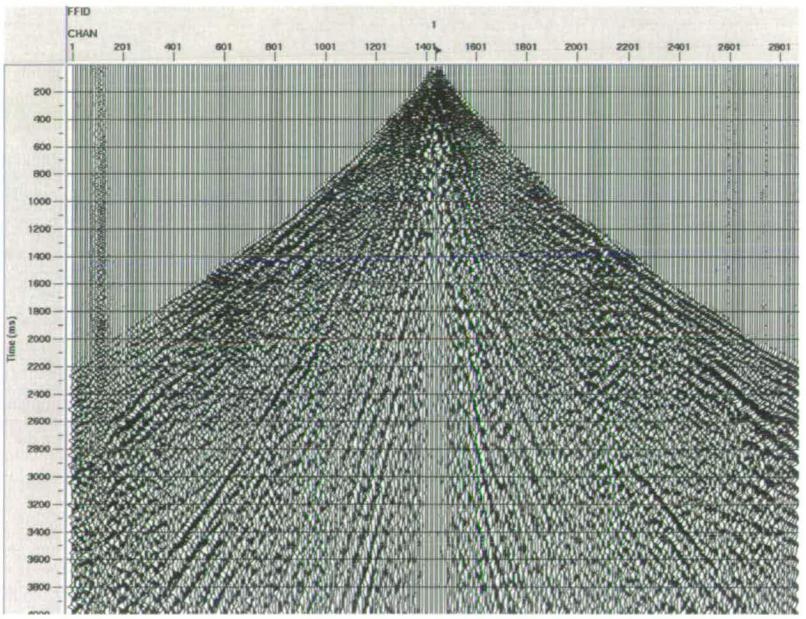

(b) Horizontal X-component

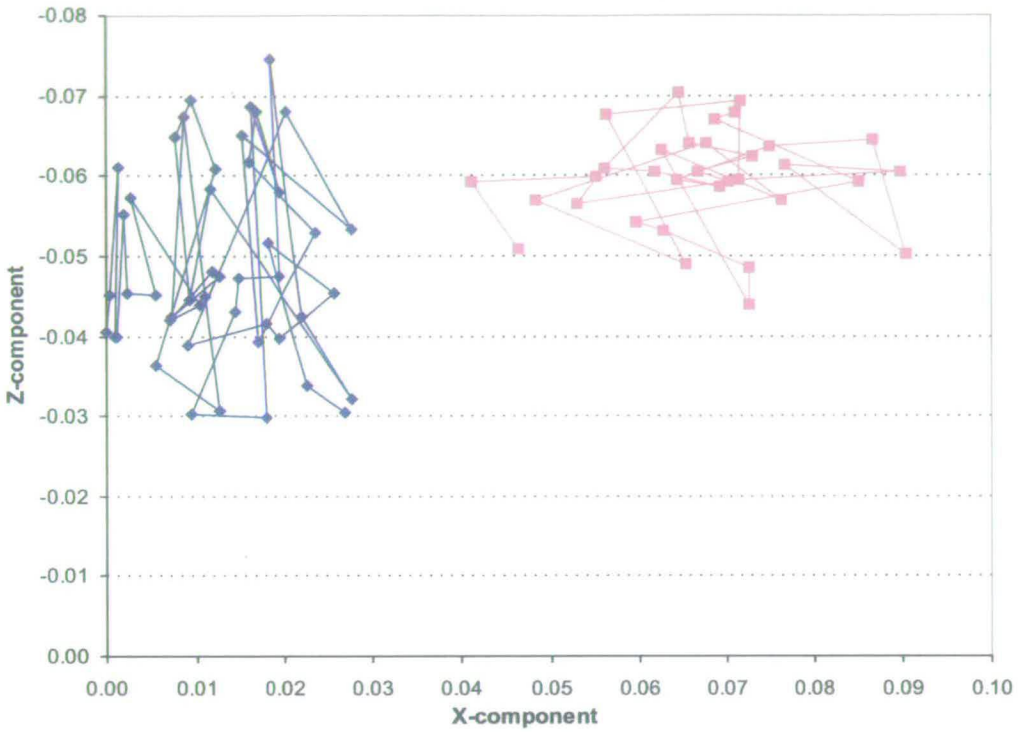

(c) Hodogram for X- and Z-components

Figure 3.7: Sample shot gathers and hodogram between X-and Z-components. Note nearly vertical particle motion at near offsets and nearly horizontal motion at far offsets. The mid offsets are not used in this graph due to noisy data.

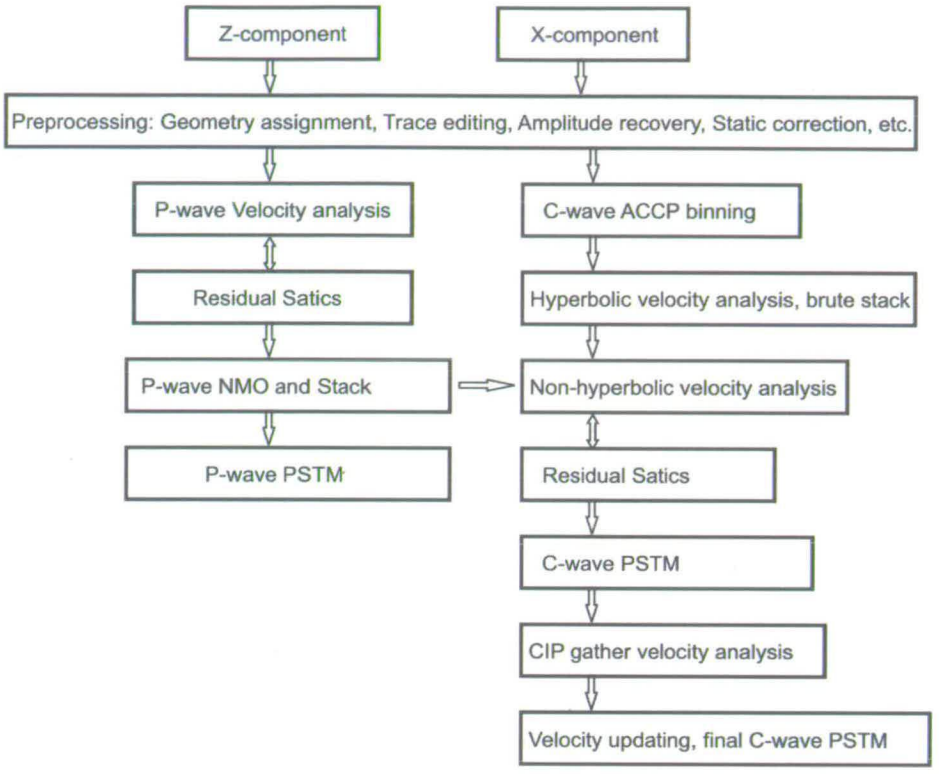

Figure 3.8: The flowchart of PP- and PS-wave data processing.

3.4.1 Static correction

The surface of the study area is covered with desert sands (Figure3.9a), and the near surface is low velocity loose soils with significant lateral variations in thickness and lack of clear vertical layering, which cause severe seismic energy attenuation and statics. Here, I use a method developed specially for this area by Wei and Liu (2002) to perform statics correction. It assumes an equivalent medium with continuous velocity variation in depth to model desert terrains. Figure 3.9b shows an example of the near-surface velocity model from PP-wave.

Figure 3.9a: Example of the study area's terrain

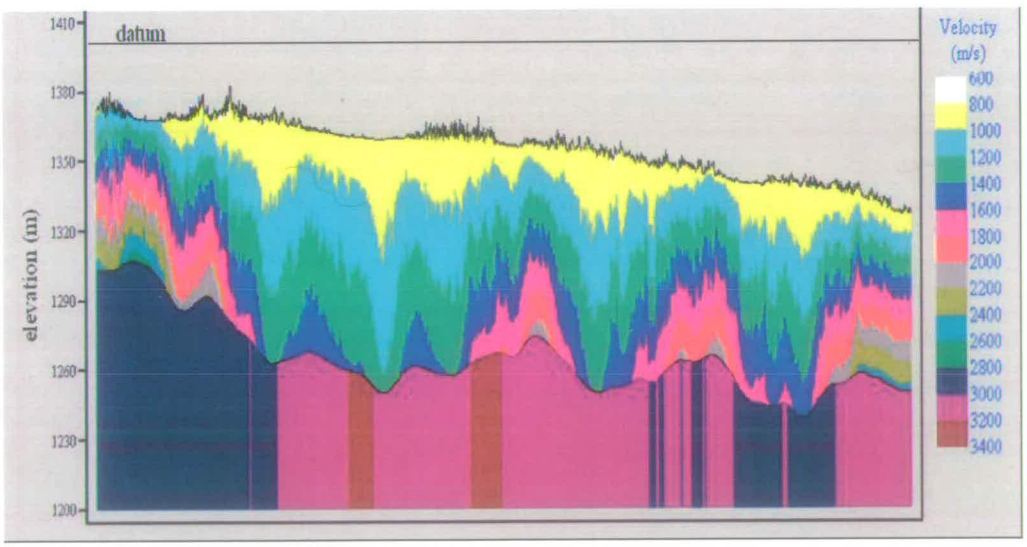

Figure 3.9b: The near-surface velocity model by Wei *et al.* (2003).

Figure 3.10a-d show a shot gather of PP- and PS-waves before and after applying the static correction. Figure 3.10e-f show a portion of PP-wave stacked sections before and after applying the static correction. The events become coherent near the reservoir below 1.8s after applying static correction. Common receiver stack is applied to remove short wavelength statics. The receiver statics for PS-wave are obtained from PP-wave, here I assume V_p/V_s ratio for near surface equals 2.

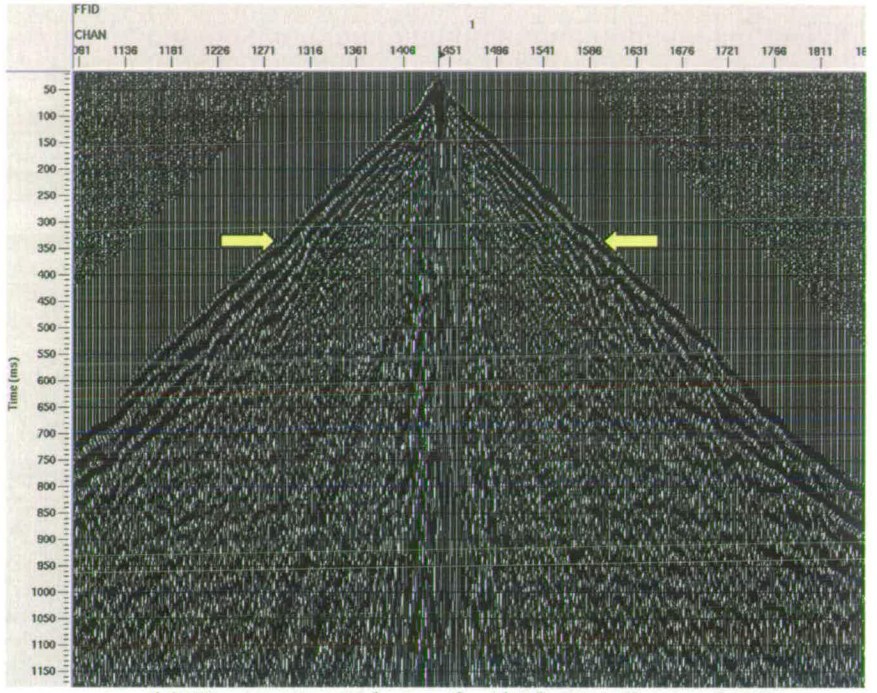

(a) Z-component shot gather before static correction.

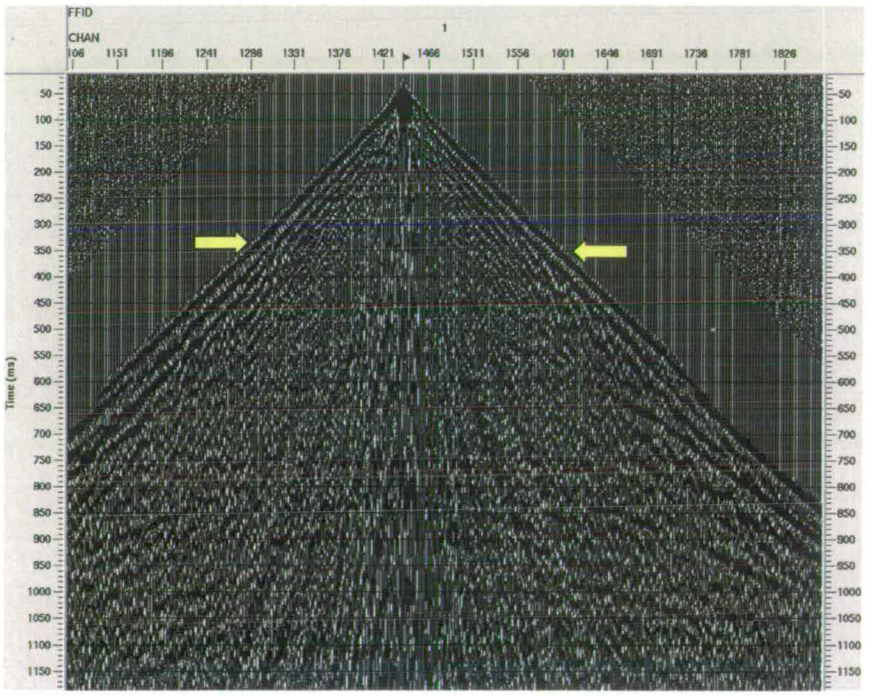

(b) Z-component shot gather after static correction.

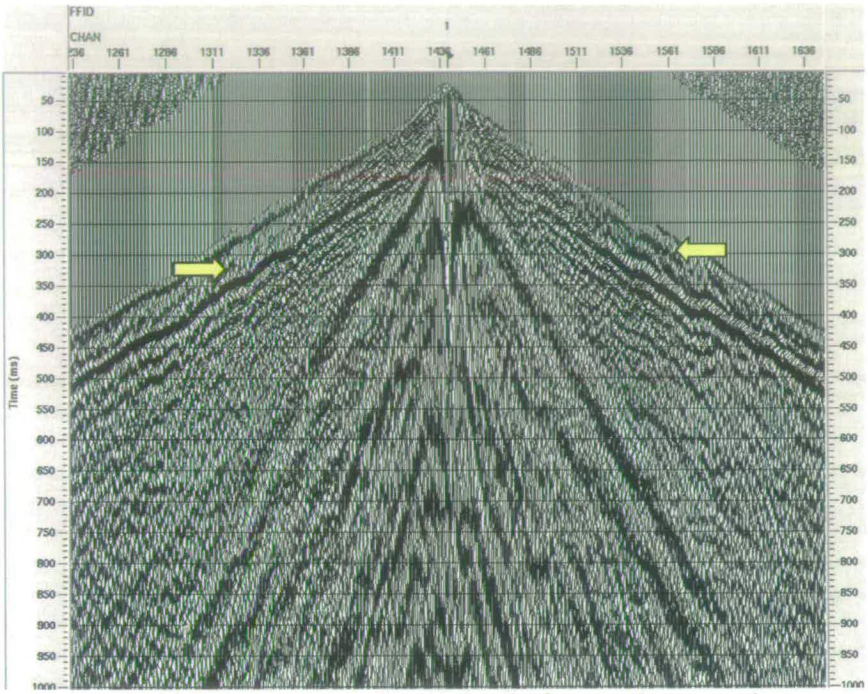

(c) X-component shot gather before static correction.

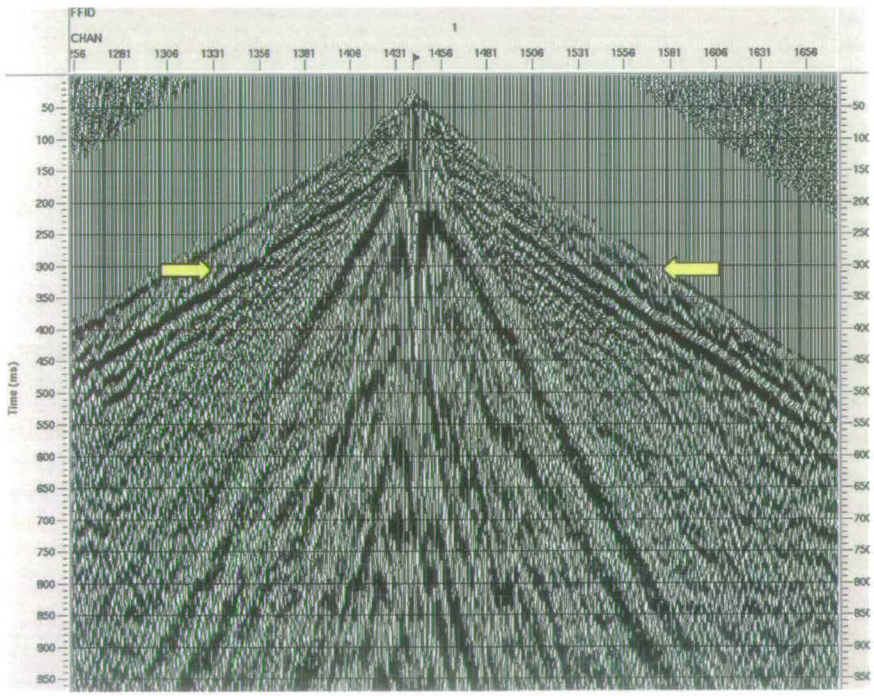

(d) X-component shot gather after static correction.

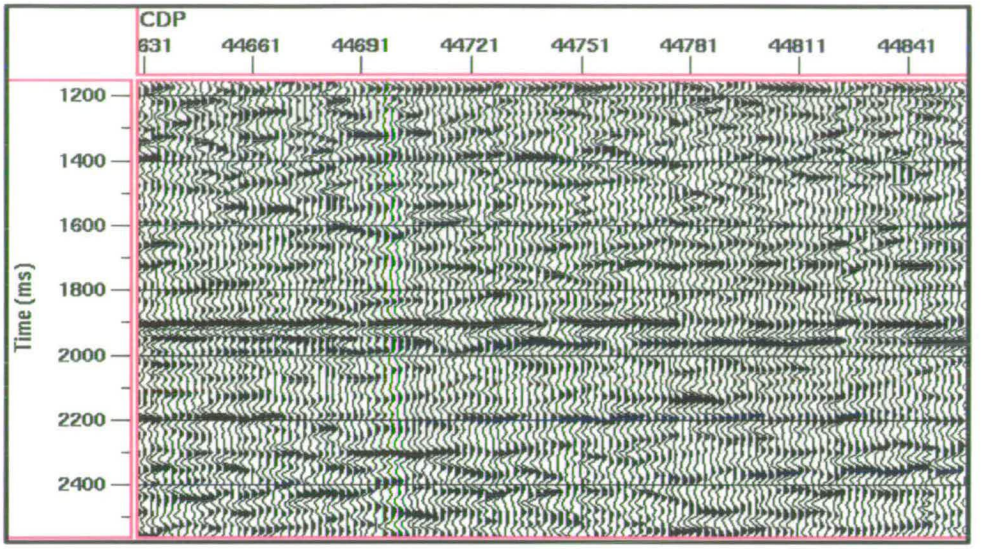

(e) PP-wave stacked section before static correction.

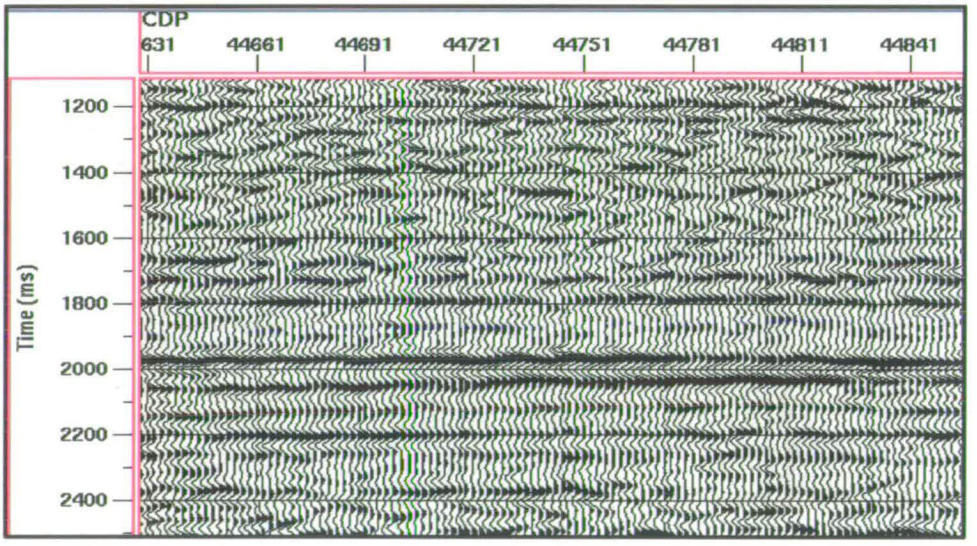

(f) PP-wave stacked section after static correction.

Figure 3.10: Comparison of the static correction effect.

3.4.2 ACCP and CCP binning for PS-wave data

Because of the asymmetry of the PS-wave raypath from the source to the receiver (Figure 3.11), the reflection points are no longer the midpoint between the source and receiver; they are closer to the receiver because of the slower S-wave velocity. CCP binning (common conversion points) replaces the CMP binning for PS-wave

processing. However, since identifying the conversion point requires knowledge of velocity ratio V_p/V_s, which is unknown at the beginning of processing, obtaining these conversion point positions becomes one of the main difficulties in converted wave processing.

If the offset (X) between source and receiver is much smaller than the reflector depth, an approximate conversion-point position (X_p) for a single layer is given by Equation 3-1 (Fromm *et al.*, 1985):

$$X_p = \frac{\gamma_0}{1+\gamma_0} x \qquad (3-1)$$

Assuming a depth independent γ_0, this equation is a starting point for initial CCP binning, called ACCP (asymptotic common conversion point) binning. However, as shown in Figure 3.11, for layered media, where γ_0 is depth variant, the conversion point trajectory departs from the asymptotic line as the offset depth ratio increases. A CCP binning technique is required to locate the real conversion point. Among other authors (Zhang, 1992; Tessmer and Behle, 1988), Thomsen (1999) gives an approximation (Equation 3-2 to 3-5) for calculating layer-media conversion points by using PS-wave stacking velocity V_{c2}, vertical velocity ratio γ_0, and effective velocity ratio γ_{eff}. t_{co} is vertical PS-wave time. Li *et al.* (2002) prove that the CCP position is not very sensitive to change in the vertical velocity ratio. γ_{eff} (Equation 3-9) is a key value for CCP binning, which can be obtained from the CCP-scanning technique (Audebert *et al.*, 1999).

$$X_p(\mathrm{x},z) \approx \mathrm{x}\left[C_0 + C_2 \frac{\left(\frac{x}{t_{c0}v_{c2}}\right)^2}{\left(1+\mathrm{C}_3(\mathrm{x}/t_{c0}v_{c2})^2\right)} \right], \qquad (3-2)$$

$$C_0 = \frac{\gamma_{eff}}{1+\gamma_{eff}}, \qquad (3-3)$$

$$C_2 = \frac{\gamma_{eff}}{2\gamma_0}\frac{(\gamma_{eff}\gamma_0 - 1)}{(1+\gamma_{eff})^3}(\gamma_0 + 1), \qquad (3-4)$$

$$C_3 = C_2/(1-C_0). \qquad (3-5)$$

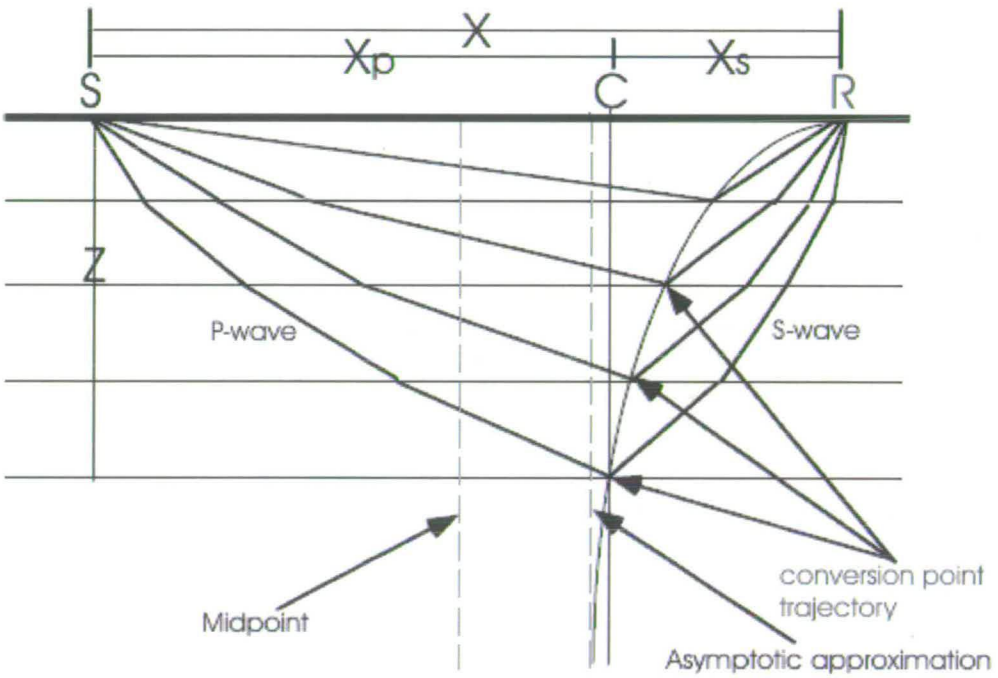

Figure 3.11: PS-wave raypath and common receiver point trajectory

3.4.3 Non-hyperbolic moveout analysis

Four-parameter (V_{c2}, γ_0, γ_{eff} and χ_{eff}) non-hyperbolic travel time equation (Equation 3-6 to 3-9), modified by Li and Yuan (2003) and Yuan *et al.* (2001) is used in velocity analysis and NMO correction. The GUI CX-tool for PS-wave analysis and processing (Dai, 2003) is used to estimate V_{c2}, γ_0, γ_{eff} and PS-wave anisotropic parameter χ_{eff}. Equation 3-9 is accurate up to an offset-depth ratio of x/z 2.0.

$$t_c^2 = t_{c0}^2 + \frac{x^2}{V_{c2}^2} + \frac{A_4 x^4}{1 + A_5 x^2}, \qquad \left(\frac{x}{z} \le 2\right) \qquad (3-6)$$

$$A_4 = -\frac{(\gamma_0 \gamma_{eff} - 1)^2 + 8(1+\gamma_0)\chi_{eff}}{4 t_{c0}^2 V_{c2}^4 \gamma_0 (1+\gamma_{eff})^2}, \qquad (3-7)$$

$$A_5 = \frac{A_4 V_{c2}^2 (1+\gamma_0)\gamma_{eff}[(\gamma_0 - 1)\gamma_{eff}^2 + 2\chi_{eff}]}{(\gamma_0 - 1)\gamma_{eff}^2 (1 - \gamma_0 \gamma_{eff}) - 2(1+\gamma_0)\gamma_{eff}\chi_{eff}}, \qquad (3-8)$$

$$\gamma_0 = \frac{t_{s0}}{t_{p0}}, \quad \gamma_{eff} = \frac{\gamma_2^2}{\gamma_0}, \quad \gamma_2 = \frac{V_{p2}}{V_{s2}}, \qquad (3-9)$$

$$\chi_{eff} = \eta_{eff}\gamma_0 \gamma_{eff}^2 - \zeta_{eff}. \qquad (3-10)$$

where η_{eff} is the P-wave anisotropic parameter (Alkhalifah and Tsvankin, 1995), and ζ_{eff} is the corresponding S-wave anisotropic parameter (Li and Yuan,2001).

Figure 3.12 shows a comparison between hyperbolic velocity analysis (Figure 3.12a) and a non-hyperbolic velocity analysis using Equation 3-6 (Figure 3.12b) for ACCP gather 800. The moveout of converted waves in the larger offset is corrected much better by non-hyperbolic correction than by hyperbolic correction. The analysis shows that the polar anisotropic parameter χ_{eff} is very small, so the anisotropic effect is ignored in the next chapters' AVO inversion. γ_{eff} is 2.0 to 1.8 from shallow to deep layer.

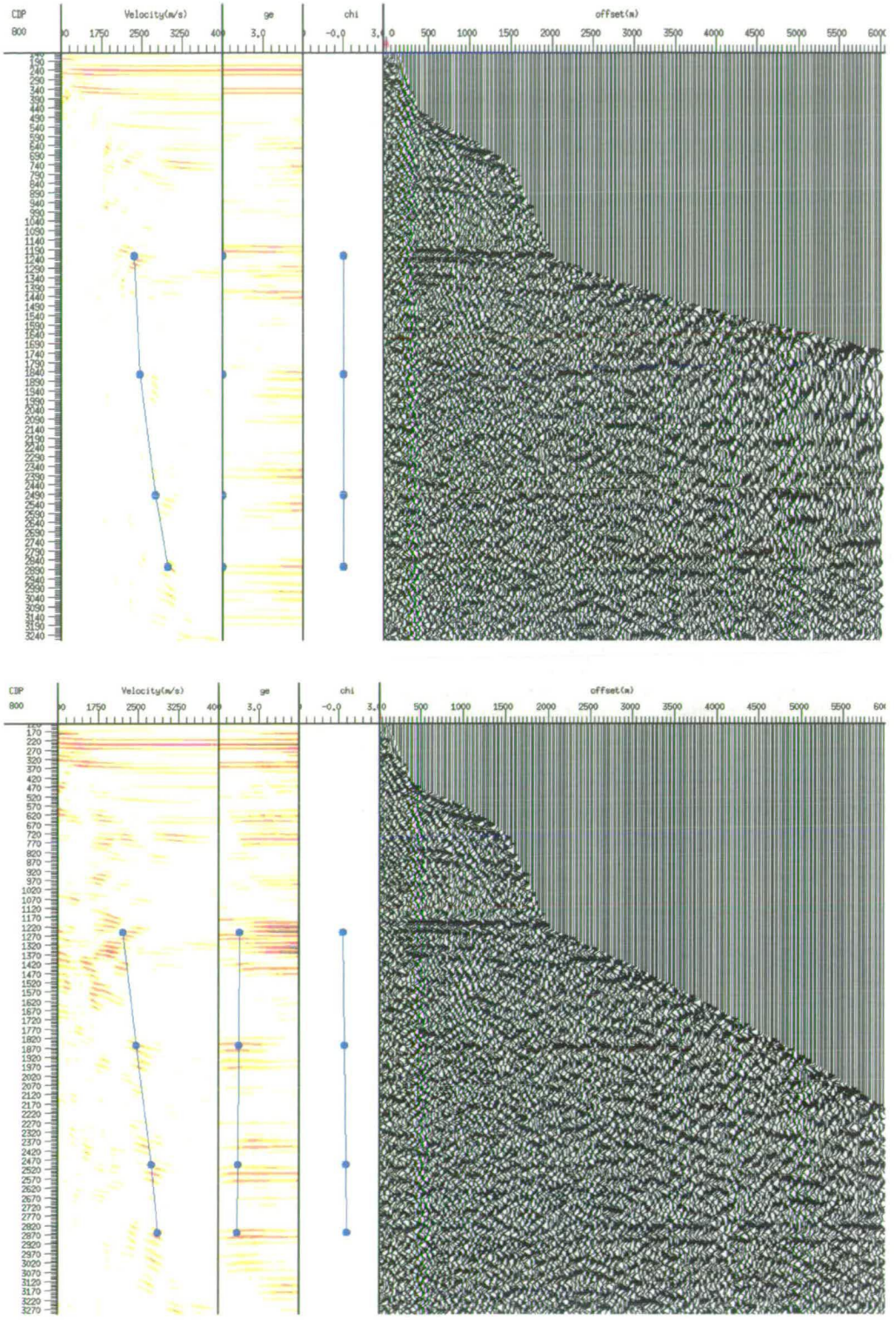

Figure 3.12: Comparison between hyperbolic (top, γ_{eff}=1, χ_{eff}=0) and Non-hyperbolic (bottom, γ_{eff}=1.8 to 2.0, χ_{eff}=0.0) moveout analysis for ACCP 800. The 1st panel is PS-wave velocity spectra, the 2nd panel is effective velocity ratio γ_{eff}, and 3rd panel is anisotropic parameter χ_{eff}.

3.4.4 Diodic effect

Because of its asymmetric ray path, for a laterally inhomogenous media, PS-wave travel time and velocities are not invariant under an interchange of source and receiver positions (Figure 3.13). Thomsen (1999) described this phenomenon as a diodic effect caused by lateral velocity variation. This means for a split-spread CMP gather with positive and negative offsets (their source and receiver positions exactly exchanged), PS-wave arrivals through laterally heterogeneous media will not have symmetric moveout. This effect does not happen for PP-waves or for any other pure-mode event.

Figure 3.14 shows an NMO-corrected ACCP gather with negative and positive offsets. In the white circles, the flattened event at positive offsets and non-flattened event at negative offsets are seen at 1.2s. This means that using the same NMO velocity, we cannot correct a split-spread gather simultaneously. Moreover, a strong and continuous reflection is seen at positive far offset at 2.8s, which is not seen in the negative part. This means the diotic effect is present not only in PS-wave travel times, but also on PS-wave reflection amplitude. Figure 3.15 shows the positive and negative offset stacked sections of the line 03858B. The event around 1.2s is more continuous in the positive offset stacked section than that of the negative offset section. The above analysis implies a significant reservoir heterogeneity, which is confirmed by a sedimentary facies and diagenesis study (He *et al.*, 2006). It is necessary to divide the data into the negative offsets part and positive offset part, and process them separately.

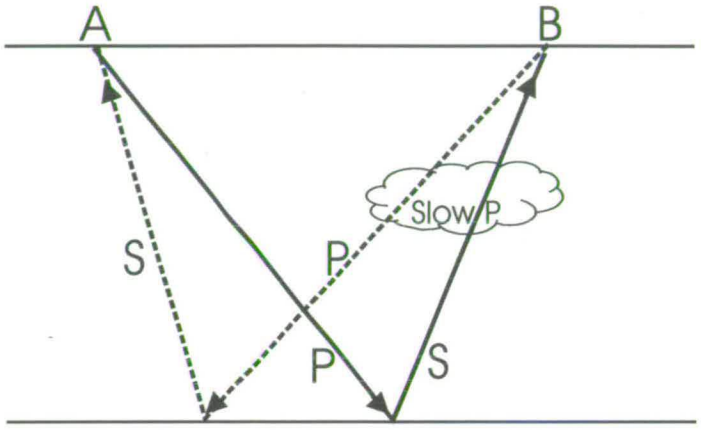

Figure 3.13: A schematic diagram showing the diotic effect. P-wave slows down when encountering the slow velocity body due to fluid effect, while S-wave is insensitive to slow P-wave body. B to A takes longer travel time than A to B.

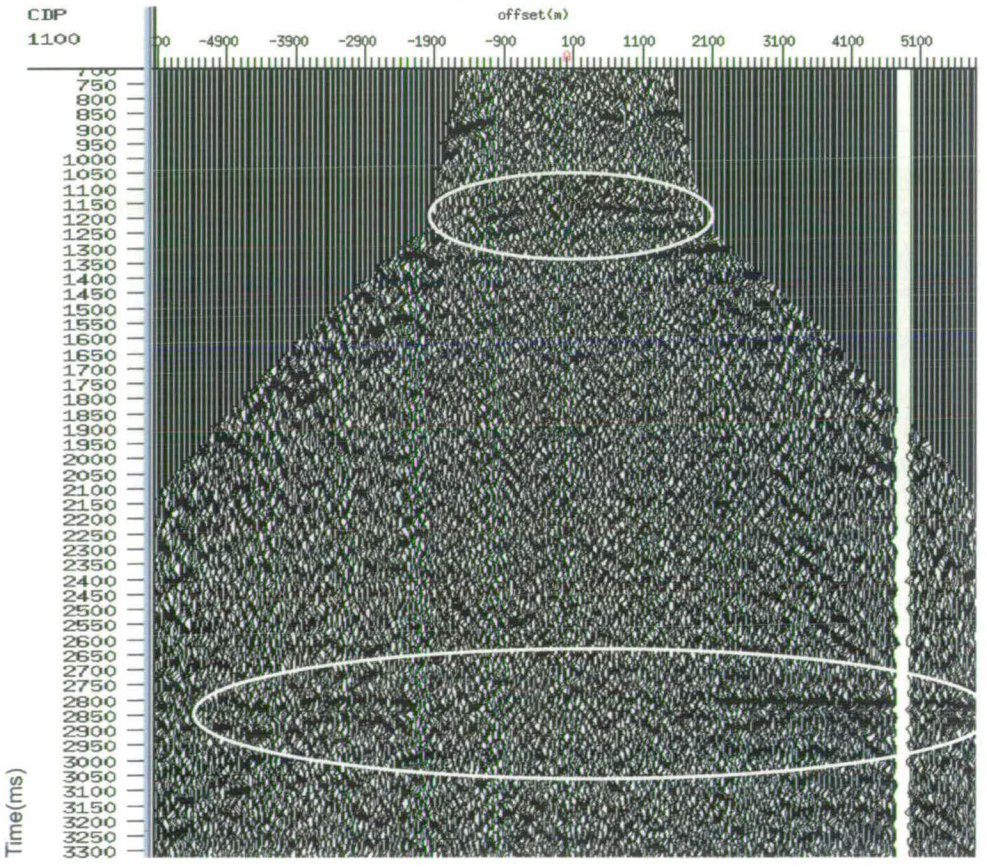

Figure 3.14: ACCP gather 1100 after NMO, the asymmetry in positive and negative offset is indicted in the white circles

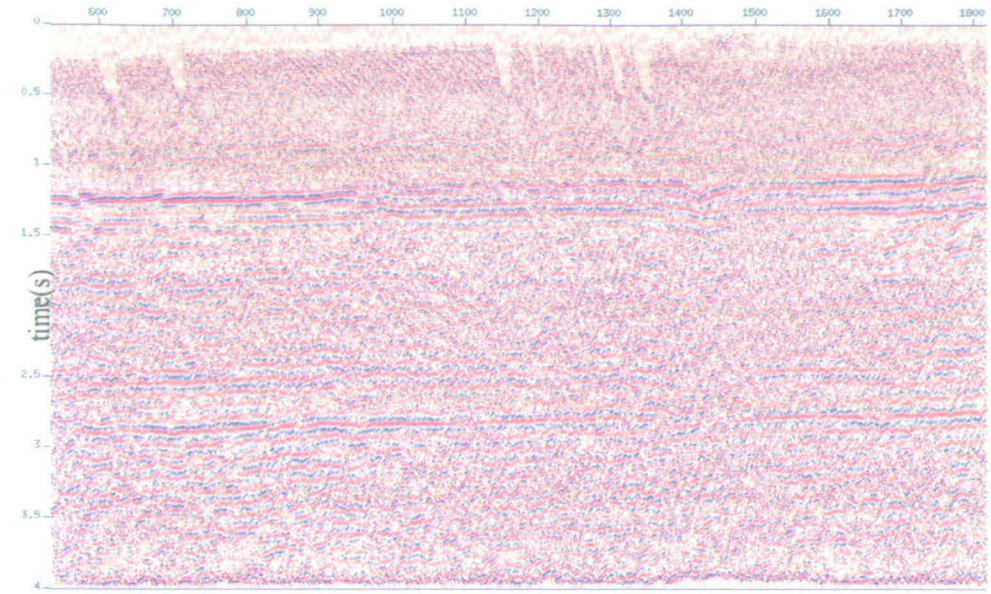

(a) Negative offset stack

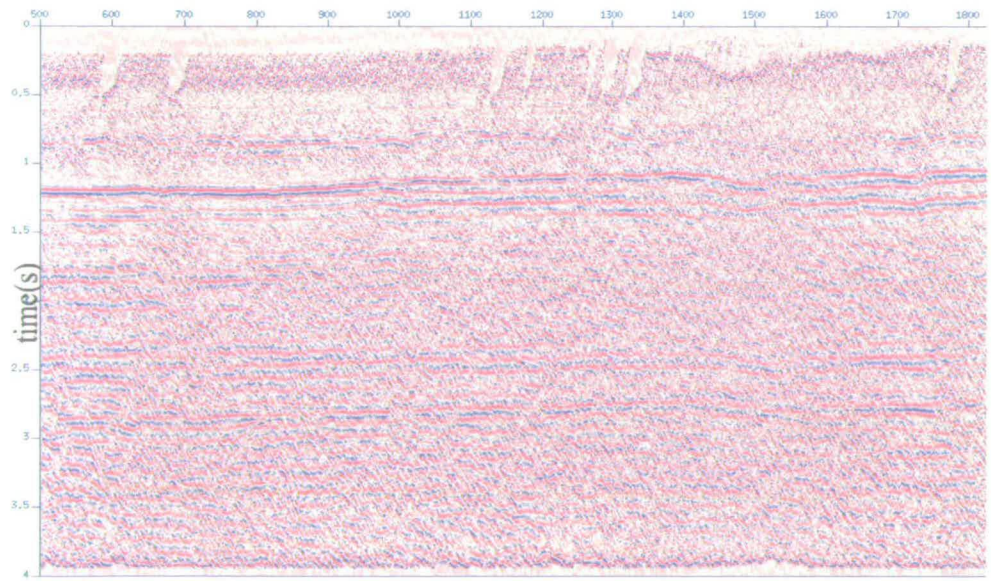

(b) Positive offset stack

Figure 3.15: Effect of the diodic velocity on the negative (a) and positive (b) offset stacking images.

3.4.5 Pre-stack Kirchhoff time migration

Kirchhoff PSTM is routinely applied on huge 3D data sets for PP-waves. Such an algorithm has also been developed to handle converted waves (e.g. Dai *et al.*, 2000;

Granli *et al.* 1999; Gresillaud *et al.*, 2003). The choice of the Kirchhoff algorithm is motivated by the fact that in the time domain the Kirchhoff PSTM is fast and requires RMS velocities, available after conventional velocity analysis. For PS-waves it has also the merit of compensating for the conversion point dispersal, as it avoids the need for CCP binning (Li *et al.*, 2001).

The principle of migration is illustrated in Figure 3.16. For a given a travel-time, the energy from a trace related to a shot and a receiver must be distributed to all possible locations of subsurface scatter-points along a diffraction curve in the time-offset domain. PSTM constructs the image of scatter-points at a possible location; the energy from all shots and receivers are summed at this location. This is usually implemented as a weighted summation based on the raypaths. The location of the reflector point in the output trace is defined as the two-way PS-travel times for zero-offset (Dai, 2001).

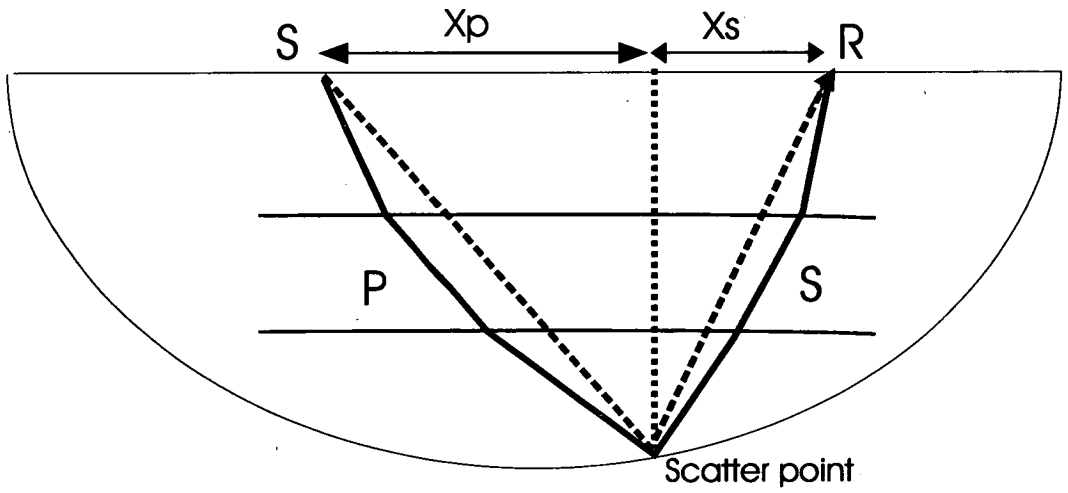

Figure 3.16: Kirchhoff PSTM for a scatter point. The scatter point position is determined by the position of the source and the receiver for each trace. The solid line is the real raypath of PS converted wave and dash line is the raypath corresponding to RMS velocity.

The algorithm used here is by Dai and Li (2001). The travel times are calculated using the Double Square Root (DSR) equation and the RMS velocities along the straight raypath in the following:

$$t_c = \sqrt{t_{p0}^{\ 2} + \frac{x_p^{\ 2}}{V_{p2}^{\ 2}}} + \sqrt{t_{s0}^{\ 2} + \frac{x_s^{\ 2}}{V_{s2}^{\ 2}}}, \qquad (3-11)$$

According to Equation 3-9 and the following 3-12 (Thomeson, 1999),

$$V_{c2}^2 = \frac{V_{p2}^2}{1+\gamma_0}(1+\frac{1}{\gamma_{eff}}), \qquad (3-12)$$

Equation 3-11 can be expressed in only PS-wave-dependent parameters as:

$$t_c = \frac{t_{c0}}{1+\gamma_0}\sqrt{1+\frac{x_p^2(1+\gamma_{eff})}{V_{c2}^2(1+\gamma_0)\gamma_{eff}}(\frac{1+\gamma_0}{t_{c0}})^2} + \frac{t_{c0}\gamma_0}{1+\gamma_0}\sqrt{1+\frac{x_s^2(1+\gamma_{eff})}{V_{c2}^2(1+\gamma_0)\gamma_0}(\frac{1+\gamma_0}{t_{c0}})^2} \qquad (3-13)$$

Equation 3-13 is defined by three parameters for isotropic media: V_{c2}, γ_0, γ_{eff}; for VTI anisotropic media, another parameter χ_{eff} is required. These four parameters are the input to the PSTM. Their estimation becomes the most important task of the processing flow. The initial velocity model is constructed from reflection moveout analysis with these four parameters. Since the velocity obtained from the conventional method (ACP or CCP binning and stacking velocity analysis) does not equal the migration velocity (Bevc, 1997; Granli *et al.*, 1999), a CIP gather obtained from PKTM is used to obtain the correct migration velocity by visually checking if the events in CIP gathers are flatted. In EAP's CX-tool, inverse NMO (INMO)-CIP gathers can be obtained by applying an INMO to a CIP gather before summation. Similarly to inversion of CDP gathers after NMO, which is called inverse NMO (INMO-CDP), the inversion can also be applied to a CIP gather. The difference between INMO-CDP and INMO-CIP is that the inverted position of each event is not its original position and is equivalent to the hyperbolic moveout that is

only dependent on the velocity itself. So far it is proved that a hyperbolic moveout analysis can be applied to improve the velocity (Dai and Li, 2003).

Figure 3.17 shows a comparison between ACCP 7433 and CIP 7433: the ACCP gather is a supergather of 15 adjacent CDP gathers before NMO. The signal energy is more continuous in the CIP gather, which is input into AVO inversion.

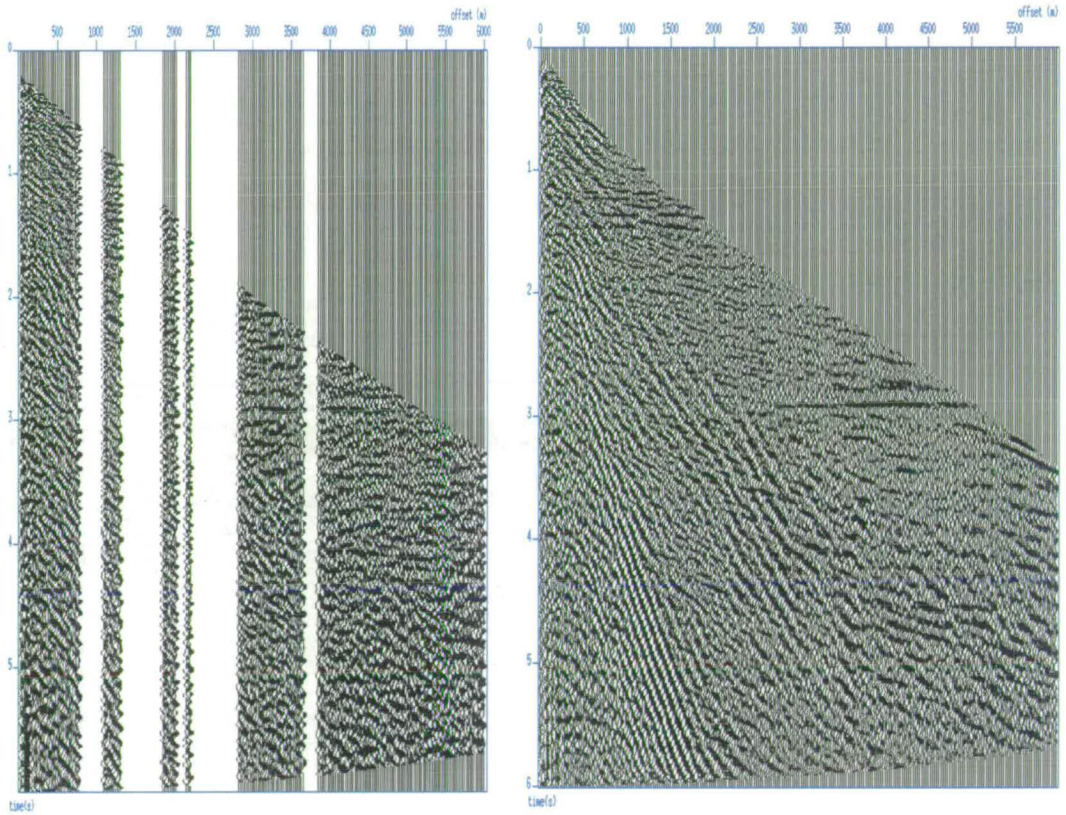

Figure 3.17: Comparison between ACCP 7433 (left) and CIP 7433 (right).

Figure 3.18 shows the final migrated PP-wave image and PS-wave image. A strong reflection from the coal layer appears in both the PP-wave section (around 2s) and the PS-wave section (around 2.8s). The strong reflections from the coal layer are good calibration points for event correlation.

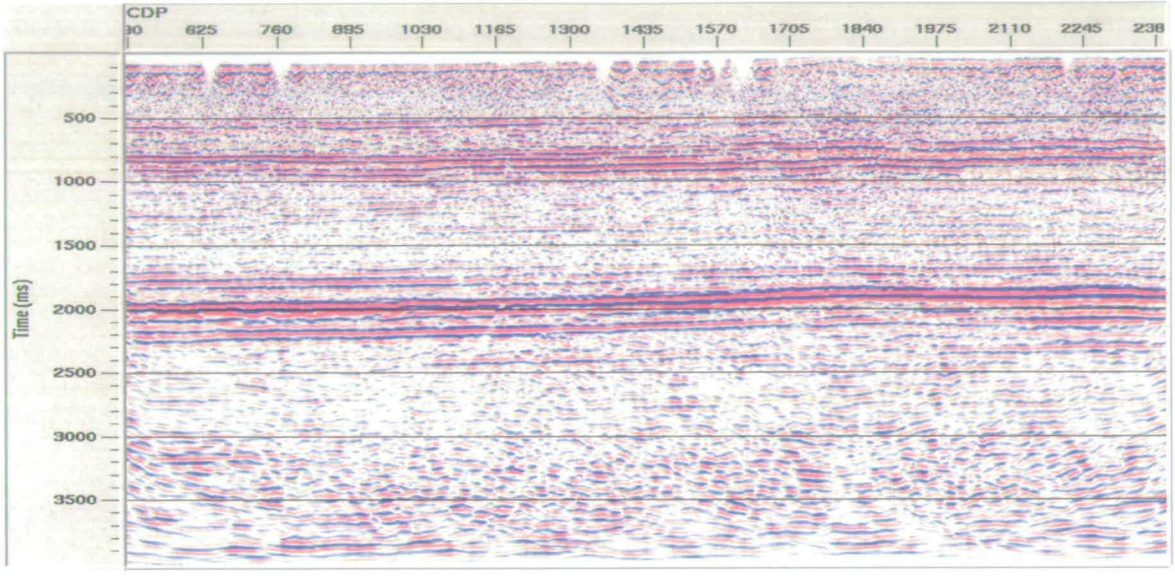

(a) The PP-wave migrated image, line 03585B

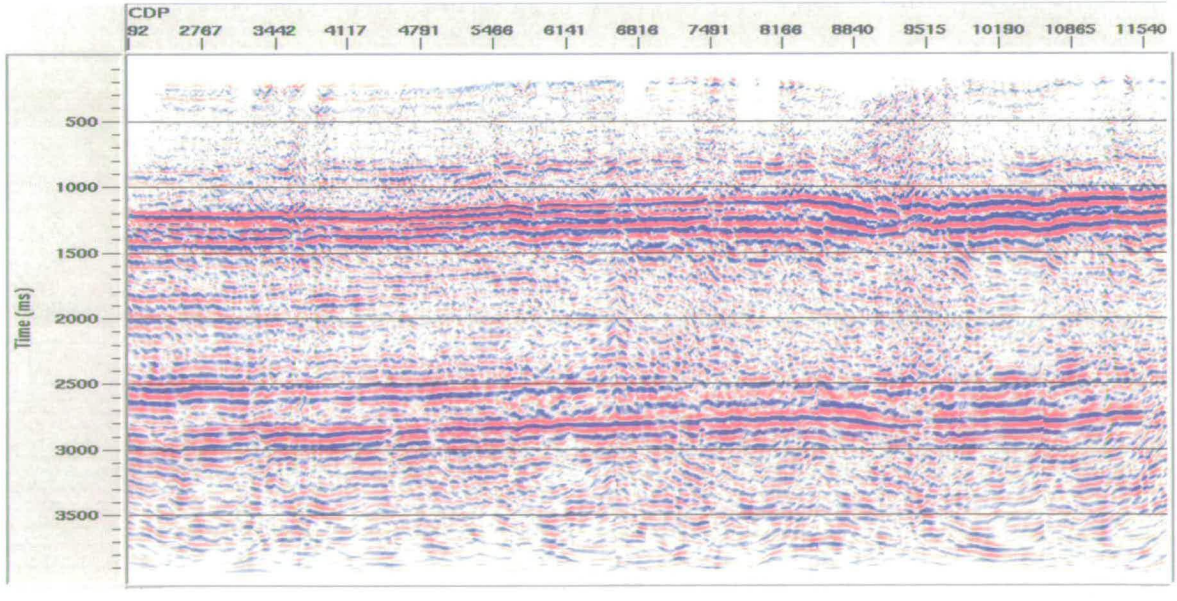

(b) The PS-wave migrated image, line 03585B

Figure 3.18: PSTM images of PP- and PS-wave

3.5 Conclusion

In order to obtain amplitude preserved-data for AVO purposes, a PSTM approach is applied to both PP- and PS-wave data. CIP gathers are derived from PSTM; signals are more energy-focused than in CDP or ACCP gathers due to accurate reflection

point positioning. The key steps of data processing in this area are static correction, non-hyperbolic moveout analysis, and migration velocity updating in PSTM. Final migrated data show a flat coal layer, which forms a calibration point for the PP- and PS-wave event correlation.

Chapter 4: PP- and PS-wave event correlation by PS-wave moveout analysis

4.1 Introduction

Correlation of PP-wave and PS-wave data is a transformation from one time domain to another (i.e. compressing from PS-wave time to two-way PP-wave time) by the determination of an average, vertical V_p/V_s (termed γ_0). Calibrating PP-wave and PS-wave seismic sections is an important step in multicomponent seismic as it enables better interpretation and use of the combined data sets. It is becoming more and more important in multicomponent processing steps such as long-period static corrections, CCP-binning, Kirchhoff prestack time migration and prestack depth imaging. Furthermore, an interval velocity ratio V_p/V_s can be obtained during the correlation and can be used for subsequent lithologic interpretation. The velocity ratio V_p/V_s is near 1.9 for limestone, 1.8 for dolomite, and 1.6-1.75 for sandstone (Pickett ,1963). V_p/V_s is sensitive to fluid in sedimentary rocks and can be used to distinguish between gas and fluid in reservoir interval. V_p/V_s can be 10-20 percent lower for gas saturation compared to liquid saturation (Gardner *et al.*, 1968).

Historically, event registration has relied on identifying similar features in the PP- and PS-data. This in itself can be difficult in certain areas, where horizons are broken up due to faulting and thus are hard to interpret, while straightforward in others. Technically, I classify PP- and PS-wave correlation methods into two types: correlation algorithms based on post-stack multicomponent data, or those based on pre-stack multicomponent data. Event correlation between PP- and PS-wave might be affected by phase and frequency differences in the data. PP- and PS-wave data need to be zero phased using estimated wavelets. PP-wave data must be filtered to a similar frequency bandwidth to the PS-wave data.

Here I review the recent work on PP- and PS-wave correlation, and then put forward a new method using PS-wave moveout analysis.

4.1.1 Post-stack data event correlation

Kristiansen *et al.* (2003) developed a method that produces an algorithm that systematically compresses the PS-wave data volume over a range of γ_0 values and crosscorrelates it with the PP-wave. The cross-correlation technique is similar to conventional velocity analysis routines. However the method needs the starting γ_0 "guide" function used for the scanning. The closer this starting γ_0 is to the correct answer, the better the correlation.

Nickel and Sonneland (2004) presented a method to estimate a high resolution V_p/V_s ratio from multi-component seismic data. The algorithm is characterized by its multi-attribute and multi-resolution approach. The process is based on attributes extracted from the seismic, e.g. reflection strength, intensity, fault attributes etc., low-pass filtering the attributes severely in the first iteration and then less severely in the following steps until finally the full bandwidth data have been run. The procedure may start without a manual interpreted initial model. Because the algorithm relies on the assumption that only the location of events has changed whereas the amplitudes remain the same, estimation of the different source signatures (PP-wave and PS-wave) is required to equalize the different spectra.

Chan (1997) transferred the zero-offset times of PP- and PS-waves into logarithmic domain, in which all events appearing in both PP- and PS- sections are different by only a static shift (log k, K is a constant). This static shift can be estimated by optimizing the cross-correlation between two sections. Once this static shift is found, V_p/V_s can be estimated. However, the method assumes that the V_p/V_s ratios are constant throughout the seismic sections, and an event on PP and PS needs to be identified first.

Fomel *et al.* (2003) used a least-squares method to estimate the warping function for PS-wave data by minimizing the difference between the PP-wave image and the warped PS-wave image. A non-stationary spectral balancing is applied to reduce the effect of the frequency content difference on event correlation. The method needs a good V_p/V_s initial guess for the warping function.

Gaiser (1996) developed a method to obtain the V_p/V_S ratio using conjugate operators. This method assumes that the reflectivity of a P-wave is similar to the reflectivity of a S-wave, and that the frequency and wavelength of the PP-wave matches those of the PS-wave. However, these conditions are not generally fulfilled.

4.1.2 Pre-stack data event registration

Behle and Dohr (1985) described a combined velocity analysis for reflection event correlation between PP- and PS-wave data in shot gathers. Using measured PP-wave values of zero-offset times T_{p0} and moveout velocities V_{p2}, PS-wave zero-offset times T_{c0} and moveout velocities V_{c2} are cast in terms of V_p/V_s and their corresponding coherence is computed. This results in a PS-wave T_{c0} time versus V_p/V_s coherence plot that is interpreted for peaks along specified windows. However, analyses applied to shot records yield sparse and ambiguous peaks.

Ogiesoba (2003) estimated V_p/V_s from multicomponent seismic data using Thomsen's (1999) non-hyperbolic traveltime equation by computing semblance to analyze for the velocity ratio (γ_0). The method assumes the γ_0 is the velocity ratio between squared PP-wave and PS-wave moveout velocities, which is only valid in a single uniform isotropic media.

Here a new approach is investigated for estimating the vertical velocity ratio γ_0 by multi-component data moveout analysis. This approach is based on matching the PP-wave moveout velocity at zero-offset time T_{p0} obtained from PP-wave data with

the PP-wave moveout velocity at zero-offset time T_{c0} obtained from PS-wave data. Instead of assuming that γ_0 is the velocity ratio between squared PP-wave moveout velocity and PS-wave moveout velocity, I calculate an independent V_{p2} from PS-wave data using semblance analysis of V_{c2} and squared PP-wave and PS-wave moveout velocity ratio γ_{iso}. The method is valid in a multi-layer isotropic media.

4.2 Method

Thomsen (1999)'s three-parameter non-hyperbolic traveltime equation for isotropic multi-layered media is given below (as simplified expression in Li and Yuan, 2001):

$$t_c^2 = t_{c0}^2 + \frac{X^2}{V_{c2}^2} + \frac{A_4 X^4}{1 + A_5 X^2}, \qquad (4-1)$$

$$A_4 = \frac{-(\gamma_0 \gamma_{eff} - 1)^2}{4 t_{c0}^2 V_{c2}^4 \gamma_0 (\gamma_{eff} + 1)^2}, \qquad (4-2)$$

$$A_5 = \frac{A_4 V_{c2}^2 \gamma_{eff} (1 + \gamma_0)}{(1 - \gamma_0 \gamma_{eff})}. \qquad (4-3)$$

Equation 4-1, 4-2 and 4-3 show that PS-wave NMO moveout for isotropic multi-layered media is controlled by three parameters PS-wave stacking velocity V_{c2}, vertical velocity ratio γ_0 and effective velocity ratio γ_{eff}. Li (2003) introduced a new parameter γ_{iso} into the above equations. γ_{iso} is defined as the velocity ratio between squared PP- and PS-wave stacking velocities V_{p2}.and V_{c2}:

$$\gamma_{iso} = \frac{V_{p2}^2(t_{c0})}{V_{c2}^2(t_{c0})} = \gamma_{eff} \frac{1 + \gamma_0}{1 + \gamma_{eff}}. \qquad (4-4)$$

Therefore, A_4 and A_5 have a rewritten expression as a function of V_{c2} and γ_{iso}.

$$A_4 = \frac{-(\gamma_{iso}-1)^2}{4t_{c0}^2 V_{c2}^4 \gamma_{iso}}, \qquad (4-5)$$

$$A_5 = \frac{\gamma_{iso}-1}{4t_{c0}^2 V_{c2}^2}. \qquad (4-6)$$

Equation 4-1, 4-5 and 4-6 show that PS-wave NMO moveout for isotropic multi-layered media is controlled by two parameters V_{c2}, and γ_{iso} instead of three, which requires less effort for parameter estimation without compromising the accuracy of Equations 4-2 and 4-3.

A model of five-layer isotropic media is used to examine the accuracy of these two-parameter equations. Table 4.1 shows the model parameters. Figure 4.1 shows the time errors of the new equations (Equations 4-1, 4-5 and 4-6), Thomsen's three-parameter equations (Equations 4-1, 4-2 and 4-3), and two-term hyperbolic equation, which is noted in Equation 4-7. The exact travel time is calculated by ray tracing.

$$t_c^2 = t_{c0}^2 + \frac{X^2}{V_{c2}^2} + \frac{A_4 X^4}{1+A_5 X^2}, \qquad (4-7)$$

	thickness (m)	V_{pk} (m/s)	V_{sk} (m/s)	T_{p0} (s)	T_{c0} (s)	γ_0
1	400	2000	667	0.400	0.800	3.00
2	400	2300	885	0.748	1.426	2.81
3	400	2500	1087	1.068	1.954	2.66
4	400	2600	1238	1.376	2.431	2.53
5	400	2700	1350	1.671	2.875	2.44

Table 4.1: Modelling parameters to examine the accuracy of the Equation 4-1, 4-5 and 4-6. V_{pk} and V_{sk} are interval velocities for P- and S-waves, T_{p0} and T_{c0} are zero-offset two-way PP time and PS-wave time, respectively. γ_0 is vertical velocity ratio and $\gamma_0 = 2T_{c0}/T_{p0}-1$

Figure 4.1 shows that the hyperbolic equation can be only accurate for short-spread moveout analysis (up to offset depth ratio 0.7 for each event in this model). Except that the two-parameter equation has the same accuracy as the three-parameter equation for the first event, the two-parameter equation is more accurate than three-parameter Thomsen equation for the other four events, and the accuracy increases with the decrease of γ_0. For the first two events, the two-parameter PS-wave time equation is accurate for offsets up to one and half the reflection depth; for the third event, the two-parameter PS-wave time equation is accurate for offsets up to twice the reflection depth; for the fourth event, the two-parameter PS-wave time equation is accurate for offsets up to two and half the reflection depth.

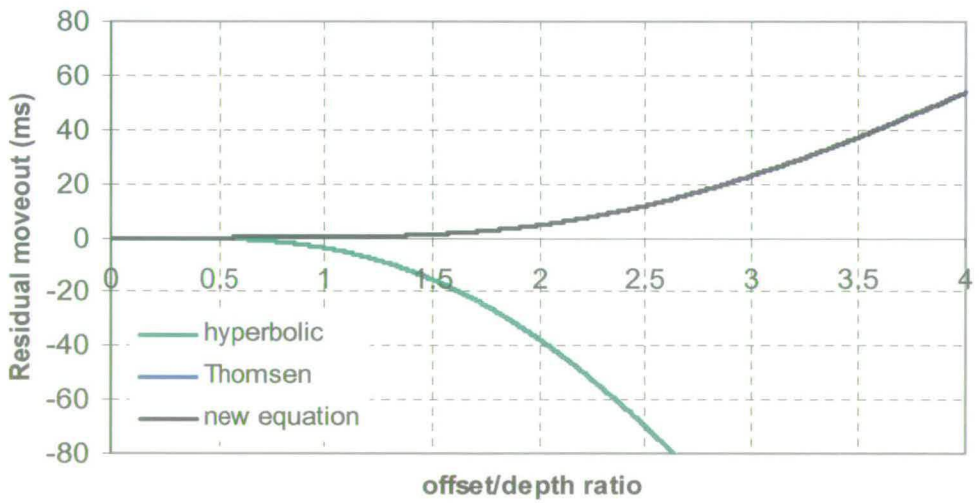

(a) The first layer in Table 4.1

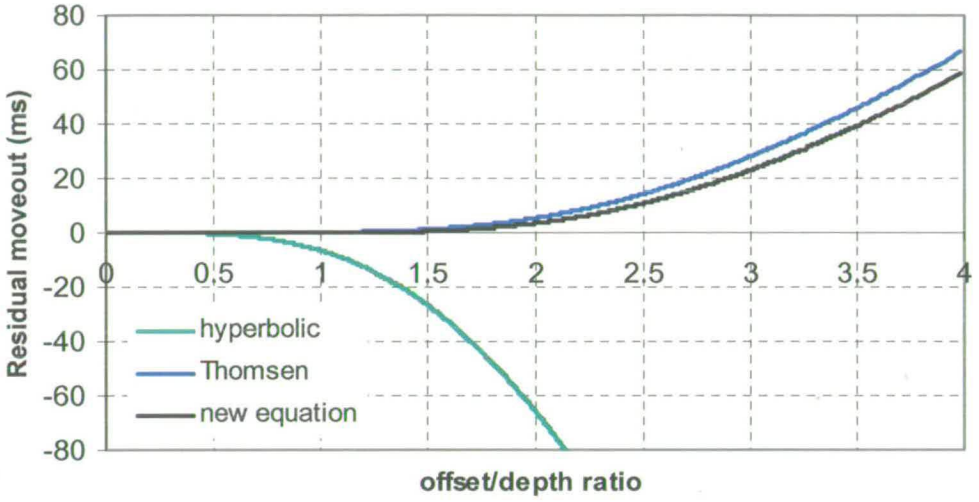

(b) The second layer in Table 4.1

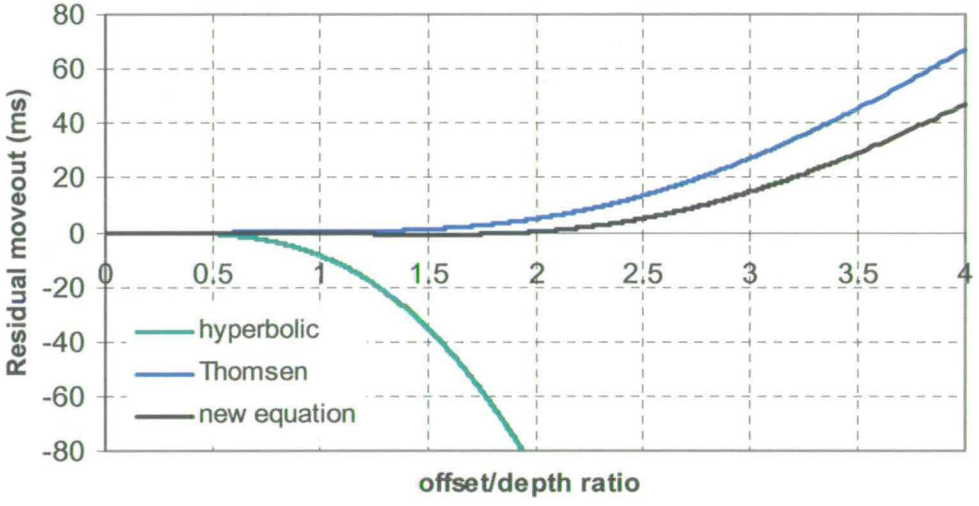

(c) The third layer in Table 4.1

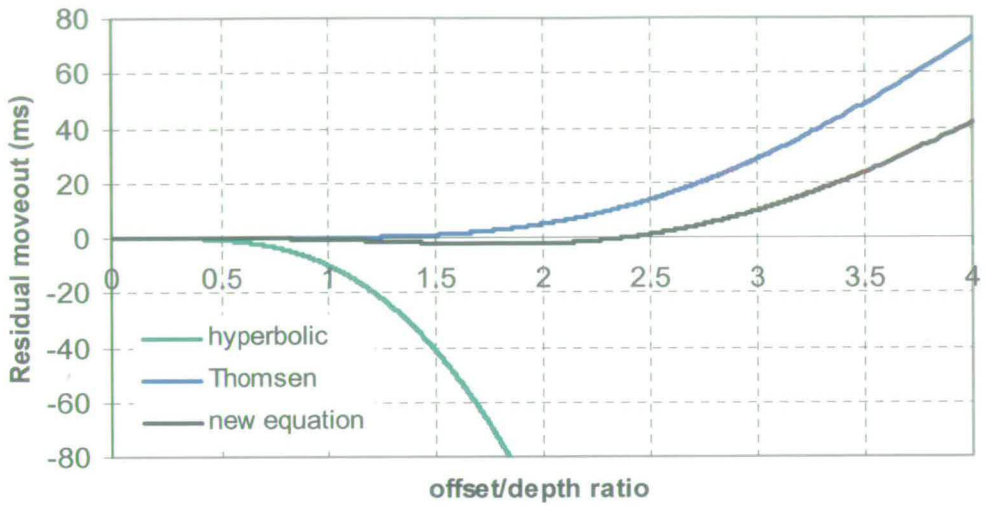

(d) The fourth layer in Table 4.1

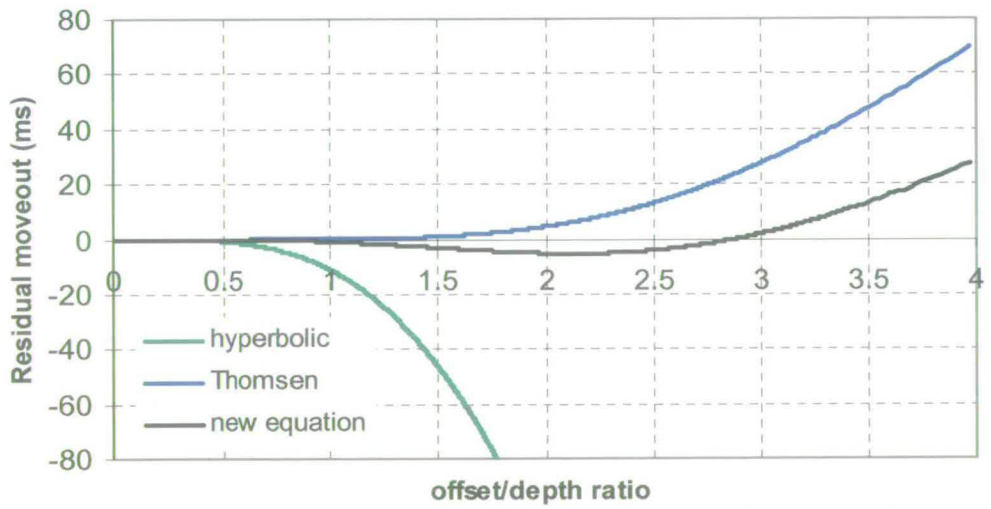

(e) The fifth layer in Table 4.1

Figure 4.1: Residual time $\Delta t = t - t^{exact}$ for the 1st to 5th reflectors of the model in Table 4.1 between the exact travel time (from ray tracing) and two-parameter PS-wave travel time equations in black curve, two term hyperbolic equation in green curve, Thomsen's three parameter equations (1999) in blue curve respectively.

Equation 4-4 indicates that V_{p2} can be obtained independently in PS-wave zero-offset time T_{c0} from PS-wave reflection moveout data alone. Meanwhile, V_{p2} in zero-offset time T_{p0} can also be obtained by PP-wave moveout analysis. If we

minimize the errors between V_{p2} in T_{c0} and V_{p2} in T_{p0}, and compare the respective travel times of the PP-wave velocity in T_{c0} and T_{p0}, the correlation between PP- and PS-wave events can then be established.

Semblance analysis can be used to obtain V_{c2} and γ_{iso} using Equation 4-1, 4-5 and 4-6. The procedure is similar to routine velocity analysis. The semblance coefficient is a statistical measure introduced into velocity analysis by Tanner and Koehler (1969). It is defined as the normalized output/input energy ratio, where the output trace is a simple compositing or sum of the input traces (Neidell and Taner, 1971).

A C code was developed to compute the semblance coefficient as a function of PS-wave velocity V_{c2} and velocity ratio γ_{iso} at the different zero-offset two-way time T_{c0}. To execute the code, a range of values of PS-wave velocities V_{c2} and velocity ratios γ_{iso} are scanned. The values corresponding to maximum semblance are extracted.

4.3 Model Study

4.3.1 Double scanning semblance analysis

Synthetic seismograms are generated for the five-layer model of Table 4.1 to test the method. The maximum offset of the data is 4000m with 50m intervals. The sample rate is 4ms. Figure 4.2 shows the converted-wave reflections of the five layers. The PS-wave travel times calculated by Equation 4-1, 4-5 and 4-6 are shown in red curves in Figure 4.2.

Based on Equation 4-1, 4-5 and 4-6, a double-scanning semblance analysis can be used to resolve V_{c2} and γ_{iso} from PS-wave data alone. The data used in the analysis are restricted to offset:depth ratio 2.0. Figure 4.3 shows semblance analysis results for resolving V_{c2} and γ_{iso}. The picked γ_{iso} values are shown in Table 4.2 as γ^*_{iso}.

Since the determination of V_{c2} relies on short spread conditions, we can see a good resolution for V_{c2} for all events. Because the picked values of V_{c2} in the double-scanning semblance analysis are quite close to the true values, I used the true values of V_{c2} in order to investigate the sensitivity of γ_{iso} in determination of the V_{p2} in T_{c0}.

From Table 4.2, I obtained good estimates of γ_{iso} for the 3rd and 4th events (error less than 1%). Based on Equation 4-4, PP-wave stacking velocity V_{p2} can be obtained in PS-wave vertical travel time T_{c0} (shown as V^*_{p2} in Table 4.2). Consequently, the 3rd and 4th reflectors have errors less than 0.5% in the calculated V_{p2}. This indicates the two-parameter equation is accurate for the 3rd and 4th layers up to at least offset:depth ratio of 2.

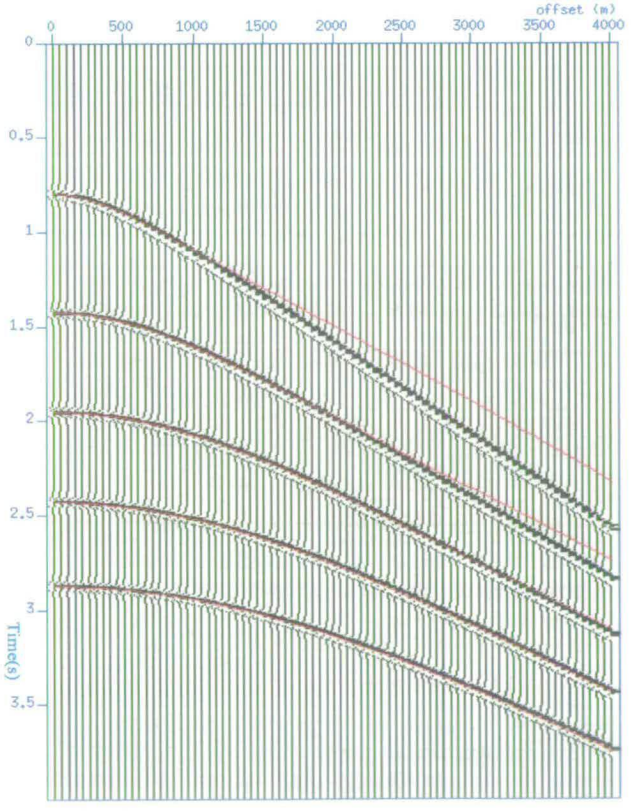

Figure 4.2: PS-wave synthetic gather calculated for the layered model in Table 4.1. The red curves are travel times calculated using Equation (4-1), (4-5) and (4-6)

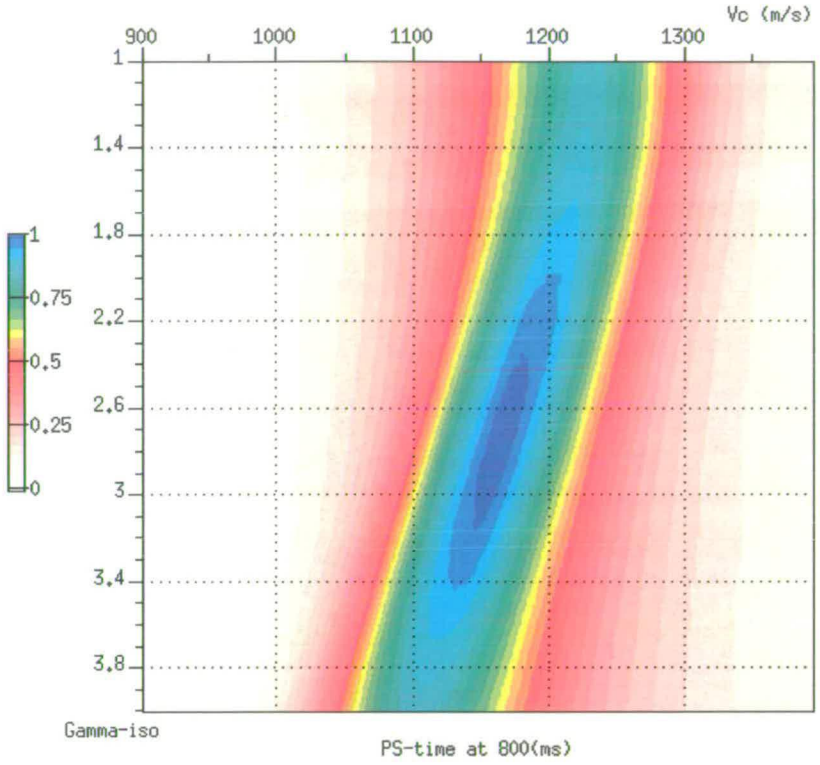
Vc (m/s)
900
1000
1100
1200
1300
1
1.4
1.8
2.2
2.6
3
3.4
3.8
1
0.75
0.5
0.25
0
Gamma-iso
PS-time at 800(ms)

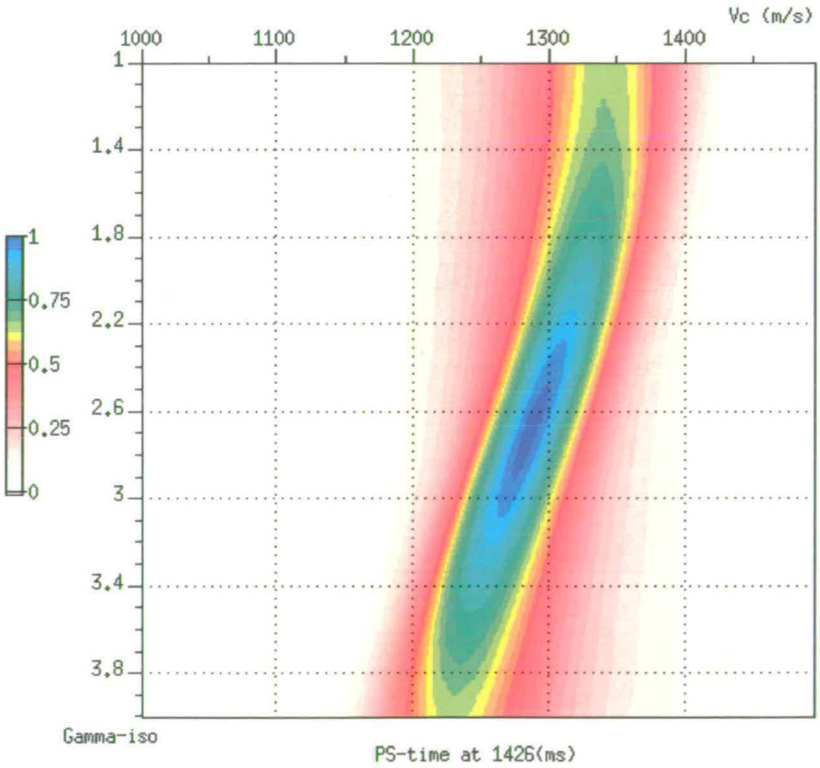
Vc (m/s)
1000
1100
1200
1300
1400
1
1.4
1.8
2.2
2.6
3
3.4
3.8
1
0.75
0.5
0.25
0
Gamma-iso
PS-time at 1426(ms)

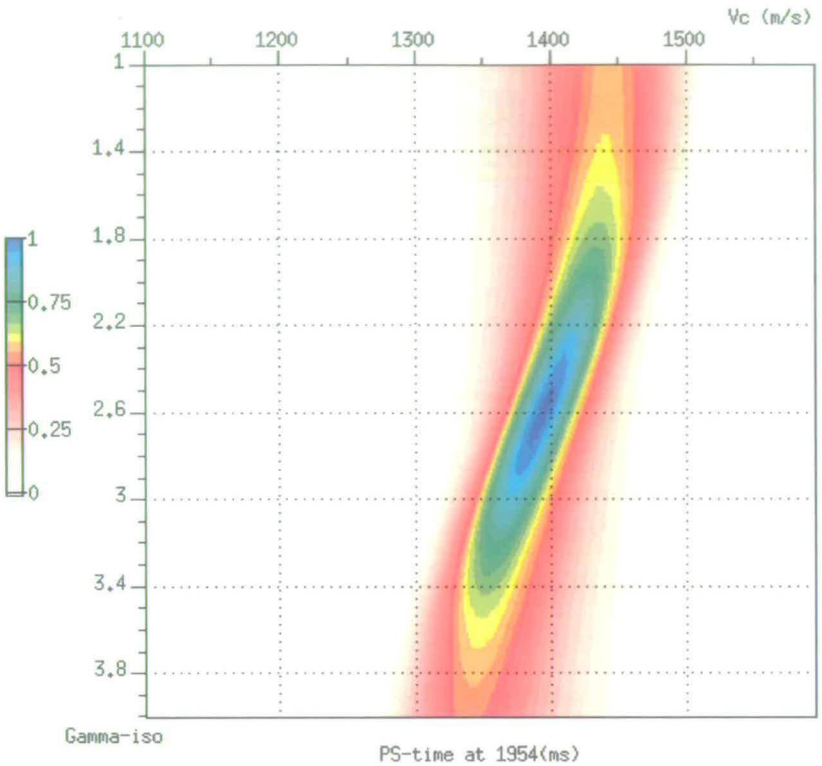
Vc (m/s)
1100
1200
1300
1400
1500
1
1.4
1.8
2.2
2.6
3
3.4
3.8
1
0.75
0.5
0.25
0
Gamma-iso
PS-time at 1954(ms)

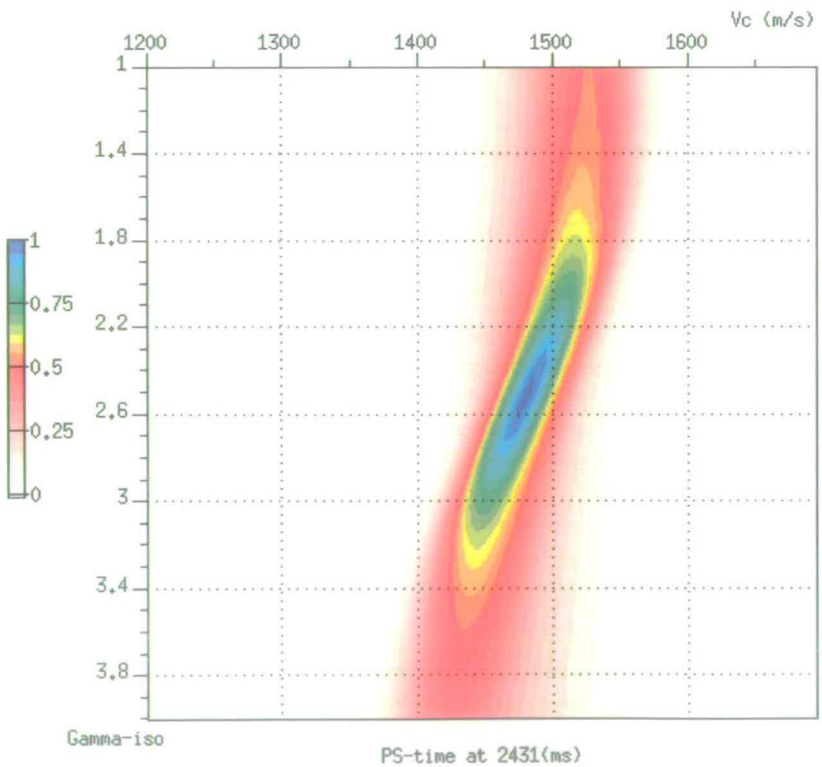
Vc (m/s)
1200
1300
1400
1500
1600
1
1.4
1.8
2.2
2.6
3
3.4
3.8
1
0.75
0.5
0.25
0
Gamma-iso
PS-time at 2431(ms)

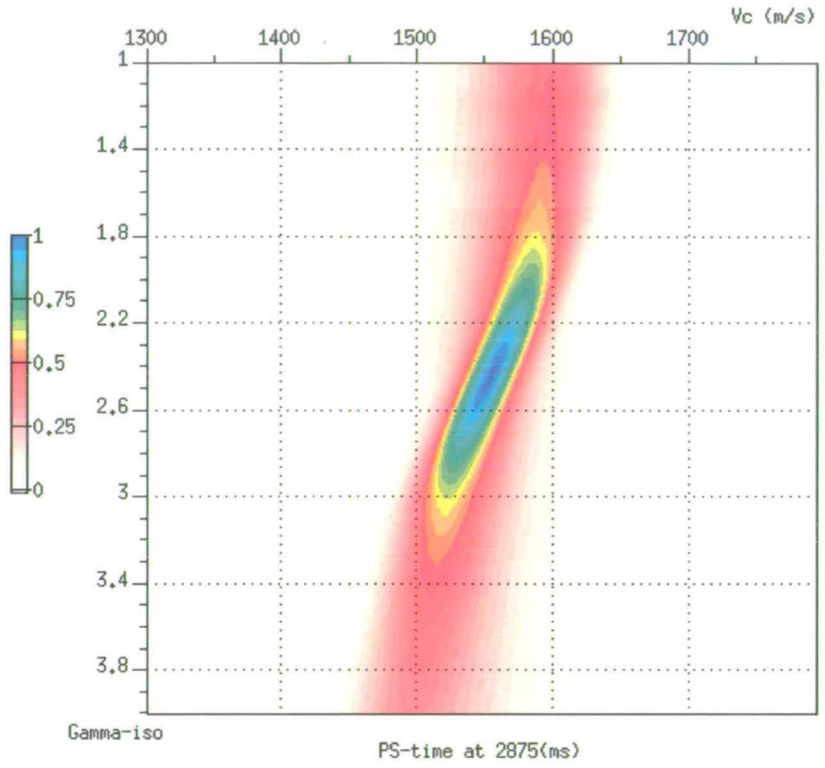

Figure 4.3: Double-scanning results for V_{c2} and γ_{iso} corresponding to the events 1, 2, 3, 4 and 5, respectively. The values are picked from the center point of the maximum semblance. The picked values of γ_{iso} are shown in Table 4.2 as γ^*_{iso}. The offset depth ratio is up to 2 for all events.

	actual V_{c2} (m/s)	actual γ_{iso}	γ^*_{iso}	error γ^*_{iso} %	actual V_{p2} (m/s)	V^*_{p2} (m/s)	error V^*_{p2} %
1	1155	3.00	2.78	7.3	2000	1926	3.70
2	1281	2.80	2.70	3.6	2144	2105	1.82
3	1390	2.64	2.63	0.4	2257	2254	0.13
4	1478	2.50	2.52	0.8	2338	2346	0.34
5	1552	2.40	2.45	2.1	2406	2429	0.96

Table 4.2: The calculated PP-wave stacking velocity V_{p2} by PS-wave moveout analysis in isotropic media from Equation 4-4. γ^*_{iso} is the obtained value from PS-wave semblance analysis. The maximum offset depth:ratio is 2 for all events.

4.3.2 Sensitivity analysis of γ_{iso} for different:offset depth ratio

Since V_{p2} can be obtained from PS-wave data through Equation 4-4, the relative error of V_{p2} from Equation 4-4 can be expressed as the following:

$$\frac{\Delta V_{p2}}{V_{p2}} = \frac{\Delta V_{c2}}{V_{c2}} + \frac{1}{2}\frac{\Delta \gamma_{iso}}{\gamma_{iso}}. \qquad (4-8)$$

From the above equation, if we assume that the V_{c2} can be resolved with very small error, the relative error of V_{p2} is the half the error of the γ_{iso}. Because γ_{iso} mainly controls the moveout of the intermediate-far offsets, the offset:depth ratio in the semblance analysis should be large enough to resolve γ_{iso}. The accuracy of travel time equation for intermediate-far offset is also important for resolving γ_{iso}.

To illustrate the above issue, I use the dataset with different maximum offset:depth ratios of x/z=1, x/z=1.5, and x/z=2.5. Figure 4.4 show the results of the double scanning semblance analysis when x/z≤1. Though there is a good resolution for V_{c2} from short spread data, a maximum x/z ratio 1 is obviously not large enough for the resolution of γ_{iso}.

As in Figure 4.3, Figure 4.5 and Figure 4.6 show the V_{c2} and γ_{iso} results for x/z≤1.5 and x/z≤2.5 respectively. The resolution of γ_{iso} increases with increasing offset:depth ratio. However, the accuracy of γ_{iso} does not increase with the increased resolution. Table 4.3 and 4.4 show the picked value γ^*_{iso} for the five events for maximum x/z ratios of 1.5 and 2.5 respectively. From the analysis of Table 4.2, 4.3 and 4.4, the optimum γ_{iso} results for the first two layers are obtained from the data with x/z ratio≤1.5; for the 3rd layer, from x/z ratio≤2; for 4th layer, from x/z ratio≤2.5. For the 5th layer, since the maximum offset in the synthetic data is 4000m, the result is the same for x/z≤2 and ≤2.5. The above analysis is summarised in Table 4.5.

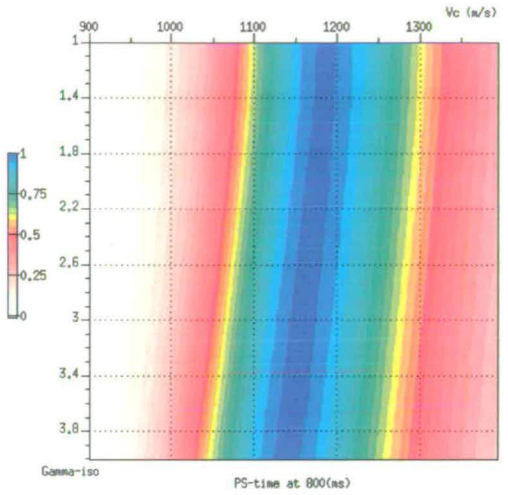

(a) the first layer

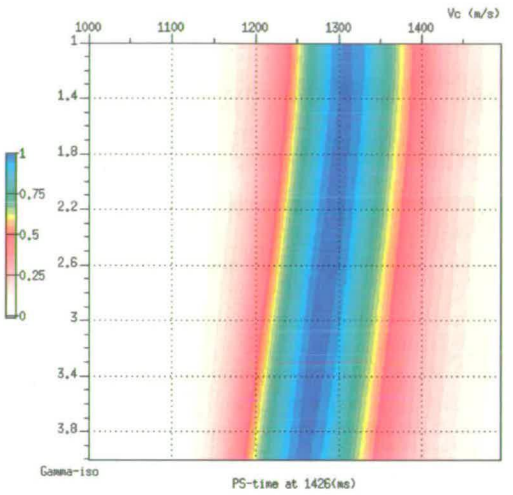

(b) the second layer

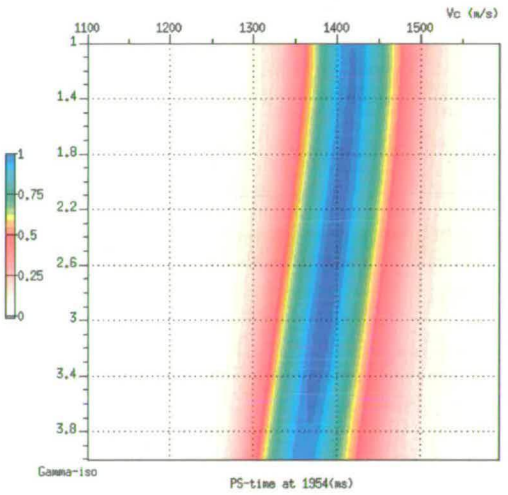

(c) the third layer

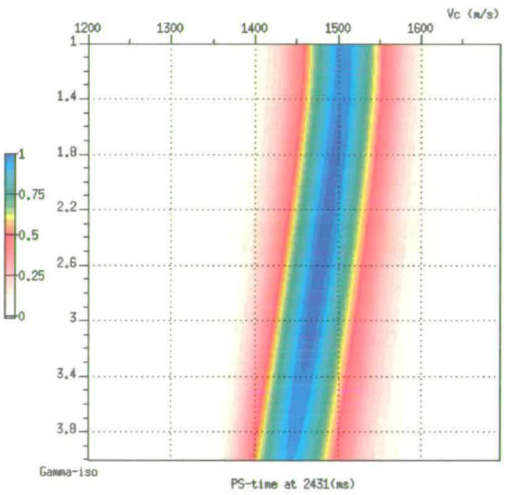

(d) the fourth layer

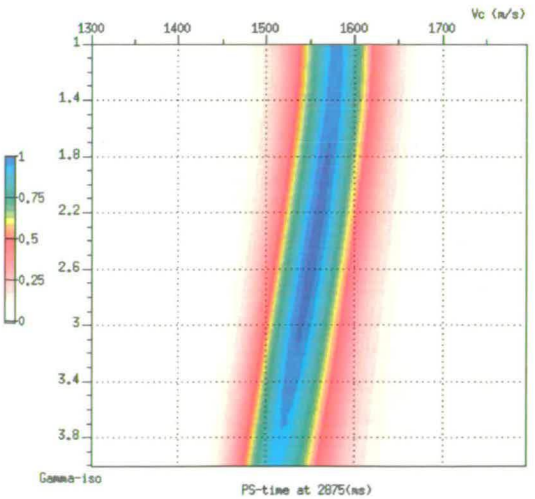

(e) the fifth layer

Figure 4.4: Double-scanning results for V_{c2} and γ_{iso} show no resolution for γ_{iso} when maximum offset:depth ratio is 1.

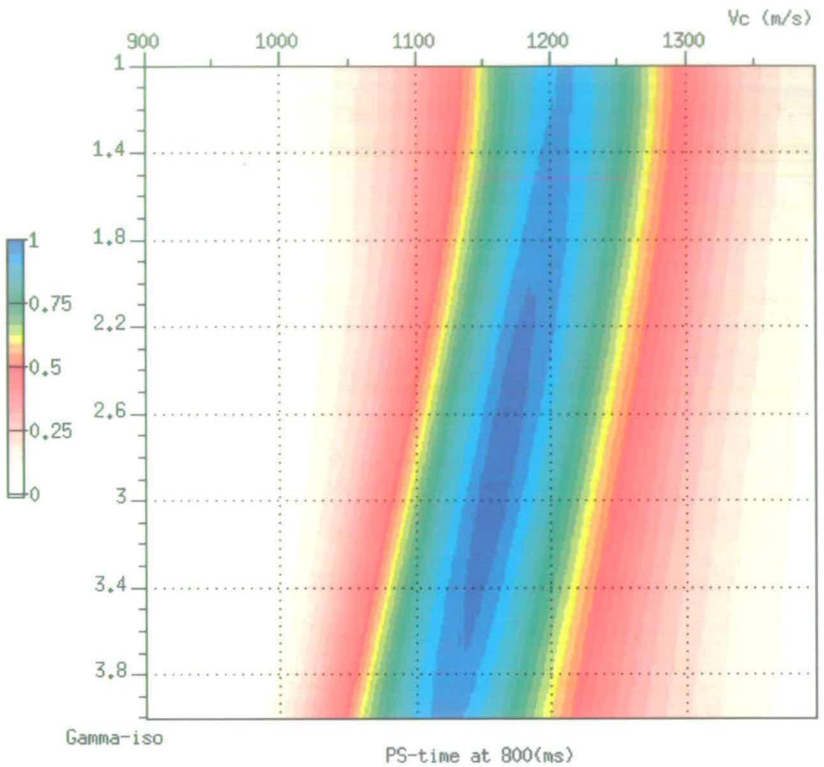
Vc (m/s)
900
1000
1100
1200
1300
1
1.4
1.8
2.2
2.6
3
3.4
3.8
1
0.75
0.5
0.25
0
Gamma-iso
PS-time at 800(ms)

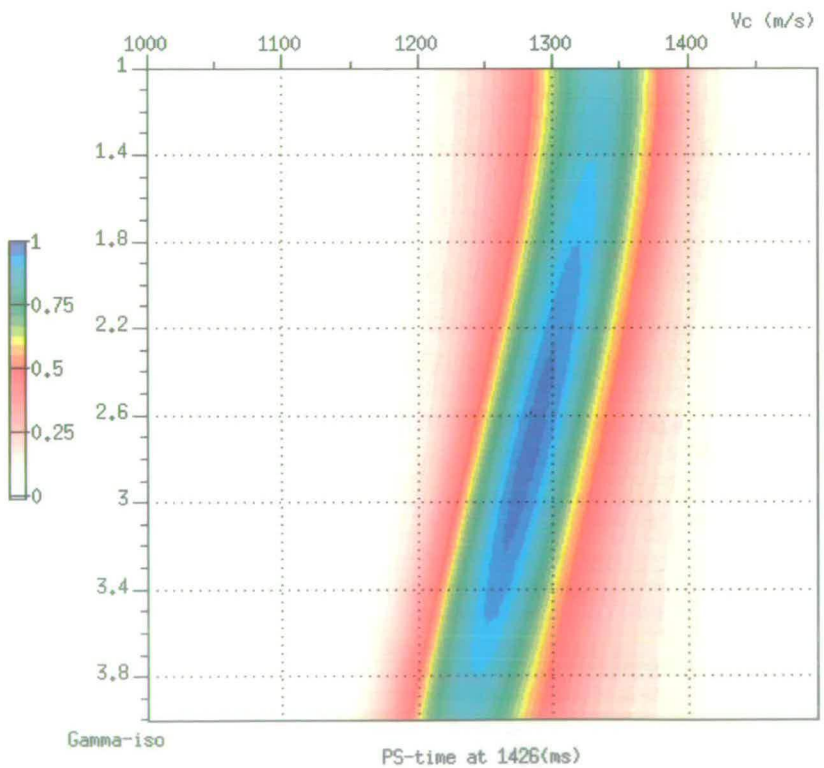
Vc (m/s)
1000
1100
1200
1300
1400
1
1.4
1.8
2.2
2.6
3
3.4
3.8
1
0.75
0.5
0.25
0
Gamma-iso
PS-time at 1426(ms)

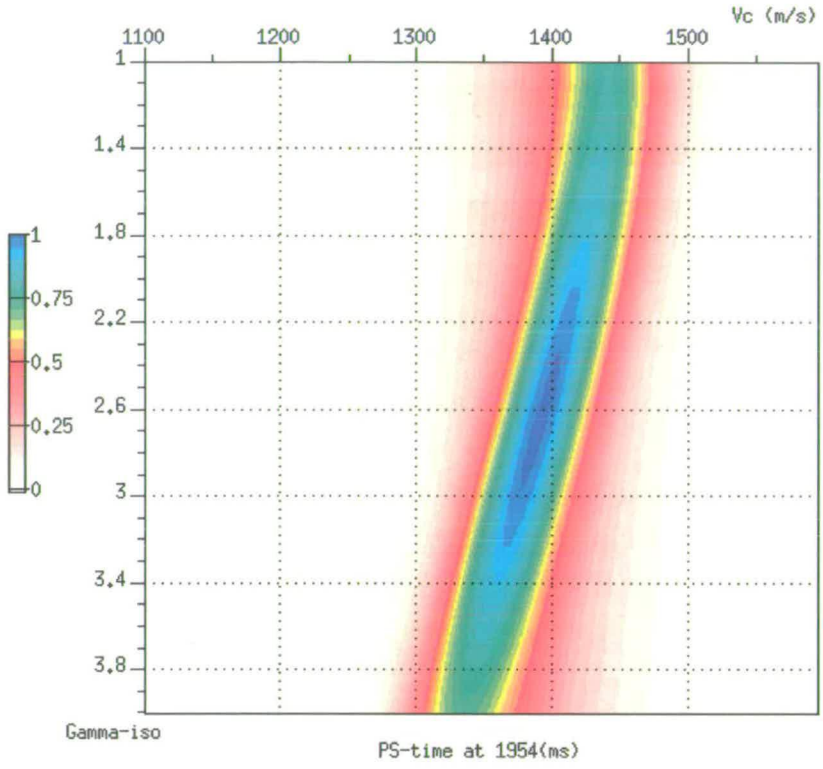
Vc (m/s)
1100
1200
1300
1400
1500
1
1.4
1.8
2.2
2.6
3
3.4
3.8
1
0.75
0.5
0.25
0
Gamma-iso
PS-time at 1954(ms)

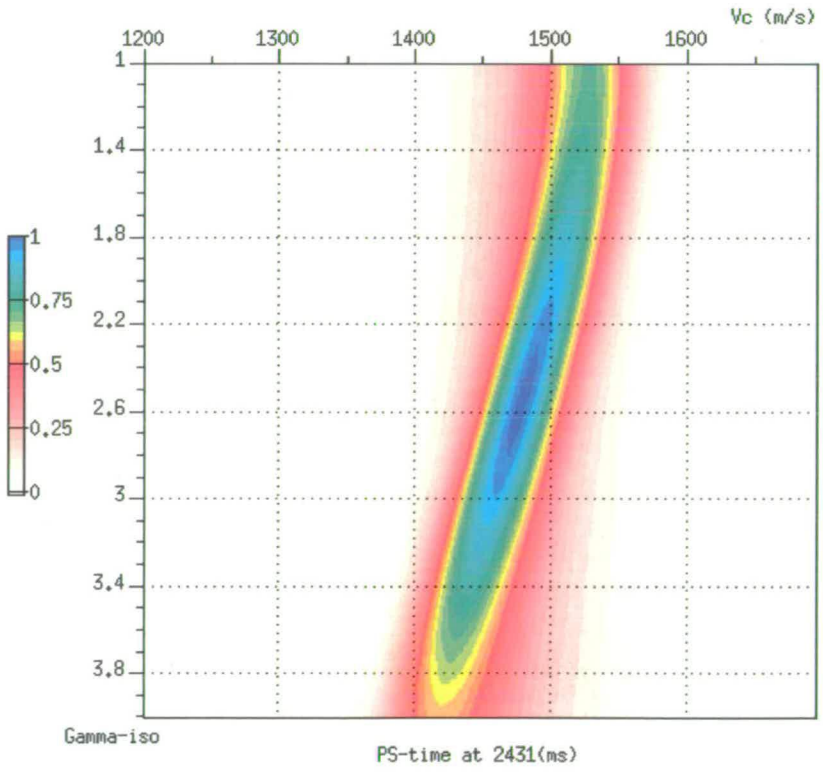
Vc (m/s)
1200
1300
1400
1500
1600
1
1.4
1.8
2.2
2.6
3
3.4
3.8
1
0.75
0.5
0.25
0
Gamma-iso
PS-time at 2431(ms)

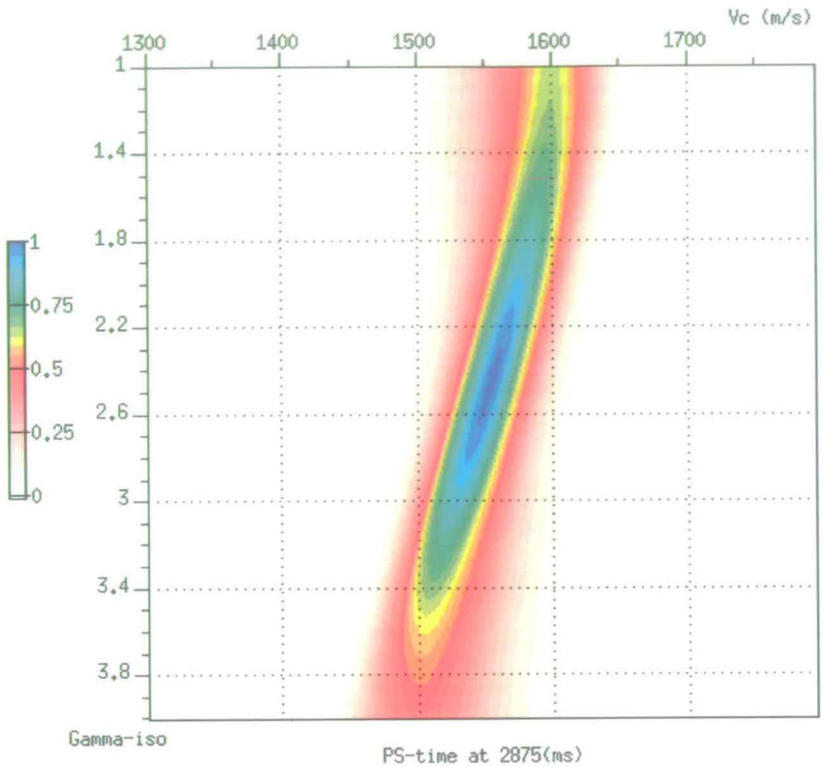

Figure 4.5: As in Figure 4.3. The picked values of γ_{iso} are shown in Table 4.3 as γ^*_{iso}. Offset:depth ratio≤1.5 for all events.

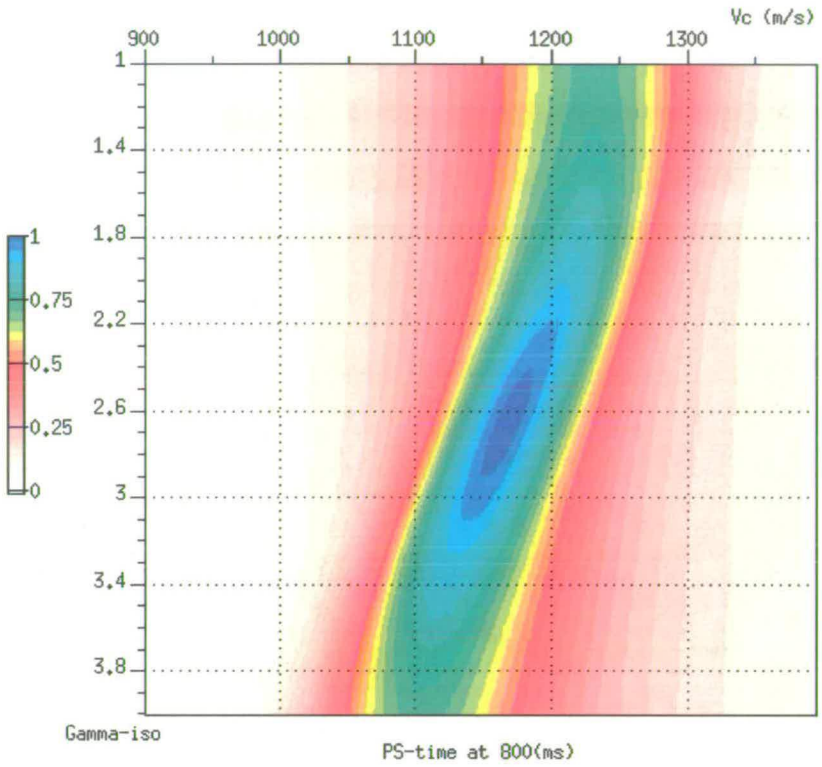
Vc (m/s)
900
1000
1100
1200
1300
1
1.4
1.8
2.2
2.6
3
3.4
3.8
1
0.75
0.5
0.25
0
Gamma-iso
PS-time at 800(ms)

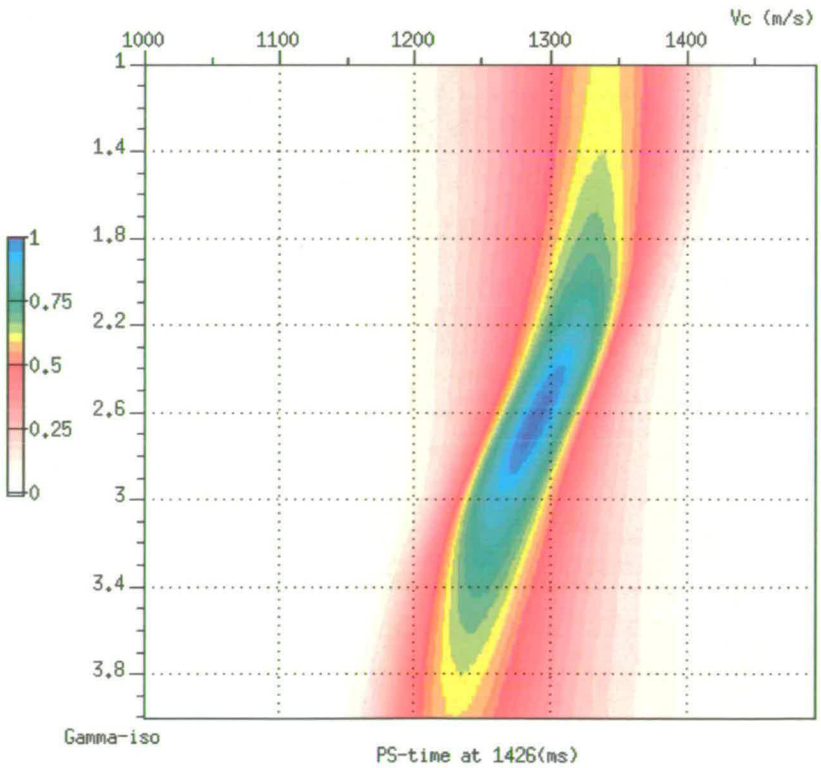
Vc (m/s)
1000
1100
1200
1300
1400
1
1.4
1.8
2.2
2.6
3
3.4
3.8
1
0.75
0.5
0.25
0
Gamma-iso
PS-time at 1426(ms)

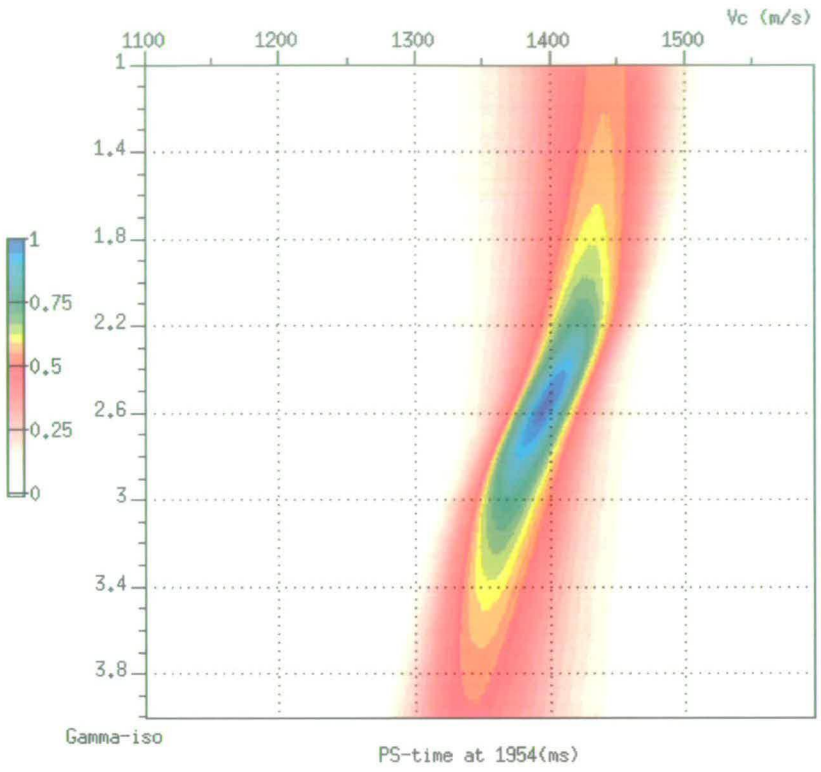
Vc (m/s)
1100
1200
1300
1400
1500
1
1.4
1.8
2.2
2.6
3
3.4
3.8
1
0.75
0.5
0.25
0
Gamma-iso
PS-time at 1954(ms)

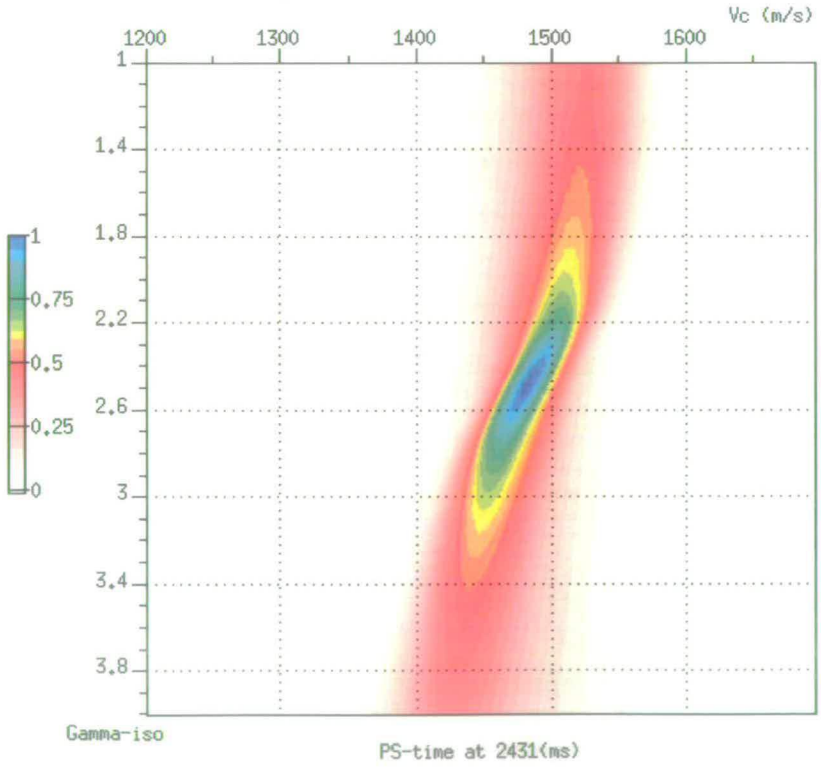
Vc (m/s)
1200
1300
1400
1500
1600
1
1.4
1.8
2.2
2.6
3
3.4
3.8
1
0.75
0.5
0.25
0
Gamma-iso
PS-time at 2431(ms)

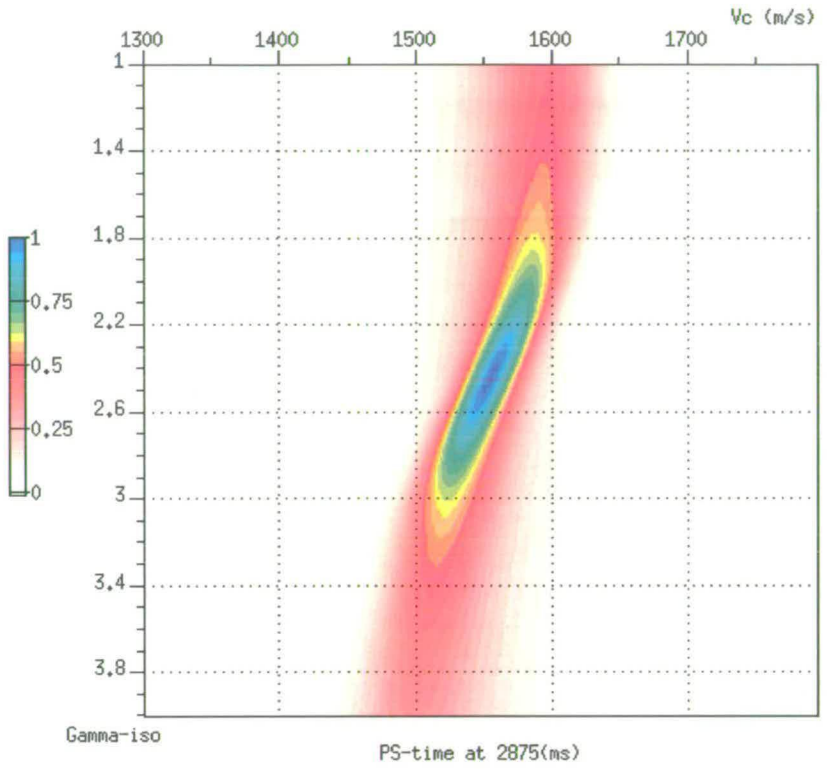

Figure 4.6: As in Figure 4.3. The picked values of γ_{iso} are shown in Table 4.4 as γ^*_{iso}. Offset:depth ratio≤2.5 for all events.

	actual V_{c2} (m/s)	actual γ_{iso}	γ^*_{iso}	error γ^*_{iso} %	actual V_{p2} (m/s)	V^*_{p2} (m/s)	error V^*_{p2} %
1	1155	3.00	2.85	5.0	2000	1950	2.50
2	1281	2.80	2.78	0.7	2144	2136	0.37
3	1390	2.64	2.66	0.8	2257	2267	0.44
4	1478	2.50	2.58	3.2	2338	2374	1.54
5	1552	2.40	2.49	3.8	2406	2449	1.79

Table 4.3: As in Table 4.2. Offset depth ratio≤1.5.

	actual V_{c2} (m/s)	actual γ_{iso}	γ^*_{iso}	error γ^*_{iso} %	actual V_{p2} (m/s)	V^*_{p2} (m/s)	error V^*_{p2} %
1	1155	3.00	2.69	10.3	2000	1894	5.30
2	1281	2.80	2.64	5.7	2144	2081	2.94
3	1390	2.64	2.59	1.9	2257	2237	0.89
4	1478	2.50	2.50	0.0	2338	2338	0.00
5	1552	2.40	2.45	2.1	2406	2429	0.96

Table 4.4:As in Table 4.2. Offset depth ratio≤2.5.

	actual V_{c2} (m/s)	actual γ_{iso}	γ^*_{iso}	error γ^*_{iso} %	actual V_{p2} (m/s)	V^*_{p2} (m/s)	Error V^*_{p2} %	X/Z ratio ≤
1	1155	3.00	2.85	5.0	2000	1950	2.50	1.5
2	1281	2.80	2.78	0.7	2144	2136	0.37	1.5
3	1390	2.64	2.63	0.4	2257	2254	0.13	2
4	1478	2.50	2.50	0.0	2338	2338	0.00	2.5
5	1552	2.40	2.45	2.1	2406	2429	0.96	2/2.5

Table 4.5: Optimum picked γ^*_{iso} and calculated V^*_{p2} in $T_{c0,}$ and their corresponding optimum maximum offset:depth ratio.

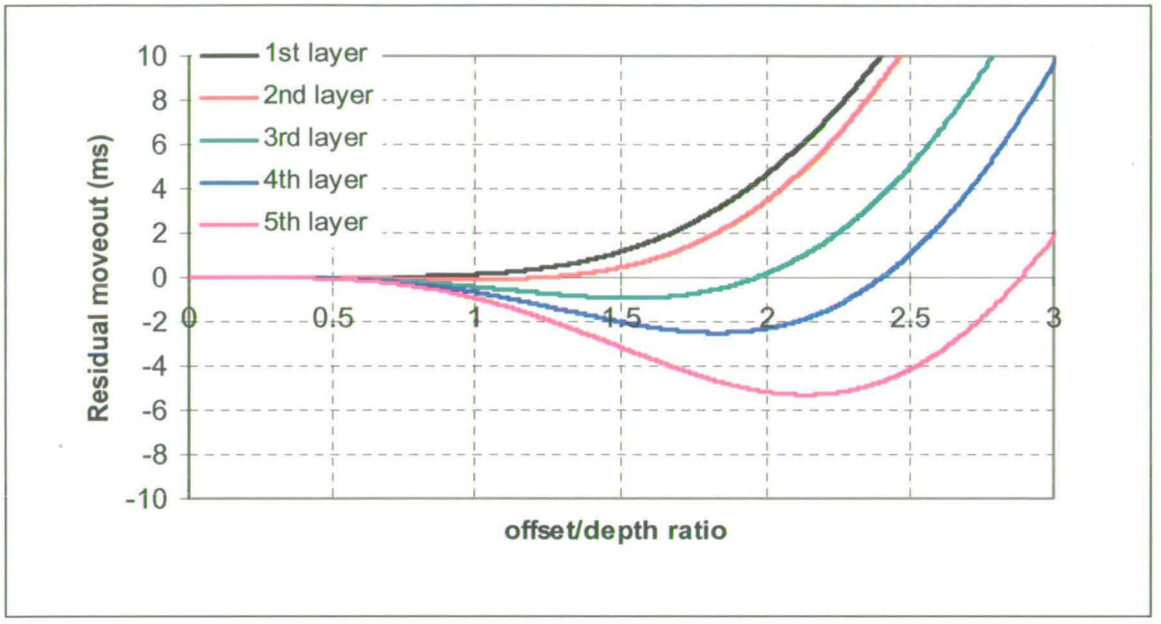

Figure 4.7: Time errors of two-parameter PS-wave travel time equations for five events in Figure 4.2

Figure 4.7 shows the residual moveout from the two-parameter equations (Equation 4-1, 4-5 and 4-6) for five reflectors in Table 4.1. Among the three different maximum x/z ratios of 1.5, 2, and 2.5, the equation has the smallest errors at maximum x/z ratio of 1.5 for the first two reflectors, maximum x/z ratio of 2 for the third reflector, and maximum x/z of 2.5 for the fourth reflector. Since offset:depth ratio is large enough for the fourth layer, I obtain the best result of γ_{iso} for the 4^{th} event. Except for the shallowest layer, the errors of the calculated V_{p2} from PS-wave data alone are less than 1%.

4.3.3 Determination of γ_0

V_{p2} in T_{c0} time can then be compared with the V_{p2} in T_{p0} time: the latter can be obtained from the PP-wave moveout analysis. I plot V^*_{p2} in T_{c0} in Table 4.5 and V_{p2} in T_{p0} in Figure 4.8. The vertical velocity ratio can be got from:

$$\gamma_0 = \frac{2t_{c0}}{t_{p0}} - 1. \qquad (4-9)$$

As shown in Figure 4.8, the marked correlation (black line) indicates the minimum difference between the values of V_{p2} in T_{c0} and those in T_{p0}. Except for the shallowest event, all events show a good one-to-one correspondence in terms of V_{p2}.

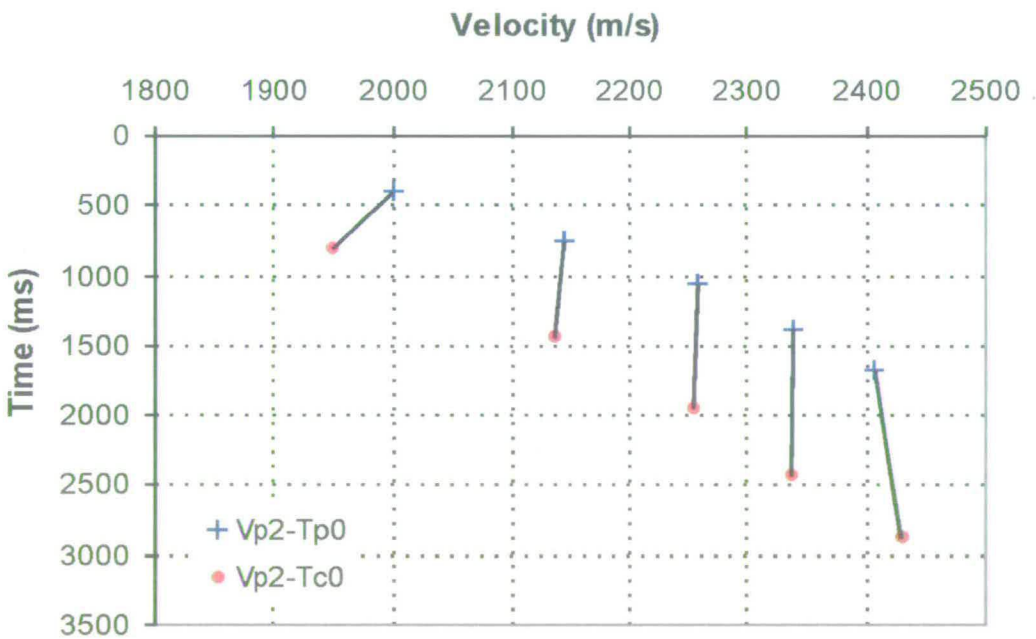

Figure 4.8: Correlation of the velocity picks. The blue crosses are V_{p2} in PP-wave vertical travel time T_{p0} and the red dots are V_{p2} in PS-wave vertical travel time T_{c0}. T_{p0} and T_{c0} are listed in Table 4.1.

4.4 Application to the Ordos data

The converted-wave data for the Ordos basin are acquired over a horizontal stratigraphy and offset:depth ratio is around 2.0, which are desirable characteristics for this correlation study. A flat coal layer (at around 2.0s in PP-wave time) is distributed across the region and provides a good calibration point to examine the

accuracy of the application to real data. I use both two passes of a single scanning semblance analysis and one pass of the double scanning semblance analysis to determine V_{c2} and γ_{iso}. Examples of the double scanning results in CCP 550 (Figure 4.9a) are shown in Figure 4.9b. The event at zero-offset time 700ms has a better resolution of γ_{iso} than at 1266ms and 2865ms, which may result from the noisy data present in mid-to-far offset in the deeper part of the data. I then perform the two passes of single scanning technique.

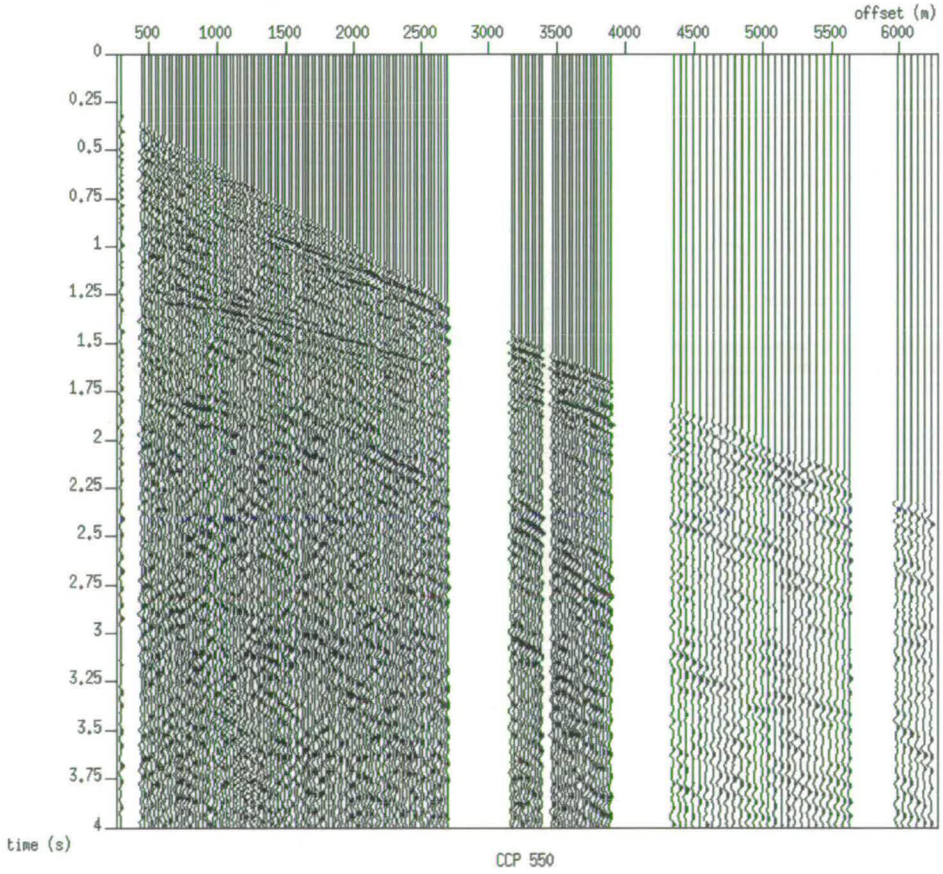

Figure 4.9a: CCP gather 550 used in the scanning analysis.

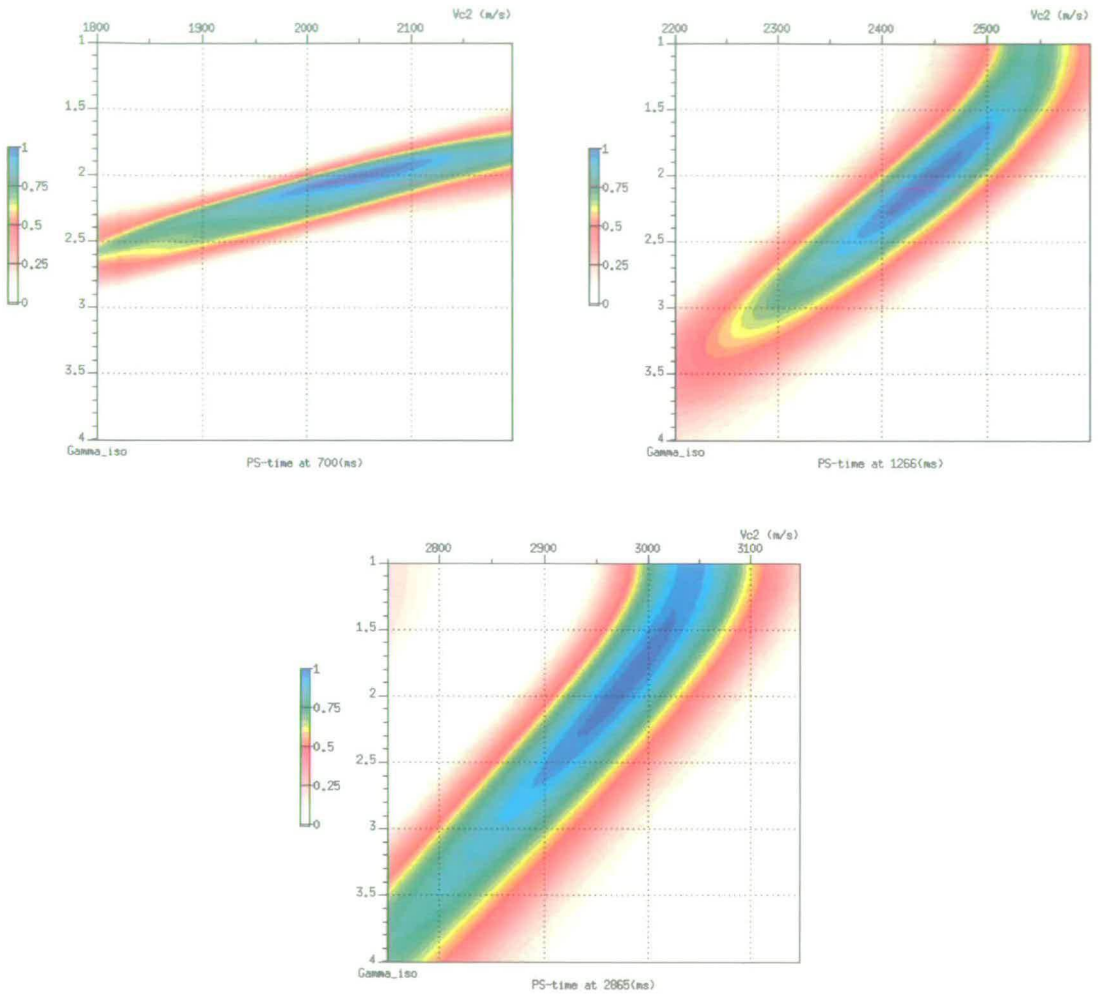

Figure 4.9b: Double scanning analysis for V_{c2} and γ_{iso} for the Ordos converted-wave data (CCP 550, event 700ms, 1266ms and 2865ms respectively. The scanning window length is 100ms).

Examples of the single-scanning results in CCP 550 are shown in Figure 4.10. V_{c2} is first acquired given a fixed value of γ_{iso} of 2.0 at the different events (Figure 4.10a). Then γ_{iso} is acquired at the obtained V_{c2} for the different events (Figure 4.10b). Figure 4.11 shows the PP-wave velocity spectra in T_{c0} and T_{P0} times (Figures 4.11a and 11b, respectively), which provide a good correlation among the three events in Table 4.6. For these three events, their V_{p2} in T_{c0} matches those in T_{p0} very closely. The resultant vertical velocity ratios (γ_0) are 1.97, 1.96 and 1.86, respectively. The spatially-variable γ_0 can be obtained by semblance analysis at

different CCP points. The compressed PS-wave section using these values of γ_0 also matches the PP-wave section very well, supporting the analysis (Figure 4.12).

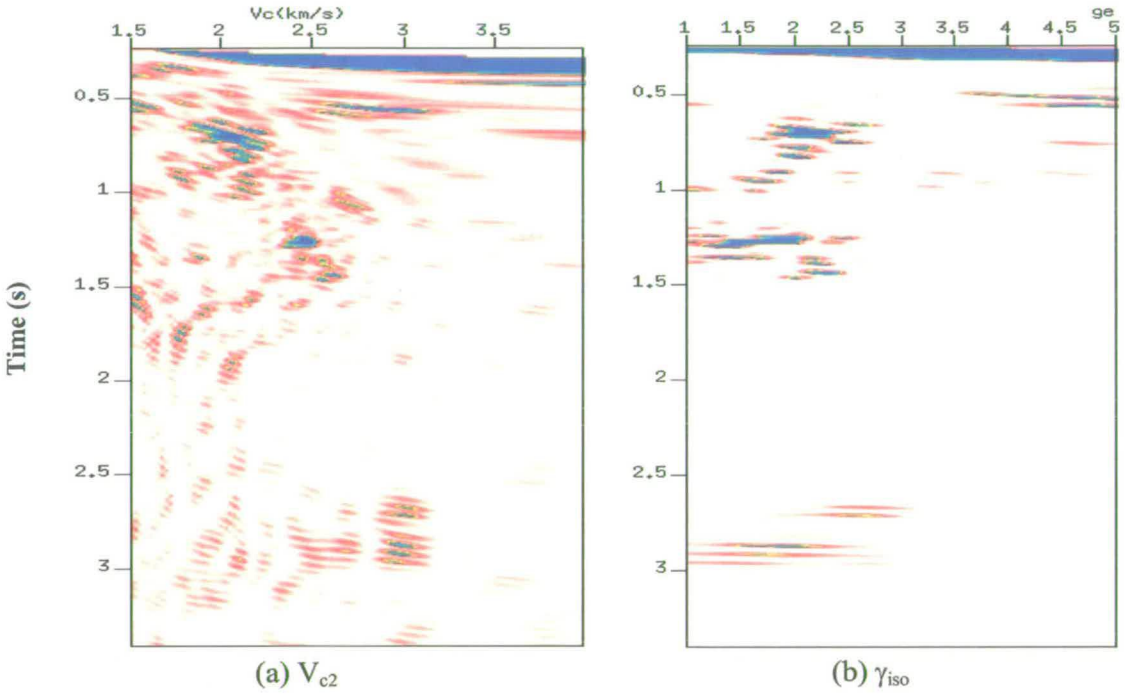

Figure 4.10: Single-scanning results for V_{c2} and γ_{iso} in the Ordos converted-wave data

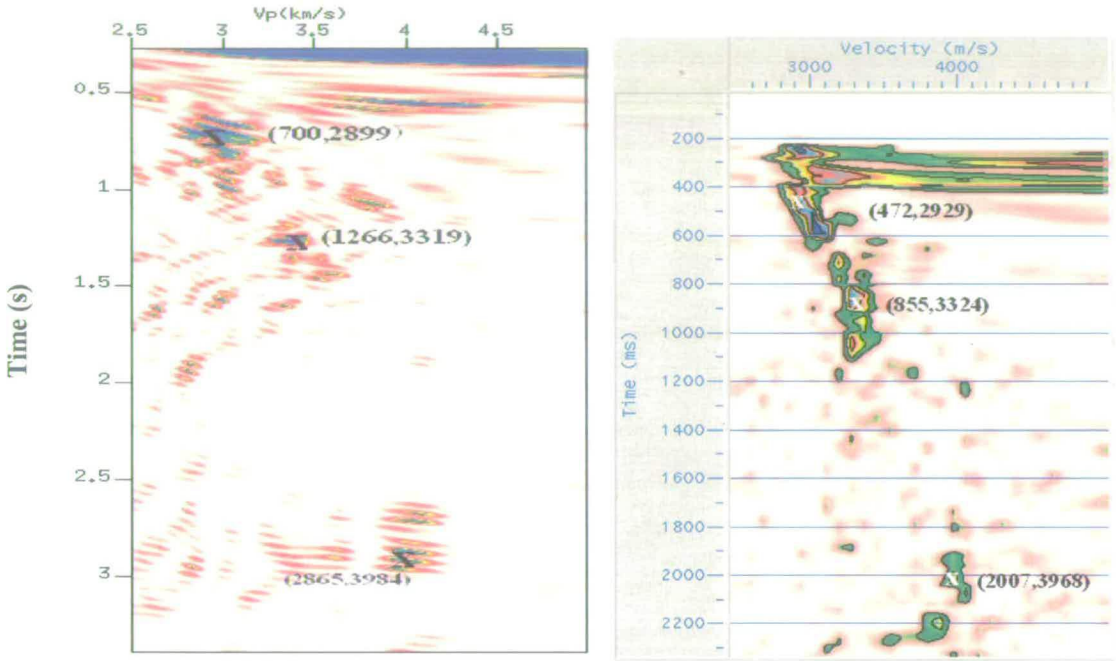

(a) PS-wave (b) PP-wave

Figure 4.11: Comparison of (a) V_{p2} spectra obtained from PS-wave moveout data with (b) V_{p2} spectra from PP-wave moveout data. The vertical time is T_{c0} in (a), but T_{p0} in (b). The crosses indicated the correlated velocity points with their corresponding time in bracket (time, velocity).

T_{c0} (ms)	V_{c2} (m/s)	γ_{iso}	V^*_{p2} (m/s)	T_{p0} (ms)	V_{p2} (m/s)	γ_0
700	2050	2.00	2899	472	2929	1.97
1266	2440	1.85	3319	855	3324	1.96
2865	2970	1.80	3984	2007	3968	1.86

Table 4.6: Results from the Ordos data showing the comparison of obtained V^*_{p2} in T_{c0} from PS-wave moveout data with V_{p2} in T_{p0} from PP-wave data

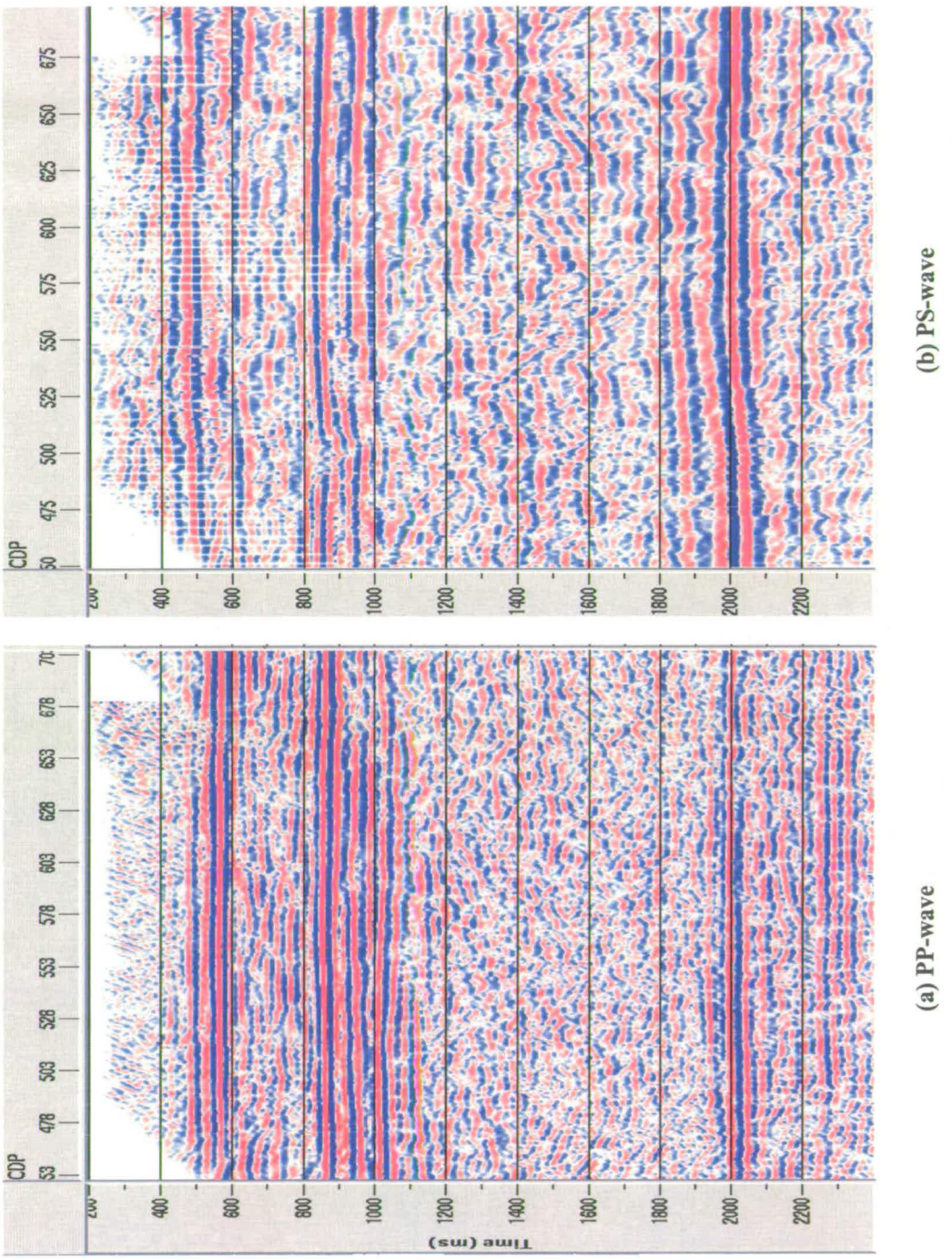

Figure 4.12: Correlation between stacked PP-wave (a) and PS-wave (b). Both sections are displayed in PP-wave vertical time

4.5 Discussion and conclusion

A model study shows that the new two-parameter PS-wave travel time equation is more accurate than three-parameter Thomsen's (1999) equation for multi-layered isotropic media for the model studied.

Synthetic and real data examples show that PS-wave semblance analysis based on the two-parameter PS-wave travel time equation can be used to resolve V_{c2} and γ_{iso} in layered media. The PP-wave stacking velocity can then be obtained independently in the PS-wave travel time domain. The reliability of the V_{p2} in T_{c0} is mainly determined by the accuracy of the stacking velocity ratio γ_{iso}.

Based on the model study, for resolving the accurate γ_{iso} (error less than 0.5%), the offset:depth ratio needs to be at least 1.5. The offset:depth ratio necessary for an accurate γ_{iso} increases with depth. The model study shows that it is possible to perform a reliable correlation through the use of γ_{iso} when two-parameter PS-wave travel time error is less 10ms at the offset:depth ratio$\leq$2. Real data from the Ordos Basin shows an accurate PP- and PS-wave correlation by two-pass single scanning semblance analysis.

The method is valid in a multi-layer isotropic media and can be used as a good reference for PP- and PS-wave correlation, if the stacking velocities are monotonically increasing with depth.

Chapter 5: AVO theory and PP-data analysis

5.1 Introduction

As a lithology and fluid analysis tool, the amplitude versus offset (AVO) method has been practiced in the petroleum industry for more than 20 years. Ostrander (1982) firstly demonstrated that the reflection coefficients of gas sands vary in an anomalous fashion with increasing offset, which started the development of the AVO method. Since then, a number of PP-wave AVO methods have been derived, including the intercept and gradient analysis (Shuey, 1985) and the weighted stacking technique (Smith and Gidlow, 1987). In recent years, the acquisition and processing of multicomponent seismic data has made it possible to analyze PP- and converted-waves (PS-wave) simultaneously. Stewart (1994) shows that the joint interpretation of PS-waves with PP-waves holds great promise for gas zone imaging and lithology identification. Larsen (1999), Goodway (2002) and Gray (2003) have discussed how to use PP- and PS-wave AVO to estimate elastic parameters and discriminate between pore fluids.

The AVO technique has been used to extract elastic parameters, e.g. V_p/V_s ratio, P- and S-wave impedance, Lamè moduli, and elastic impedance (EI, Connolly, 1999), from prestack seismic data to infer the subsurface lithology and fluid content (Castagna *et al.*, 1993). In order to estimate the fractional V_p and V_s velocity, Smith and Gidlow (1987) developed a "weighted stacking" method using least-squares inversion to apply a set of model-based weights in an offset-dependent manner. They used a smooth P-wave velocity background and the assumption of Gardner's (1974) P-wave velocity and density relation. Barlona and White (2001) investigate Gardner's relation with AVO inversion, and show that Gardner-type relation introduces biases into S-wave related estimations. The biases are dependent on AVO class and fluid content. Fatti *et al.* (1994) estimated the fractional P-wave and S-wave impedance with the weighted-stacking method, which does not need an

empirical relation between V_p and density but ignores the density effect by assuming a small density contrast. Goodway *et al.* (1997) show an enhanced sensitivity to pore fluid from Lamè modulus parameters and extract $\lambda\rho$ and $\mu\rho$ from P- and S- wave impedance. However, the noise may also be enhanced in the $\lambda\rho$ data due to the square of impedance. Gray *et al.* (1999) present a PP-AVO equation in terms of the rock properties of Lamè modulus and density. Inversion through this equation keeps a similar noise level to the impedance inversion. Here, I further combine this equation with the PS-AVO equation to perform joint PP-and PS-inversion without cancelling the density item.

5.2 AVO class definition

First, the basic definition for AVO class is reviewed. According to the AVO classification for gas sand by Rutherford and William (1989) and Castagna and Swan (1997), there are four AVO classes for clastic rocks shown in Figure 5.1.

Class I gas sands have higher impedance than that of the overlying layer. The intercept A is relatively large and positive, and the reflection magnitude decreases with offset faster than the background trend (dimming effect). Product of intercept A and gradient B is negative at top. These sands lie in quadrant IV (Figure 5.1b).

Class II gas sands have nearly the same impedance as that of the overlying layer: the normal-incidence coefficient A value is less than 0.02 in magnitude. The reflection magnitude may increase or decrease with offset, and may reverse polarity, the product A*B is indeterminate. This type of sand is usually moderately compacted and consolidated, and can lie in either II, III, or IV quadrants. Class II sands may or may not correspond to amplitude anomalies on stacked data.

Class III gas sands have lower impedance than that of the overlying unit (classical bright spots). The A value is negative and large, the reflection amplitude increases

with offset, the product A*B is positive at top. Class III sands are usually undercompacted and unconsolidated.

Class IV gas sands have a lower impedance than that of the overlying unit. The A value is negative and large, but reflection amplitude decreases with the increasing offset, the product A*B is negative at top. Class IV gas sands frequently occur when a porous sand is overlaid by a high velocity unit, such as hard shale, siltstone, tightly cemented sand, or a carbonate. Since the AVO gradient from a class IV brine sand may be almost identical to the gradient from a class IV gas sand, these gas sands may be difficult to detect by the conventional approach of comparing partial offset stacks.

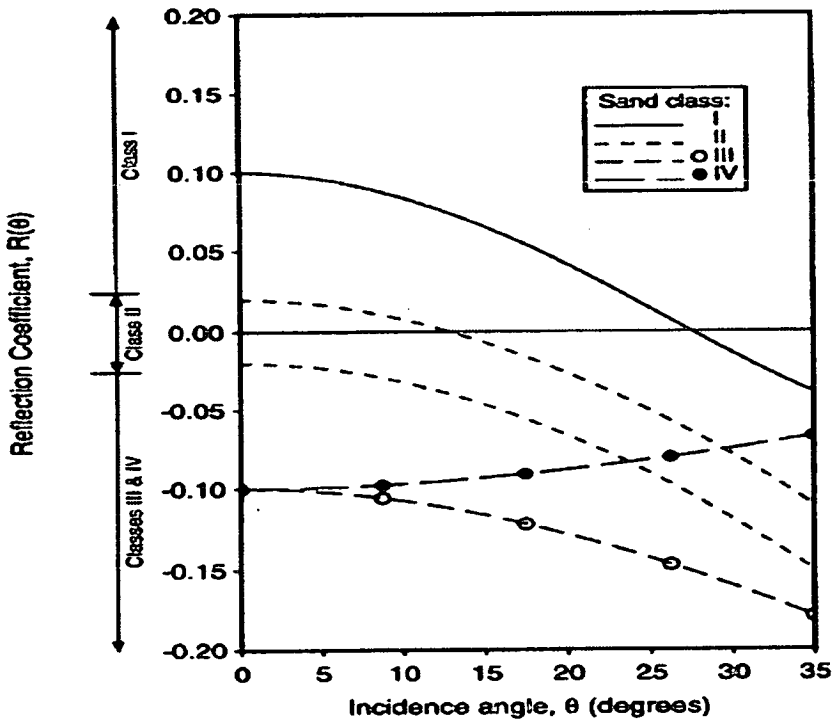

Figure 5.1a: Plane-wave reflection coefficients at the top of each Rutherford & Williams (1989) classification of gas sand. (Castagna *et al.*, 1998)

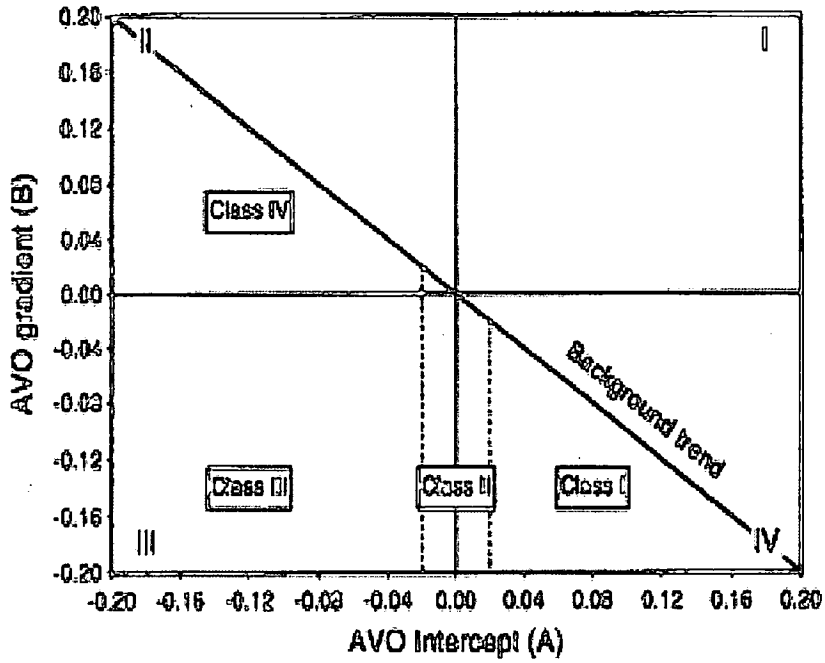

Figure 5.1b: AVO intercept (A) versus gradient (B) crossplot showing four possible quadrants. For a limited time window, brine-saturated sandstones and shales tend to fall along a well-defined background trend. Top sand reflectors tend to fall below the background trend, whereas bottom gas-sand reflections tend to fall above the trend. (Castagna *et al.*, 1998)

5.3 Lithology and fluid effect on rock properties

5.3.1 Gassmann fluid substitution

Fluid substitution is an essential part of AVO analysis. Fluid substitution essentially refers to prediction of seismic velocities in rocks saturated with one fluid from dry rocks or rocks saturated with another fluid (Mavko *et al.*, 1998). Gassmann's equation has been frequently used for such prediction of effects of fluid saturation on seismic properties.

Gassmann (1951) developed a method to derive the P- and S-wave velocities in terms of elastic modulus, and derived his equation using a rigorous mechanical

analysis. The theory assumes that the solid phase of the rock is elastic and homogenous, and the pore space is statistically isotropic. The theory is valid at sufficiently low frequency (<100Hz) such that there is enough time for the pore fluid to flow and eliminate wave-induced pore pressure gradients. Therefore, it performs less well at ultrasonic frequency ($\approx 10^6$Hz).

In Gassmann theory, a cube of rock is characterized by four components: the rock matrix, the pore/fluid system, the dry rock frame, and the saturated frame (Figure 5.2). The 'dry rock' or 'dry frame' is not the same as gas-saturated rock. In the drained case, it means that pore fluids can flow freely in or out of the sample to ensure constant pore pressure; in the undrained case, pore fluid has zero bulk modulus and thus pore compressions do not induce changes in pore pressure, which is approximately the case for air-filled sample at standard temperature and pressure. At reservoir conditions (high pore pressure), gas takes on a non-negligible bulk modulus and should be treated as a saturated fluid.

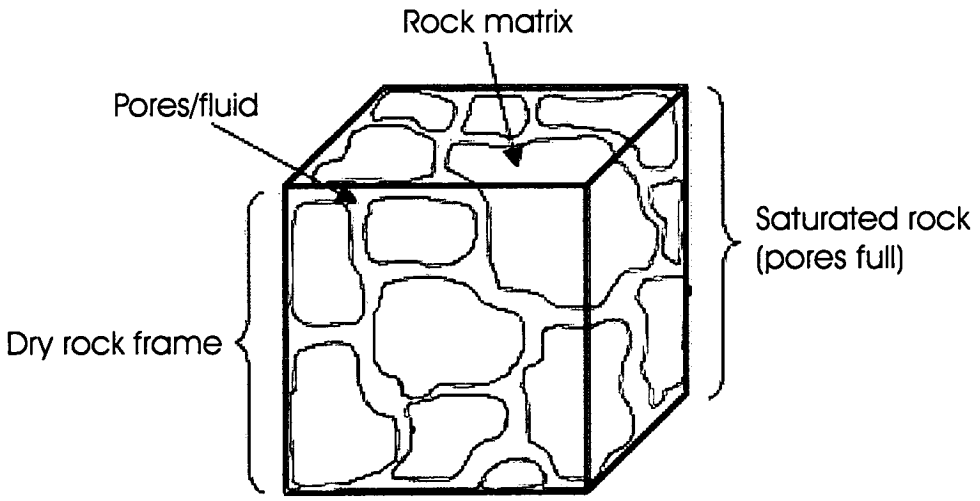

Figure 5.2: A cube of porous rock described by Gassmann theory

Assuming that the porous rock contains only one type of solid with a homogeneous mineral modulus and statistically isotropic pore space, P-wave and S-wave velocity can be written in the low-frequency Gassmann's formulation:

$$V_p = \sqrt{\frac{K_{dry} + \frac{4}{3}\mu_{dry} + \frac{(1 - K_{dry}/K_m)^2}{(1 - \phi - K_{dry}/K_m)/K_m + \phi/K_f}}{\rho_{sat}}}, \qquad (5\text{-}1)$$

where

K_{dry} = effective bulk modulus of dry rock
K_m = bulk modulus of rock matrix
K_f = effective bulk modulus of pore fluid
μ_{dry} = effective shear modulus of dry rock
ϕ = porosity
ρ_{sat} = density of saturated rock

Since μ_{dry} is not affected by the pore fluid, thus

$$\mu_{dry} = \mu, \qquad (5\text{-}2)$$

$$V_s = \sqrt{\frac{\mu}{\rho_{sat}}}. \qquad (5\text{-}3)$$

For the porous rock contains two type of fluids, water and hydrocarbon, the effective bulk modulus of pore fluid is:

$$K_f = 1/(S_w/K_w + (1 - S_w)/K_{hc}), \qquad (5\text{-}4)$$

where

S_w = water saturation
K_w = bulk modulus of water
K_{hc} = bulk modulus of hydrocarbon

and ρ_{sat} can be calculated by Wyllie *et al.*'s 1956 Equation,

$$\rho_{sat} = \rho_m(1 - \phi) + \rho_w s_w \phi + \rho_{hc}(1 - s_w)\phi, \qquad (5\text{-}5)$$

where

ρ_m = density of rock matrix

ρ_w = density of water

ρ_{hc} = density of hydrocarbon

For fluid substitution, given a rock with an initial V_{p0} (and optional density ρ_{sat0}), ϕ_0, S_{w0}, P-wave and S-wave velocities can be obtained at different porosities ϕ and water saturation S_w by introducing a further parameter: the dry rock Poisson's ratio σ_{dry}. Gregory (1977) points out that for most dry rocks and unconsolidated sands, σ_{dry} is about 0.1 and is independent of pressure. The calculated P-wave velocity is not very sensitive to the value of σ_{dry}. However, for consolidated rocks, the effect of σ_{dry} is the opposite. The lithology and porosity need to be known for an accurate P-wave velocity calculation. In this case, it is difficult to estimate a value for the dry rock Poisson's ratio, and the method depends heavily on this estimate.

K_{dry} can be solved for by the following equations using Gregory's 1977 formulation:

$$\beta = 1 - K_{dry}/K_m, \qquad (5\text{-}6)$$

where β is the Biot coefficient,

$$S = 3(1-\sigma_{dry})/(1+\sigma_{dry}), \qquad (5\text{-}7)$$

$$\begin{aligned}\beta^2(S-1) + \beta\left(\phi_0 S(K_m/K_f - 1) - S + \rho_0 V_{p0}^2/K_m\right) \\ - \phi_0(S - \rho_0 V_{p0}^2/K_m)(K_m/K_f - 1) = 0,\end{aligned} \qquad (5\text{-}8)$$

K_{dry} is derived from equation 5-6, we have

$$K_{dry} = K_m(1-\beta), \qquad (5\text{-}9)$$

and

$$\mu_{dry} = \frac{3(1-2\sigma_{dry})}{2(1+\sigma_{dry})} K_{dry}. \qquad (5\text{-}10)$$

From equation 5-1, V_p is obtained for the different porosity and water saturation. This is the process of fluid substitution using an estimate of dry rock Poisson's ratio to estimate the Biot coefficient and then K_{dry} in case that S-wave velocity is not available. If P-and S-wave velocities and density are available, the estimate of K_{dry} is straightforward by equations 5-1, 5-2 and 5-3.

P-wave velocity can also be written in a simplified formulation:

$$V_p = \sqrt{\frac{K + \frac{4}{3}\mu}{\rho_{sat}}}, \qquad (5\text{-}11)$$

where K is the effective bulk modulus of saturated rock,

$$K = K_{dry} + \frac{(1 - K_{dry}/K_m)^2}{(1-\phi - K_{dry}/K_m)/K_m + \phi/K_f}, \qquad (5\text{-}12)$$

K is related to the Lamè moduli λ and μ by:

$$K = \lambda + \frac{2}{3}\mu, \qquad (5\text{-}13)$$

and

$$V_p = \sqrt{\frac{\lambda + 2\mu}{\rho_{sat}}}. \qquad (5\text{-}14)$$

From the above equations, we can see that the link between velocity and rock properties for pore fluid is through the bulk modulus, and for lithology is through shear modulus (Castagna *et al.*, 1993). When a compressive gas enters pore space replacing incompressible brine water, the bulk incompressibility (bulk modulus) is

reduced. Since the rigidity of a sand matrix is larger than a shale matrix, the sandstone shear modulus is higher than that of shale. Goodway *et al.* (1997) and Goodway (2001) showed an improved petrophysical discrimination of rock properties using $\lambda\rho$ and $\mu\rho$ (the products of Lamè constant and density) over conventional V_p and V_s analysis, and indicated that the Lamè modulus λ is a direct proxy for fluid, the rigidity μ is less ambiguous in discriminating lithology. Since V_p is dependent on both λ and μ, the effect of decreasing λ with the increasing sand porosity could be offset by the increase in μ from shale to sand, which makes conventional P-wave velocity and impedance analysis ambiguous in lithology and fluid discrimination.

From Equations 5-3 and 5-14, $\lambda\rho$ and $\mu\rho$ have the following relationship with the P- and S-wave impedance I_p (ρV_p) and I_s (ρV_s), where ρ is actually ρ_{sat}:

$$\lambda\rho = I_p^2 - 2I_s^2, \qquad (5\text{-}15)$$

$$\mu\rho = I_s^2. \qquad (5\text{-}16)$$

Equation 5-1 gives V_p in two terms: a dry skeleton term and a mixed fluid and rock term. A study by Russell *et al* (2003) defines the fluid component ρf and the dry component ρs, where f is a mixed fluid and rock term:

$$f = \frac{(1 - K_{dry}/K_m)^2}{(1 - \phi - K_{dry}/K_m)/K_m + \phi/K_f}, \qquad (5\text{-}17)$$

and s is dry-skeleton term:

$$s = K_{dry} + \frac{4}{3}\mu_{dry}. \qquad (5\text{-}18)$$

P-impedance I_p can then be expressed as the following:

$$I_P^2 = \rho(f + s). \qquad (5\text{-}19)$$

Similar to λρ in equation 5-15, we give the fluid component ρf in the following expression:

$$\rho f = I_p^2 - cI_s^2, \qquad (5\text{-}20)$$

where c is a factor to scale I_s^2. From equations 5-16, 5-19 and 5-20,

$$I_P^2 - cI_s^2 = \rho(f + s) - c\rho\mu, \qquad (5\text{-}21)$$

the dry component ρs can be obtained:

$$\rho s = c\rho\mu = cI_s^2, \qquad (5\text{-}22)$$

c is estimated in the following from equation 5-18 and 5-22:

$$c = \frac{K_{dry}}{\mu} + \frac{4}{3} = \left(\frac{V_p}{V_s}\right)^2_{dry}. \qquad (5\text{-}23)$$

By the definition of Poisson's ratio, we have

$$\sigma_{dry} = \frac{\frac{1}{2}\left(\frac{V_p}{V_s}\right)^2_{dry} - 1}{\left(\frac{V_p}{V_s}\right)^2_{dry} - 1} = \frac{c-2}{2c-2}. \qquad (5\text{-}24)$$

Murphy *et al.* (1993) measured the K_{dry}/μ ratio for clean quartz sandstones over a wide range of porosities and found that this value was, on average, equal to 0.9. This corresponds to a σ_{dry} value of 0.095 and a c value of 2.233. If the K_{dry}/μ value is rounded to 1.0, this implies a σ_{dry} of 0.125 and a corresponding c value of 2.333. These values are also confirmed by Wang (2000). Obviously, there is a range of values for c that will depend on the particular reservoir being studied. Comparing this technique with Goodway's λρ-μρ method, c is equal to 2 in the λρ-μρ method,

then σ_{dry} is equal to zero. Russell *et al.* (2003) suggested besides being in an acceptable range, the selection of c value should be based on locally measured logs.

Gassmann's equation assumes that rocks are monomineralic. In practice, we substitute an effective bulk modulus for mixed mineralogy. However, it is difficult to know the details of how the minerals are distributed at the microscopic scale. Mavko (2005) points out that for high porosities (> 20%), the Gassmann predictions are relatively insensitive to details of the distribution. Gassmann theory also assumes only pure saturations, i.e., 100% water, 100% oil, or 100% gas, without mixtures. In reality, reservoirs always have mixtures of fluids, yet we estimate the average density and compressibility of the mixture of pore fluids and substitute these averages into Gassmann's equation (e.g. Batzle-Wang approach, 1992). Mavko (2005) indicates that the proper way to estimate the effective compressibility of the fluid mix depends on the way in which the water, oil, and gas are distributed throughout the pore space. We have to consider whether the fluids are uniformly mixed at a fine scale, or whether the saturation is "patchy."

5.3.2 Fluid effect on rock properties from laboratory data

To review the influence of pore fluid on the relevant reservoir physical rock properties, i.e. V_p/V_s ratio, P- and S- impedance, Lamè moduli and density ($\lambda\rho$, $\mu\rho$), and the fluid component (ρf) and the dry component (ρs), I use laboratory data, provided by PetroChina, for sandstone core samples from 15 wells in the study area. The measurements are conducted under different temperatures and pressures (30 to 47Mpa, 78 to100°C). P-wave velocities have been measured at 800kHz and S-wave velocities at 600kHz, for different gas saturations (i.e. fully water-filled, around 35%, 65%, and fully air-filled). For this particular data set, porosity varies from 3% to 12%, and permeability from 0.05 to1mD. Such reservoirs are described by Masters (1979) as tight gas sandstone reservoirs with low porosity (7-15%) and low permeability (0.15 to 1mD).

Figure 5.3 shows the relationship between the P- and S-wave velocities and gas saturation. There is no rapid P-wave velocity decrease at low gas saturation that is described by Gassmann's equations (Figure 5.3a). In fact, the P-wave velocities display a slow decline with the increasing gas saturation until about 70%. A rapid P-wave velocity drop appears between quite high gas saturation (about 70%) to the full gas saturation. Another direct observation is a relative high P-wave velocity at the small porosity. S-wave velocity shows a less sensitivity to the gas saturation as expected (Figure 5.3b).

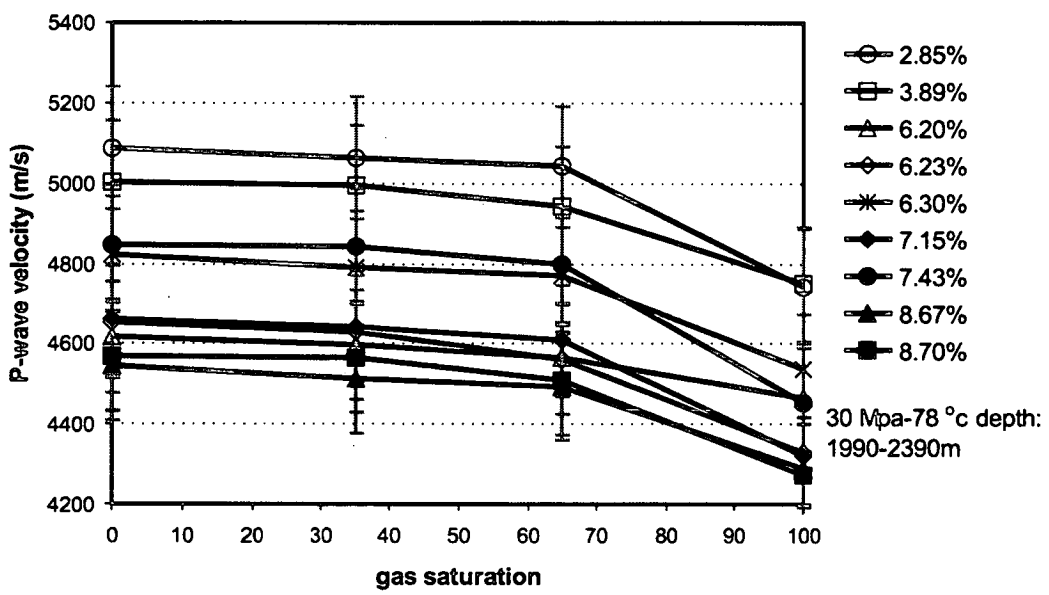

Figure 5.3a: P-wave velocity versus gas saturations at 30Mpa and 78°C. The legend is for sample porosity. The shadowed lines are error bars with 3% errors of the measured values.

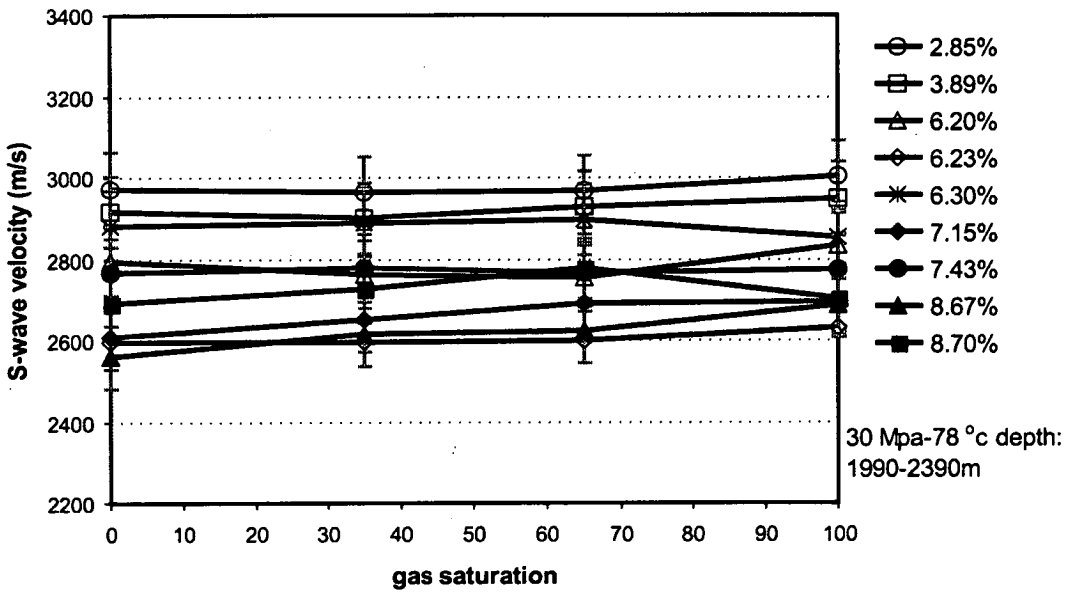

Figure 5.3b: S-wave velocity versus gas saturations at 30Mpa and 78°C. The legend is for sample porosity. The shadowed lines are error bars with 3% errors of the measured values.

Figure 5.4a, b and c show the V_p/V_s ratio vs. gas saturation at 30Mpa-78°C, 45Mpa-95°C, and 47Mpa-100°C, respectively. We observe a rapid drop in V_p/V_s from gas saturation 65% to gas saturation 100%. Generally, there is no rapid decrease at the low gas saturation. The V_p/V_s ratio ranges from 1.55 to 1.66 for 100% gas saturated sand samples. V_p/V_s shows a less sensitivity to the porosity for these tight sand samples, which is also shown in Figure 5.5 where V_p/V_s has no clear correlation with the porosity for tight gas sands.

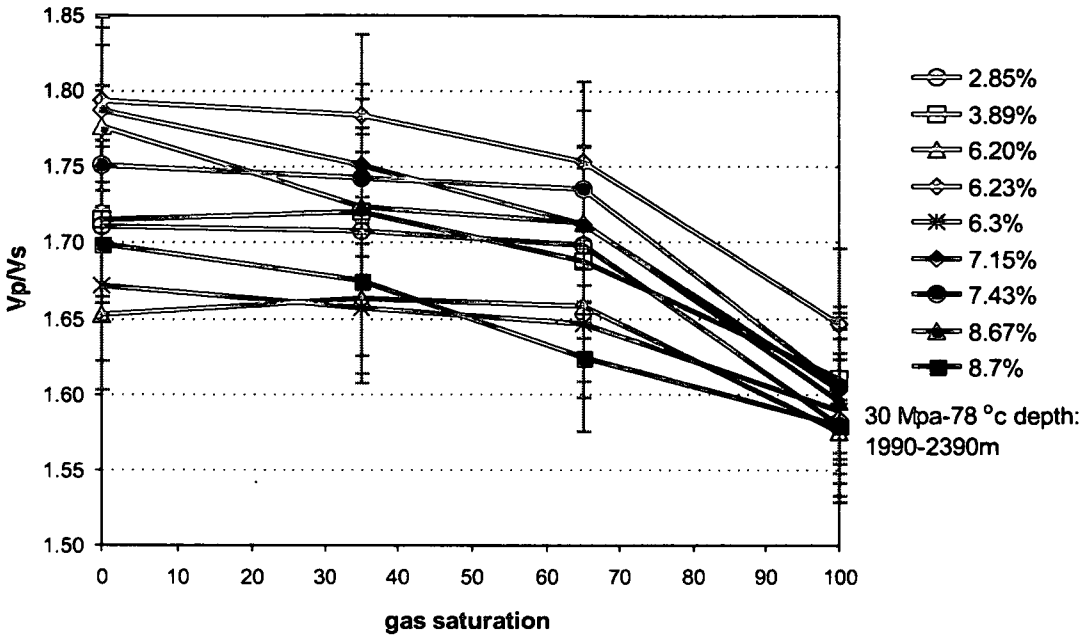

Figure 5.4a: The variation of V_p/V_s with the gas saturation at 30Mpa and 78°C. The legend represents sample porosity. The shadowed lines are error bars with 3% errors of the measured values.

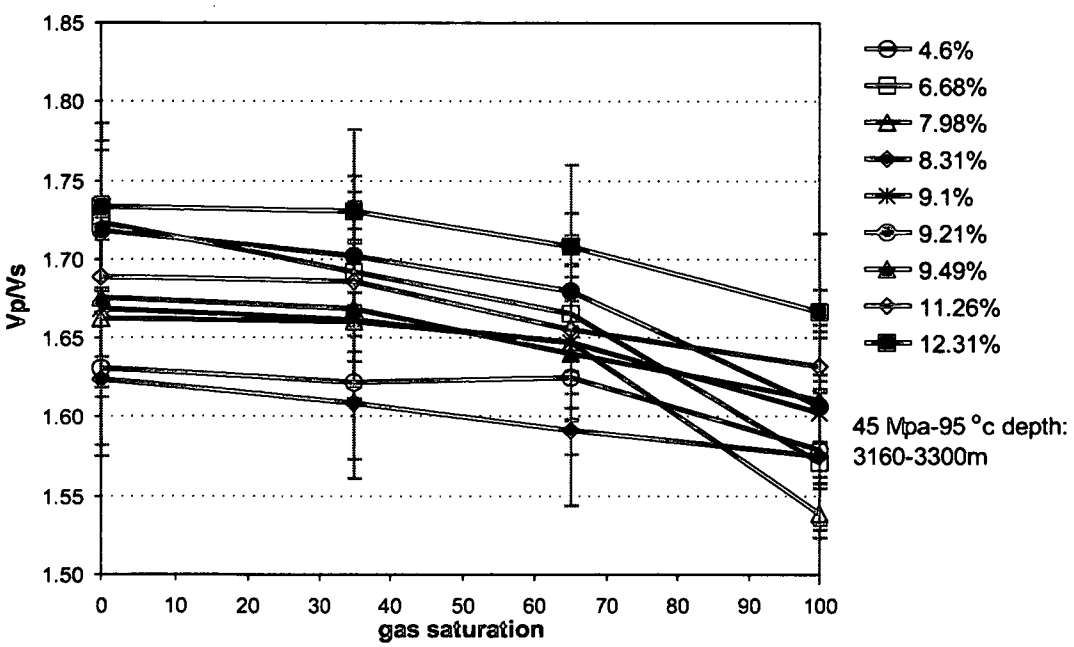

Figure 5.4b: The variation of V_p/V_s with the gas saturation at 45Mpa and 95°C. The legend represents sample porosity. The shadowed lines are error bars with 3% errors of the measured values

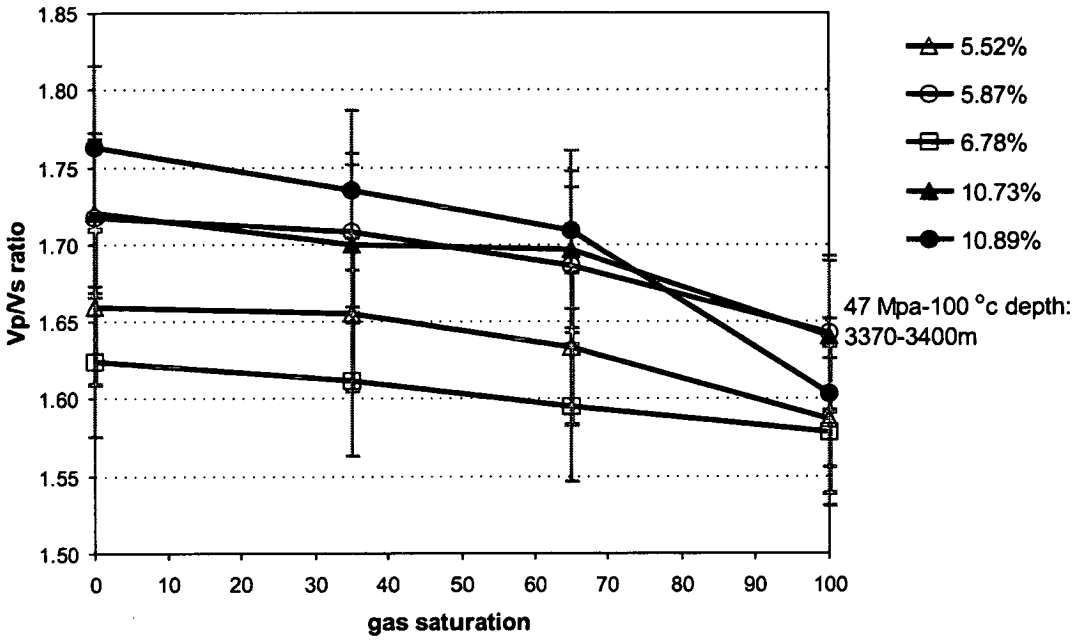

Figure 5.4c: The variation of V_p/V_s with the gas saturation at 47Mpa and 100°C. The legend represents sample porosity. The shadowed lines are error bars with 3% errors of the measured values.

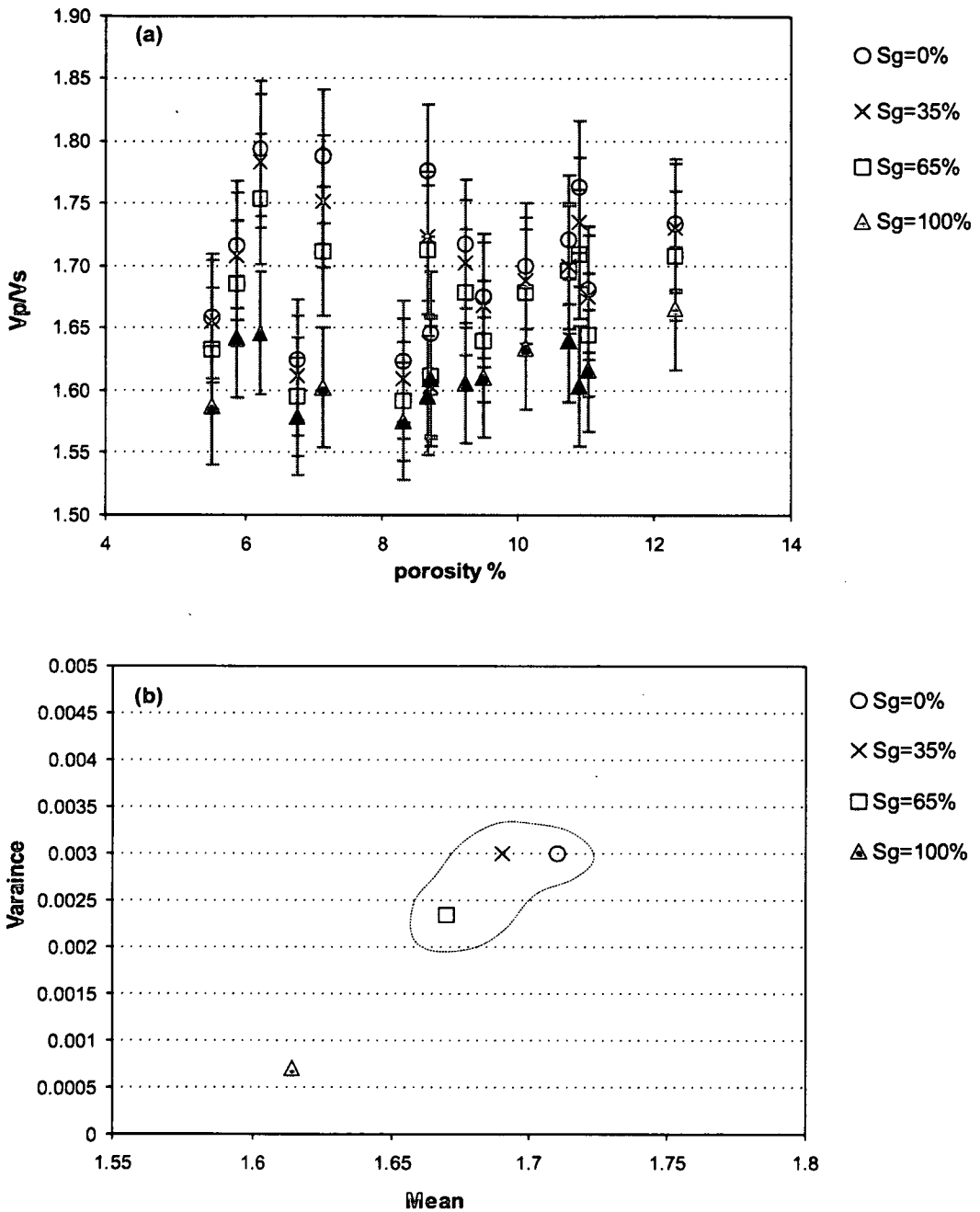

Figure 5.5: (a) V_p/V_s versus porosity for tight gas sand at different saturations. The shadowed lines are error bars with 3% errors of the measured values. (b) The V_p/V_s mean values and variance distribution for these samples. The legend represents sample saturation.

Figure 5.6a shows P-impedance vs. S-impedance for these tight sandstone samples. Statistical analysis in Figure 5.6b shows there is no separation in P-impedance

between different saturations. $\lambda\rho$ vs. $\mu\rho$ of these samples is shown in Figure 5.7a. All except one of $\lambda\rho$ values with 100% gas saturation is less than 33 Gpa·g/cc, and statistical analysis in Figure5.7b shows $\lambda\rho$ of 100% gas saturation is separated very well from other gas saturations. The $\lambda\rho$ value decreases with the increasing gas saturation. Compared to P-impedance, $\lambda\rho$ is more capable of distinguishing fluid content.

Figure 5.8 shows the fluid component *pf* vs. dry component *ps* defined as the previous section, where c equals 2.33 (σ_{dry} of 0.125). Comparing to $\lambda\rho$ in Figure 5.7 (where σ_{dry} of 0), *pf* has a similar ability in discriminating gas-filled samples.

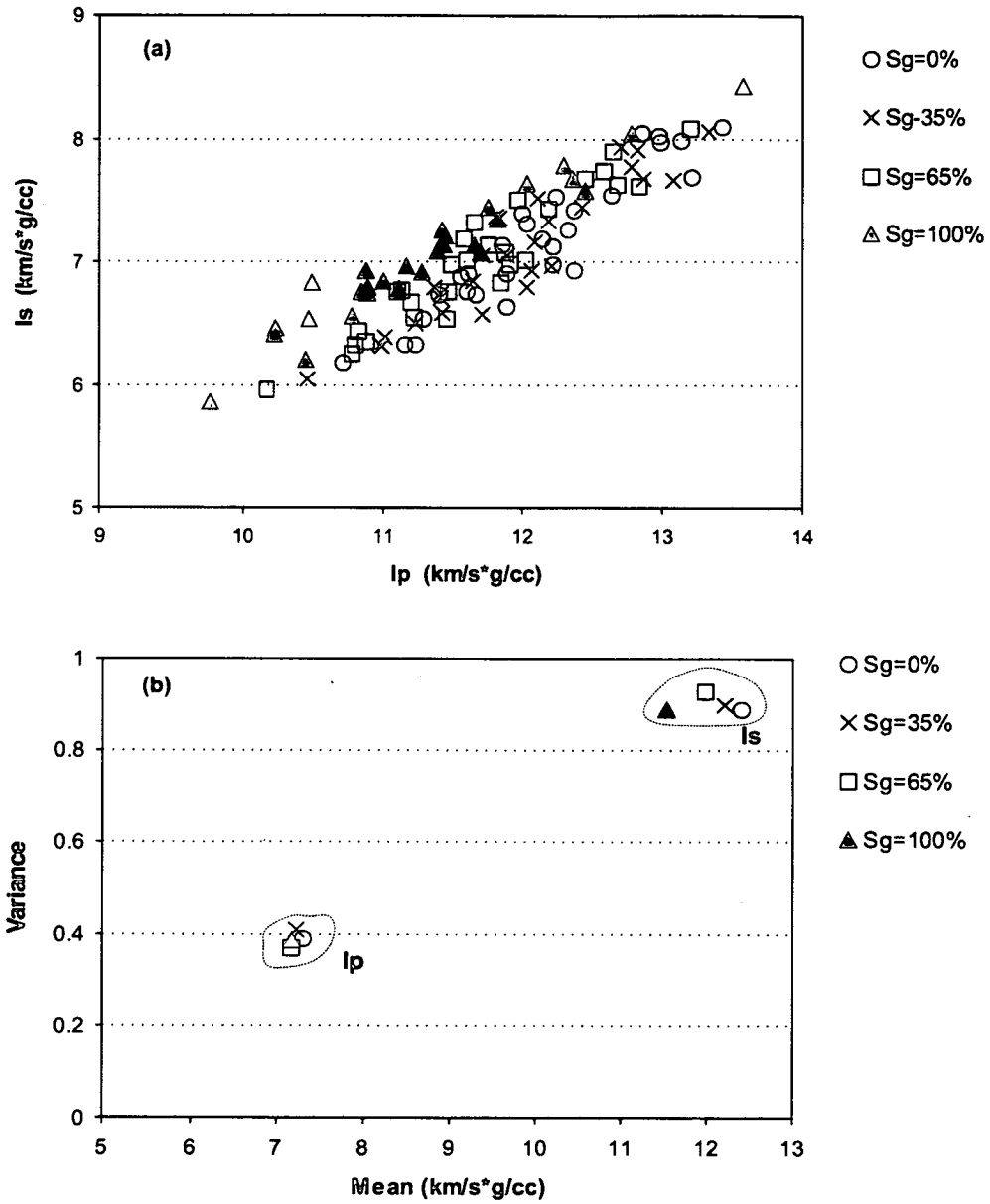

Figure 5.6: (a) P-impedance versus S-impedance for tight sandstone. (b) P- and S-impedance mean and variance analysis.

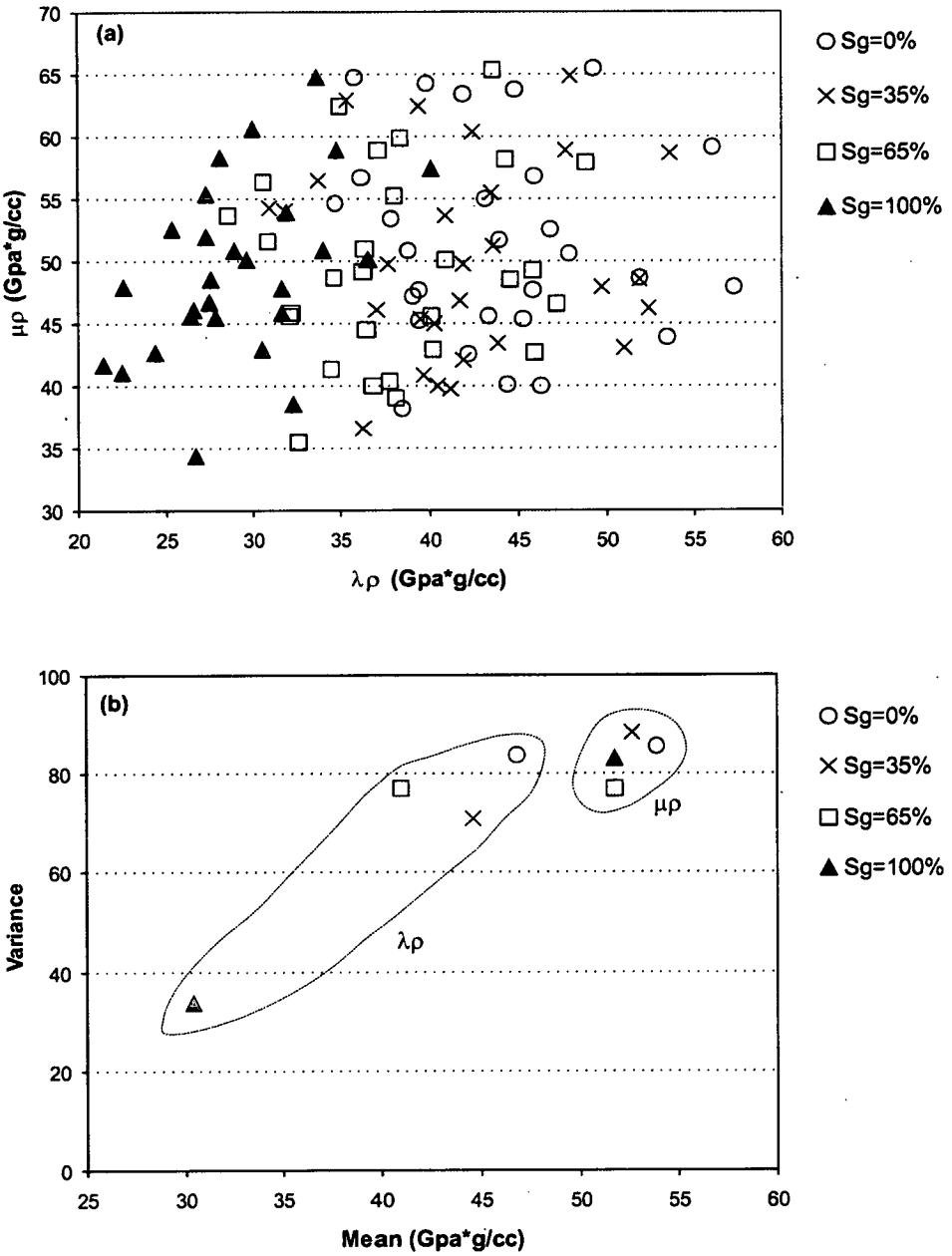

Figure 5.7: (a) λρ versus μρ for tight sandstone. (b) λρ and μρ mean and variance analysis.

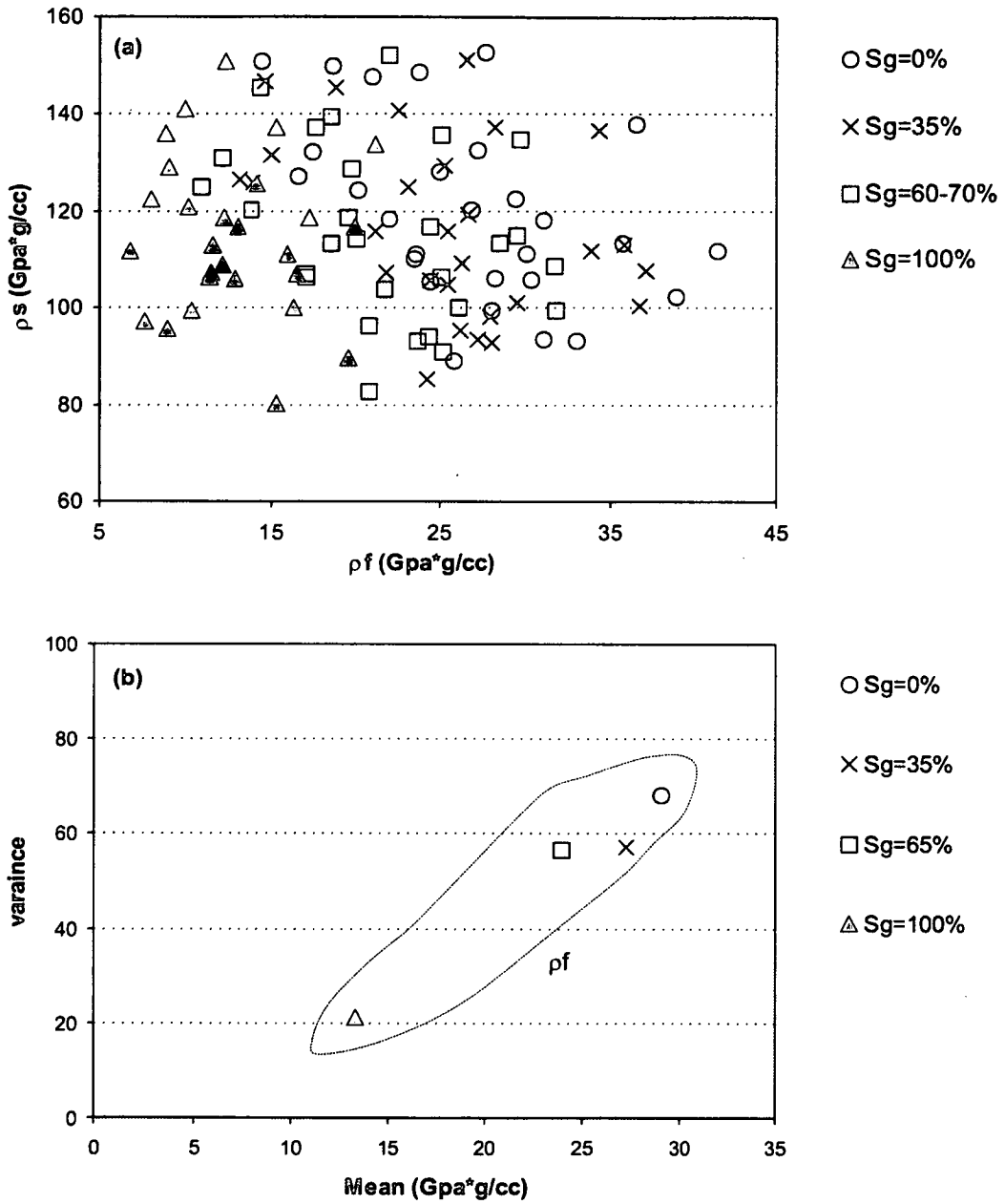

Figure 5.8: (a) ρf versus ρs for tight sandstone. c equals 2.33 (σ_{dry} of 0.125). (b) ρf mean and variance analysis.

5.3.3 Lithology and fluid effect on rock properties from log data

A cross-dipole sonic log is acquired for the depth range of interest, i.e., 3100m to 3300m. Figure 5.9 shows the crossplot between velocity ratio and P-impedance. P-

impedance alone is ambiguous in distinuishing lithology and is also affected by fluid effects. However, we can observe it is possible using V_p/V_s to discriminate lithology. V_p/V_s for shale ranges from 1.75 to 2, and for low shale content sandstone from 1.5 to 1.75 approximately. V_p/Vs can also be used as fluid indicator, because we observe a low V_p/V_s value (1.5 to 1.6) for gas-saturated sandstone, and an increased V_p/V_s value (1.6 to 1.7) for water-saturated sandstone, which are consistent with the core sample measurement in the previous section. Comparing the V_p/V_s change due to lithology and due to the pore fluid content, lithology gives rise to a larger effect on V_p/V_s than fluid. There is approximately 22% relative change of V_p/V_s for shale to clean sandstone, and 12.5% for gas-saturated sandstone to water-saturated sandstone.

Figure 5.10 shows a crossplot between V_p/V_s and S-wave impedance. S-wave is a good lithology indicator due to it being less sensitive to fluid effect. The S-wave impedance value is more than 6900 m/s·g/cc for sandstone, and less than 7000 m/s·g/cc for clay-bearing sandstone and shale.

The crossplot between $\lambda\rho$ and $\mu\rho$ shown in Figure 5.11 indicates that it is possible to discriminate between fluid using $\lambda\rho$ and lithology using $\mu\rho$. Among the sandstones (blue dots with low gamma ray values), the gas layer values (in red circle) have the smallest $\lambda\rho$, which is consistent with the analysis of the core data. Comparing to the mudstone, the gas layer has the larger value of $\mu\rho$. Figure 5.12 is a crossplot between fluid component *pf* and dry component *ps* assuming σ_{dry} equals 0.1. It is observed that *pf* values of the gas layer are close to the zero axis, more closely clustered than $\lambda\rho$ values.

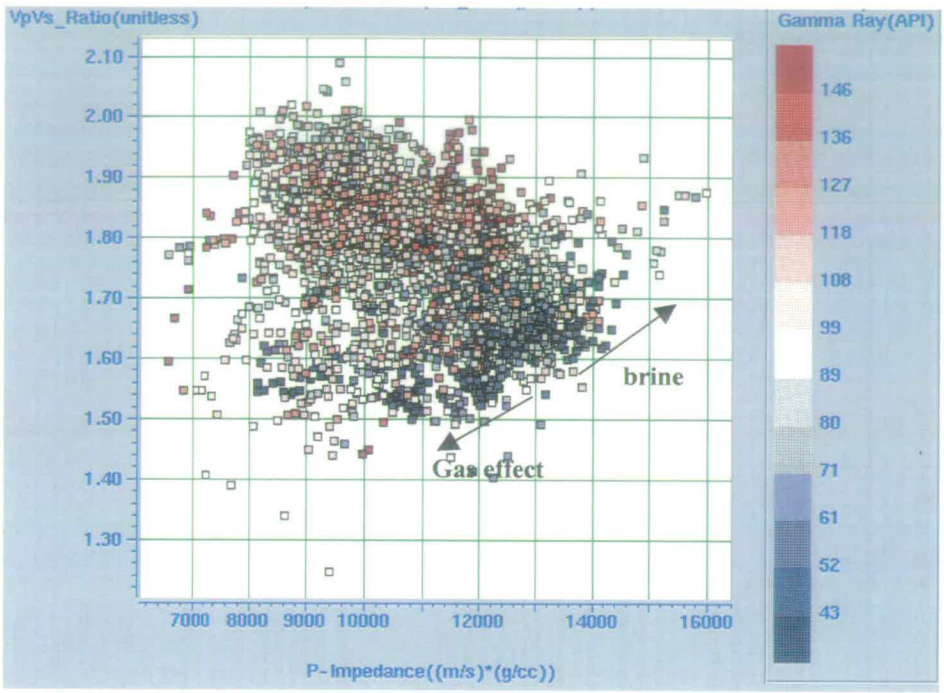

Figure 5.9: V_p/V_s versus P-impedance calculated for the low porosity and low permeability sands and shales at depth of 3100m-3300m, from a dipole sonic log in the Sulige field. The colour legend is for gamma ray value. The gas and brine effects are shown by arrows.

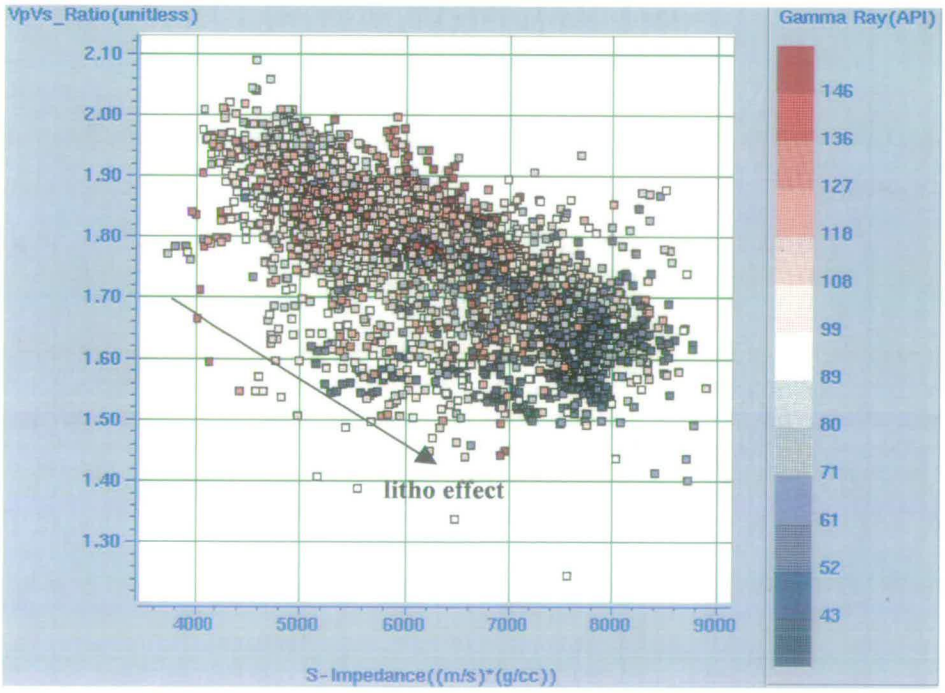

Figure 5.10: As in Figure 5.9, but V_p/V_s versus S-impedance. The lithology effects is shown by arrow.

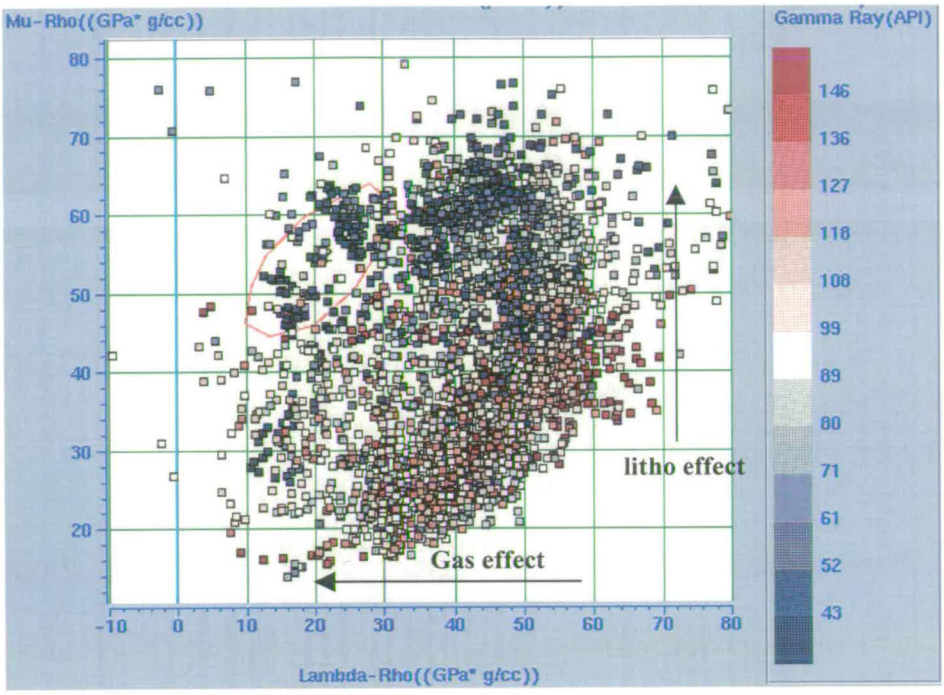

Figure 5.11: As in Figure 5.9, but $\lambda\rho$ versus $\mu\rho$. The fluid effect is shown by $\lambda\rho$, and the lithology effect is shown by $\mu\rho$.

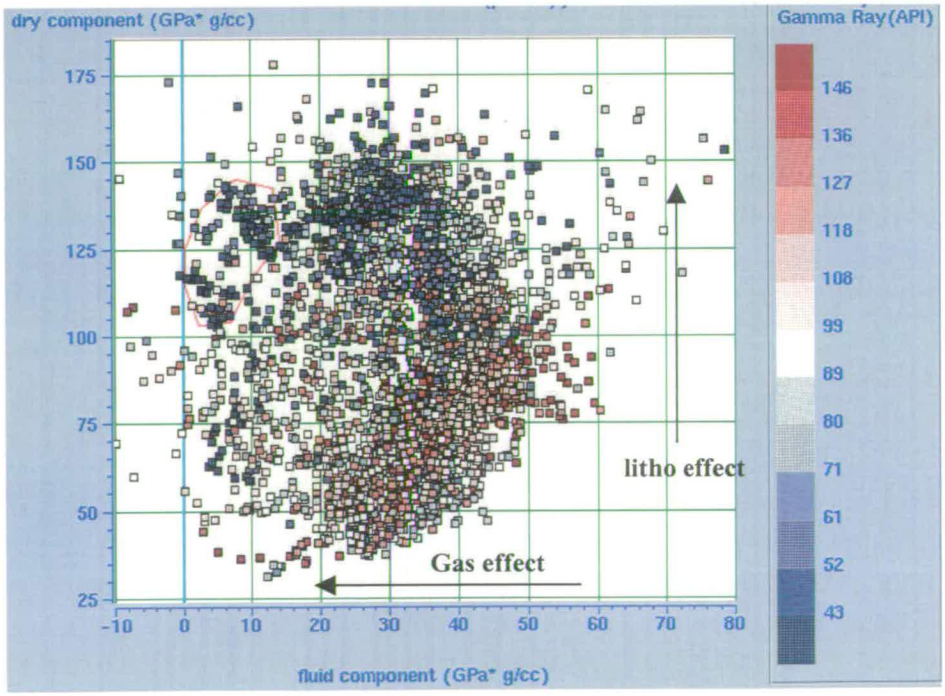

Figure 5.12: As in Figure 5.9, but the fluid component *pf* versus and the dry component *ps*. The fluid effect is shown by *pf*, and the lithology effect is shown by *ps*.

5.4 PP-wave AVO analysis

For a comprehensive study of the Ordos data, I start AVO analysis from the conventional PP-wave. Shuey (1985) reformulated the Aki-Richards approximation as two terms and developed a gradient-intercept method that measures the zero-offset reflectivity and change in Poisson's ratio. The method requires a fixed V_P/V_S ratio (usually assumed as 2). Castagna and Swan (1997) developed the intercept-versus-gradient crossplot method for identification of fluid anomalies, a useful technique for identifying anomalies from the background trend.

5.4.1 Intercept and gradient analysis

Under the small incident angle approximation, Shuey (1985) gives the prestack P-wave reflection coefficient equation as the following simplified equation. The complete equation of the Aki-Richards approximation will be described in Chapter 6.

$$R_{pp}(\theta) \approx A + B\sin^2\theta, \qquad (5\text{-}25)$$

where A and B are intercept (zero offset reflection coefficient) and gradient respectively, and defined as:

$$A = \frac{1}{2}\left(\frac{\Delta\alpha}{\alpha} + \frac{\Delta\rho}{\rho}\right) = R_{pp}(0), \qquad (5\text{-}26)$$

$$B = \left(\frac{1}{2}\frac{\Delta\alpha}{\alpha} - 4\frac{\beta^2}{\alpha^2}\frac{\Delta\beta}{\beta} - 2\frac{\beta^2}{\alpha^2}\frac{\Delta\rho}{\rho}\right). \qquad (5\text{-}27)$$

Poisson's ratio (σ) is introduced to equation 5-25 by the following relation:

$$\sigma = \frac{\frac{1}{2}(\frac{\alpha}{\beta})^2 - 1}{(\frac{\alpha}{\beta})^2 - 1} = \frac{\lambda}{2(\lambda+\mu)}, \qquad (5\text{-}28)$$

though Thomsen (1990) argues that Poisson's ratio σ is not useful in exploration geophysics, reflection coefficient versus angle has showed an intuitive expression in terms of Poisson's ratio. Poisson's ratio for carbonate rocks is about 0.3, for sandstones about 0.2, for shale above 0.3, and for coal around 0.4. Verm and Hilterman (1995) simplify Shuey's equation by assuming V_p/V_s equals 2 and have the following equation:

$$R_{pp}(\theta) = R_{pp}(0)\cos^2\theta + \frac{9}{4}\Delta\sigma\sin^2\theta. \qquad (5\text{-}29)$$

Smith and Gidlow (1987) define Pseudo Poisson's ratio reflectivity $\Delta\sigma/\sigma$ as:

$$\frac{\Delta\sigma}{\sigma} = \frac{\Delta\left(\alpha/\beta\right)}{\alpha/\beta} = \frac{\Delta\alpha}{\alpha} - \frac{\Delta\beta}{\beta}. \qquad (5\text{-}30)$$

If V_p/V_s is assumed to equal 2 and Gardner *et al.* (1974)'s V_p and density relation is valid, the Pseudo Poisson's ratio reflectivity can be expressed as:

$$\frac{\Delta\sigma}{\sigma} = A + B. \qquad (5\text{-}31)$$

The fluid factor also defined by Smith and Gidlow (1987) is expressed as the following based on an ARCO mudrock baseline:

$$\Delta F = \frac{\Delta\alpha}{\alpha} - 1.16\frac{\beta}{\alpha}\frac{\Delta\beta}{\beta}. \qquad (5\text{-}32)$$

5.4.2 Well and seismic data analysis

Table 5.1 shows the ranges of P-wave velocities, densities, and P-impedance values of sandstones and mudstone in the Ordos basin found by reading the acoustic and density logs. The impedance values between gas sand and tight sand have an

obvious gap, while values for gas sand and shale are close and cannot be separated easily.

	P-Velocity (m/s)	Density (g/cm^3)	P-Impedance ($m/s*g/cm^3$)
Coal	<3800	<2.3	<8740
Mudstone	4200~4400	2.54~2.67	10668~11748
Siltstone	4400~4650	2.60~2.65	11440~12415
Sandstone	4500~4600	2.50~2.60	11250~11960
Gas sand	3900~4200	2.30~2.43	8970~10206

Table 5.1: P-wave velocity, density data in the Ordos basin

I use a gas well, T5 (Figure 3.1a), to analyse the AVO class in the study area. Note that the data acquisition in the Ordos area uses the SEG normal polarity standard: decreasing impedance corresponds to a peak in reflection amplitude. Since it is common practice in AVO analysis that the decreasing impedance corresponds to a trough in reflection amplitude, the polarity of the seismic data in this area may need to be changed and indicated in the context where it is necessary.

From the log curves and log interpretation of Well T5 (Figure 5.13), we can see the gas layer of T5 has no obvious impedance contrast with the overlaid shale layer. In the stacked section (Figure 5.14, Line1 in Figure 3.1a), a weak reflection amplitude is shown around the gas layer, which makes the post-stack interpretation and inversion difficult.

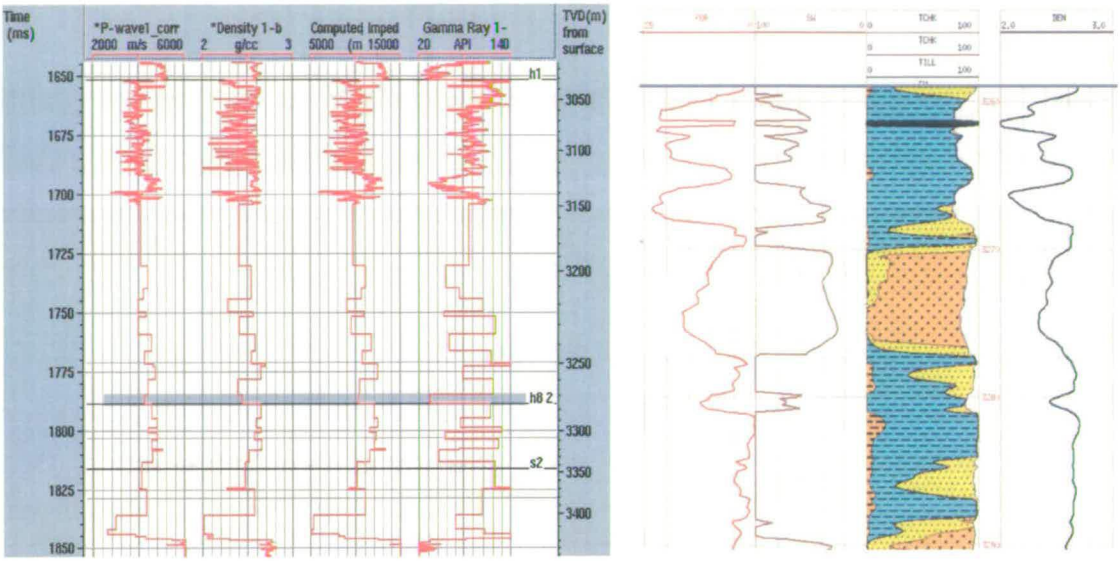

(a) (b)

Figure 5.13: (a) T5 blocked log curves. From left to right are: P-wave velocity, density, P-wave impedance and Gamma Ray logs, respectively. The gas layer is shown in the grey zone. (b) T5 petrophysics interpretation for porosity, water saturation, lithology and density between 3260-3290 m.

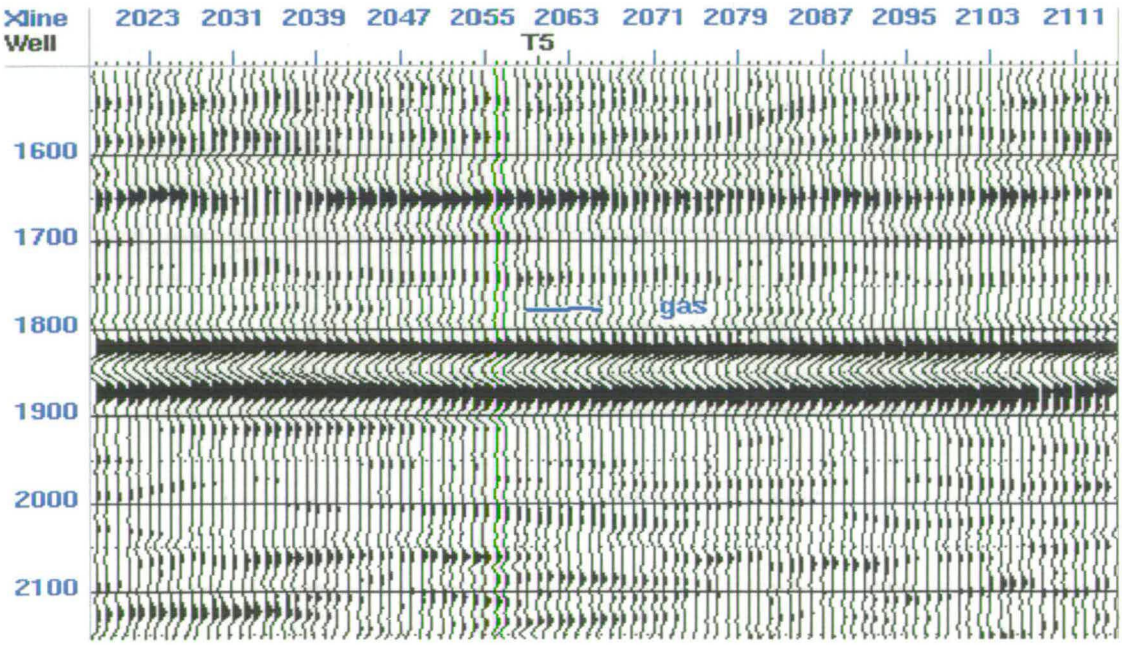

Figure 5.14: Stacked section across well T5, the blue line is the interpreted gas top by seismic tie to logs.

Fluid substitution based on the Biot-Gassmann equation is used to build a wet sand model for well T5, which is shown in Figure 5.15.

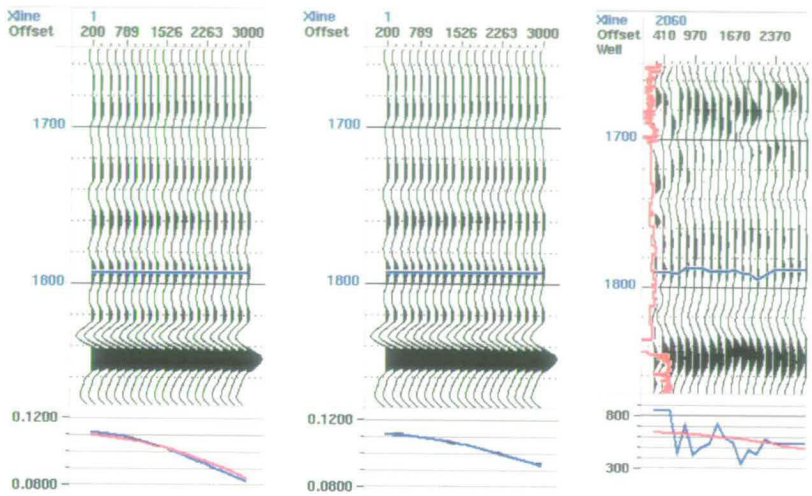

(a) (b) (c)

Figure 5.15: AVO synthetics for (a) the wet sand model, (b) in situ gas case and (c) the CDP gather at the well location, the insert red curve is the P-wave sonic log. The bottom graphs show the picked amplitudes (blue curve) of the target base with Shuey's gradient analysis (red curve). The wavelet is a zero-phased 25 Hz richer wavelet.

Figure 5.15 shows the AVO synthetic data obtained using Aki and Richards's equation for the wet case and in situ gas case of the well T5, and the CDP gather at the well location. The picked amplitude of the base target for both wet and gas sand decreases with increasing offset. Figure 5.16a shows the intercept and gradient analysis for the wet and gas sand. The flat gradient causes the blank reflection at the target top and base (around 1790 ms) for the gas model in the A*B section, and no AVO anomaly can be seen in this section.

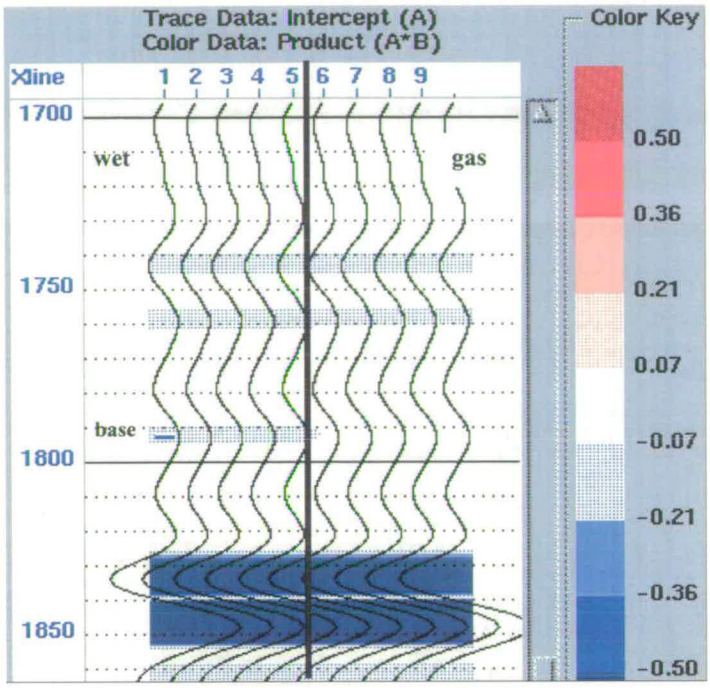

(a) Intercept and gradient section for wet case (first five traces) and for gas case (last five traces). Intercept A is in black wiggle, the product A*B is in colour.

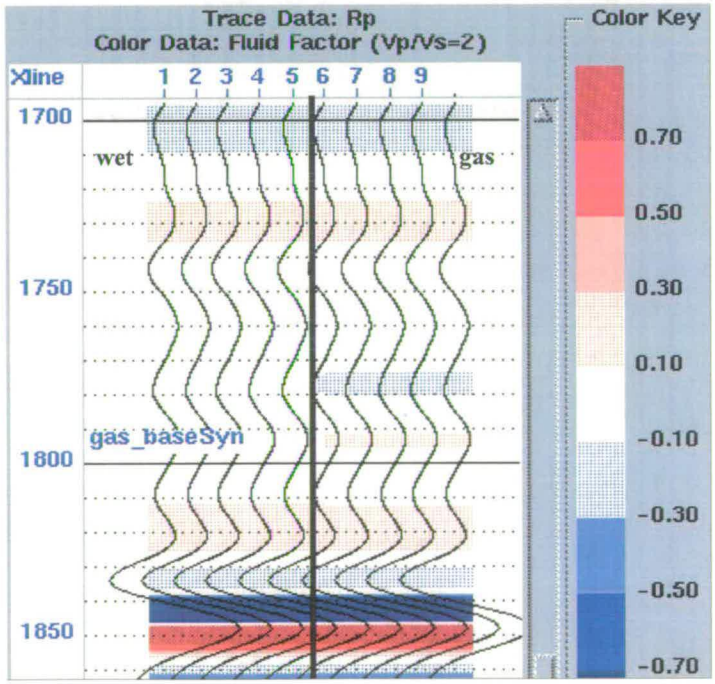

(b) Fluid factor section for wet case (first five traces) and for gas case (last five traces). The fluid factor is in colour.

Figure 5.16: AVO analysis for the wet sand and gas sand.

Figure 5.16b is the fluid factor section for the both models. The fluid factor is derived using a local relation between P-wave and S-wave velocity (Equation 5-33), which is obtained from the measured V_p and V_s data (Figure 5.17) for the sand samples in this area. ΔF in Figure 5.16b shows an weak anomaly in the gas model, which does not appear on the wet model.

$$V_s = 0.72V_p - 612 \quad (m/s). \qquad (5\text{-}33)$$

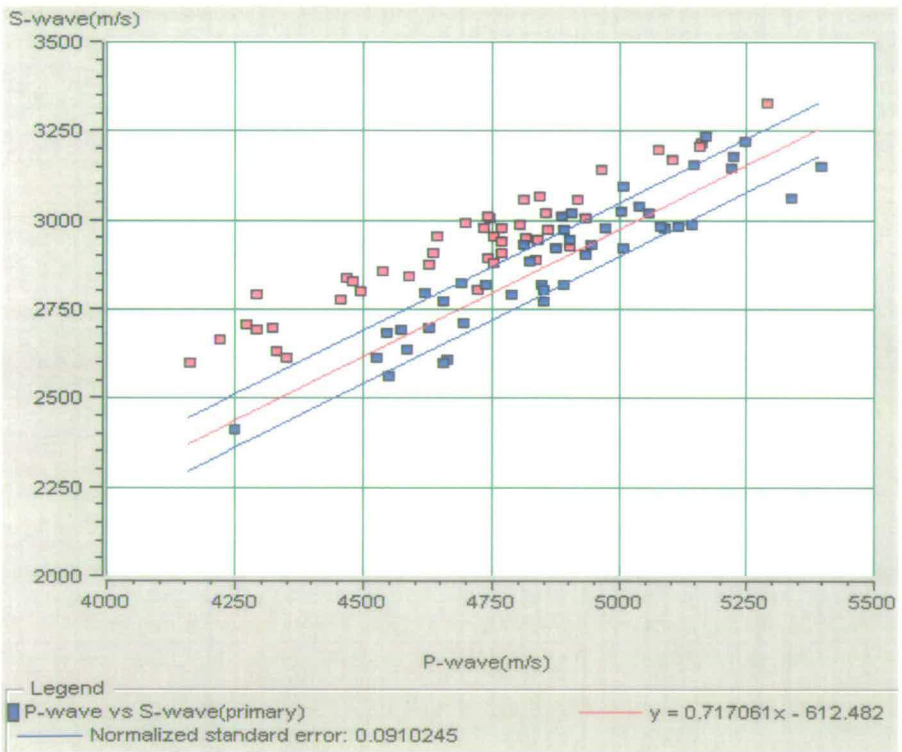

Figure 5.17: Wet sand and gas sand V_p and V_s relation from the rock samples measurement. Blue dots are water-saturated, and red dots are gas-saturated samples.

A similar analysis has been performed for the seismic data near well T5. The polarity of seismic data here has been reversed so that the increasing impedance corresponds to the positive reflection amplitude. Figure 5.18a is the A*B product section, and Figure 5.18b is the corresponding fluid factor section. We can trace the peak amplitude with red colour in the fluid factor section as the gas-related anomaly, which is the same as the fluid factor response for the gas sand model in

Figure 5.16b. In Figure 5.18a, there is no A*B anomaly and the corresponding zone is nearly blank.

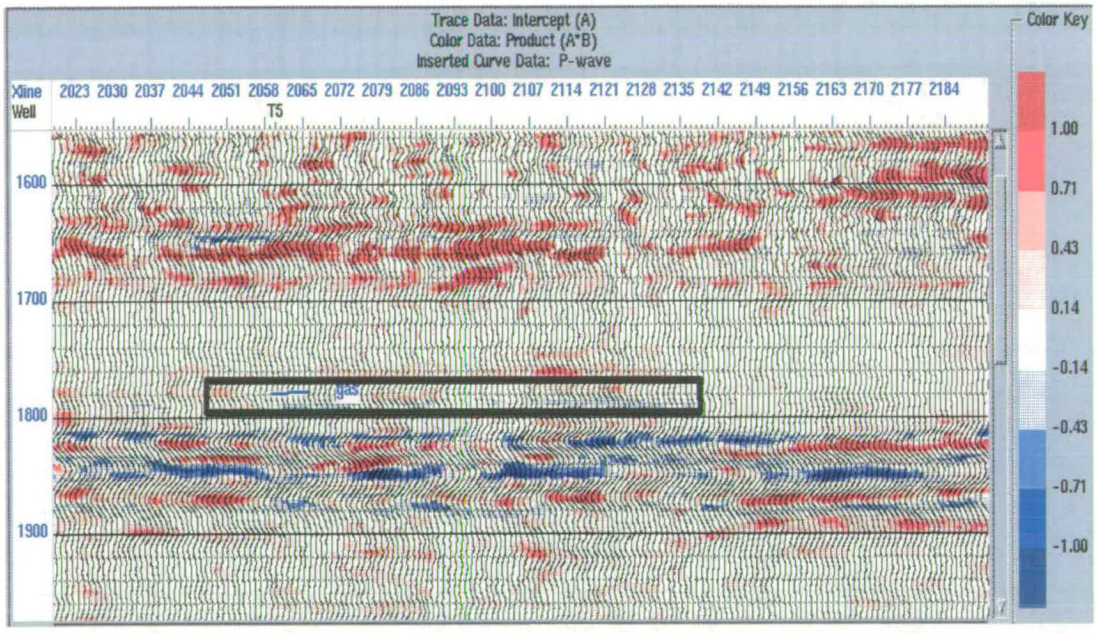

Figure 5.18a: AVO attribute section of the A and B product across the well T5.

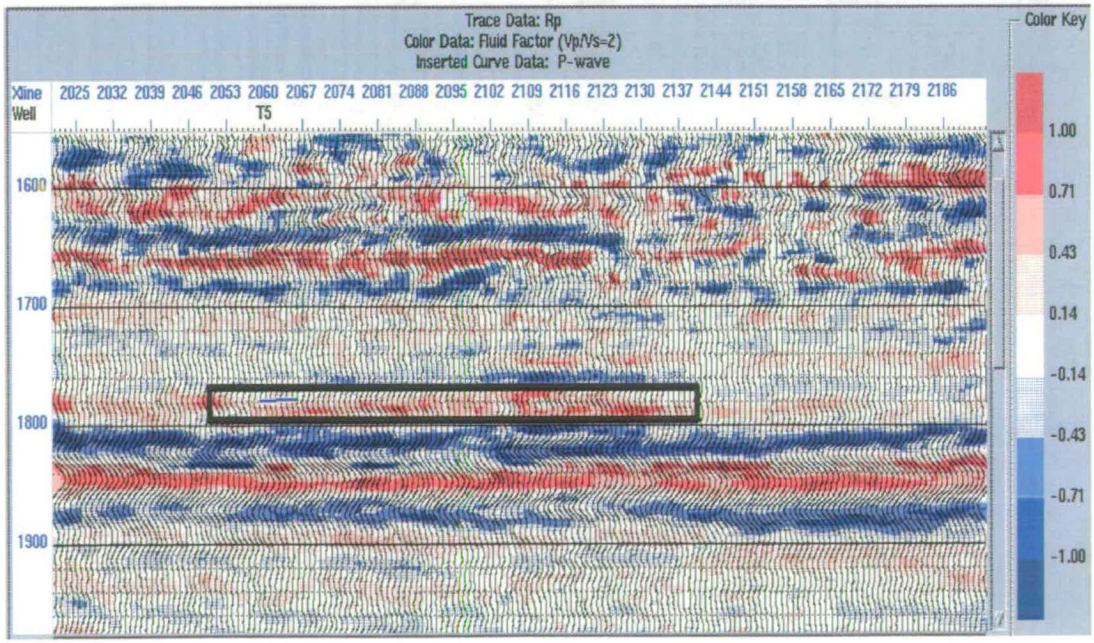

Figure 5.18b: The fluid factor section across the well T5.

Due to a very small P-impedance contrast between the gas sand and the capping shale for gas well T5, the $\lambda\rho$-$\mu\rho$ estimation is performed for its sensitivity to gas saturation. $\lambda\rho$ and $\mu\rho$ values of the blocked T5 are crossploted in Figure 5.19. $\lambda\rho$ values of the gas layer shown in the pink zone are lowest and can be separated from the surrounding rocks. $\mu\rho$ values of the gas layer are larger than the overlying shale. This makes sense because the sand matrix has a higher shear modulus than the shale matrix, and the very low porosity tight sand has the highest $\mu\rho$ value. The shaly sand has a similar $\mu\rho$ value to the gas sand.

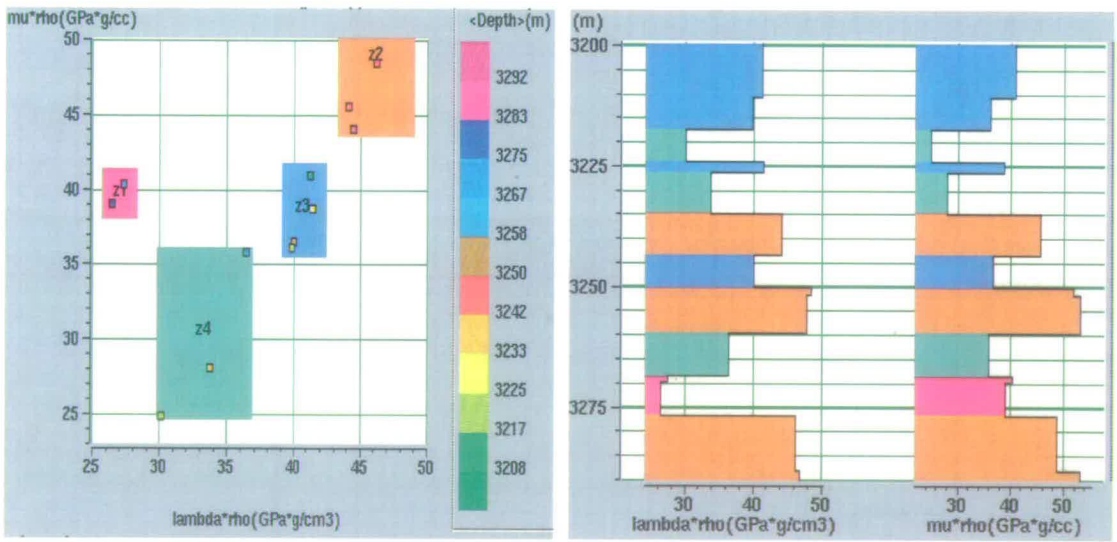

(a) $\lambda\rho$ versus $\mu\rho$, the gas layer in the pink square (b) the corresponding log curves

Figure 5.19: Crossplot of $\lambda\rho$ versus $\mu\rho$ for the gas layer of the well T5. z1 stands for gas sand, z2 for low porosity tight sand, z3 for shaly sand and z4 for shale.

Since only PP-wave data were acquired near the well T5, I extract the fluid term $\lambda\rho$ from P- and S-wave impedance using PP-data alone. The advantage of this technique is that the two-way times of P- and S-wave reflectivity are the same since they are controlled by the P-wave velocity, which avoids the complexity of correlation between P- and S-wave events. A model-based impedance inversion was used to invert the P- and S-reflectivity to P- and S- wave impedance, I_p and I_s.

Figures 5.20 and 5.21 show the P- and S-wave impedance inversion section passing through well T5. There is a small P-impedance drop in the gas-filled channel below the Horizon 2. The S-wave impedance does not show much drop for the gas sand.

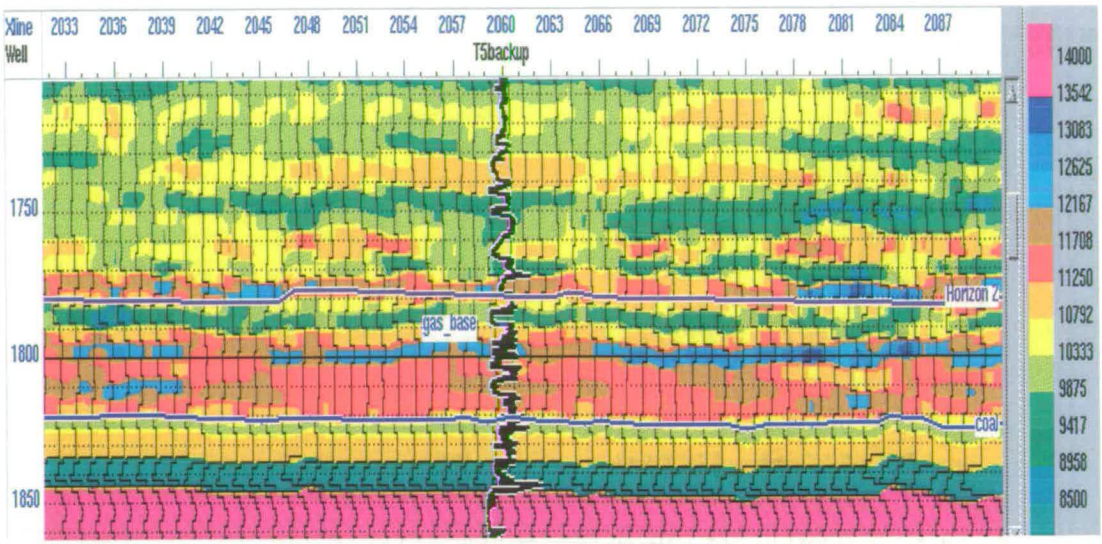

Figure 5.20: The P-wave impedance I_p, by inverting the P-reflectivity. Horizon 2 is picked near the top of the gas sand. The inserted curve is the Gamma Ray log of well T5.

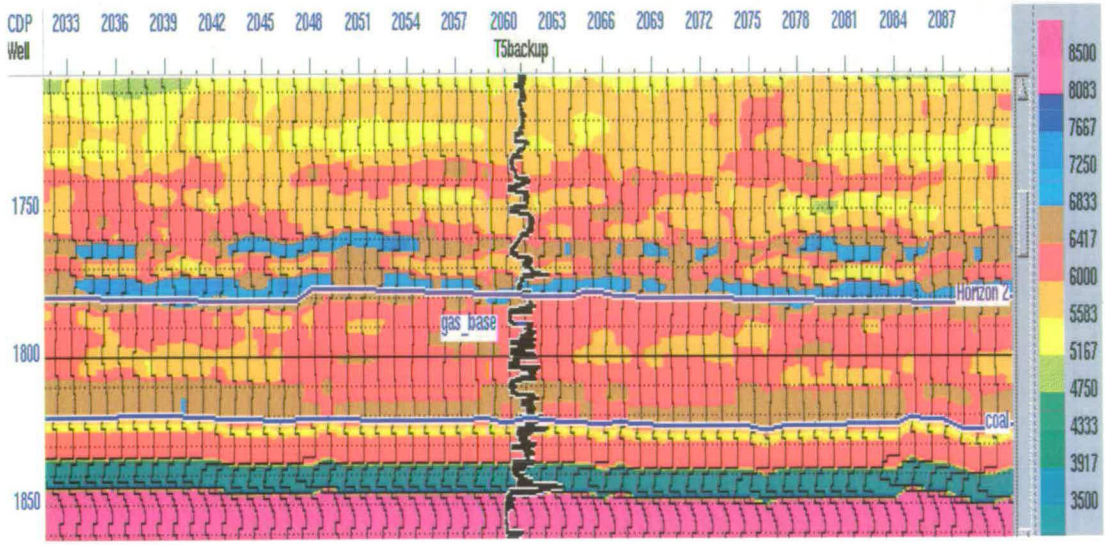

Figure 5.21: The S-wave impedance I_s, by inverting the S-reflectivity. Horizon 2 is picked near the top of the gas sand. The inserted curve is the Gamma Ray log of well T5

Figures 5.22 and 5.23 show the $\lambda\rho$ and $\mu\rho$ sections computed from the P- and S-wave impedance shown in Figures 5.20 and 5.21. The $\lambda\rho$ section shows a large

decrease in the gas filled layer. Figure 5.24 shows a crossplot of $\lambda\rho$ and $\mu\rho$ sections from Horizon 2 to Horizon coal. We can see a low value $\lambda\rho$ zone and a medium value $\mu\rho$ zone in the pink zone. The pink zone can be interpreted as the gas zone, and the higher value $\lambda\rho$ zone as non-gas zone. Then the pink area is plotted on the seismic section in Figure 5.25, the gas zone is shown as we expect.

Since the $\lambda\rho$-$\mu\rho$ analysis is based on equations 5-15 and 5-16, the noise may also be enlarged in the $\lambda\rho$ and $\mu\rho$ data through the square of impedance, thus the signal-to-noise ratio is reduced. Since the squares of the impedance are positive, calculating $\lambda\rho$ by subtracting them increases its potential error. Gray (2002) gives some mathematic proof that the error on $\lambda\rho$ is twice the error in $\mu\rho$, and four times on I_s. The density effect is also one of the issues in the $\lambda\rho$-$\mu\rho$ analysis.

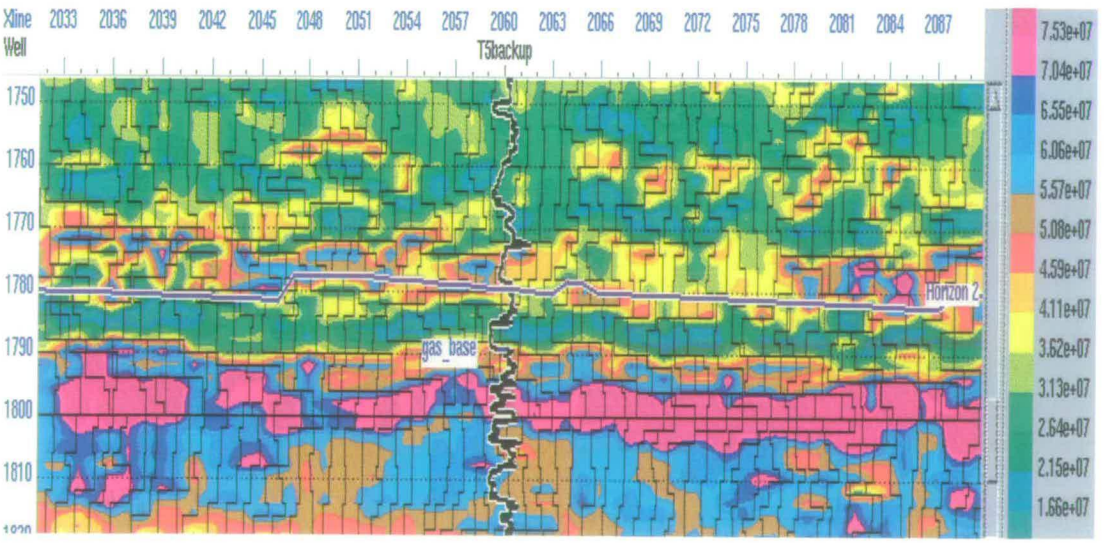

Figure 5.22: The $\lambda\rho$ section by combining the I_p and I_s inversions of Figures 5.20 and 5.21.

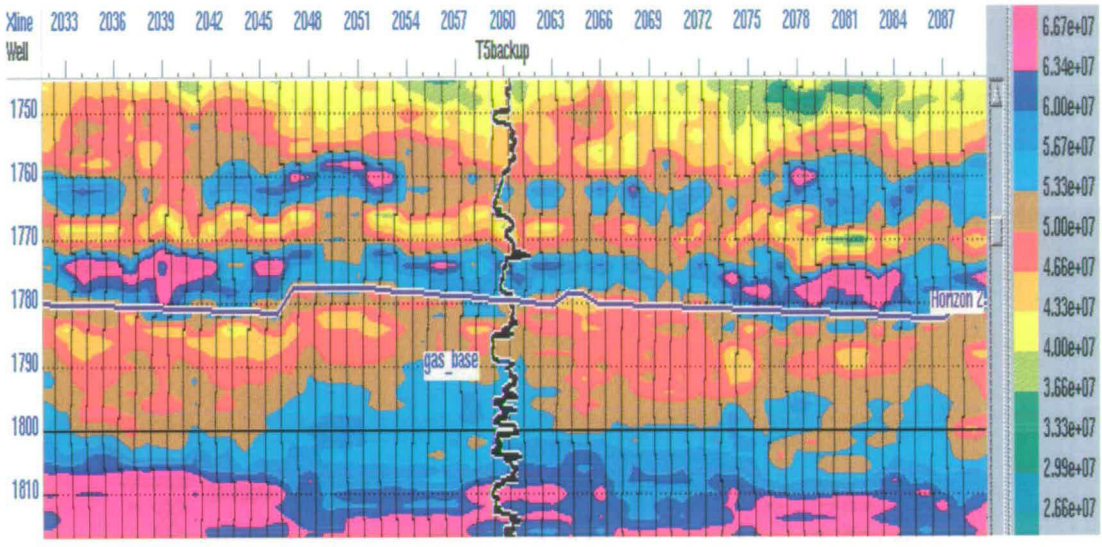

Figure 5.23: The μρ section by I_s inversions of Figure 5.21.

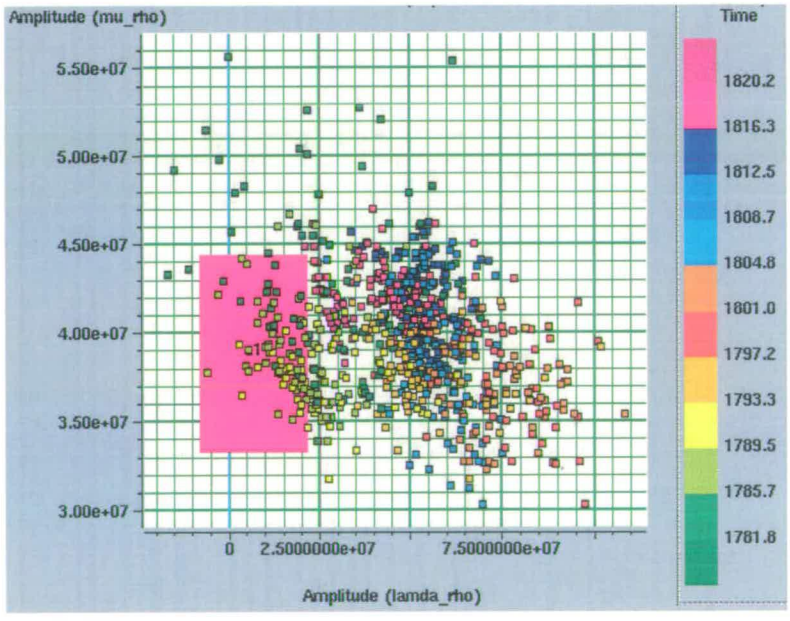

Figure 5.24: A crossplot between λρ and μρ section of Figures 5.22 and 5.23 from Horizon 2 to the coal horizon.

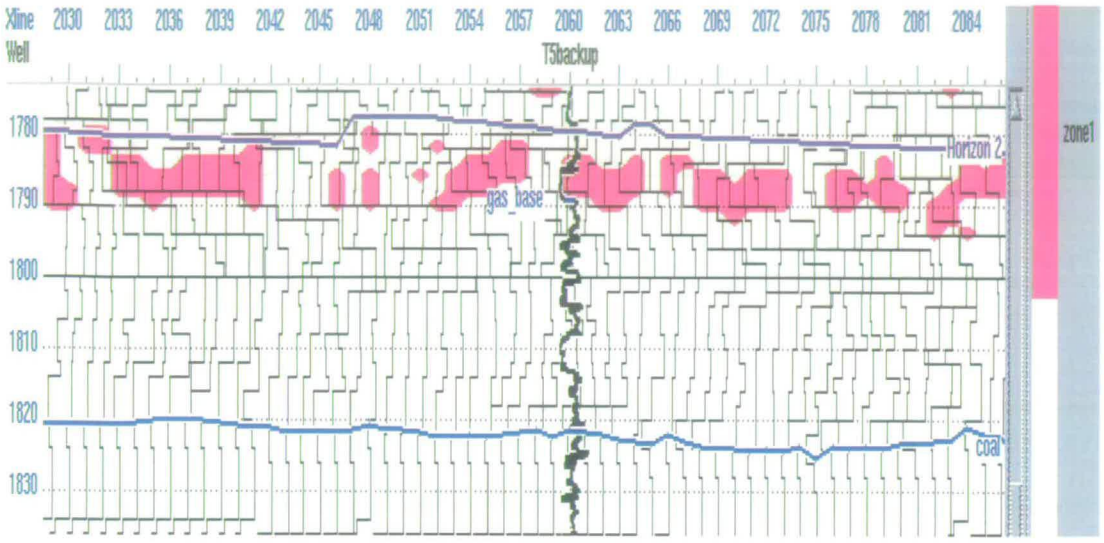

Figure 5.25: The pink zone is the H8 gas sand area where expected. The inserted curve is the Gamma Ray log.

5.5 Pitfalls in PP-wave AVO analysis

AVO analysis is based on approximations of the Zoeppritz equations, which assume plane waves at an elastic interface and a constant wavelet across the near to far offsets. However, the real data never exactly conform to these conditions. Several factors interfere with the effect of the AVO analysis. The wavelet always varies with offset due to earth absorption and NMO stretch. Inaccurate estimation of incidence angles and noise (multiples and converted waves) results in noise-leakage and overrides the signals. In addition, prestack amplitude balancing leads to the problem of "statistical leakage".

5.5.1 The reliability of AVO attributes

Cambois (2000) points out that the typical acquisition geometry cannot yield reliable gradient estimates, while the estimation of intercept is always accurate. A offset-varying wavelet will harm gradient attributes by increasing the noise level by at least 15 dB. This is because the gradient essentially corresponds to the difference between minimum and maximum angle stacks, divided by the square of sine of the

maximum incidence angle. Because the latter number is generally very small, the slightest amount of noise between the two angle stacks is boosted compared with the expected signal.

5.5.2 Wavelet variation and NMO stretch effect

There are two factors that result in the lower frequency content in far offsets: earth absorption and NMO stretch effect. Due to earth absorption on the longer travel path, the far offsets have lower bandwidth than the near offsets. Due to NMO stretch, the far offset stack has significantly lower frequency content compared to the near offset stack. Cambois (2000) simulates NMO stretch effect on Poisson's reflectivity extraction. The wavelet gradually changes with angle: at 30°, the wavelet has lost 10 Hz in high frequencies and gained 5 Hz in low frequencies. The resulting Poisson's reflectivity is extremely noisy.

5.5.3 Prestack amplitude balancing effect

In seismic acquisition, some receivers' amplitude responses are relatively weaker or stronger than others, and some of the source strengths vary along the survey line. This is usually due to varying air gun pressure and misfires in sea, and varying near subsurface conditions on land. Source and receiver amplitude variations can distort AVO analysis of prestack seismic reflection data. Therefore, amplitude balancing of the traces is necessary to compensate for average amplitude variation with offset and source location. Berlioux *et al* (2001) have discussed an amplitude balancing method by estimating amplitude correction coefficients for both offset and shot direction. However, Cambois (2000) points out that any statistical attempt at prestack amplitude balancing will result in a constant amplitude level for all offsets.

5.6 Conclusions

Laboratory measurement indicates that the P-wave velocity of tight sand has no rapid drop at low gas saturation (< 30%), which is not what is expected from Biot-Gassmann theory. The V_p/V_s ratio is more sensitive to gas saturation than P-wave velocity. Lithology has a larger effect on V_p/V_s than does fluid. Lamè parameter $\lambda\rho$ and fluid factor ρf are more capable of detecting fluid than P-impedance and V_p/V_s ratio. $\mu\rho$ is sensitive to the lithology.

From PP-wave data analysis, due to a small P-impedance contrast between the gas layer and the upper shale, and tuning effect, there is no AVO anomaly seen in the intercept and gradient attributes. Fluid factor shows a better response to gas than the product of intercept and gradient. $\lambda\rho$ and $\mu\rho$ from PP-wave only shows promise in fluid detection, however, this can be degraded by the cumulative errors from impedance inversion. The reliability of S-wave related information estimated from PP-wave is a big concern in AVO analysis. We hope that combing the converted PS-wave data, the estimation of S-wave information become more reliable, which is described in Chapter 6.

Chapter 6: Joint PP- and PS-Wave AVO Inversion – modelling and data application

6.1 Method

The Zoeppritz equations fully describe the relationship between incident and reflectivity/transmission amplitudes for plane waves at an elastic interface, but do not give a clear understanding of how these amplitudes relate to the various physical parameters. Aki and Richards (1980) provide a linearized 3-term approximation to the Zoeppritz equations based on the assumptions of small fractional velocity and density changes across the interface with the second order terms ignored for incident angles less than the critical angle. The equations for PP-wave and converted PS-wave are shown as the following:

$$Rpp(\theta) \approx \frac{1}{2}\left(1-4\frac{\beta^2}{\alpha^2}\sin^2\theta\right)\frac{\Delta\rho}{\rho}+\frac{1}{2\cos^2\theta}\frac{\Delta\alpha}{\alpha}-\frac{4\beta^2}{\alpha^2}\sin^2\theta\frac{\Delta\beta}{\beta}, \qquad (6\text{-}1)$$

$$Rps(\theta,\varphi) \approx -\frac{\alpha\tan\varphi}{2\beta}\left[\left(1-\frac{2\beta^2}{\alpha^2}\sin^2\theta+\frac{2\beta}{\alpha}\cos\theta\cos\varphi\right)\frac{\Delta\rho}{\rho}-\left(\frac{4\beta^2}{\alpha^2}\sin^2\theta-\frac{4\beta}{\alpha}\cos\theta\cos\varphi\right)\frac{\Delta\beta}{\beta}\right] \qquad (6\text{-}2),$$

where α, β, and ρ are the average P-wave, S-wave velocities V_p and V_s and density across the interface, $\Delta\alpha$, $\Delta\beta$, and $\Delta\rho$ are the contrasts in V_p, V_s and density across the interface, θ is an average of P-wave angles of incidence and transmission across the interface, and φ is the average of the shear wave angles of reflection and transmission across the interface. The above equations are accurate up to angles of incidence of around 50 degrees for typical velocity and density contrasts (Smith and Gidlow, 1987).

Fatti *et al.* (1994) reformulated Equation 6-1 in terms of P- and S-impedance:

$$Rpp(\theta) \approx \frac{1+\tan^2\theta}{2}\frac{\Delta I_p}{I_p} - 4\frac{\beta^2}{\alpha^2}\sin^2\theta\frac{\Delta I_s}{I_s} - \left(\frac{1}{2}\tan^2\theta - 2\frac{\beta^2}{\alpha^2}\sin^2\theta\right)\frac{\Delta\rho}{\rho}, \qquad (6\text{-}3)$$

Correspondingly, Equation 6-2 can be rearranged as:

$$Rps(\theta,\varphi) \approx -\frac{\alpha\tan\varphi}{2\beta}\left[\left(1+2\sin^2\varphi - \frac{2\beta}{\alpha}\cos\theta\cos\varphi\right)\frac{\Delta\rho}{\rho} - \left(4\sin^2\varphi - \frac{4\beta}{\alpha}\cos\theta\cos\varphi\right)\frac{\Delta I_S}{I_S}\right] \qquad (6\text{-}4),$$

where $\frac{\Delta I_p}{I_p}$ and $\frac{\Delta I_s}{I_s}$ are, respectively, P- and S-impedance reflectivity, and $\frac{\Delta\rho}{\rho}$ is density reflectivity.

The above equations show that R_{pp} and R_{ps} vary with incident and reflection angles θ and φ. We note the angle-dependant coefficients in Equation 6-3 and 6-4 as the following:

$$C = \frac{1+\tan^2\theta}{2}, \qquad (6\text{-}5)$$

$$D = -4\frac{\beta^2}{\alpha^2}\sin^2\theta, \qquad (6\text{-}6)$$

$$E = 2\frac{\beta^2}{\alpha^2}\sin^2\theta - \frac{1}{2}\tan^2\theta, \qquad (6\text{-}7)$$

$$F = -\frac{\alpha\tan\varphi}{\beta}\left(1+2\sin^2\varphi - 2\frac{\beta}{\alpha}\cos\theta\cos\varphi\right), \qquad (6\text{-}8)$$

$$G = \frac{\alpha\tan\varphi}{\beta}\left(2\sin^2\varphi - 2\frac{\beta}{\alpha}\cos\theta\cos\varphi\right). \qquad (6\text{-}9)$$

Therefore, Equation 6-3 and 6-4 are given in a simple form as the following:

$$Rpp(\theta) \approx C\frac{\Delta I_p}{I_p} + D\frac{\Delta I_s}{I_s} + E\frac{\Delta \rho}{\rho}, \qquad (6\text{-}10)$$

$$Rps(\theta, \varphi) \approx F\frac{\Delta \rho}{\rho} + G\frac{\Delta I_s}{I_s}. \qquad (6\text{-}11)$$

In Equation 6-10, the density effect is small for near-to-mid offsets, and contributes mainly for far offsets. Usually the inversion to density is problematic for real noisy data. The density term in Equation 6-10 can be replaced by P-impedance through Gardner's (1974) equation between P-wave velocity and density when such relation holds in practice.

Alternatively, if Gardner's relationship does not hold, AVO inversion using only PP-wave data just drops the third term in Equation 6-10, justified by its small effect for incident angles less than 35 degree and α/β ratios between 1.5 and 2.0 (Gidlow *et al.*, 1992). When the PS-waves are included in the inversion, the density term can be accounted for by rearranging Equation 6-11. The density reflectivity can be obtained from PS-wave reflection coefficient R_{ps}:

$$\frac{\Delta \rho}{\rho} = \frac{1}{F}\left[Rps(\theta, \varphi) - G\frac{\Delta I_s}{I_s} \right], \qquad (6\text{-}12)$$

Replacing $\frac{\Delta \rho}{\rho}$ in Equation 6-10 using Equation 6-12, we obtain

$$Rpp + W_{imp} Rps = C\frac{\Delta I_p}{I_p} + H\frac{\Delta I_s}{I_s}, \qquad (6\text{-}13)$$

where the coefficient W is the angle-dependant scalar for PS-data and determined by the following equation:

$$W_{imp} = \frac{(\frac{4\beta^2}{\alpha^2}\sin^2\theta - \tan^2\theta)\cos\varphi}{2\sin\theta - \sin(\theta + 2\varphi)}, \qquad (6\text{-}14)$$

and the angle dependent coefficient C is defined by Equation 6-5, and H is the following:

$$H = \frac{(\frac{4\beta^2}{\alpha^2}\sin^2\theta - \tan^2\theta)(\sin\theta - \sin(\theta + 2\varphi))}{2\sin\theta - \sin(\theta + 2\varphi)} - \frac{4\beta^2}{\alpha^2}\sin^2\theta. \qquad (6\text{-}15)$$

Gray *et al.* (1999) derive the *Rpp* equation in terms of Lamè parameters and density:

$$Rpp(\theta) \approx \left(\frac{1}{4} - \frac{\beta^2}{2\alpha^2}\right)\sec^2\theta\frac{\Delta\lambda}{\lambda} + \frac{\beta^2}{\alpha^2}\left(\frac{\sec^2\theta}{2} - 2\sin^2\theta\right)\frac{\Delta\mu}{\mu} + \left(\frac{1}{2} - \frac{\sec^2\theta}{4}\right)\frac{\Delta\rho}{\rho}, \qquad (6\text{-}16)$$

therefore we can further combine this with the *Rps* equation:

$$Rps(\theta,\varphi) \approx -\frac{\alpha\tan\varphi}{2\beta}\frac{\Delta\rho}{\rho} + \frac{\beta}{\alpha}\left(\sin^2\theta\tan\varphi - \sin\theta\cos\theta\right)\frac{\Delta\mu}{\mu}. \qquad (6\text{-}17)$$

Then a similar formulation to Equation 6-13 in terms of Lamè parameters λ and μ can be written in the following expression:

$$Rpp + W_{lame}Rps = I\frac{\Delta\lambda}{\lambda} + J\frac{\Delta\mu}{\mu}, \qquad (6\text{-}18)$$

where

$$W_{lame} = 1 - \frac{\beta\sec^2\theta}{2\alpha\tan\varphi}, \qquad (6\text{-}19)$$

$$I = \left(\frac{1}{4} - \frac{\beta^2}{2\alpha^2}\right)\sec^2\theta, \qquad (6\text{-}20)$$

$$J=\frac{\beta^2}{\alpha^2}\left(\frac{\sec^2\theta}{2}-2\sin^2\theta\right)-\frac{\beta}{\alpha}\left(1-\frac{\sec^2\theta}{2}\right)\cos(\theta-\varphi). \qquad (6\text{-}21)$$

Both Equations 6-13 and 6-21 can be used in the standard least-squares technique to minimise the error between the Aki-Richards model and the real data. P- and S-impedance reflectivity $\frac{\Delta I_p}{I_p},\frac{\Delta I_s}{I_s}$ and Lamè's reflectivity $\frac{\Delta\lambda}{\lambda},\frac{\Delta\mu}{\mu}$ can then be inverted from the following matrix:

$$\begin{pmatrix}\frac{\Delta I_P}{I_P}\\ \frac{\Delta I_S}{I_S}\end{pmatrix}=\begin{pmatrix}\sum_{i=1}^{N}C_i^2 & \sum_{i=1}^{N}C_iH_i\\ \sum_{i=1}^{N}C_iH_i & \sum_{i=1}^{N}H_i^2\end{pmatrix}^{-1}\begin{pmatrix}\sum_{i=1}^{N}C_iR_i\\ \sum_{i=1}^{N}H_iR_i\end{pmatrix}, \qquad (6\text{-}22)$$

$$\begin{pmatrix}\frac{\Delta\lambda}{\mu}\\ \frac{\Delta\mu}{\mu}\end{pmatrix}=\begin{pmatrix}\sum_{i=1}^{N}I_i^2 & \sum_{i=1}^{N}I_iJ_i\\ \sum_{i=1}^{N}I_iJ_i & \sum_{i=1}^{N}J_i^2\end{pmatrix}^{-1}\begin{pmatrix}\sum_{i=1}^{N}I_iR_i\\ \sum_{i=1}^{N}J_iR_i\end{pmatrix}, \qquad (6\text{-}23)$$

where

$$Ri=Rpp+WRps. \qquad (6\text{-}24)$$

I have reformulated the PP- and PS-wave joint inversion equations in the Equations 6-13 to 6-21, therefore a new form of P- and S-impedance reflectivity and Lamè's reflectivity has been obtained in Equations 6-22 and 6-23. The above PP- and PS-wave joint inversion method is a use of the Aki-Richards equation. This joint method does not assume the density and velocity relation of the Gardner (1974) relation. This is important for areas where the Gardner relation does not apply. Incident and reflection angles are calculated from ray tracing, and the V_p/V_s ratio comes from event registration.

6.2 Method testing

In order to test the performance of the linearized, joint PP- and PS-data inversion algorithm, I built a multi-layer isotropic elastic model (Figure 6.1), which shows the general P-wave velocity structure of the study area. Since we are interested in the effects of gas sand on S-waves, Poisson's ratios for each layer are set to 0.33, and then changed to 0.1 for the target layer at a depth of 3200m indicating presence of gas in the second model. PP-inversion and PS-inversion alone are also carried out for comparison of the inversion accuracy.

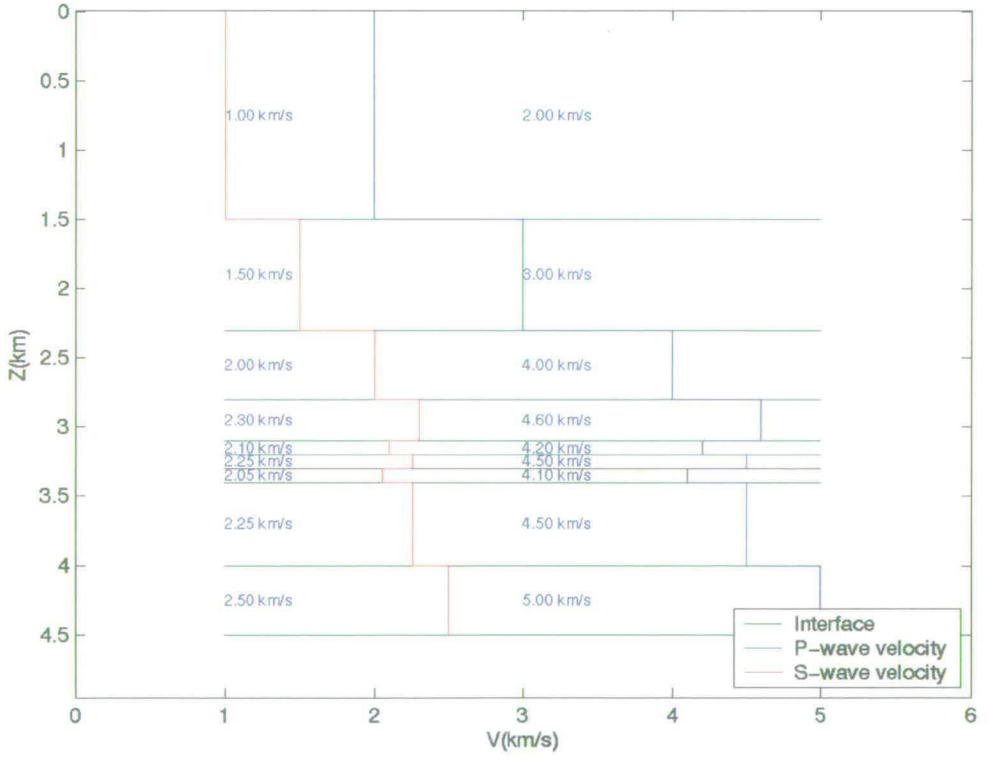

Figure 6.1: A multi-layer model for inversion testing, density is set to 2.3 g/cc for each layer, and initial V_p/V_s=2.0.

There are many methods available to generate the synthetic PP- and PS-seismograms. To include a bending ray effect, we use the exact Zoeppritz equation with ray tracing to calculate primary reflectivity only. Figure 6.2 shows the primary

reflection raypath of PP- and PS-waves. Through amplitude spectrum analysis, PP-data and PS-data in the study area are shown to have a 8-40Hz bandwidth for PP-data and 8-30Hz for PS-data, thus a 30Hz Ricker wavelet is used to convolve the calculated reflection coefficients at each depth and offset for PP-wave synthetic data and a 25Hz Ricker wavelet for PS-wave synthetic data (Figure 6.3). The offsets range from 0 m to 4000 m with 100m interval. The traces with incident angle beyond the critical angle are muted.

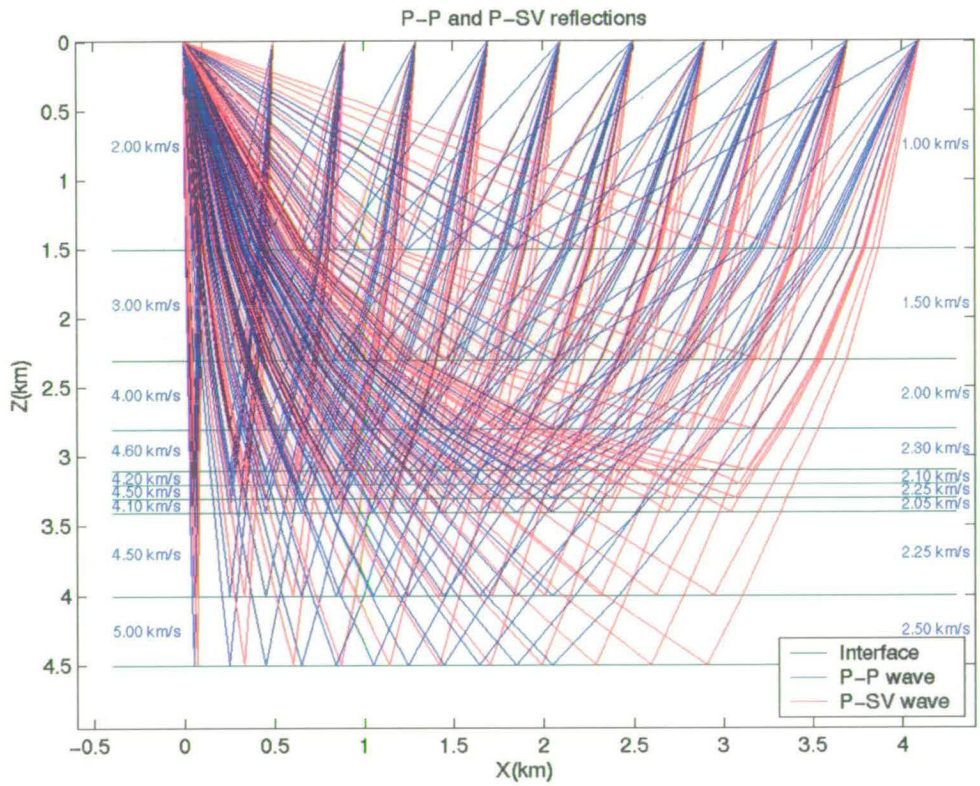

Figure 6.2: Ray–tracing paths of both PP-wave (blue) and PS-wave (red) for the model in Figure 6.1.

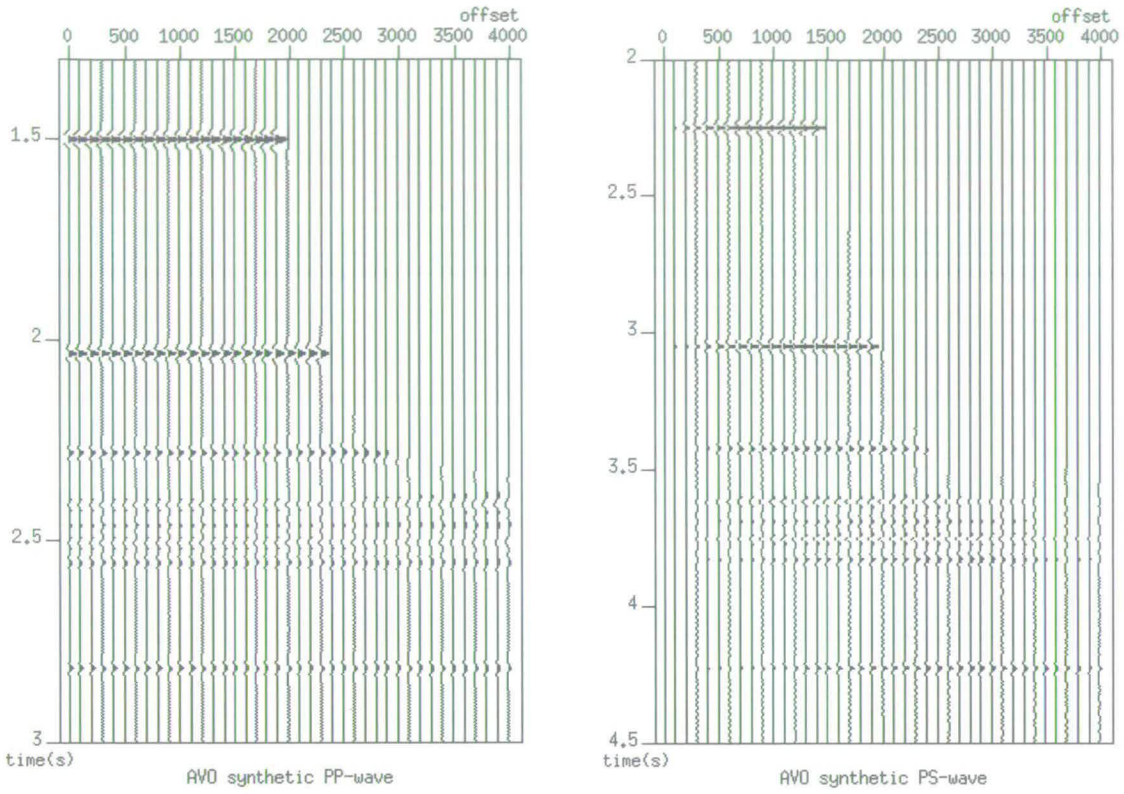

Figure 6.3: PP-wave and PS-wave synthetic gathers by Zoeppritz equation for the model in Figure 6.1.

In order to compare the effect of the exact velocity-depth model and a smoothed velocity-depth model on the inversion results, a linearly smoothed velocity-depth model is built in Figure 6.4.

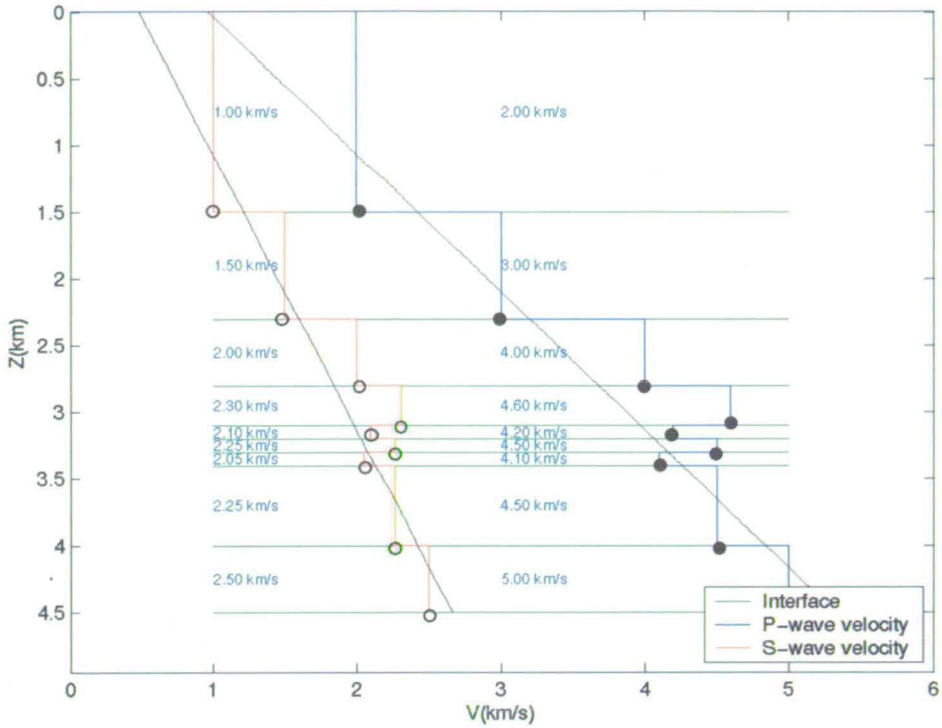

Figure 6.4: The linear regression of P- and S-velocity for simulating a smoothed velocity model for comparing the velocity effect on the inversion results.

6.2.1 PS-inversion alone

Since we are interested in the accuracy of S-impedance as estimated from PS-wave inversion, PS-wave inversion alone is performed using Equation 6-4. P-wave incident and S-wave reflection angles are calculated for both the exact model and the linear smoothed model (Figure 6.5), and angle-dependent weights are calculated and plotted in. Figure 6.6.

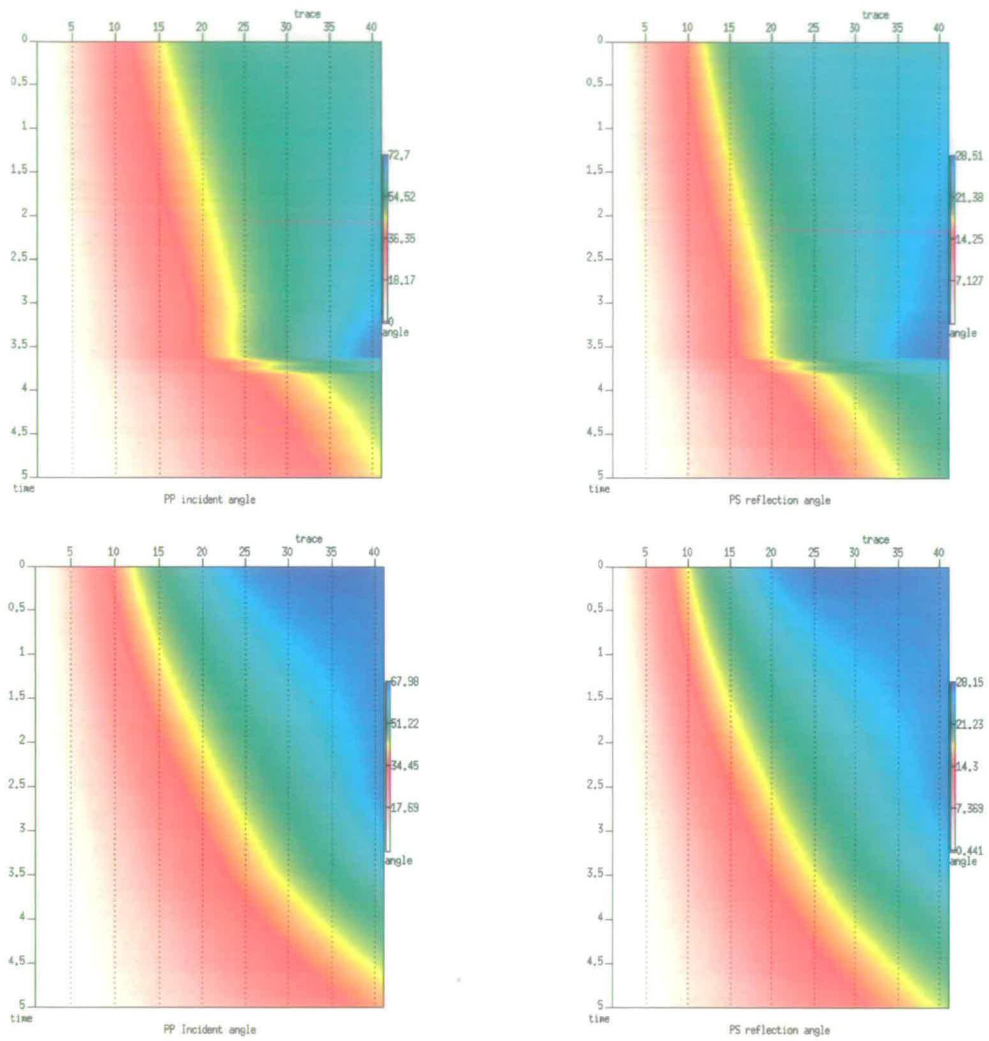

Figure 6.5: Ray-traced PS-wave incident angles (left) and reflection angles (right) for the exact model (above) in Figure 6.1 and the linear smoothed model (below) in Figure 6.4.

Figure 6.6 shows the weight distribution on the PS-reflection amplitude for S-impedance reflectivity and density reflectivity. The mid-offset contributes the largest weight for the S-reflectivity estimation, while the far-offset contributes the most for density reflectivity estimation. Because of the noise and far-offset stretch effect, the quality of far offset data is usually worse than the near to mid offset, so the accuracy of S-reflectivity is usually better than the density reflectivity.

Figure 6.7 shows the inversion results for S-impedance reflectivity and density reflectivity. The first trace in Figure 6.7a is S-impedance reflectivity using the exact model, the second trace using the smoothed velocity model, and the third trace is the true value of S-impedance reflectivity of the model. The fourth trace is the error of inverted S-impedance reflectivity with the exact model, and the fifth trace is the error of inverted S-impedance reflectivity with the smoothed velocity model. The large error of the first two layers is mainly caused by the violation of one of the Aki-Richards equation assumptions, that of a small reflection coefficient between the interface: the S-impedance reflectivity of the first layer is 0.4, the second layer is nearly 0.3, much greater than the assumption. This effect can also be seen clearly in Figure 6.7b, where the density reflectivity is expected to be zero, since the same density is given to each layer. The difference between the exact Zoeppritz equation and linearized Aki-Richards equation is also another reason for the difference. Although there are differences between the actual S-impedance reflectivity and inversion results, on the whole the inversion results are acceptable except for the first two layers (Table 6.1).

The inversion results in Figure 6.7a show a similarity between the smoothed model and the exact model. For the density reflectivity in Figure 6.7b, the inversion with the smoothed model is even better than the exact model. PS-wave inversion testing confirms that the smoothed velocity-depth model can be used successfully for a velocity background.

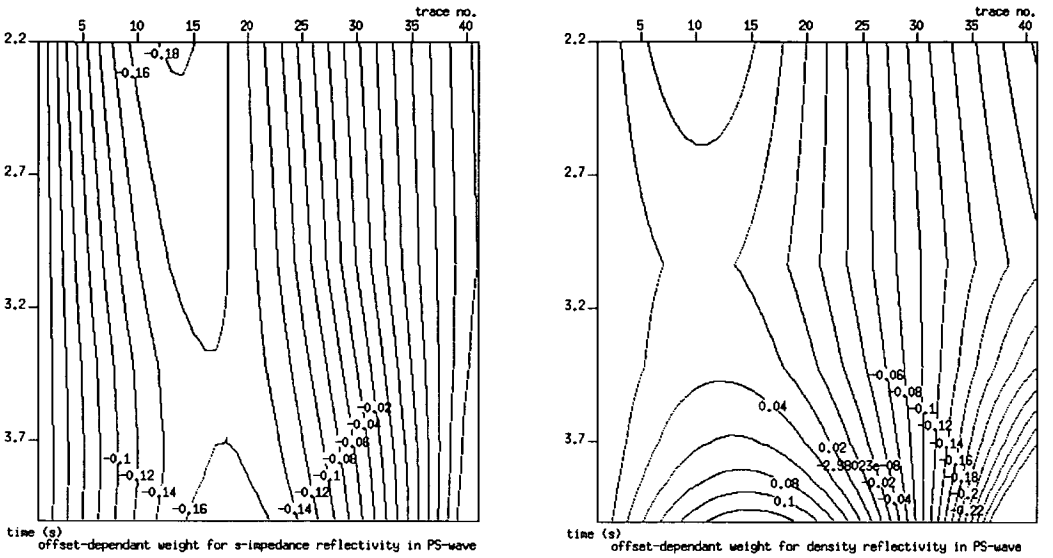

Figure 6.6: Weight distribution for S-impedance and density reflectivity from PS-wave inversion.

Interface depth (m)	True S-impedance reflectivity	Exact velocity model and error (%)		Smoothed velocity model and error (%)	
1500	0.4000	0.174	56.5	0.175	56.3
2300	0.2857	0.167	41.5	0.169	40.8
2800	0.1395	0.106	24.0	0.107	23.3
3100	-0.0909	-0.083	8.7	-0.088	3.2
3200	0.0689	0.070	1.6	0.065	5.6
3300	-0.0930	-0.094	1.1	-0.093	0.0
3400	0.0930	0.100	7.5	0.090	3.2
4000	0.1053	0.123	16.8	0.116	10.2

Table 6.1: The S-impedance reflectivity for the model and the PS-wave inversion results.

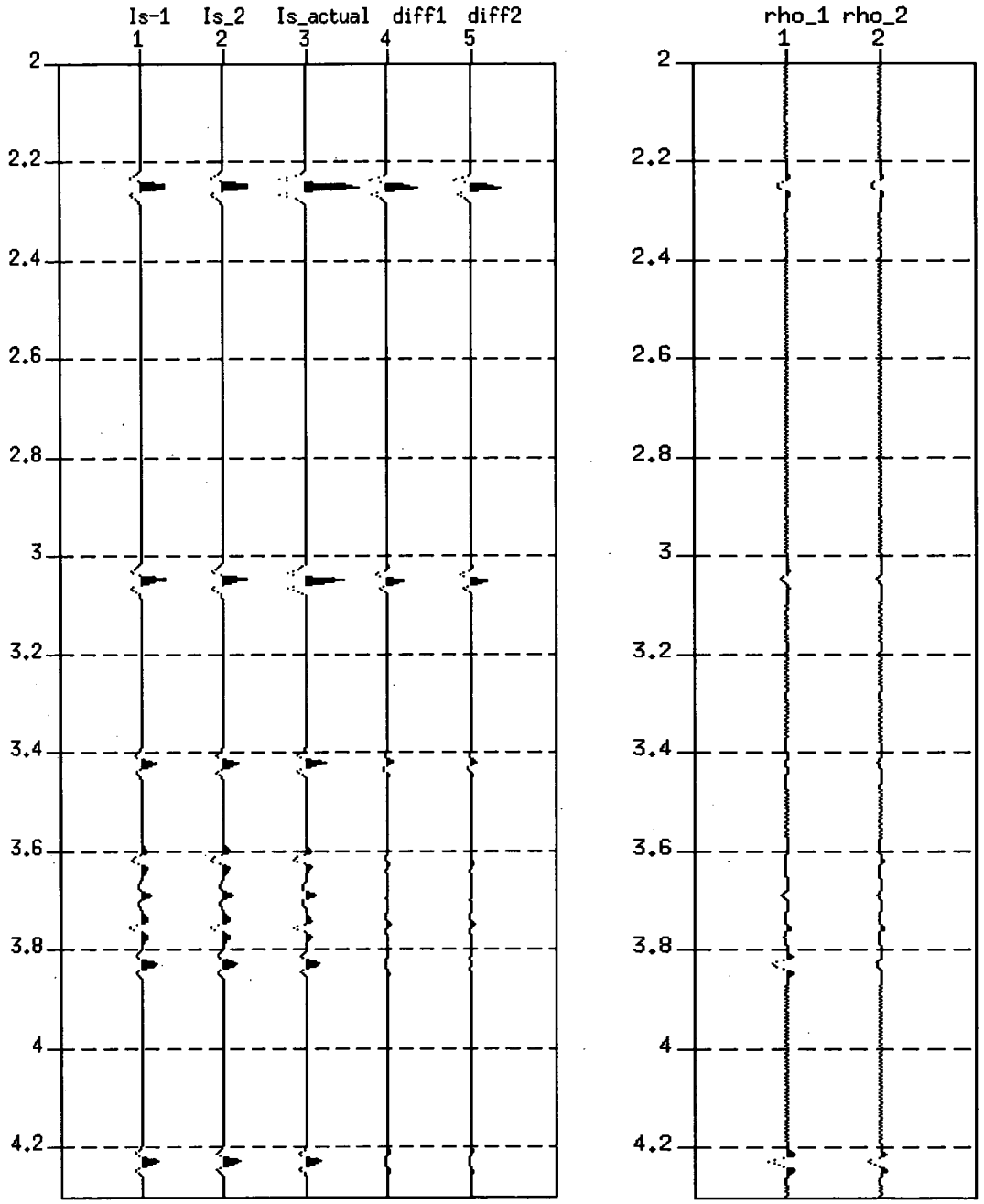

(a) S-impedance reflectivity: the 1st inverted trace is for the exact velocity model, the 2nd trace for the smoothed velocity model, and the 3rd trace is the true S-impedance reflectivity. The 4th trace is the difference between the1st and 3rd traces, and the 5th trace is the difference between the2st and 3rd traces.

(b) Density reflectivity: the 1st inverted trace is for the exact velocity model, the 2nd trace for the smoothed velocity model, the true density reflectivity coefficient is zero since the same density is applied to each layer

Figure 6.7: Inverted results from PS-data alone

For investigating S-impedance inversion accuracy in the presence of gas, the S-wave velocity at interval from 3100m to 3200m is increased from 2100m/s to 2800m/s so that Poisson's ratio becomes 0.1, whilst the P-wave velocity and density is unchanged. Figure 6.8 shows the PS-data used for this inversion. The far offsets are muted for comparison of the inversion results from Figure 6.11b. Note that the polarity at interface 3100m (the 4th reflection) and 3200m (the 5th reflection) has been changed due to gas presence compared to Figure 6.3b.

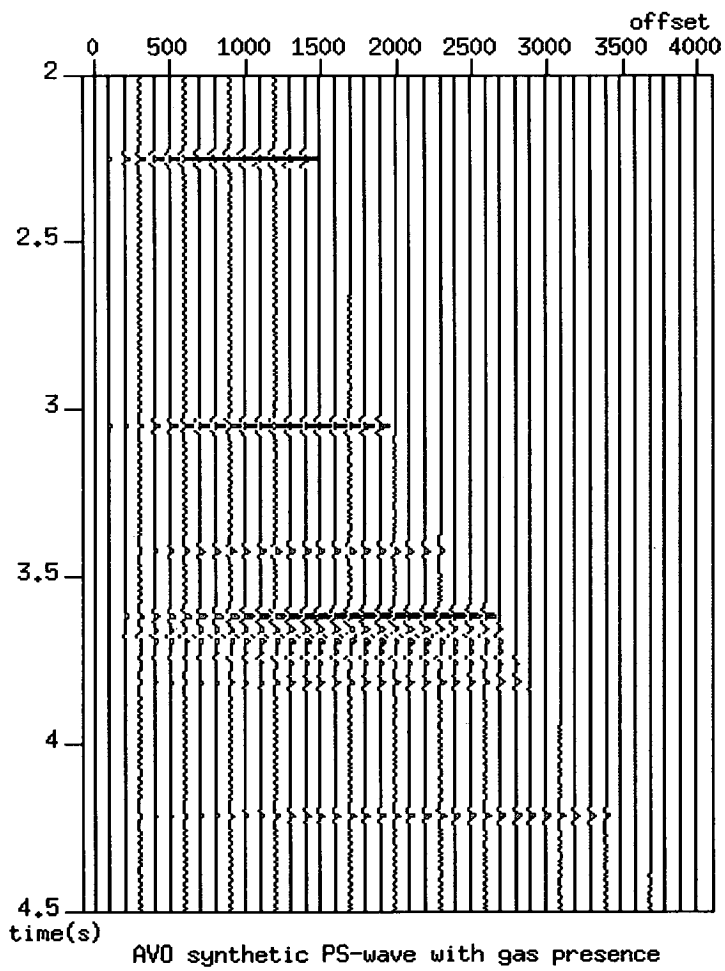

Figure6 8: PS-wave synthetic gathers by Zoeppritz equation for the model in the presence of gas.

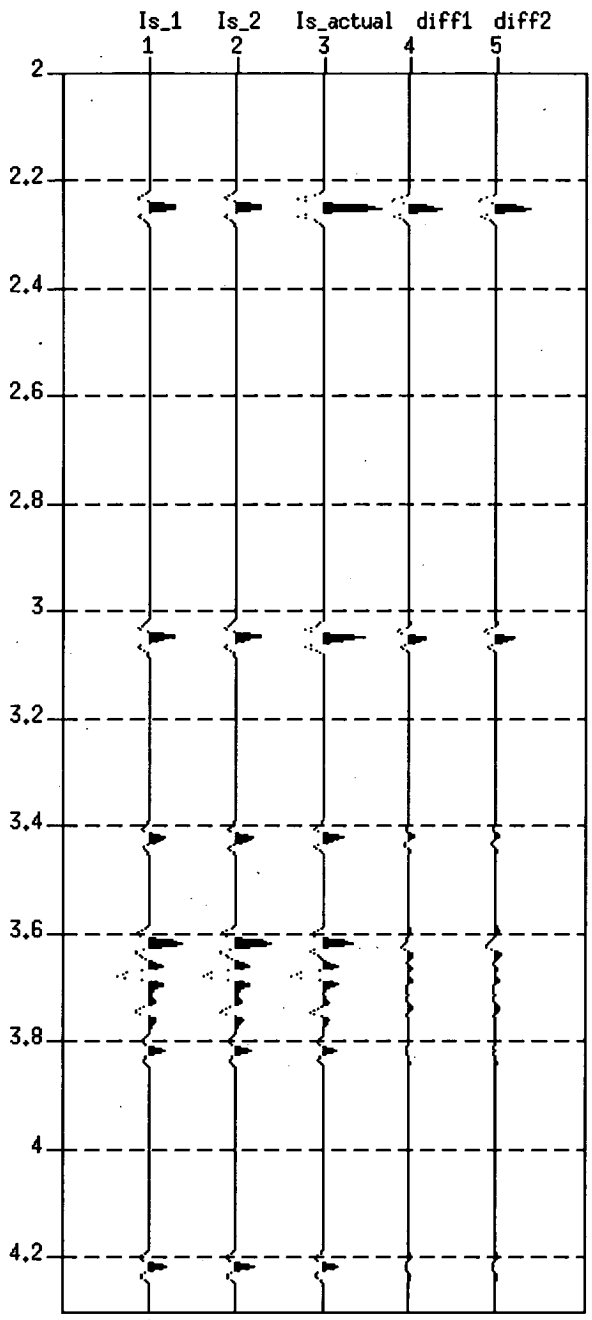

(a) S-impedance reflectivity: the 1st inverted trace is for the exact velocity model, the 2nd trace for the smoothed velocity model, and the 3rd trace is the true S-impedance reflectivity. The 4th trace is the difference between the1st and 3rd traces, and the 5th trace is the difference between the2st and 3rd traces.

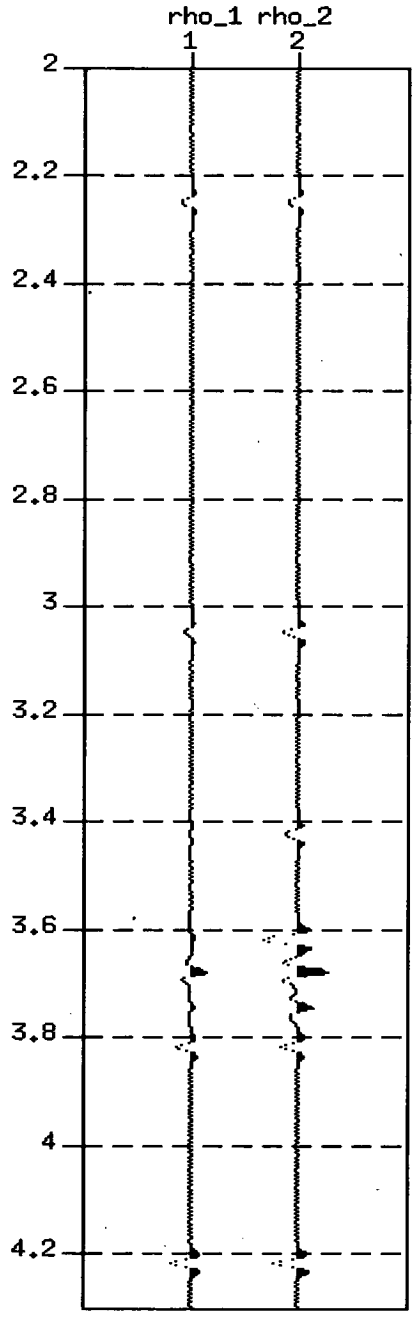

(b) Density reflectivity: the 1st inverted trace is for the exact velocity model, the 2nd trace for the smoothed velocity model, the actual density reflectivity coefficient is zero since the same density is applied to each layer

Figure 6.9: Inverted results from PS-data alone with presence of gas at depth from 3100m to 3200m.

The inversion results are shown in Figure 6.9. Table 6.2 shows the differences between the true S-impedance reflectivity and inversion results. The S-impedance reflectivity inversion results show a similarity between the smoothed model and the exact model. For the density reflectivity, lack of far-offset data causes the unacceptable the inverted results.

Interface depth (m)	True S-impedance reflectivity	Exact velocity model and error (%)		Smoothed velocity model and error (%)	
1500	0.4000	0.174	56.5	0.164	59.0
2300	0.2857	0.167	41.5	0.162	43.3
2800	0.1395	0.105	24.7	0.110	21.1
3100	0.1961	0.220	12.2	0.250	27.5
3200	-0.2178	-0.210	3.6	-0.220	1.01
3300	-0.0930	-0.094	1.1	-0.100	7.5
3400	0.0930	0.100	7.5	0.098	5.4
4000	0.1053	0.122	15.8	0.123	16.8

Table 6.2: The S-impedance reflectivity for the model with gas filled interval from 3100m to 3200m and the PS-wave inversion results.

6.2.2 PP-inversion alone

PP-wave inversion based on Equation 6-3 is performed to test the accuracy of the impedance reflectivity from PP-data alone. Figure 6.10 shows the distribution of weights across the offset range from 0 m to 4000 m. For P-impedance, weights from the near offsets take a dominant role, and gradually decrease to the far offsets. For S-impedance, both the near offset and far offsets over 3000m contribute the most.

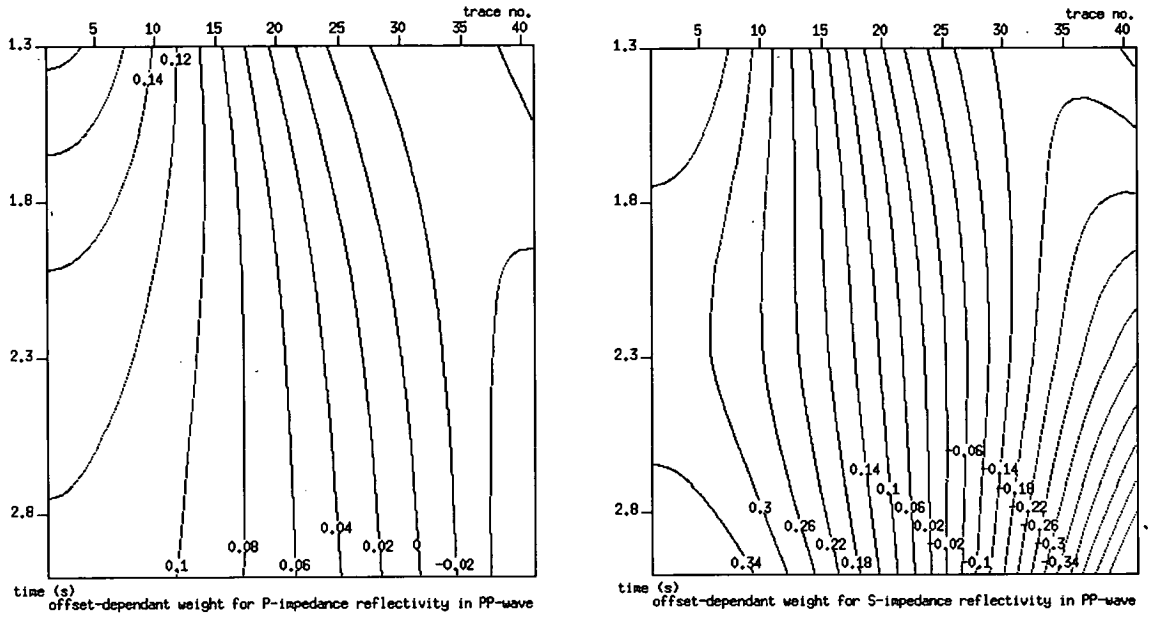

Figure 6.10: Weight distribution for P- and S-impedance reflectivity from PP-wave inversion.

To illustrate the importance of the far offset on S-wave impendence estimation from PP-data, I generate two PP-data datasets, one with all offsets from 0 m to 4000 m except trace muting beyond the critical angles in the shallow layers (Figure 6.11a), the other with the offsets limited to 0 m to 3000 m (Figure 6.11b, where the offset to the target depth ratio X/Z is less than 1). The inverted P- and S- impedance are shown in Figure 6.12.

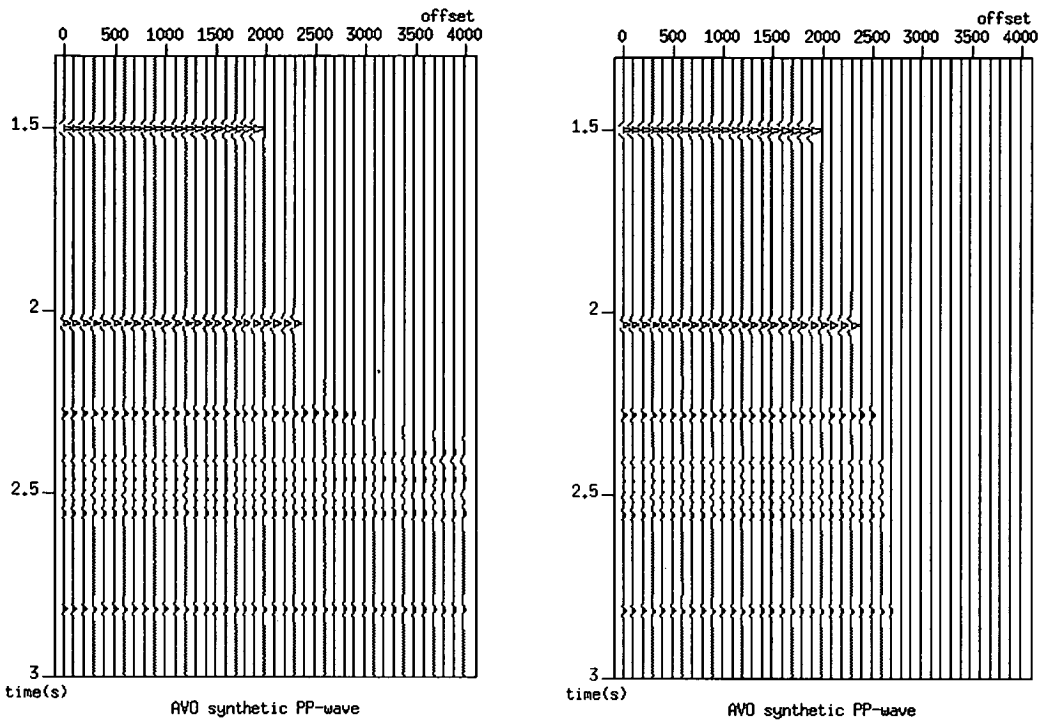

(a) PP-gather (0-4000m) (b) muted PP-gather (0-3000m)

Figure 6.11: Full offset data (a, trace muted beyond the critical angles in the shallow layers) and the muted data (b) to illustrate the importance of the far offset on S-wave impendence estimation.

Figure 6.12 shows that the inversion of P-impedance from both datasets is similar, whilst the accuracy of S-impedance from the full offsets is better than that of the limited offsets of 0 to 3000 m. Therefore, for S-wave estimation from PP-data alone, offsets should be long enough for an accurate inversion, since the far offset contributes a large part for S-impedance reflectivity. The accuracy of P-impedance for both offset sets is similar because the weight of P-impedance mainly distributes in the near to mid offset. On the whole, from PP-data alone, the inversion accuracy of P-impedance is better than S-impedance. Table 6.3 and 6.4 supports this analysis.

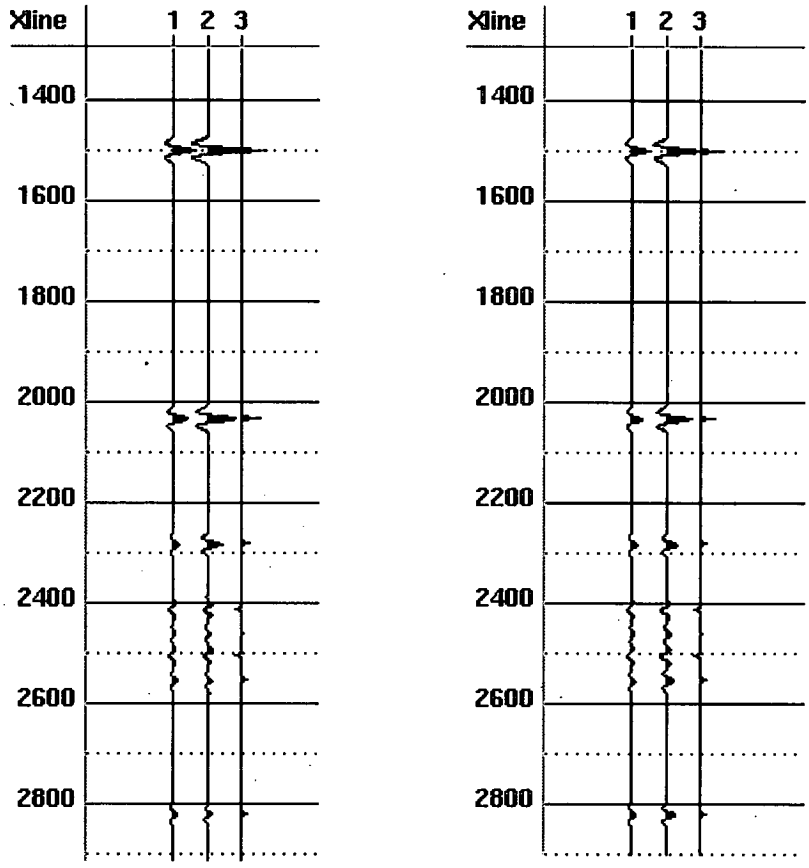

(a) Inverted impedance traces without data muting

(b) Inverted impedance traces with muted data

Figure 6.12: Inverted results for the full offset data and the muted data in Figure 6.11. The 1st trace in each diagram is P-impedance reflectivity, the 2nd trace is S- impedance reflectivity, and the 3rd trace is the actual P- and S-impedance reflectivity coefficients.

Interface depth (m)	True P-impedance reflectivity	Data in Figure 6.11a and error (%)		Data in Figure 6.11b and error (%)	
1500	0.4000	0.478	19.5	0.478	19.5
2300	0.2857	0.324	13.4	0.324	13.4
2800	0.1395	0.157	12.5	0.161	15.4
3100	-0.0909	-0.084	7.6	-0.097	6.7
3200	0.0689	0.064	7.1	0.076	10.3
3300	-0.0930	-0.085	8.6	-0.099	6.5
3400	0.0930	0.087	6.5	0.101	8.6
4000	0.1053	0.099	6.0	0.114	8.3

Table 6.3: The P-impedance reflectivity and PP-wave inversion results of the data in Figure 6.11.

Interface depth (m)	True S-impedance reflectivity	Data in Figure 6.11a and error (%)		Data in Figure 6.11b and error (%)	
1500	0.4000	0.962	140.5	0.962	140.5
2300	0.2857	0.637	122.9	0.636	122.
2800	0.1395	0.288	106.4	0.315	125.8
3100	-0.0909	-0.093	2.3	-0.189	107.9
3200	0.0689	0.076	10.3	0.147	113.3
3300	-0.0930	-0.089	4.30	-0.19	104.3
3400	0.0930	0.077	17.2	0.208	123.6
4000	0.1053	0.092	12.6	0.254	141.2

Table 6.4: The S-impedance reflectivity and PP-wave inversion results of the data in Figure 6.11.

The S-impedance from PP-data alone with full offset (0-4000m) and gas presence at interval 3100m to 3200m is shown in Figure 6.13. The model parameters are the same as the case for PS-data alone in Figure 6.9a. Compared to PS-data inversion alone shown in Figure 6.9a, although the amplitude and polarity have been changed due to gas presence in Figure 6.13, the accuracy from PP-wave inversion for S-impedance is reduced. The waveform becomes wider because of the far-offset stretch on the PP-data.

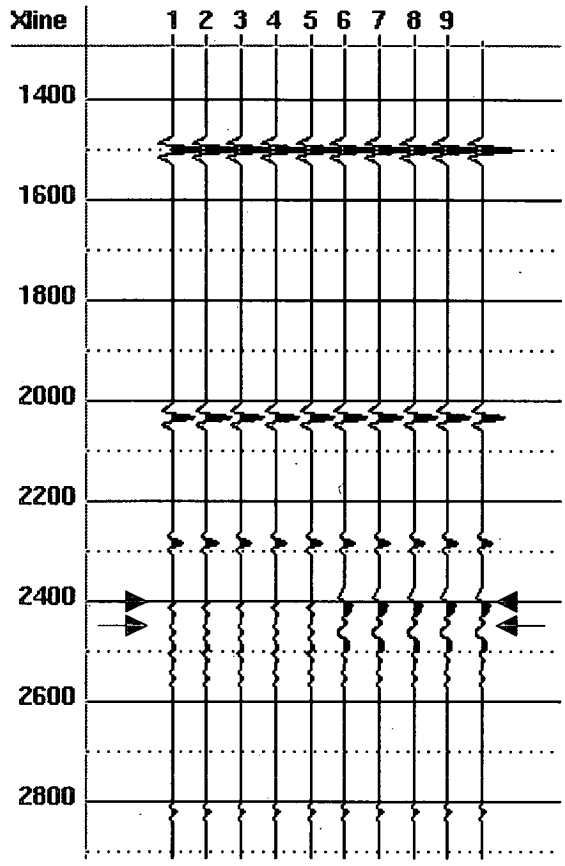

Figure 6.13: S-impedance reflectivity in the absence of gas (the left five traces) and in the presence of gas (the right five traces), indicated by the arrow, from PP-data alone.

6.2.3 Joint inversion of PP- and PS-data

Joint PP- and PS-data inversion is performed based on Equation 6-13 for S-wave impedance estimation. Figure 6.14 shows PP-wave and PS-wave synthetic gathers by Zoeppritz equation for the model with gas and noise (S/N=8) presence. The PS-data are combined into the inversion with PP-data by multiplying a parameter W_{imp}. The distribution of the weight W_{imp} for the model in Figure 6.1 is shown in the Figure 6.15. W_{imp} increases with increasing offset, which implies that PS-data will contribute more at the far offsets and therefore make an impact on the estimation of S-wave impedance. Figure 6.16 confirms this analysis, where S-impedance estimation is more accurate using PP- and PS-data together comparing to PP-data alone, especially when noise is present in the data.

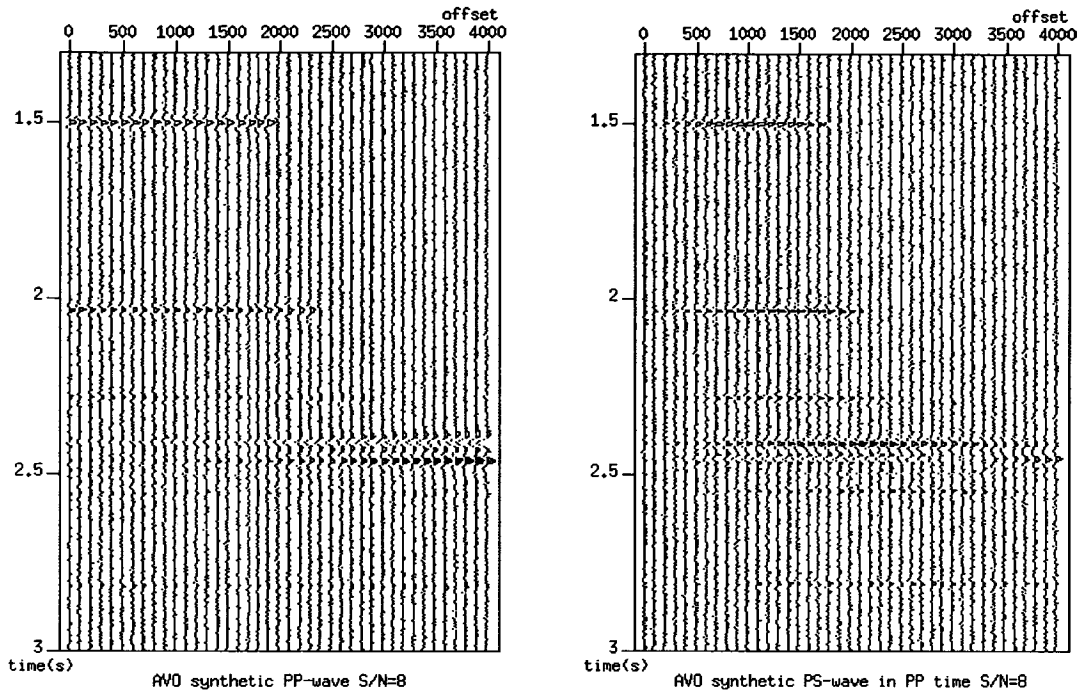

(a) PP-gather with S/N=8 (b) PS-gather in PP-wave time with S/N=8

Figure 6.14 PP-wave and PS-wave synthetic gathers by Zoeppritz equation for the model with gas and noise (S/N=8) presence.

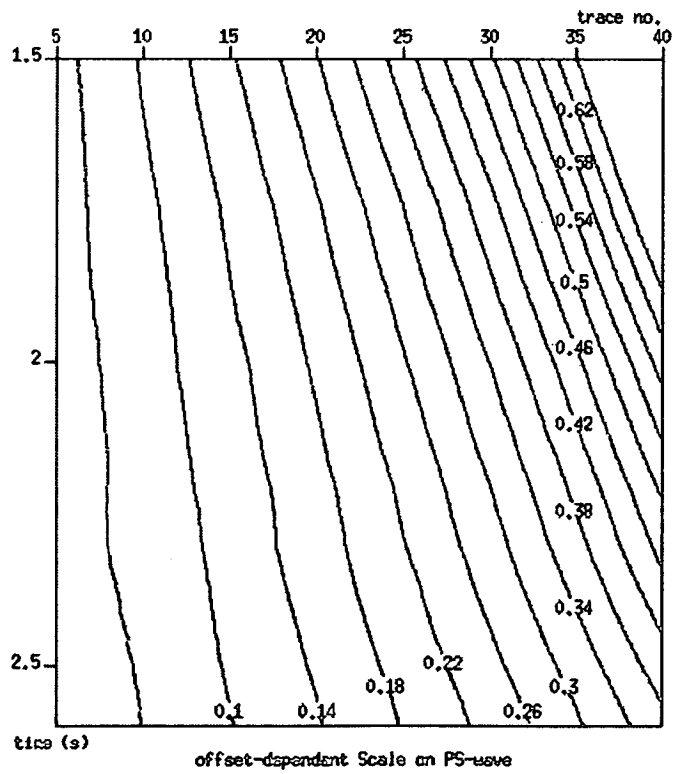

Figure 6.15: Weight W_{imp} applied to PS-data in joint inversion

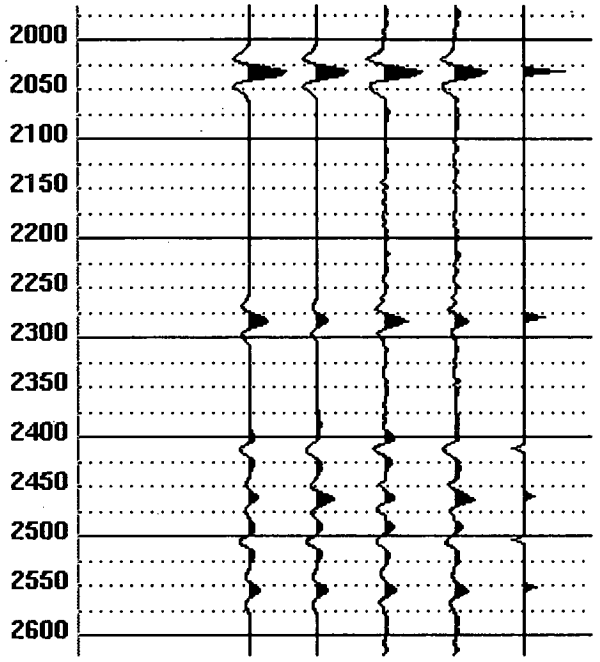

(a) P-impedance

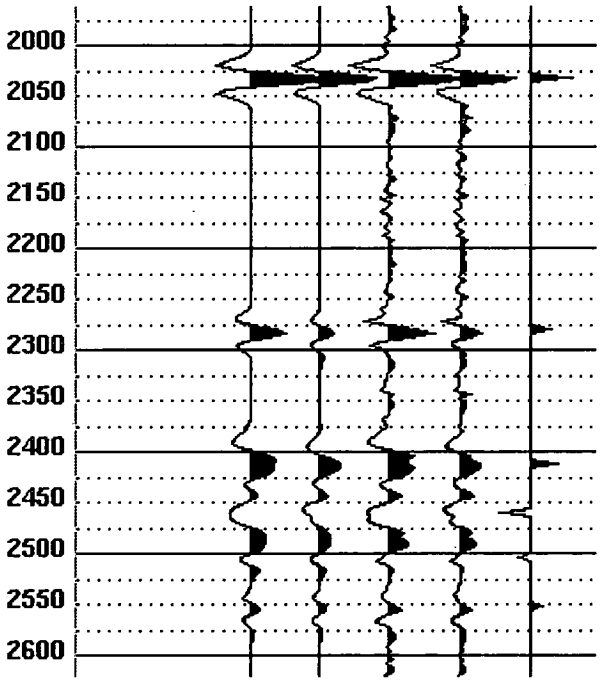

(b) S-impedance

Figure 6.16: The 1st trace in each diagram is PP-alone inversion for noise-free data, and the 2nd trace is joint inversion for noise-free data; The 3rd trace is for PP-alone with S/N=8, and the 4th trace for joint inversion with S/N=8;The 5th trace is the real P or S-impedance reflectivity coefficient.

In summary, for S-impedance estimation from noise free synthetic data, PS-inversion alone gives the best result, while for P-impedance, PP-data alone and joint method lead to a similar result. Joint inversion improves the S-impedance accuracy compared to PP-data alone, especially when noise is present in data. This joint method is a full use of Aki-Richard equation; two parameters are inverted instead of three (including density item) and more stable than an inversion for three parameters. In the meantime, the density effect is also factored into the inversion without any further assumptions.

6.3 Offset-dependent tuning effect on AVO

In the study area of the Ordos basin, the Permian formations are composed of many interbedded thin sandstone and shale layers. The H8 gas layers are usually less than 10 meters thick, which is far less than the tuning thickness (around 33m) if a dominant frequency is 30Hz and the interval velocity is 4000m/s. Chung and Lawton (1990) investigate the offset-dependent tuning effect on a single low-velocity thin layer embedded in a homogeneous thick layer, and illustrate the offset-dependent tuning effect has an adverse effect on PP-AVO, but an enhanced effect on PS-AVO signature.

Here I investigate the offset-dependent tuning effect on two thin layers embedded in a homogeneous thick layer. Two different models each consisting of two thick layers and two 10 m thick beds are shown in Table 6.5 for simulating the geology of the gas layer and its surrounding layers in the study area. Model 1 has a small P-wave impedance contrast between the gas layer and the upper layer, representing a class II AVO; and Model 2 has a larger P-wave impedance contrast representing a class III AVO. Models 1a and 2a are for investigating the AVO effect without the tuning effect. The gas layer's Poisson's ratio is set to 0.15 for gas fill and 0.25 for brine. Models 1b and 2b are for investigating how the tuning affects AVO.

Thickness (m)	V_p (m/s)	ρ (g/cc)	σ
3177	4360	2.38	0.25
300	4191	2.44	0.25/0.15

(a) Model 1a

Thickness (m)	V_p (m/s)	ρ (g/cc)	σ
3167	4534	2.64	0.25
10	4360	2.38	0.25
10	4191	2.44	0.25/0.15
290	4534	2.64	0.25

(b) Model 1b

Thickness (m)	V_p (m/s)	ρ (g/cc)	σ
3177	4486	2.58	0.25
300	4143	2.40	0.25/0.15

(c) Model 2a

Thickness (m)	V_p (m/s)	ρ (g/cc)	σ
3167	4577	2.59	0.25
10	4486	2.58	0.25
10	4143	2.40	0.25/0.15
290	4577	2.59	0.25

(d) Model 2b

Table 6.5: Model 1 with a weak P-impedance contrast and Model 2 with a large P-impedance contrast between two thin layers

PP- and PS-wave shot gathers for each model are generated with a 25Hz zero-phased Ricker wavelet. The offsets spread from 0 to 4000 m with 100 m interval. For this geometry and the model parameters, there are no traces beyond critical angles.

Figure 6.17 and 6.18 show the PP and PS-seismograms of Model 1. Transmission losses, multiple reflections, and spherical divergence are neglected.

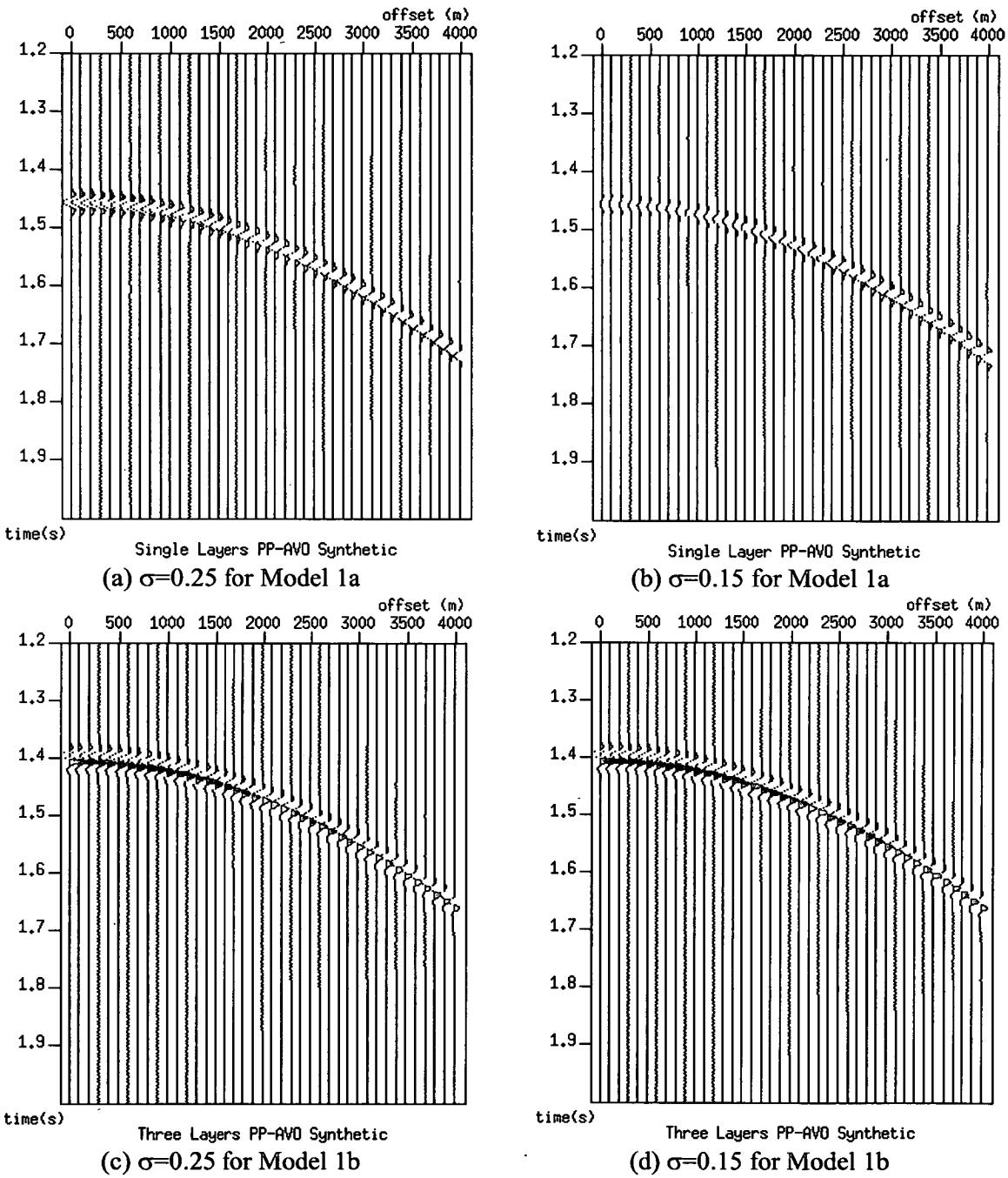

(a) σ=0.25 for Model 1a

(b) σ=0.15 for Model 1a

(c) σ=0.25 for Model 1b

(d) σ=0.15 for Model 1b

Figure 6.17: PP synthetic shot gathers for Model 1

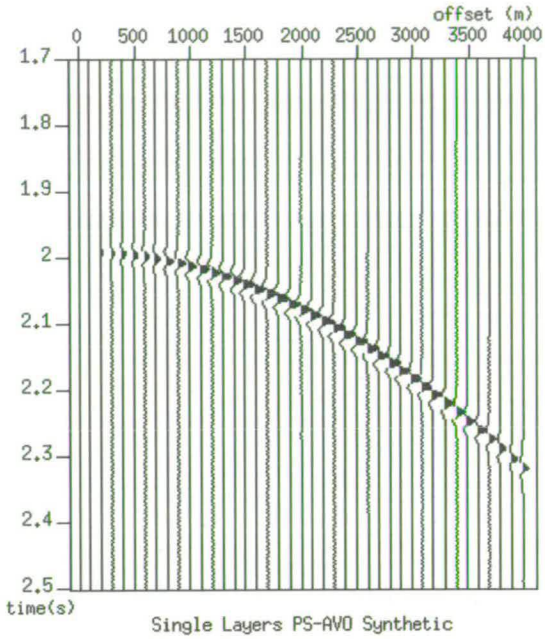

(a) σ=0.25 for Model 1a

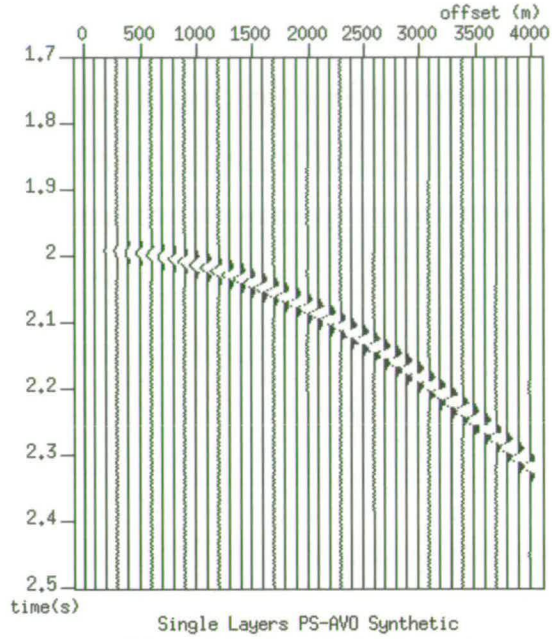

(b) σ=0.15 for Model 1a

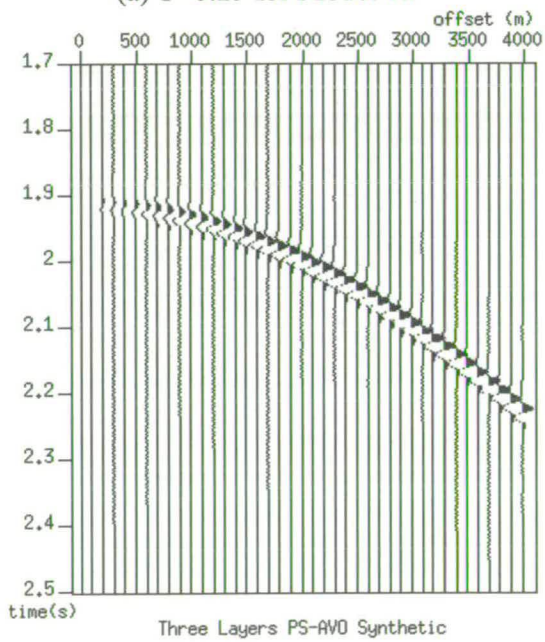

(c) σ=0.25 for Model 1b

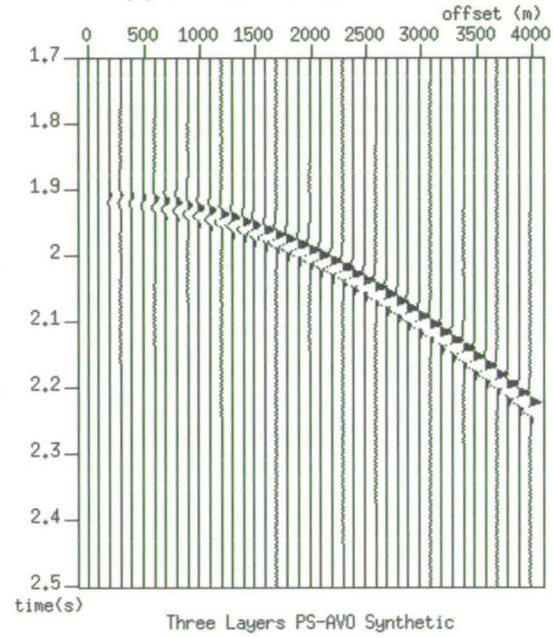

(d) σ=0.15 for Model 1b

Figure 6.18: PS-synthetic shot gathers for Model 1

Figure 6.19a shows the picked maximum amplitude from the seismograms shown in Figure 6.17 for PP-wave. The amplitude change rate between brine fill (σ=0.25) and gas fill (σ=0.15) is calculated by Equation 6-25, and plotted in Figure 6.19b.

$$changerate = \left| \frac{amp_{\sigma=0.25} - amp_{\sigma=0.15}}{amp_{\sigma=0.25}} \right| \times 100\%. \qquad (6\text{-}25)$$

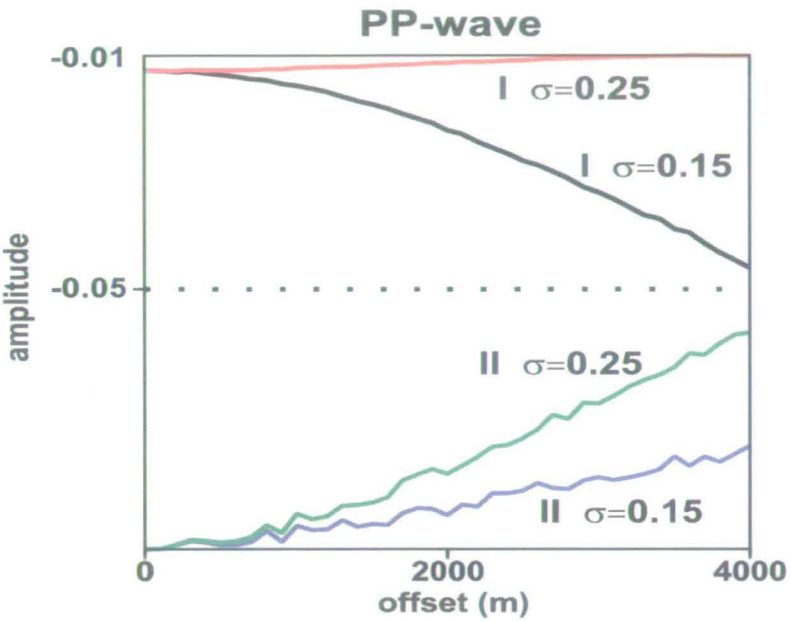

(a) Picked amplitude for PP-wave of Model 1; I stands for the single interface of Model 1a, II for the two thin layers model with tuning of Model 1b.

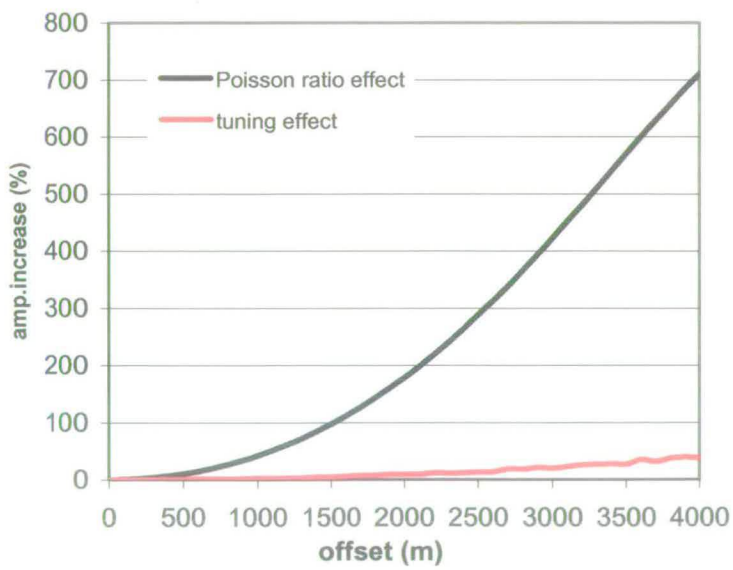

(b) Amplitude increase rate from σ=0.25 to σ=0.15 with or without tuning effect

Figure 6.19: Effect of Poisson's ratio and tuning on PP-wave for Model 1.

Figure 6.19 shows that for Poisson's ratio 0.15 in PP-wave data, the offset-dependent tuning effect cancels the class II AVO trend which exits in the single interface. In fact, the amplitude decreases with offset, and the normal incidence amplitude increases due to a higher P-impedance from the top layer. Compared to the large amplitude increase from Poisson's ratio 0.25 to Poisson's ratio 0.15 in Model 1a, the amplitude increase in Model 1b is very small (less than 40%), which means tuning has a dramatic adverse effect on this model.

Figure 6.20 shows that for Poisson's ratio 0.15 in PS-wave data, the offset-dependent tuning effect enhances the amplitude-increasing trend. When Poisson's ratio changes from 0.25 to 0.15 in Model 1a, the polarity of the PS-wave is reversed, the change in amplitude is huge (ranging from 600% at near offset to 1400% at far offset). However, when tuning is present, the amplitude decrease is just about 30%, and the change trend is fairly flat from the near to far offsets. From the analysis of Model 1, the tuning effect has a significant adverse influence on both PP-and PS-waves.

A similar analysis has been carried out for Model 2 (Table 6.5c and 6.5d). It is interesting that the tuning effect on Model 2 differs significantly from Model 1. For Model 2, the tuning effect causes a small amplitude change (less than 20%) on both PP- and PS-waves (Figures 6.21 and 6.22). For both Model 1 and Model 2, the tuning effect makes the class II (Model 1) and class III (Model 2) PP-AVO signature disappear.

We can also observe that for Model 2, both the Poisons' ratio effect and tuning effect increase with the offsets for PP-wave, and decrease with the offsets for PS-wave.

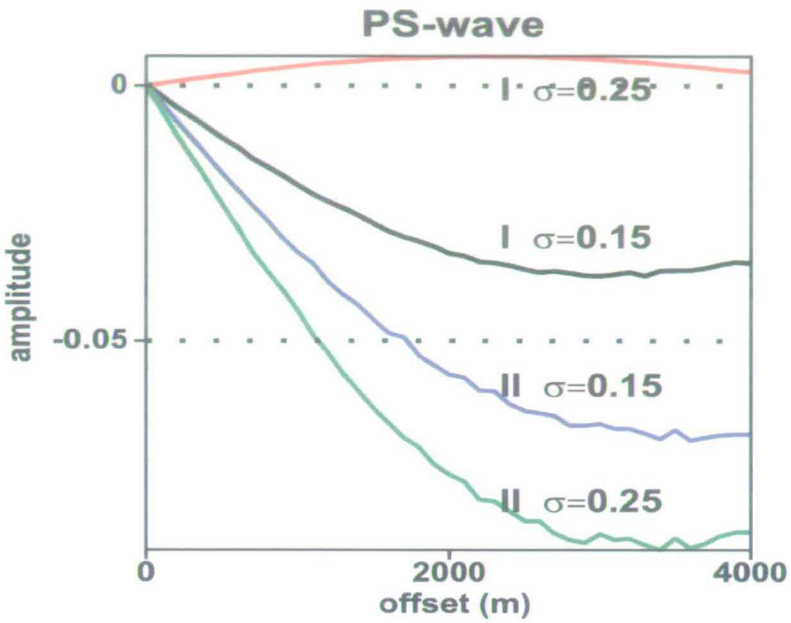

(a) Picked amplitude for PS-wave of Model 1; I stands for the single interface, II for the two thin layers model with tuning

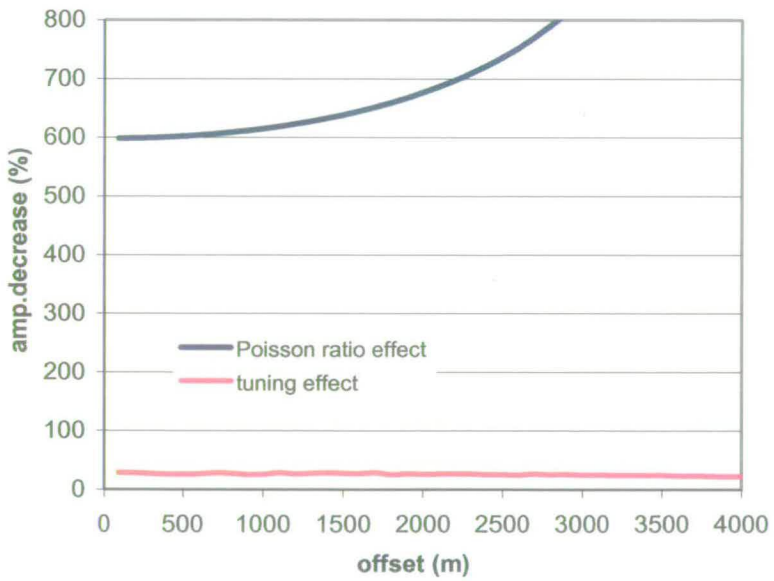

(b) Amplitude decrease rate from σ=0.25 to σ=0.15 with or without tuning effect

Figure 6.20: Effect of Poisson's ratio and tuning on PS-wave for Model 1

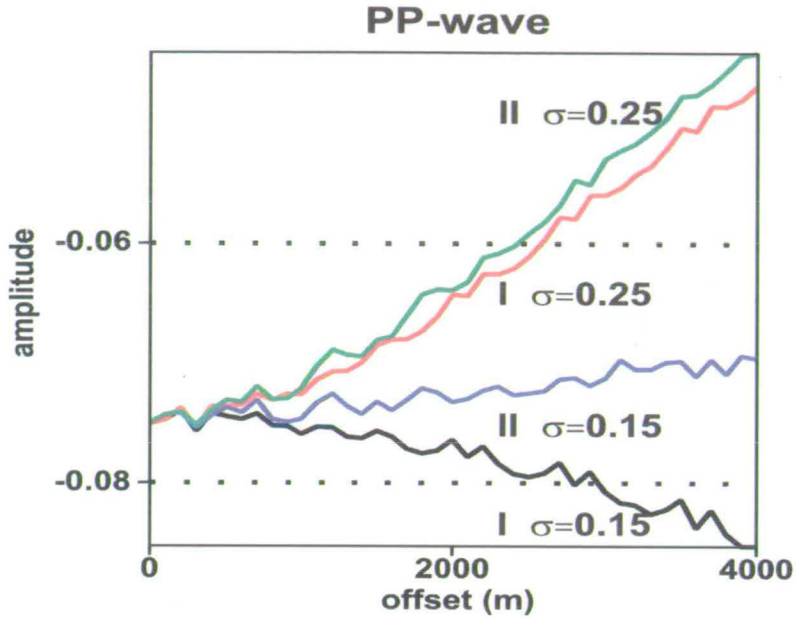

(a) Picked amplitude value for PP-wave of Model 2; I for single interface, II for two thin layers with tuning

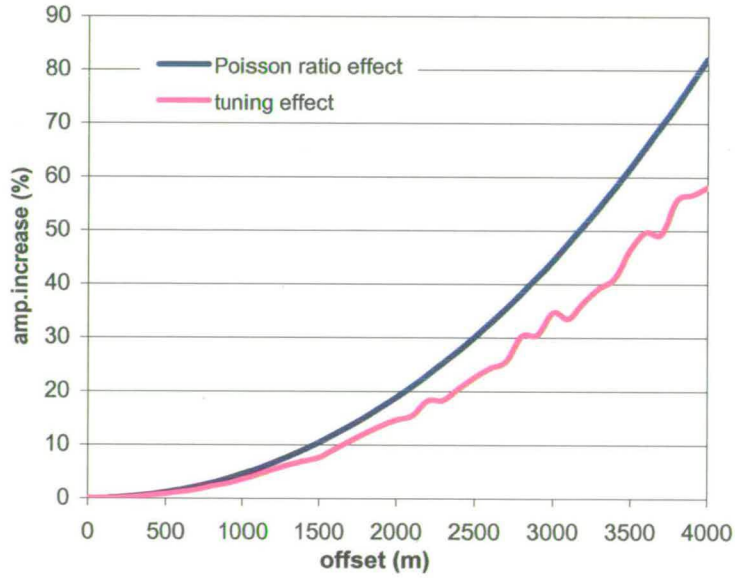

(b) Amplitude increase rate from σ=0.25 to σ=0.15 with or without tuning effect

Figure 6.21: Effect of Poisson's ratio and tuning on PP-wave for Model 2.

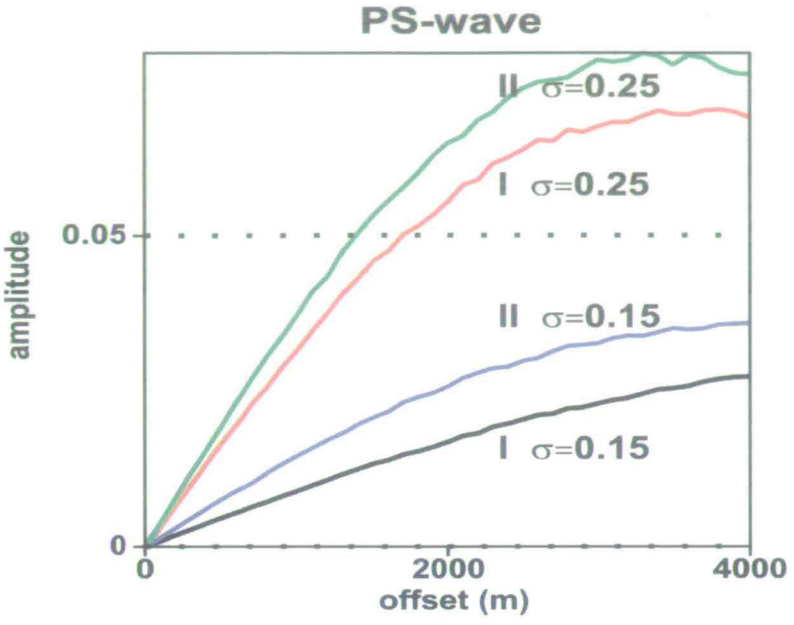

(a) Picked amplitude value for PS-wave of Model 2; I for single interface, II for two thin layers with tuning

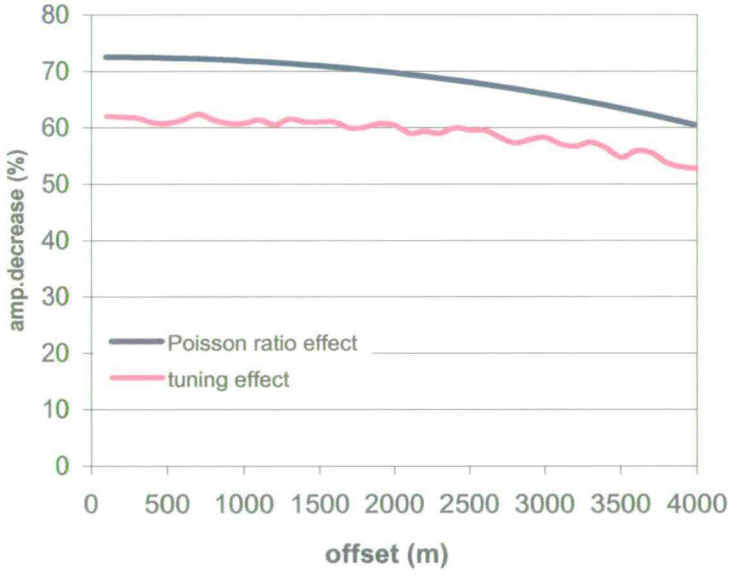

(b) Amplitude decrease rate from σ=0.25 to σ=0.15 with or without tuning effect

Figure 6.22 Effect of Poisson's ratio and tuning on PS-wave for Model 2.

The Pseudo Poisson's ratio reflectivity is calculated by a joint inversion of P- and S-impedance reflectivity for both Model 1b and Model 2b. A clear trough associated with the gas top can be seen when Poisson's ratio is 0.15 in Figure 6.23, which does not appear when Poisson's ratio is 0.25.

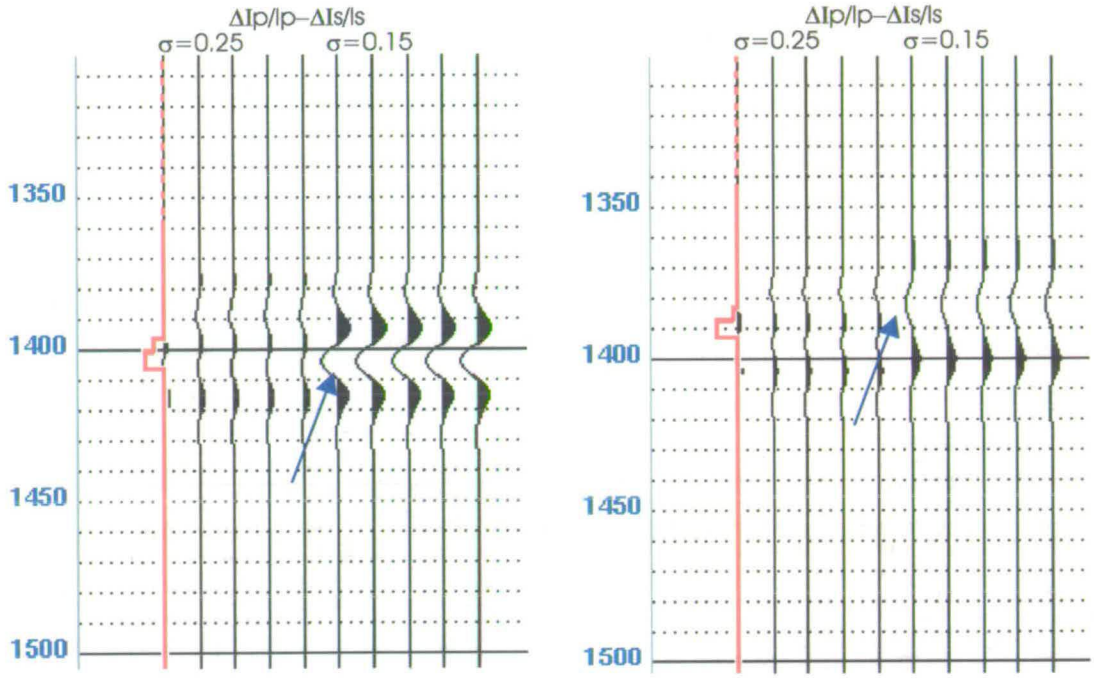

Figure 6.23 Pseudo Poission's ratio reflectivity of Model 1b(left) and Model 2b (right), Red line is P-wave velocity.

6.4 Data application

The method of joint AVO inversion of PP- and PS-data described in the previous sections is tested on the 3C-2D seismic data acquired in the Ordos basin. The logs of Well S6 are blocked, where a low P-velocity and density sand layer (around 3320m) in the Permian has a very good gas production (Figure 6.24). In order to predict how the fluid content affects the elastic parameters, brine fill and gas fill cases are analyzed in Table 6.6. For both cases, the elastic parameters I_p, I_s, $\lambda\rho$, $\mu\rho$, λ, and μ decrease from the cap rock to the sand. The magnitude of the decrease between the shaly sand and the gas reservoir in Table 6.6b is larger than

between the shaly sand and brine case in Table 6.6a. Among these elastic parameters, $\lambda\rho$ and λ are more sensitive than the impedance. Compared to a larger average change in $\mu\rho$ for the gas case, μ keeps a similar value since the density effect is removed from $\mu\rho$, and the gas sand has a similar rigidity with the wet sand.

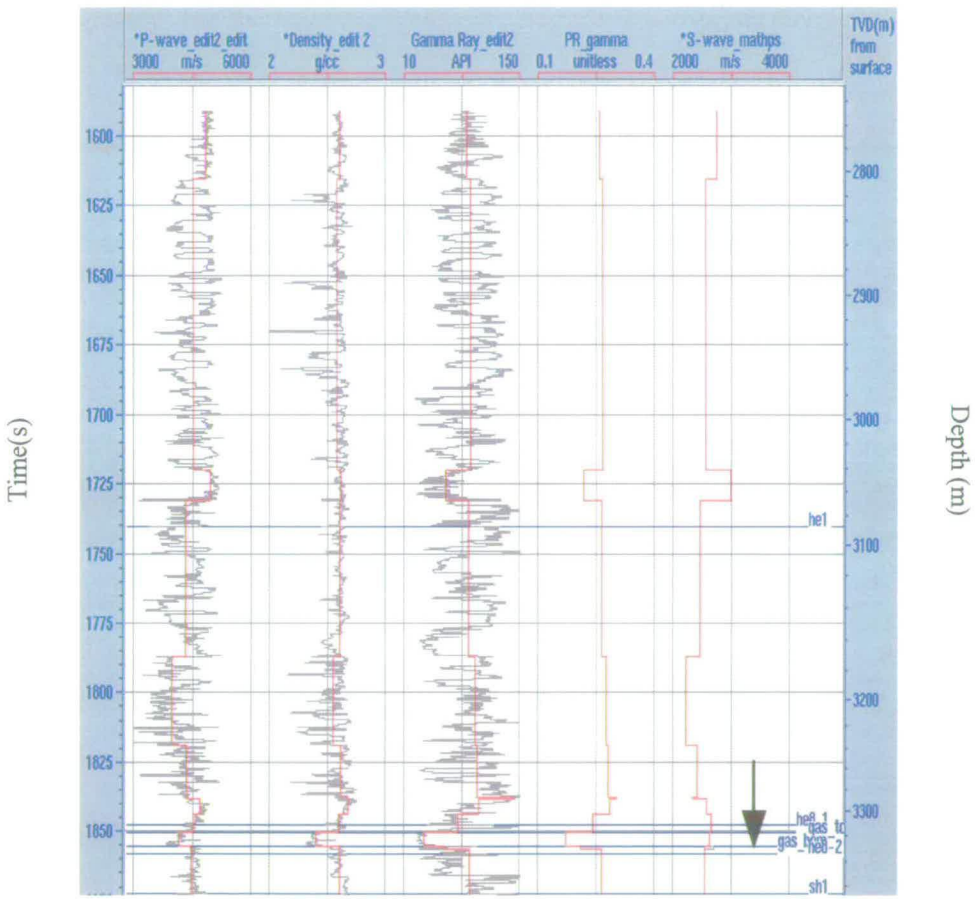

Figure 6.24: Blocked logs of the gas well S6. The parameters are used to build the velocity and depth model, the arrow indicating the gas zone.

	Ip (m/s *g/cc)	Is (m/s *g/cc)	λρ (GPa*g/cc)	λ (GPa)	μρ (GPa*g/cc)	μ (GPa)
Shaly sand	11636	6807	42.7	16.6	46.3	17.9
Wet sand	10699	6367	33.4	13.4	40.5	16.3
Ave change	8.4%	6.6%	24%	21%	14%	9%

Table 6.6a: Impedance, Lamè constants average change in brine water sand case

	Ip (m/s *g/cc)	Is (m/s *g/cc)	λρ (GPa*g/cc)	λ (GPa)	μρ (GPa*g/cc)	μ (GPa)
Shaly sand	11636	6807	42.7	16.6	46.3	17.9
Gas sand	9912	6250	20.1	8.4	39.1	16.3
Ave change	16%	8.5%	72%	65%	16%	9%

Table 6.6b: Impedance, Lamè constants average change in gas sand case

The elastic parameters from the blocked well logs are used to produce the synthetics shown in Figure 6.25. PS-wave data are correlated with PP-wave data in PP-time. Although PS-data are commonly observed to have the half bandwidth of PP-data in land acquisition, the amplitude analysis shows that the PP-data has a bandwidth 8-40Hz, and for PS-data of 8-30Hz. PS-data have a similar resolution as PP-data.

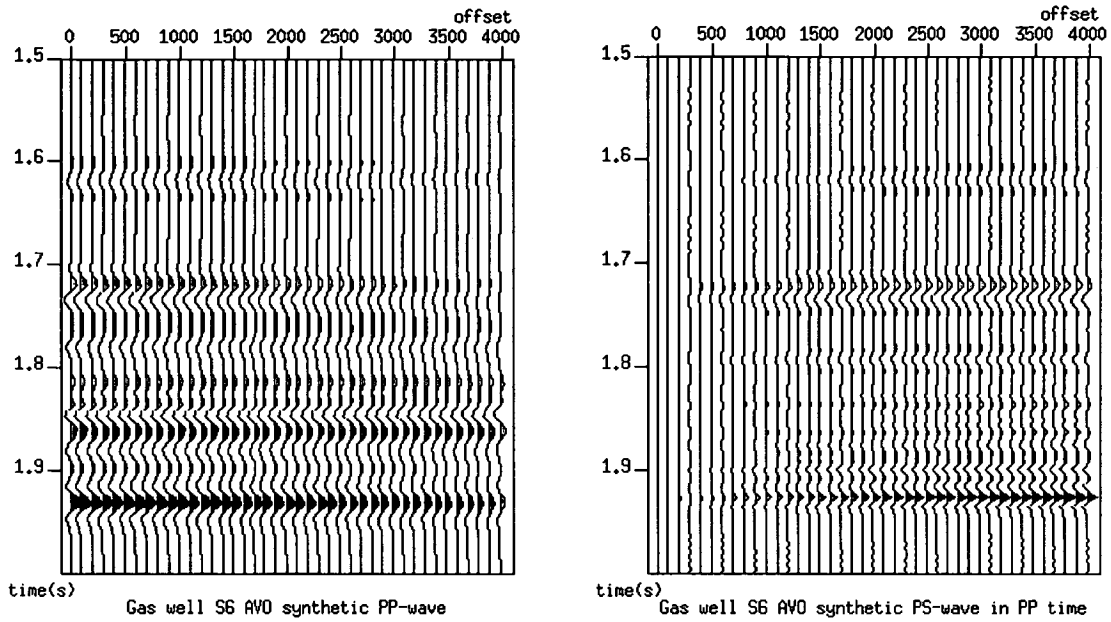

Figure 6.25: Synthetic seismogram of PP-data and PS-data

Figure 6.26 shows P- and S-impedance reflectivity from the joint inversion for synthetic data. P-impedance has a more obvious change from wet case to gas case than S-impedance. The $\lambda\rho$ reflectivity calculated from the impedance reflectivity is shown in Figure 6.27a, where V_p/V_s is assumed as 2. λ reflectivity from the joint inversion directly is shown in Figure 6.27b. Compared to the impedance reflectivity, $\lambda\rho$ and λ reflectivity have a better result due to a clear contrast between the wet case and gas case. λ reflectivity has the best data quality since it has the same noise level as the impedance, while $\lambda\rho$ value is calculated from impedance, and errors can accumulate.

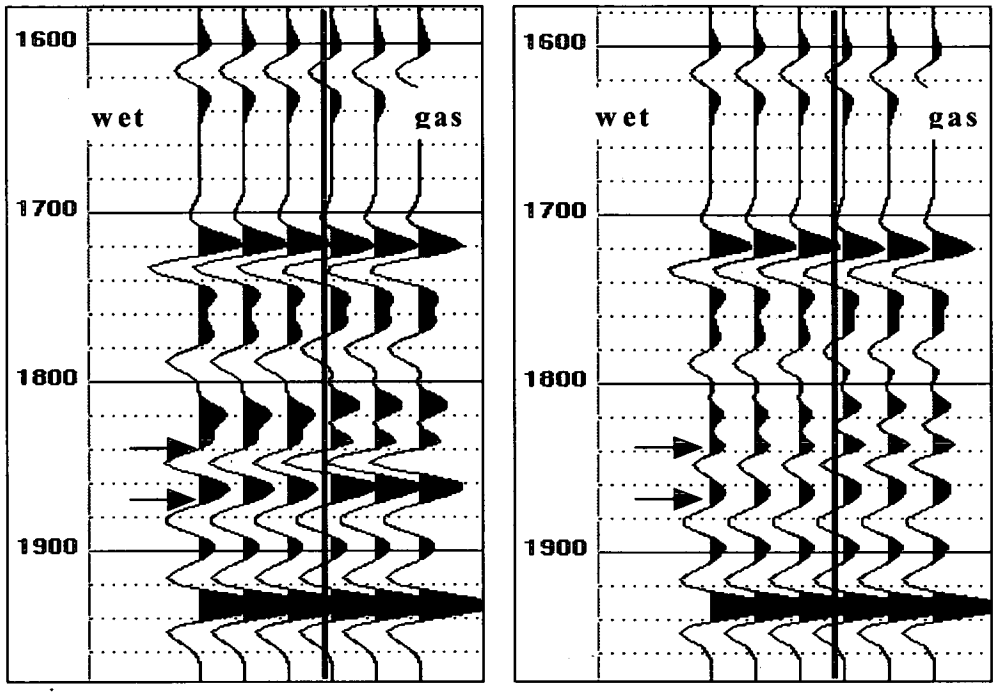

(a) P- impedance reflectivity (b) S-impedance reflectivity

Figure 6.26: Joint inversions for the elastic impedance. The first 3 traces are for the wet case and the last 3 traces for the gas case. The target top and base are indicated by arrow.

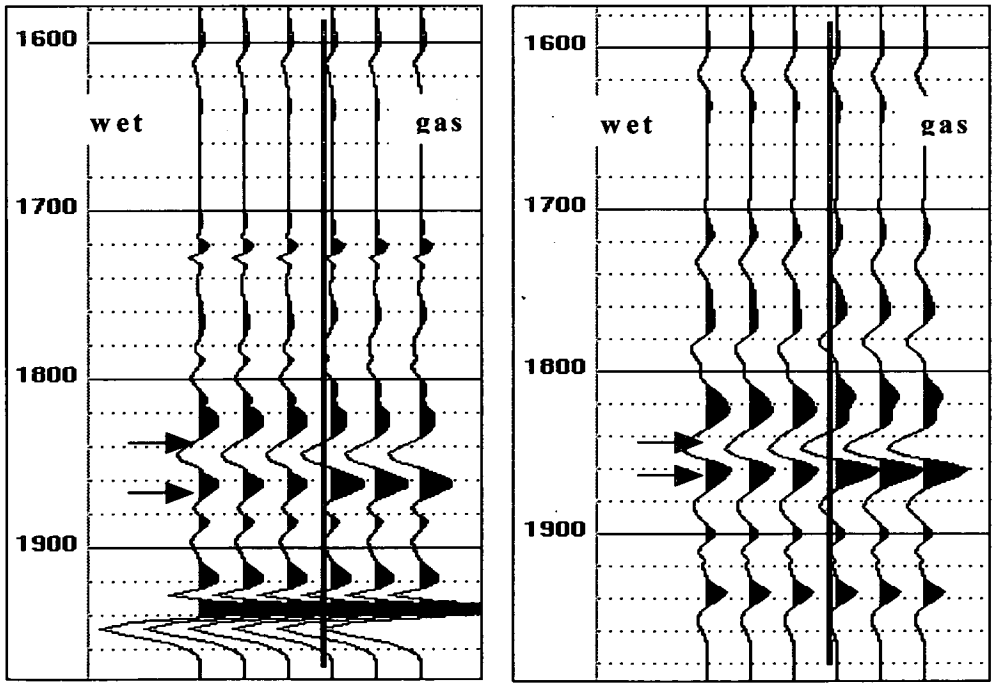

(a) $\lambda\rho$ reflectivity (b) λ reflectivity

Figure 6.27: $\lambda\rho$ reflectivity from joint impedance inversion and λ reflectivity. The first 3 traces are for the wet case and the last 3 traces for the gas case. The target top and base are indicated by arrow.

For the joint inversion of PP- and PS-data, event correlation is one of the practical difficulties, which means the PP-data and PS data used in the joint inversion should be from the same reflection points. Ideally, a pre-stack depth migration should be performed in both PP- and PS-data using correct P- and S-velocity. This would collapse Fresnel zones and build the event correlations automatically. However, this requires an intensive computation, therefore a pre-stack time migration is performed and common-image gathers (Figure 6.28) of PP- and PS-data are used. CIP gathers have the advantage that they represent the same subsurface location for PP- and PS-data, the imaging is usually better than CDP gather. Migrated sections for PP- and PS-wave are shown in Figure 6.29; event correlation is performed between the two images. In order to compare the inversion results, both joint data inversion and PP-data inversion are performed on the real data.

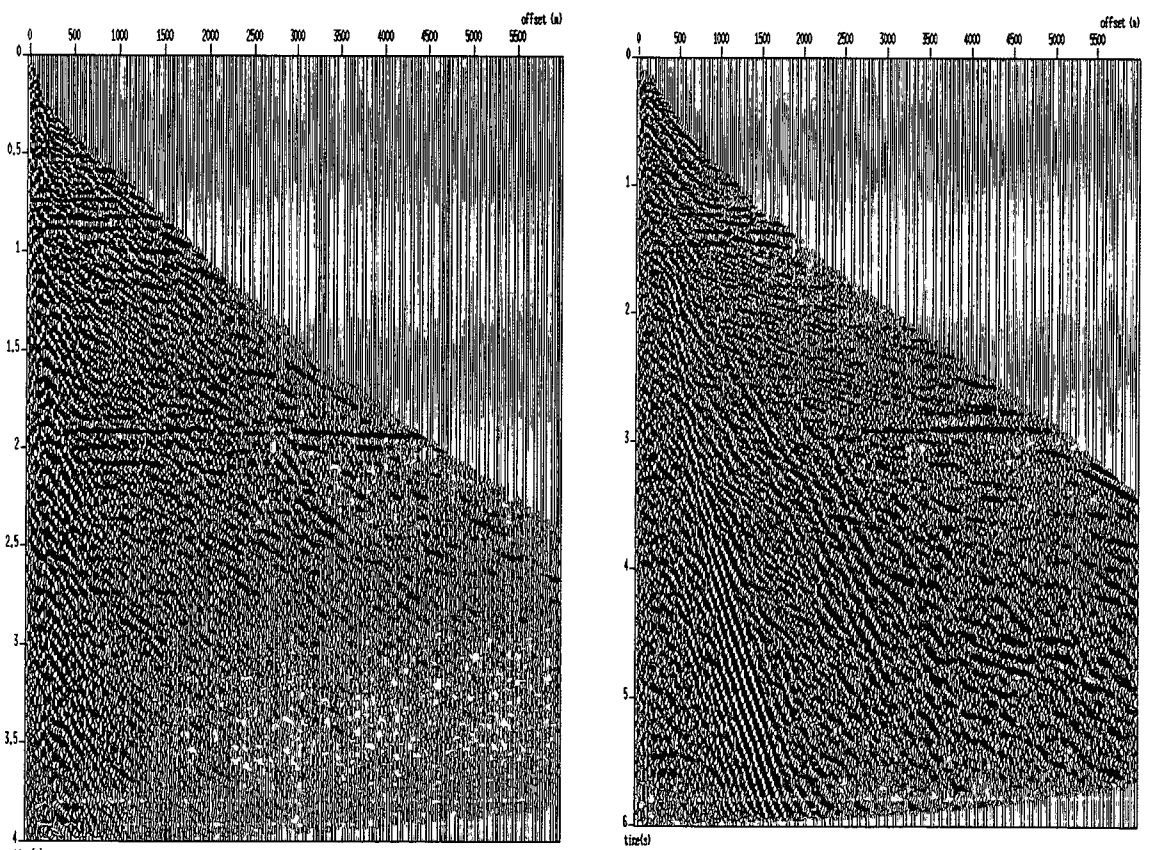

CIP gather for PP-data CIP gather for PS-data

Figure 6.28: Common image point gathers at the gas well S6.

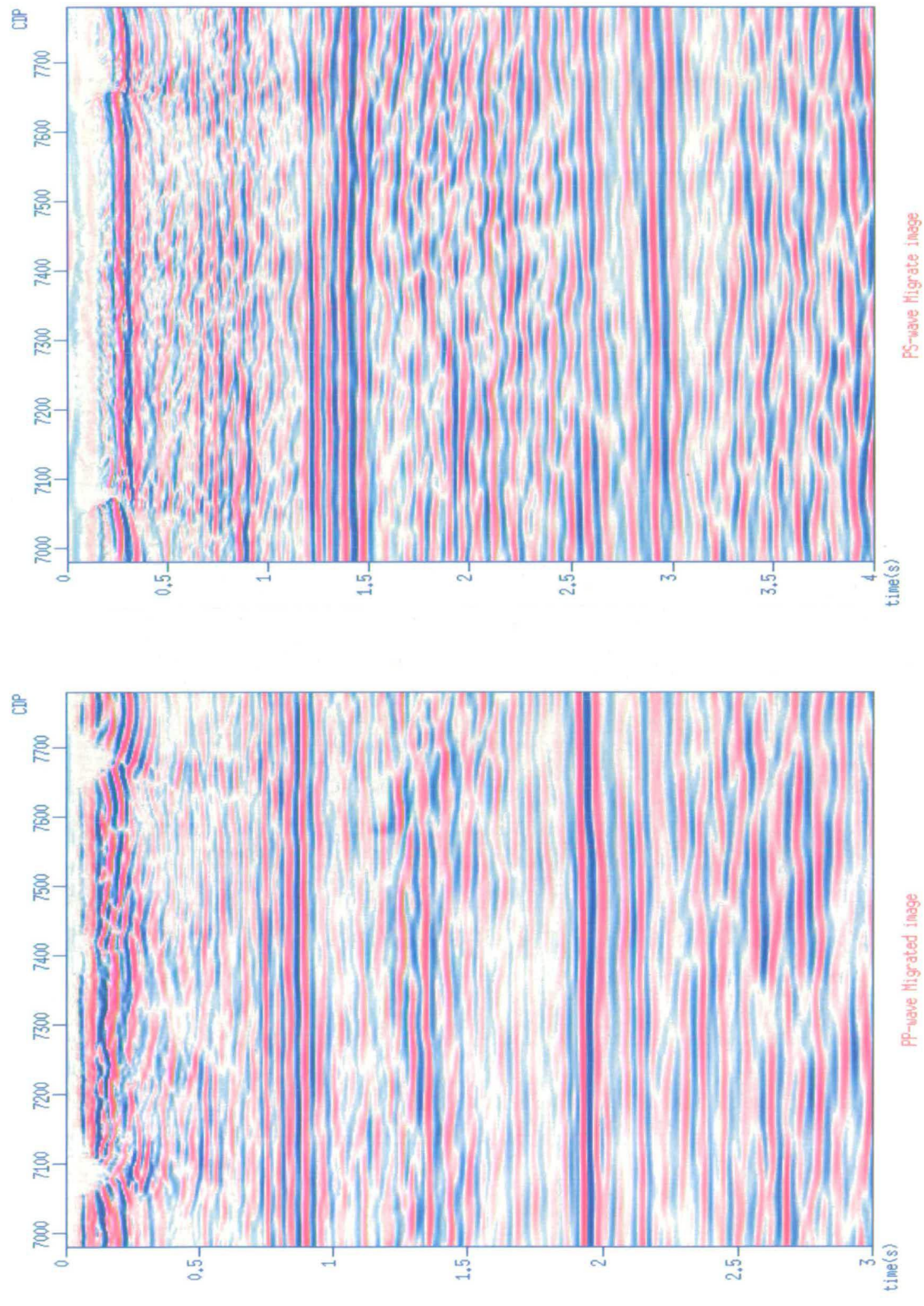

Figure 6.29: Final migrated image of PP- and PS-data

Figures 6.30a and 6.30b show the P-impedance reflectivity from PP-data alone and from joint inversion, respectively. Both PP data alone and joint inversion give a similar result. The negative value zone (red colour indicated by the arrow) calibrated by Well S6 as gas sand is shown on both the sections.

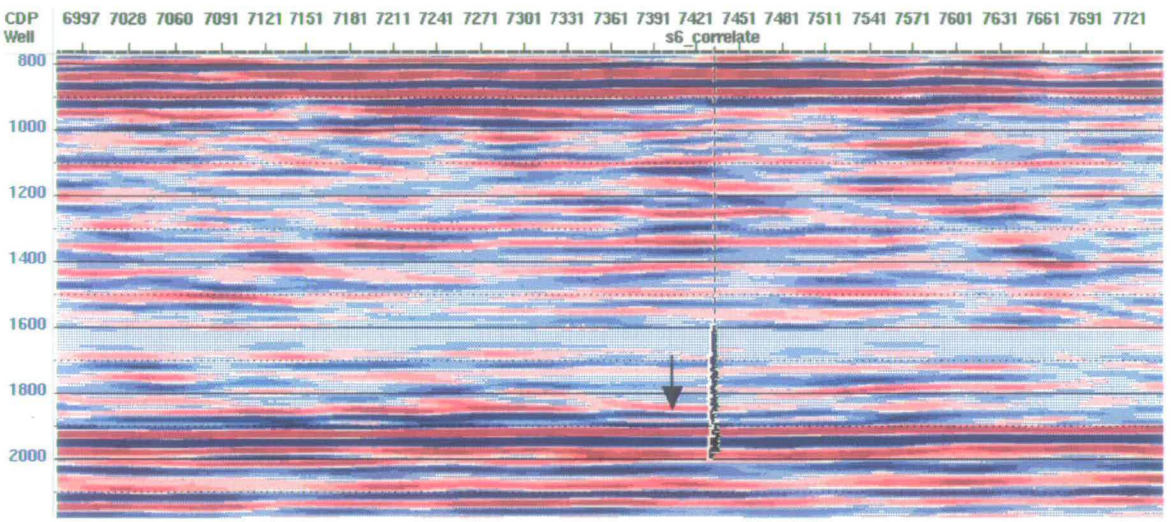

(a) P-impedance reflectivity from PP-data inversion

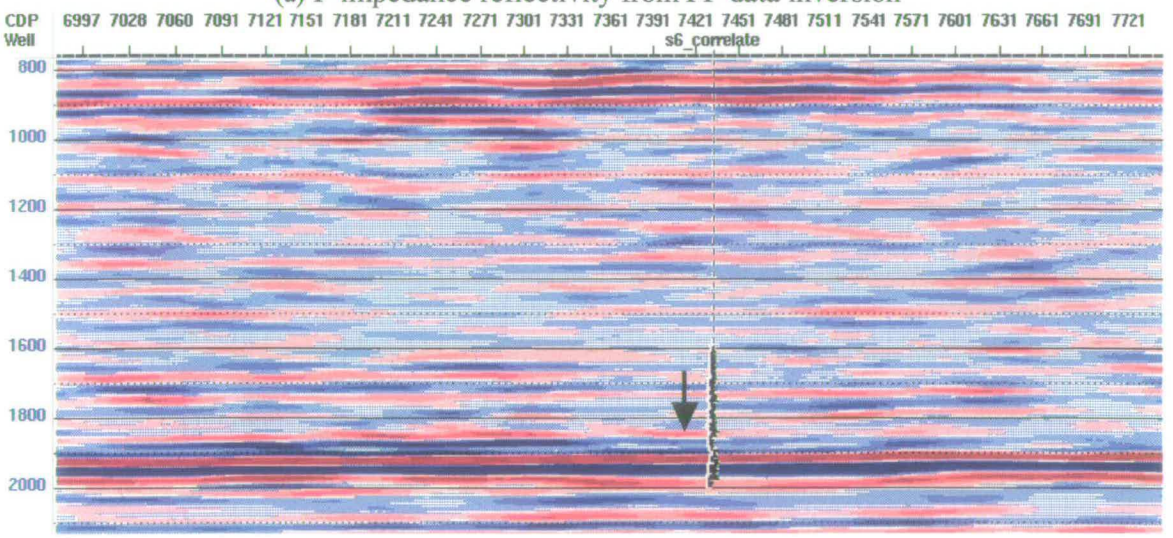

(b) P-impedance reflectivity from joint inversion

Figure 6.30: P-impedance reflectivity from PP-data alone and both PP- and PS-data, the inserted curve is Gamma log. Negative value in red color indicated by arrow is calibrated as the gas sand.

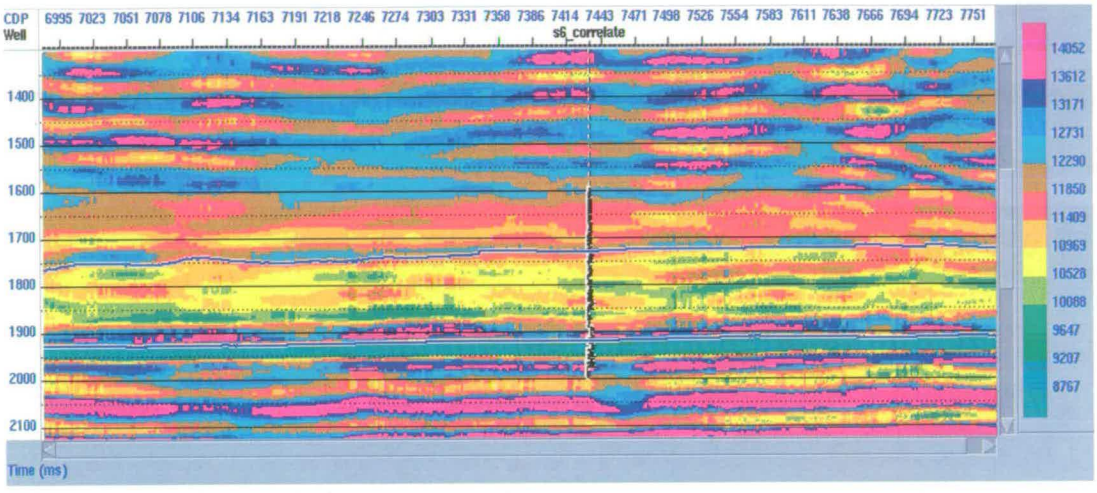

(a) P-impedance estimated from the P-reflectivity in Figure 6.30a

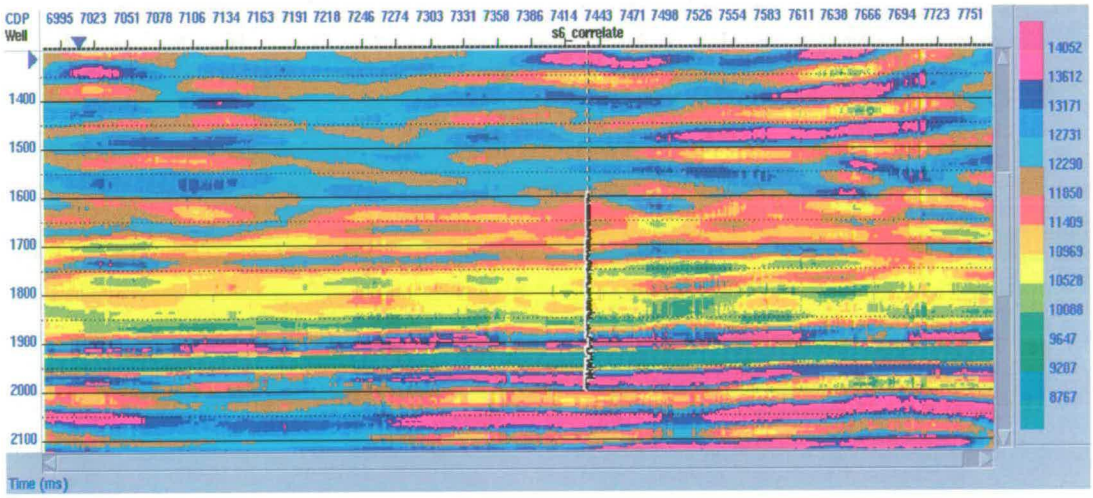

(b) P-impedance estimated from the P-reflectivity in Figure 6.30b

Figure 6.31: model-based inversions for P-impedance.

Figures 6.31a and 6.31b show the absolute P-impedance value inverted from the reflectivity by model-based inversion. The low P-impedance for gas zone is shown on both sections.

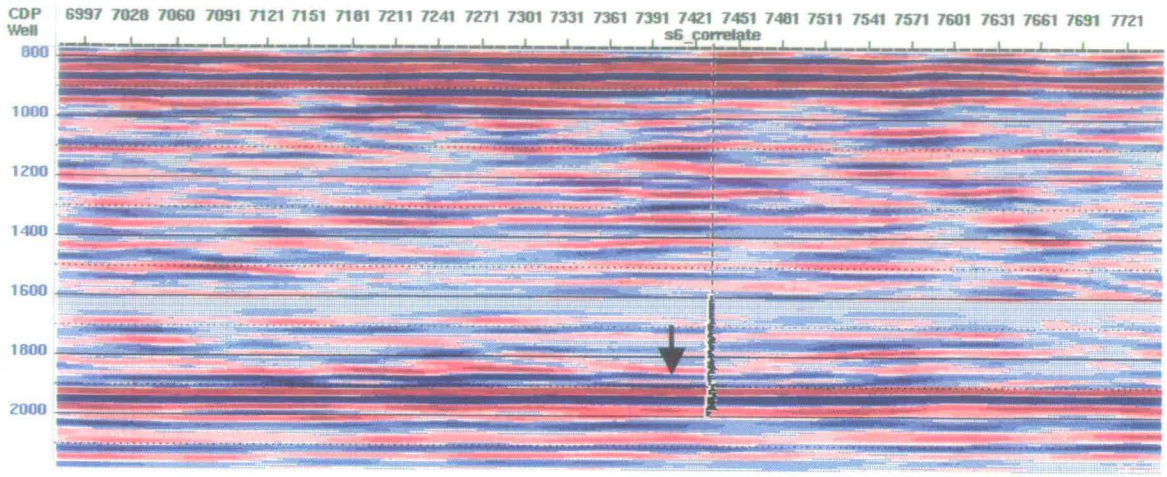

(a) S-impedance reflectivity from PP-data inversion

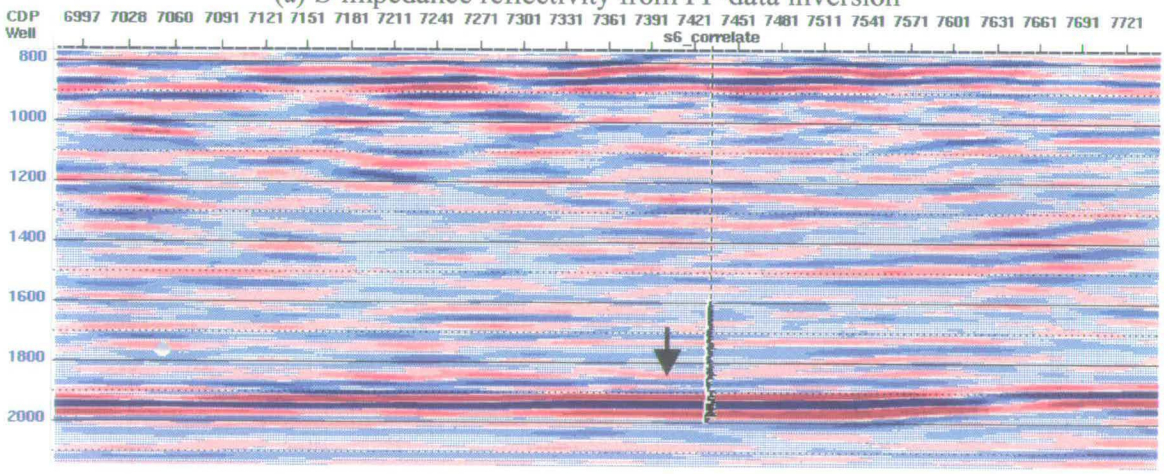

(b) S-impedance reflectivity from joint data inversion

Figure 6.32: S-impedance reflectivity from PP-data alone (a) and joint data (b), the inserted curve is Gamma log. Negative value in red color indicated by arrow is calibrated as the gas sand.

Figure 6.32 shows the S-impedance reflectivity from PP-data and joint data, respectively. S-reflectivity from PP-data alone in Figure 6.32a shows a strong similarity with the P-reflectivity in Figure 6.30a. From joint inversion, a weak S-impedance contrast is shown near the gas well, which is consistent with Table 6 and the synthetic data in Figure 6.26, where S-impedance reflectivity is smaller than P-impedance reflectivity. Figure 6.33 is the model-based inversion for S-impedance.

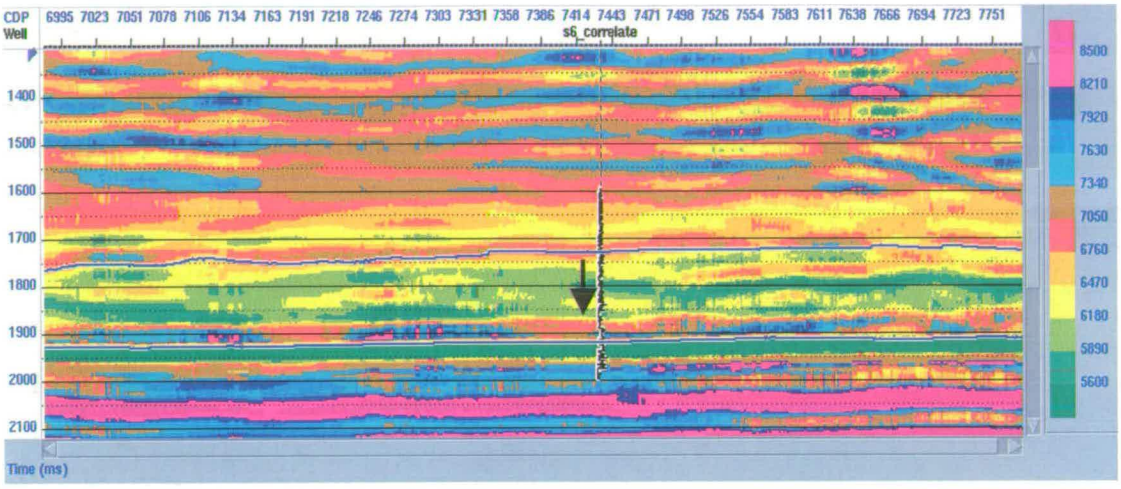

(a) S-impedance estimated from the S-reflectivity in Figure 6.32a

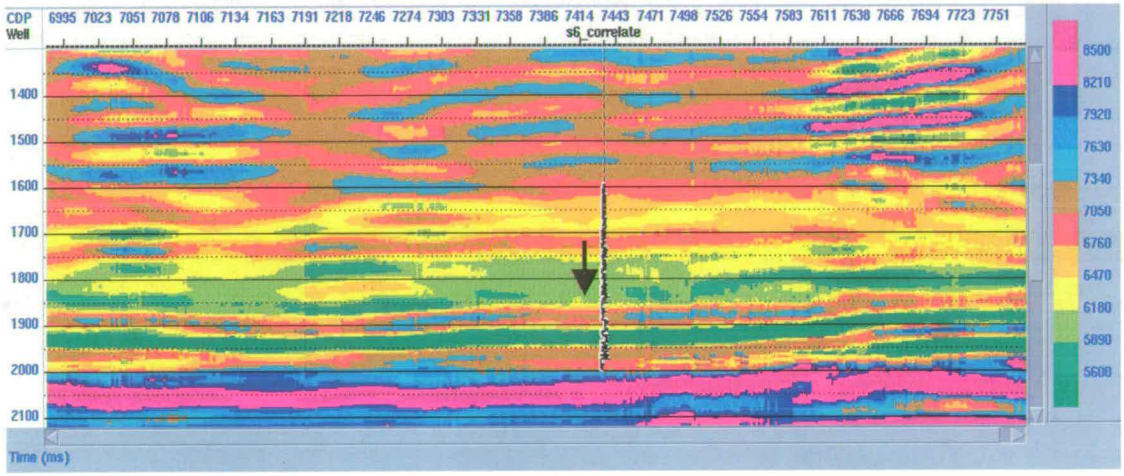

(b) S-impedance estimated from the S-reflectivity in Figure 6.32b

Figure 6.33: model-based inversion for S-impedance.

Figure 6.34 is $\lambda\rho$ from PP-data and from joint data inversion, a clear low value $\lambda\rho$ zone (black circle) appears in joint inversion section, which is not shown on PP-inversion section.

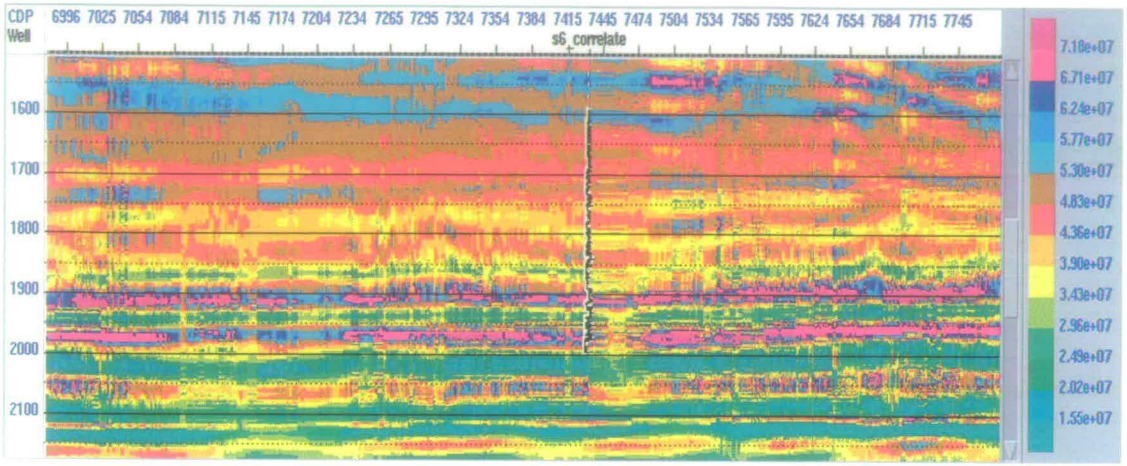

(a) $\lambda\rho$ estimated from PP-data

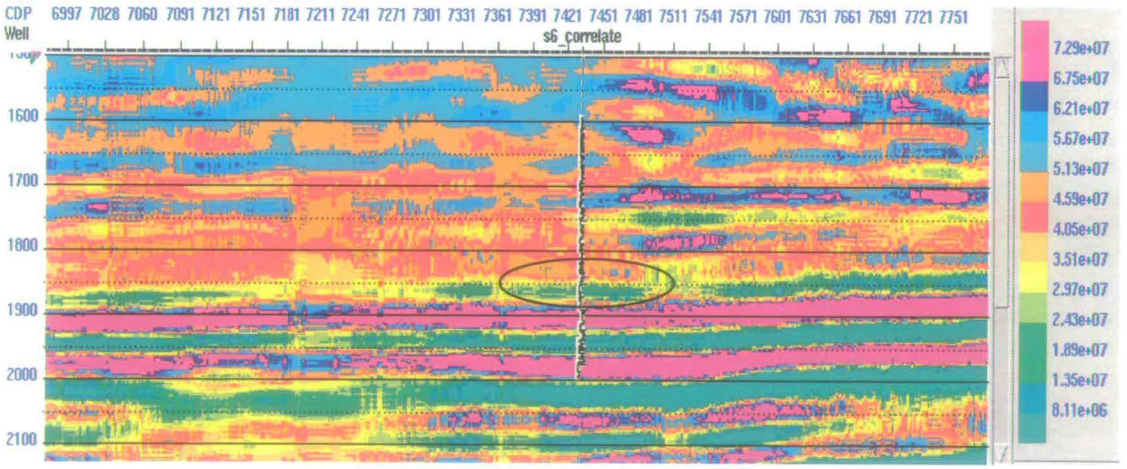

(b) $\lambda\rho$ estimated from joint data

Figure 6.34: $\lambda\rho$ from both PP- and joint-inversion

6.5 Conclusions

A joint PP- and PS-AVO inversion algorithm is developed and tested on both model and real data. It can overcome the problem that traditional AVO intercept and gradient analysis cannot determine an AVO anomaly due to a class II AVO type of gas sand in the study area of the Ordos basin, China. This is one of the first such multi-component AVO projects in this area. The combination of the different data modes is beneficial for supporting gas sand detection.

A model study reveals that joint inversion of $\lambda\rho$ and λ reflectivity yield better results compared to impedance reflectivity; λ reflectivity has the best data quality since it has the same noise level as the impedance; while $\lambda\rho$ values are calculated from impedance, noise may also be amplified because the impedance is squared.

Model and real data studies indicate that S-impedance inversion from PP-data alone has is accurate than that from the PS-data alone. An offset-to-depth ratio X/Z less than 1 is not enough for using PP-waves to invert S-impedance correctly. Joint inversion improves the S-impedance accuracy, especially when noise is present on data. For P-impedance, the joint inversion method has a similar accuracy to PP-data alone.

From two models simulating the local geophysical parameters, one can conclude that for low P-wave velocity thin layers embedded in a homogeneous high velocity thick layer, the tuning effect has an adverse effect on both PP- and PS-wave AVO. For the model of two 10-meter thick layers with small P-impedance contrast, the strong AVO effect caused by the decrease of Poisson's ratio is eliminated. On the other hand, for the model of two 10-meter thick layers with a large P-impedance contrast, although tuning is detrimental to the AVO effect, the tuning effect causes a small amplitude change on both PP- and PS-wave. For both models the tuning effect makes the class II and class III PP-AVO disappear.

Chapter 7: Frequency-dependent AVO for fluid detection

7.1 Introduction

Traditional AVO studies are based on pure elastic Gassmann theory. Absorption due to the presence of fluid in porous media is not taken into account by Gassmann theory, and AVO effect is treated as being frequency independent. However, either seismic scatting or intrinsic absorption can lead dispersion and attenuation of seismic waves. In this chapter, frequency-dependent AVO is demonstrated through numerical modeling, which considers dispersion during fluid-substitution. In the following chapter, a physical modeling dataset will be used to further verify the findings in this chapter.

Due to increasing path length with offset, overburden attenuation influences seismic amplitude variation with offset. The most significant intrinsic attenuation in overburdens typically results from poor consolidation or partial gas saturation (Castagna *et al.*, 1993). Although the attenuation effect is to be subtle due to small variations in target zone path length with offset, extremely high attenuation in gas reservoirs has been observed on both VSP and surface seismic data. Taner *et al.* (1979) have observed a shift toward lower frequencies on reflections from reflectors below gas sands, condensate, and oil reservoirs, though there was no good understanding for the mechanism. Kan *et al.* (1983) have shown the quality factor Q is frequency dependent in broadband VSP data. Castagna *et al.* (1993) show a strong high attenuation related to a known gas reservoir in VSP data, which is consistent with laboratory observations.

The apparent correlation between attenuation and the saturating fluid suggests that we should model the phenomenon based on mechanisms in which the fluid plays a

key role. The squirt-flow mechanism (Mavko and Nur, 1979), with its modern development (Chapman *et al.*, 2002, 2006) appears to be a reasonable candidate mechanism. I have performed numerical modeling of reflection data, based on the squirt-flow concept which gives rise to fluid-sensitive dispersion and attenuation. Chapman *et al.* (2005, 2006) argue that in many cases the dominant wave propagation effect of the change in fluids lay in the frequency dependence of the reflection coefficient. The reflections arise because of a contrast in the elastic properties, and in the dispersive case, due to frequency-dependent velocity, this contrast is frequency dependent. Hydrocarbon saturation gives rise to increased attenuation, and through the Kramers-Kronig relation this is associated with increased dispersion, implying that the reflection coefficient from hydrocarbon saturated layers is more frequency dependent. This leads to the suggestion that reflections from hydrocarbon reservoirs should often have anomalous frequency characteristics, the details of which depend on the AVO behaviour of the interface. Because of the instantaneous characteristic of reflection coefficients, spectral decomposition is an ideal tool to detect the effect of frequency-dependent variation in amplitude (Castagna *et al.*, 2003, Liu and Chapman, 2006).

Odebeatu *et al.* (2006) have shown that reflections from a hydrocarbon-saturated zone appear to display systematic frequency anomalies. In this study, these anomalies can be reproduced with synthetic modeling which is also consistent with the AVO analysis. However, it can be difficult to distinguish between spectral anomalies due to the dispersion effects and due to tuning effects without detailed information about the velocity model.

Previous studies have reported the low frequency effect (Tanner *et al.*, 1979; Castagna, 1993, 2003; and Liu *et al.*, 2006), which displays a systematic boost to the low frequencies relative to the high frequencies. These findings have been explained by Chapman *et al.* (2006) as being associated with Class III bright spots, which are expected to be particularly rich in low frequencies. In this chapter, by

contrast, I observe a high frequency effect in a reflection from a known gas reservoir. I demonstrate that the effect can be explained and modelled with the Chapman *et al.* (2006) framework. The spectral anomaly is also shown in gas saturation on the physical models of the study area, and the analysis of these data appears in the following chapter.

Tuning is an important issue in the study area (Chapter 6). Based on the log data, a multi-layer model is created with two 10m thick sand layers and four 10m thick shale layers interbedded in pure elastic overburdens and half space. The shale layer is also assumed to be purely elastic. Only the sand layers are assumed to have frequency-dependent properties. Partyka *et al.* (1999) show that the amplitude spectrum interference pattern from a tuned reflection defines the relationship between acoustic properties from individual beds that comprise the reflection. However, since in this model each thin bed here is only 10 m thick, far less than the tuning thickness (60m), and seismic bandwidth is always narrow (below 100Hz), the periodic notches in the amplitude spectrum representing the temporal thickness cannot be easily seen. It is also difficult to model this effect as being a traditional attenuation mechanism in such thin layer. It is concluded that a combination of the tuning effect and gas related dispersion is necessary to explain the AVO and spectral response of the gas reservoir under consideration.

Chapman *et al.* (2005) have shown that fluid-sensitive dispersion and attenuation can give rise to a frequency-dependent AVO response, and that such signatures can be detected using spectral decomposition methods. In particular, it has been suggested that for a class I AVO interface in which hydrocarbon saturation appears as a dimming of amplitude, the presence of gas tends to shift the reflection towards higher frequencies. This is in contrast to the standard view that attenuation would lead to a loss of high frequencies. I present a case study of field data where a known gas reservoir produces the characteristic dimming effect. Application of spectral decomposition techniques shows that indeed the reflection from the reservoir has

been shifted to higher frequencies, as predicted by theory. I construct velocity models relevant to the area, and perform reflectivity modeling with both the Gassmann and dispersive theories. The dispersive modeling is able to reproduce the observed spectral response of the gas reservoir. It is demonstrated that the effect of tuning has a strong effect on the frequency response of the reservoir, but we are still able to observe the dispersion effect. I conclude that the cause of the spectral anomaly in the data is most likely gas-related dispersion combined with tuning.

7.2 Theory

7.2.1 Dynamic fluid substitution

Chapman (2003) has presented an equivalent medium theory, which encompasses the Thomsen low frequency limit and Hudson high frequency limit, for modeling attenuation. He argues that by introducing larger scale heterogeneity (centimeter to meter scale), the transition frequency shifts from a high frequency band into the seismic band. The modeling assumes that low frequencies correspond to the case of pressure equalization, where fluid has time to move to relieve local pressure gradients within the time period of a seismic wave. Correspondingly at high frequencies, the fluid does not have time to move and the pressure gradients persist. Between these 2 cases, velocity dispersion and associated attenuation occurs as the elastic properties move between the compliant low-frequency case and the stiffer high-frequency case. The modeling begins with the case of an isotropic rock, provides a correction to Gassmann and calculates the elastic constants for each frequency. The input parameters are the velocities at a particular reference frequency, the density, porosity and fluid bulk modulus, together with a crack density and a transition frequency (time-scale parameter). The mathematical procedure of calculating the frequency dependent constants is outlined in the Appendix A, extracted from Chapman *et al.* (2006).

Figure 7.1 shows an example of the velocity and attenuation variation with frequency. Figure 7.1a shows P-wave velocities drift from high frequency to low frequency for both gas and water saturations for a sand rock. The parameters in sand are V_p=2790m/s, V_s=1463m/s, and ρ=2.08g/cc with water saturation, 2.06g/cc with gas saturation, porosity=30%. The gas bulk modulus is taken as 400Mpa, water as 2000Mpa. Reference frequency is 10Hz, crack density is 0.1, and time-scale value $2x10^{-5}$s. The Gassmann effect is shown on the decreasing P-wave velocity when gas replaces water. P-wave velocity with gas saturation shows a larger drift from high to low frequency and higher attenuation than the water saturation case, which provides that gas saturation can lead to abnormally high attenuation. Figure 7.1b shows there is no Gassmann effect for the S-wave case because at low frequency the shear-modulus is decoupled from the saturating fluid. S-wave attenuation is very small for gas saturation compared to the P-wave case.

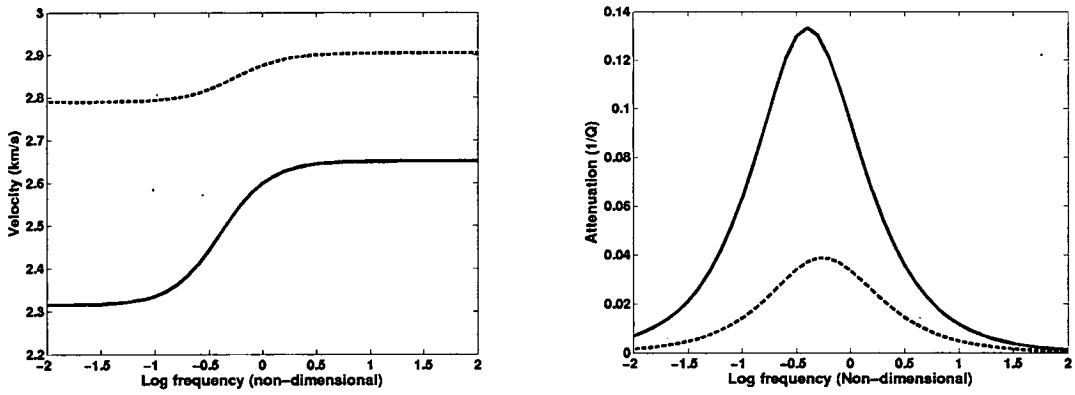

(a) P-Velocity (b) P-wave attenuation

Figure 7.1a: Predicted P-velocity and attenuation as a function of non-dimensional frequency $\omega\tau$ under gas and water saturation (solid line-gas, dashed line-water) (Chapman *et al.*, 2005).

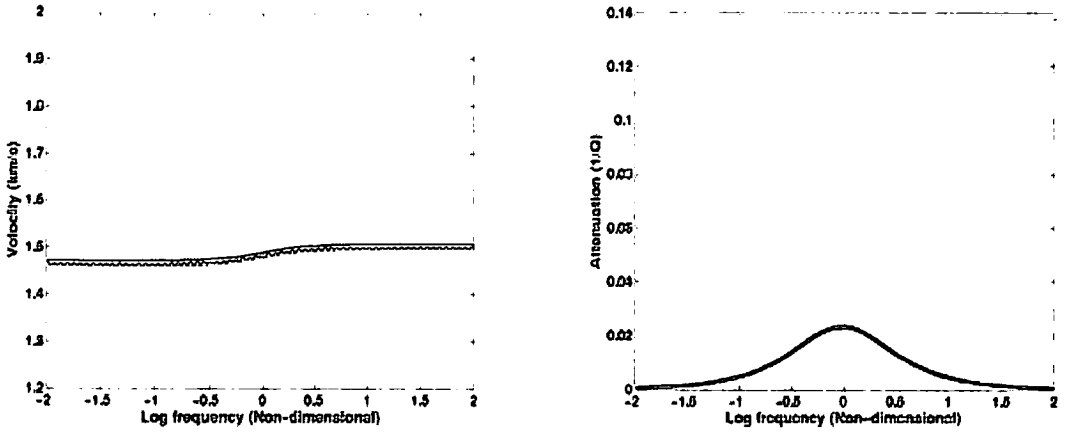

(a) S-Velocity (b) S-wave attenuation

Figure 7.1b: Predicted S-velocity and attenuation as a function of non-dimensional frequency $\omega\tau$ under gas and water saturation (solid line-gas, dashed line-water) (Chapman *et al.*, 2005).

Since the elastic constants of dispersive materials are frequency-dependent, P-wave reflection coefficients vary with frequency. This variation depends on the AVO behaviour at the interface. For class III sand with low impedance, the absolute value of impedance contrast will be decreased with frequency in dispersive case, so reflection shifts toward lower frequency ends. For class I AVO with high impedance, the absolute value of impedance contrast will be increased with frequency in dispersive case, so reflection tends to shift towards higher frequency ends.

7.2.2 Spectral decomposition technique

Since the attenuation has the character of instantaneous frequency, spectral decomposition is an ideal tool to detect the effect of frequency dependent variation. Spectral decomposition has been used for an actuate structure mapping over the last few years. Recently, it has been used as a Direct Hydrocarbon Indicator (Partyka *et al.,* 1999). The traditional spectrum generated by the Fourier transform gives the spectral amplitudes at each frequency over the entire record length and contains no

information about the evolution of the frequency content over the time. The spectral decomposition overcomes this problem and provides an instantaneous frequency analysis for each time sample.

To perform spectral decomposition, there are several techniques available such as short time Fourier transform (STFT), Gabor transform, Wigner-Ville transform, Stockwell transform, continuous wavelet transform, the maximum entropy method, and matching pursuit decomposition. Castagna *et al.* (2003) and Liu and Chapman (2006) compare the different techniques and point out the resultant time-frequency analysis is not unique: many different time-frequency decompositions can result from the same seismogram.

Here I compare two techniques, STFT with a Gaussian window function, and a wavelet transform with a Gaussian wavelet. In STFT, a Gaussian function is used to window Fourier transform and expressed in the following (Chui, 1992):

$$g_a(t) = \frac{1}{2\sqrt{\pi a}} e^{-\frac{t^2}{4a}} \quad . \qquad a > 0 \qquad (7-1)$$

STFT with a Gaussian function is defined as:

$$(\zeta_b^a f)(\omega) = \int_{-\infty}^{\infty} (e^{-i\omega t} f(t)) g_a(t-b) dt \qquad (7-2)$$

The Gaussian window length is controlled by the constant a. Figure 7.2 shows the STFT with time windows 32ms, 64ms and 128ms for a synthetic seismogram, which is composed of 1 single reflection at 0.2s, and 3 composite reflections at 0.5s, 0.8s and 1.1s (Figure 7.2a). The single reflection is a Ricker wavelet with the dominant frequency 40Hz. The composite reflection at 0.5s is two Ricker wavelets with 10Hz and 40Hz dominant frequency at the same time. The composite reflection at 0.8s is two 30Hz Ricker wavelets with a close time delay. The

composite reflection at 1.1s is composed of four Ricker wavelets (two 20Hz and two 30Hz) with close time delay. The amplitude spectra by long window Fourier transform of the seismogram are shown in Figure 7.3.

Figure 7.2b of a STFT with 32ms window shows an excellent vertical time resolution. However, the frequency response is smeared because the spectrum is convolved with the Gaussian function. Side lobes appear as distinct events at low frequency. Figure 7.2d of a STFT with 128ms window improves the frequency resolution, but the spectrum is spread over the time window.

Due to the above problems in the STFT, it is better to avoid the windowing in time-frequency analysis. The wavelet transform provides an adjustable time-frequency window. It is defined in the following:

$$(W_{\varphi} f)(b,a) = |a|^{-\frac{1}{2}} \int_{-\infty}^{\infty} f(t)\overline{\varphi(\frac{(t-b)}{a})}dt \qquad (7-3)$$

A wavelet transform with a Gaussian wavelet is used in this paper. Figure 7.4 shows the amplitude spectra with different band parameters for the same synthetic seismogram as in Figure 7.2a. Figure 7.4b shows that, when the band is too small, stripes appear parallel to the time axis. Figure 7.4d shows that when the band is too big, the stripes are parallel to the frequency axis. Figure 7.4c shows a better time-frequency resolution. This technique and parameter choice is applied in our numerical and physical modeling.

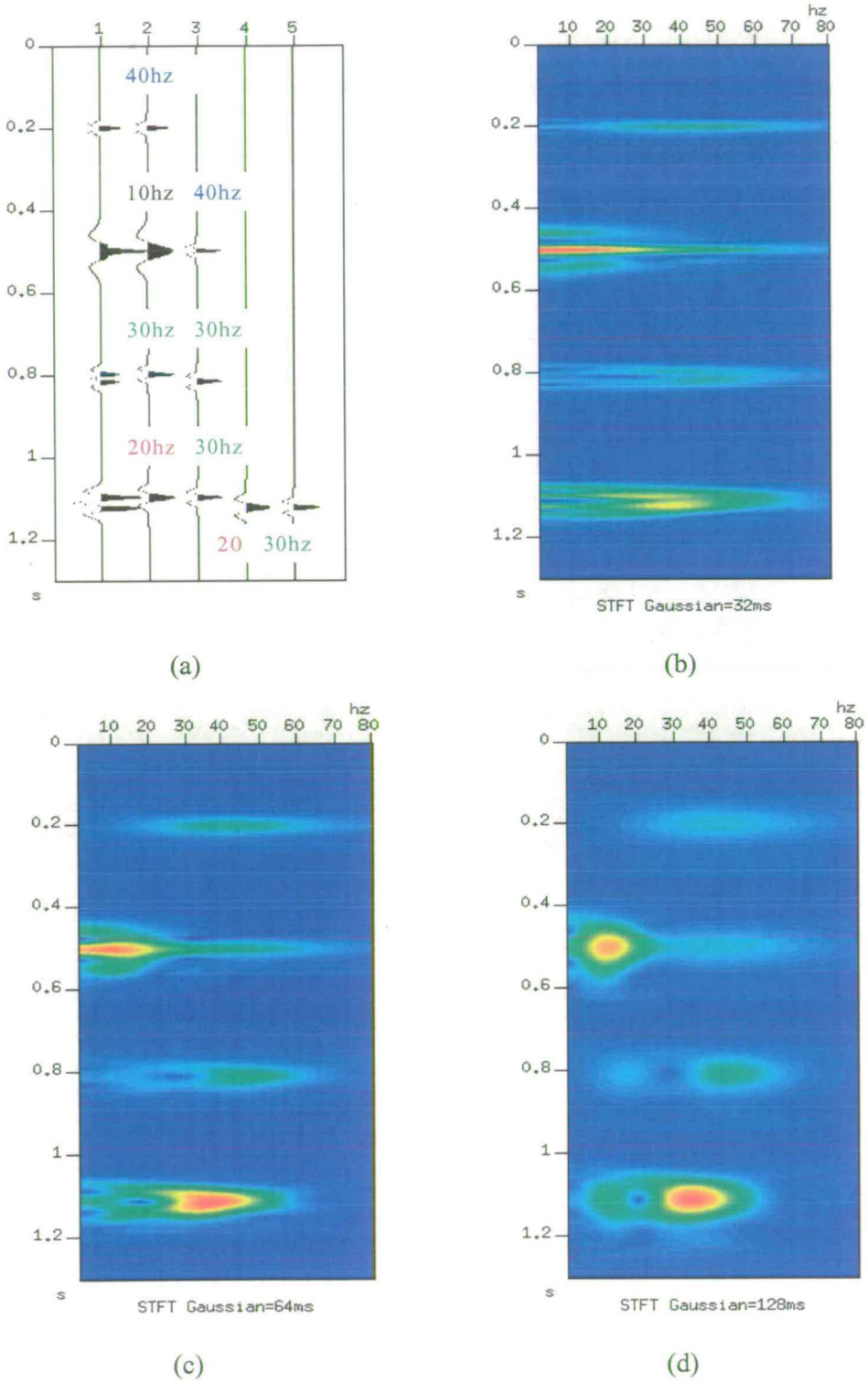

Figure 7.2: A synthetic seismogram and its short time Fourier transform with Gaussian window function at the different time window. (a) the synthetic seismogram (1st trace and its component, 2nd to 5th traces) (b) time window 32ms, (c) time window 64ms, (d) time window 128ms

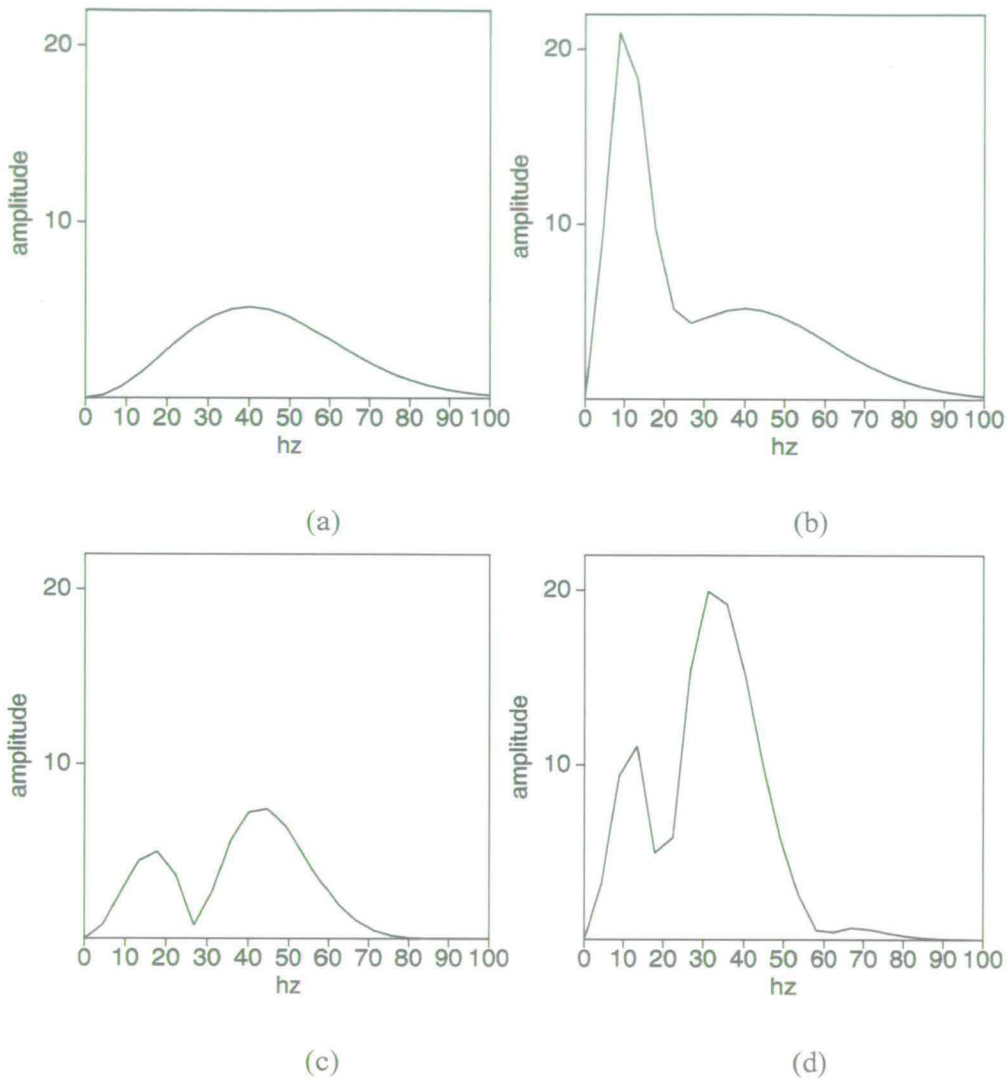

Figure 7.3: The amplitude spectra for the synthetic seismogram shown in Figure 7.2a. (a) is for event at 0.2s, (b) at 0.5s, (c) at 0.8s and (d) at1.1s.

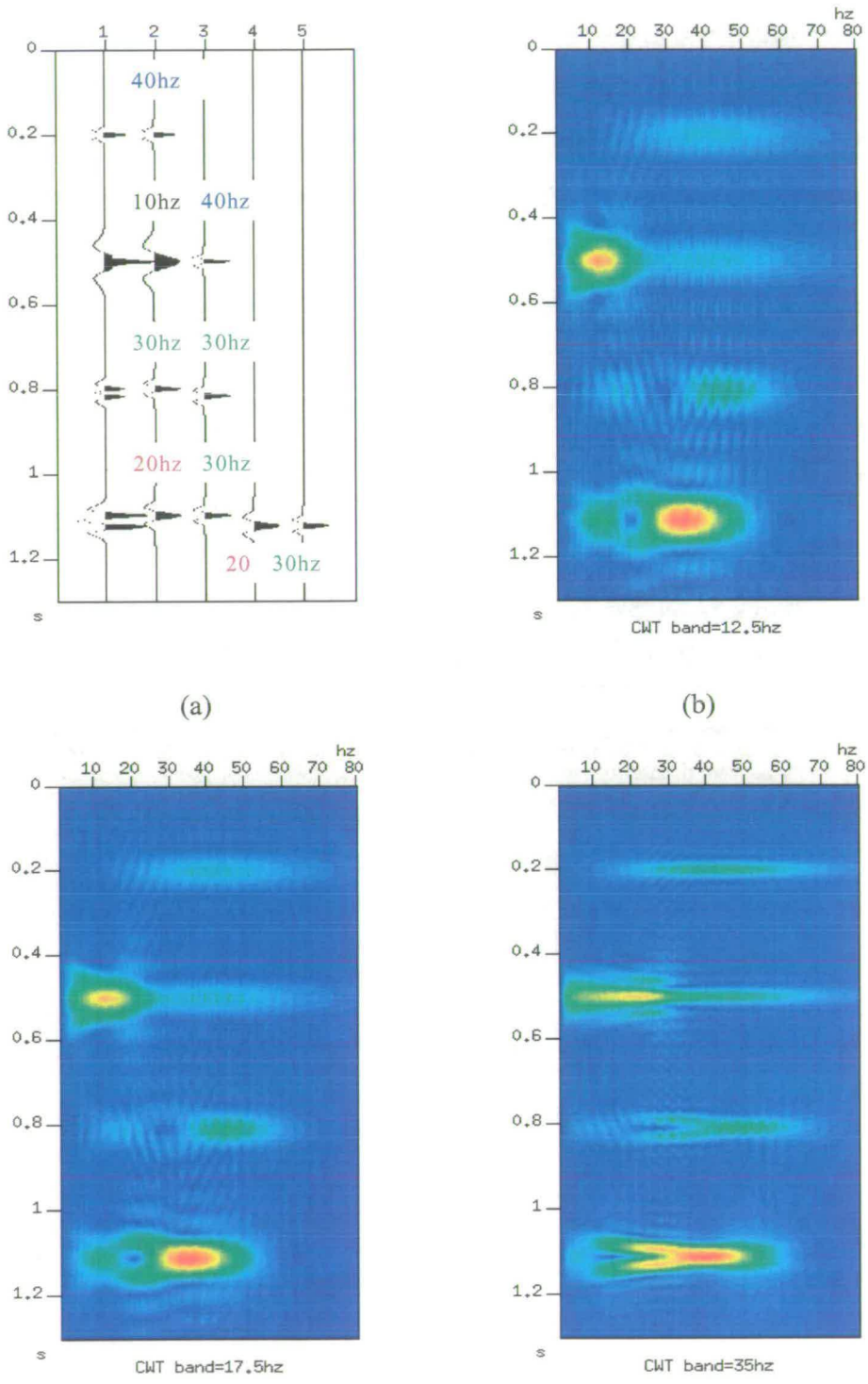

Figure 7.4: A synthetic seismogram and its wavelet transform with Gaussian wavelet at the different frequency band (a) the synthetic seismogram (b) frequency band 12.5Hz, (c) frequency band 17.5Hz, (d) frequency band 35Hz.

7.3 Data example

7.3.1 Example 1

My first example is from the Ordos basin, onshore China. The potential reservoirs in the area are primarily located in the fluvial sandstone in the Permian. The subsurface has a flat-layered structure with gas reservoirs typically below 3000 meters. The targeted gas beds are thin and have a small P-wave velocity difference between the gas sand and the overlaid shale, giving rise to a weak amplitude on the PP-wave reflection. Standard AVO analysis suggested that the top of the reservoir was in principle a class III interface, but that the reservoir reflection itself was a composite event, which led to an apparent negative reflection coefficient whose absolute amplitude declined with increasing angle of incidence, resembling the behaviour of a class IV interface (see Model 2 in Table 6.5 and Figure 6.21a for more details).

Figure 7.5 shows the results of filtering the final stack into low- and high-frequency bands. It is clear that in the high-frequency section the reservoir appears as a low-amplitude anomaly, but this is not the case in the low-frequency section. This highlights the fact that in practice the concepts of amplitude and AVO anomalies are frequency-dependent phenomena. Since the reservoir is only 10 m thick it is difficult to model this effect as being due either to a traditional attenuation mechanism or fluid-related changes in the tuning-thickness. To explain the behaviour we turned to the dispersive modeling. Based on log data I created an idealised multi-layer model, with a 10 m thick gas sand and 10 m thick shale layer encased in a halfspace of higher impedance (Table 7.1). This arrangement was able to model effectively the observed AVO behaviour within the reservoir.

I used a commercial reflectivity code (ANISEIS), which permits the use of materials with frequency dependent velocities and attenuations. Our modeling had

three components: the simple Gassmann effect, the Gassmann effect with tuning and the full dynamic modeling with attenuation and associated dispersion.

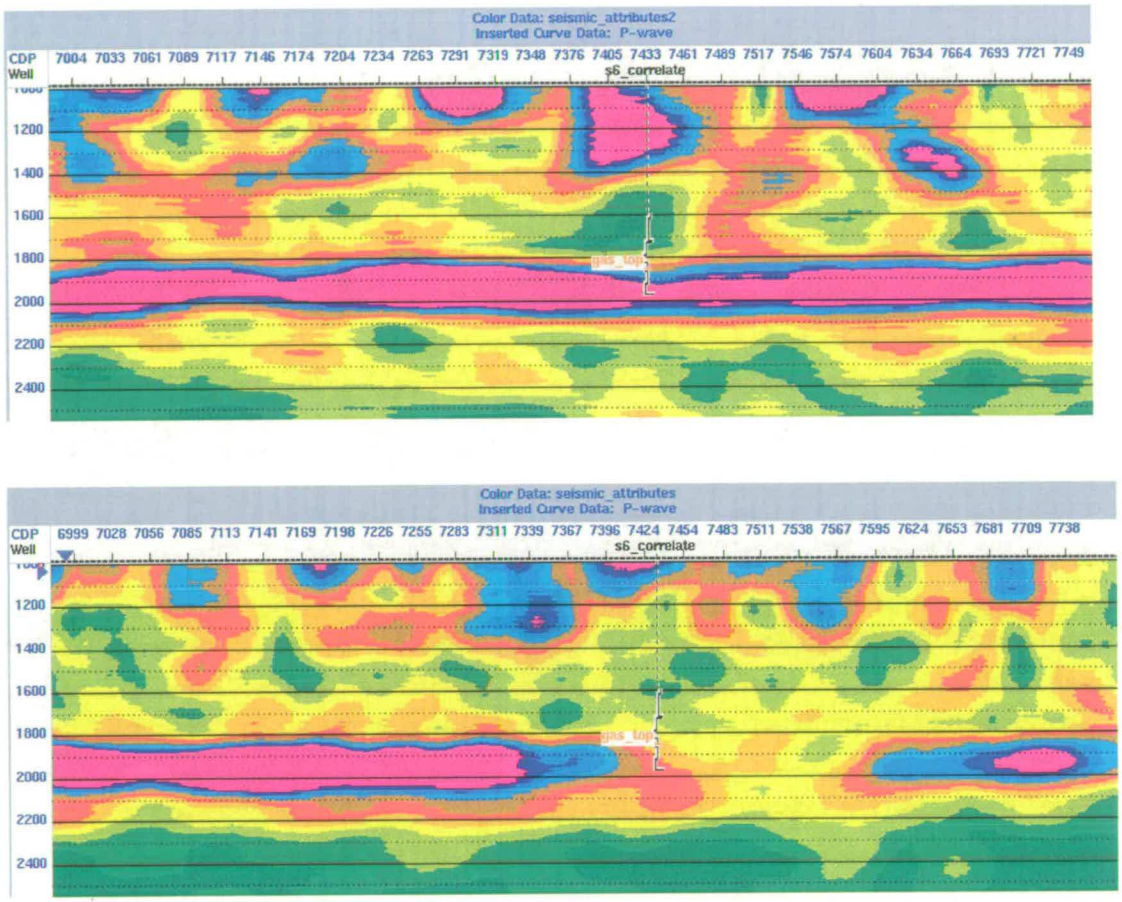

Figure 7.5: PP-stacked sections from example 1, band-passed into low- (top) and high (bottom) frequency sections. Note how the reservoir level (around 2s) appears dim in the high frequency section but not in the low frequency section.

	Thickness (m)	**V_p (m/s)**	**V_s (m/s)**	**ρ (g/cc)**
	halfspace	4577	2642	2.59
Shale	10	4486	2586	2.58
Sand	10	4143	2658	2.4
	halfspace	4577	2642	2.59

Table 7.1: Parameters used in the computations. The sand velocities assume gas saturation. In all cases, the reference frequency is 10Hz, the reference value of τ_0=1e-6s, and crack density is 0.1. The bulk modulus is taken as 400MPa for gas, 2000MPa for water.

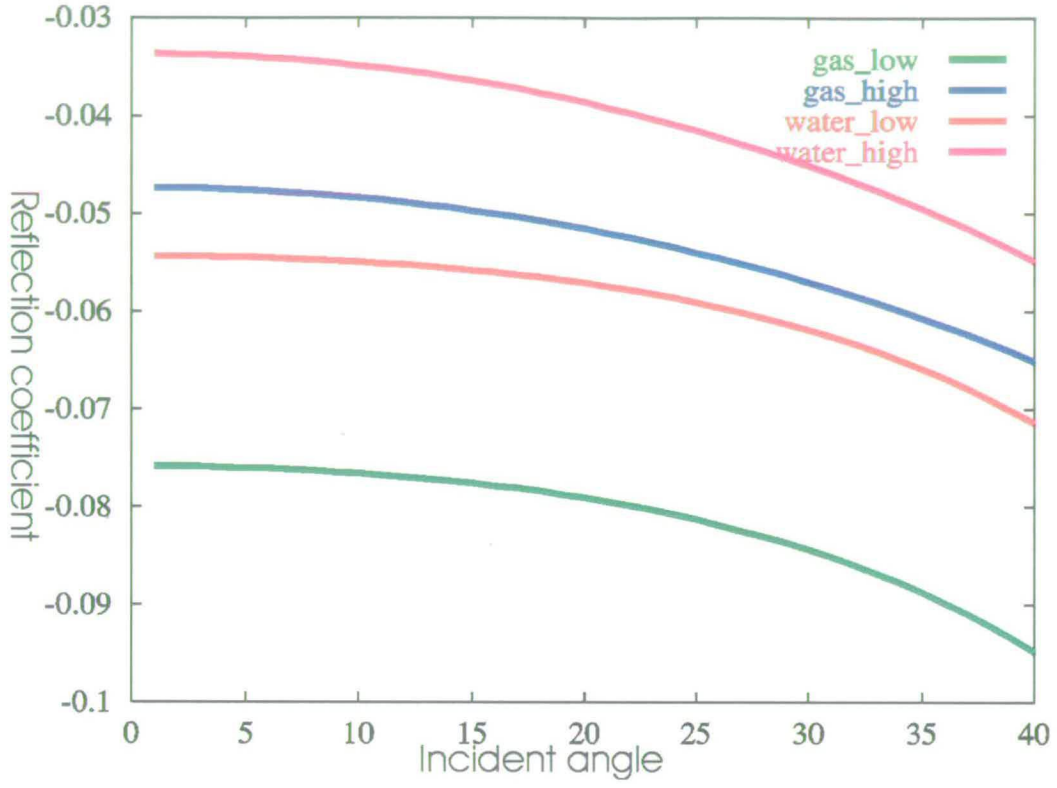

Figure 7.6: PP-wave reflection coefficients under both water and gas saturation in low (10Hz) and high frequency (1e7Hz) limits.

Figure 7.6 shows both gas- and water-saturated PP-wave reflection coefficients for the low and high frequency limits for top sand of the model. A Gassmann effect for class III AVO is displayed, in that gas saturation produces a larger reflection coefficient than the water saturation. Because P-wave velocity increases in both gas and water layer from the low to high frequency limit, the normal incidence of reflection coefficients is greater at low frequency than at the high frequency. The reflection coefficients in the gas-saturated case move further apart between the low and high frequency limits than the water saturated case.

To illustrate the low frequency effect in the dispersive case, we ran eight models corresponding to water and gas saturation for both low/high frequency limits and the dispersive cases, then stacked the data and formed iso-frequency traces. Since neither the source nor the earth's reflectivity has white spectra, we should expect to

find markedly different amplitudes at different frequency. The procedure for compensating for these effects is to use spectral balancing. Here I used the low frequency limit gas-saturated case as reference, performed a consistent spectral balancing to eight models at each frequencies (10Hz to 50Hz, 5hz interval). As might be expected, these sections showed similar energy in low and high limit frequency section (Figure 7.7a, b); the frequency sections were no longer balanced when dispersion is introduced into the reservoir layer. The low frequencies appear to have much more energy (Figure7.7c, d).

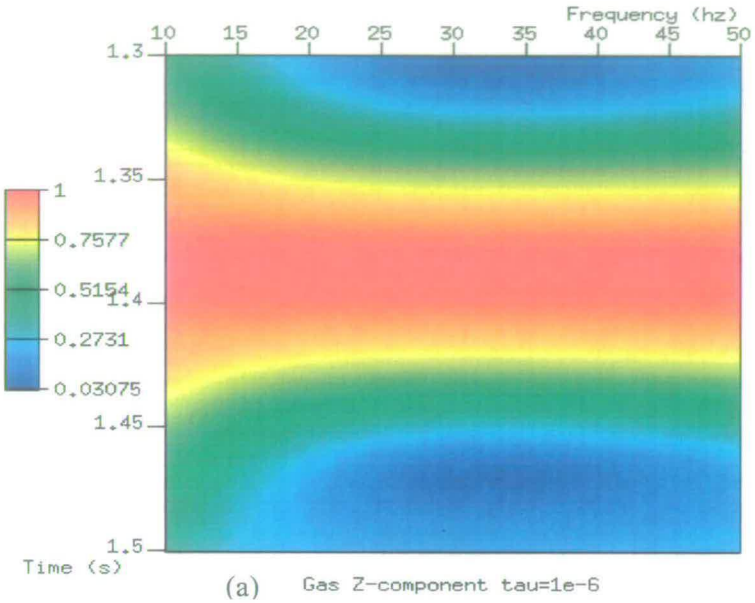

(a) Gas Z-component tau=1e-6

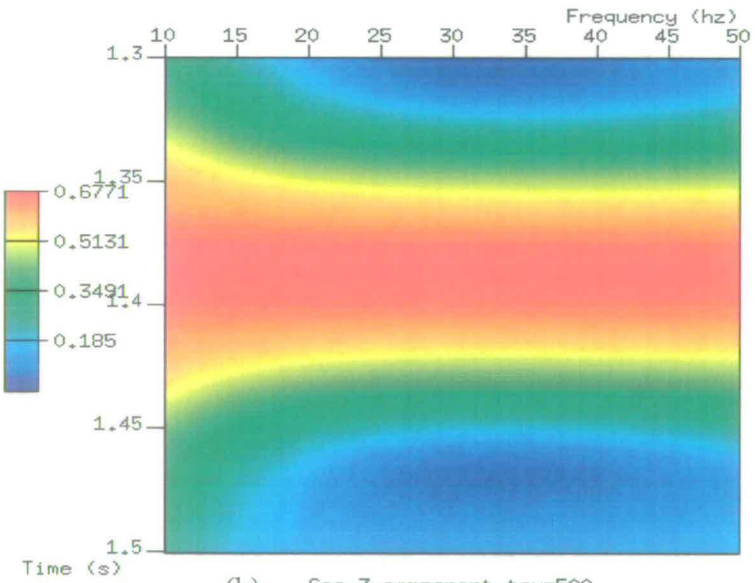

(b) Gas Z-component tau=500

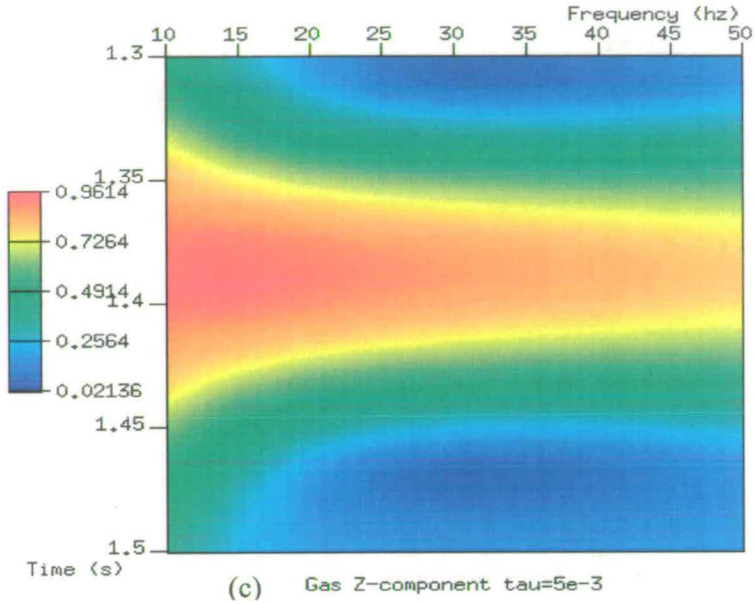

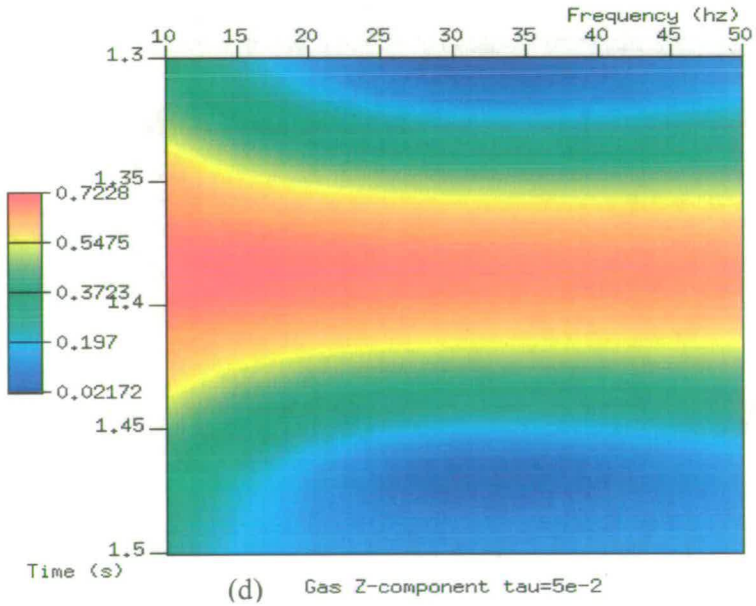

Figure 7.7: Balanced spectra for PP-wave gas saturation at the different frequencies for the different time scales. All spectra were balanced by the low frequency limit gas case at each frequency. The first two graphs are for low and high frequency limit cases, which are well balanced. The last two graphs are for dispersive cases, which are not balanced any more.

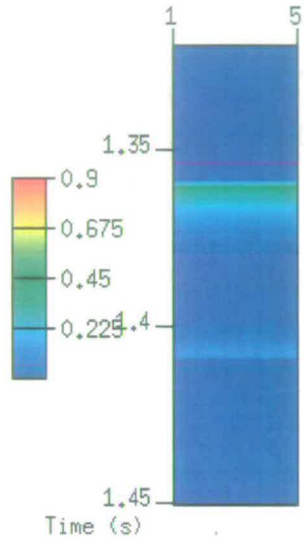

(a) Water, Gassmann modeling

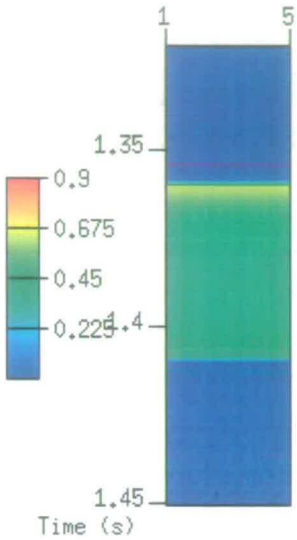

(b) Water, dispersive modeling

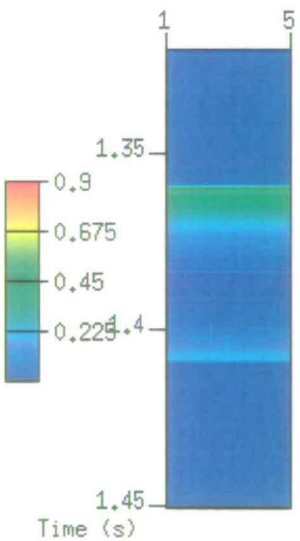

(c) Gas, Gassmann modeling

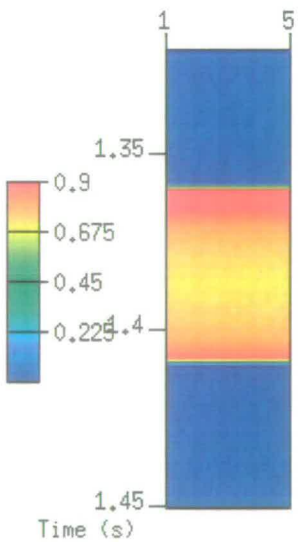

(d) Gas, dispersive modeling

Figure 7.8: "Difference traces" formed by stacking the synthetic data, performing spectral decomposition, consistent spectral balancing and subtracting the 30 Hz trace from the 15 Hz trace. The reservoir layer is 10m thick, and we consider water and gas saturation in both the dispersive and Gassmann cases. Note that the Gassmann modeling gives small absolute values, but that gas saturation is associated with a strong positive amplitude when we perform dispersive modeling.

We then subtracted the resulting 30Hz trace from the 15Hz trace for both water and gas models at Gassmann case and dispersive case, and windowed around the main arrival to compensate for the different time durations of the signals. The results are illustrated in Figure 7.8. For each Gassmann trace there is little residual energy, implying that the traces were well balanced. In the dispersive case there was residual energy for both saturations, but it was much stronger in the gas-saturated case.

A similar procedure was carried out on the data shown in Figure 7.5. The two sections were balanced and a difference was taken, with the result shown in Figure 7.9. As can be seen, in the vicinity of the reservoir we have a response very similar to the gas response we saw in our synthetics.

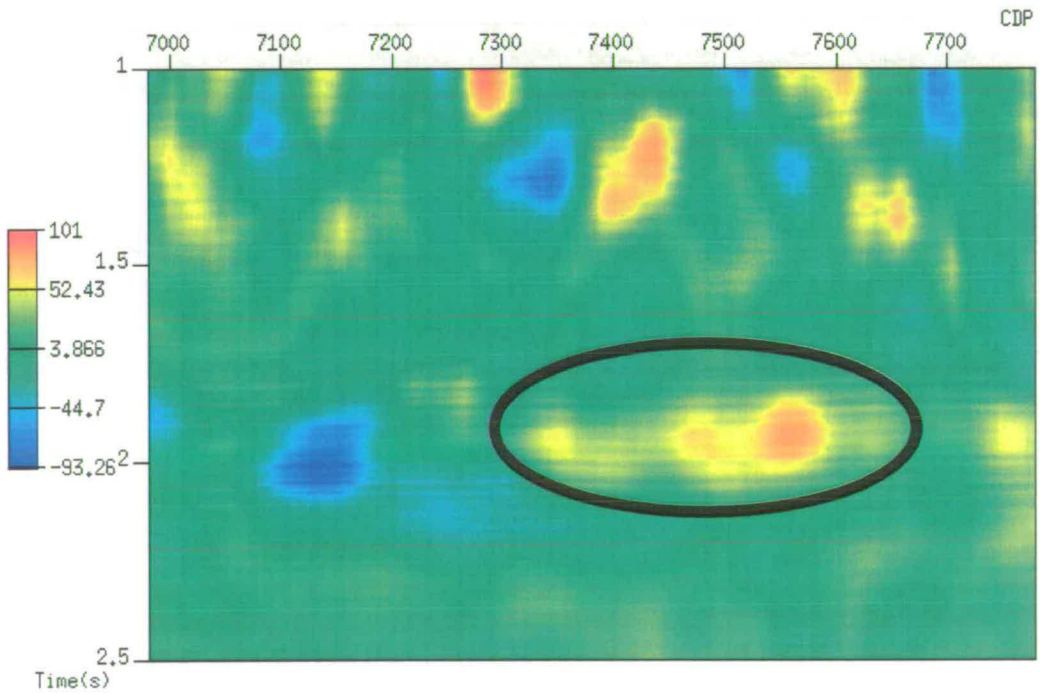

Figure 7.9: The results of balancing and differencing the sections from Figure 7.5. Notice that the gas reservoir shows as a positive anomaly (ringed) in accordance with our synthetic modelling.

Similar ideas are applied to PS-wave data to check for any fluid dispersive effect. Figure 7.10 shows both gas- and water-saturated PS-wave reflection coefficients at low and high frequency limits for top sand of the model in Table 7.1. The direct observations are the low frequency effect (larger reflection coefficients at low frequency limit than the high frequency limit) for both water and gas cases, which is consistent with PP-wave in Figure 7.6. The difference lies in that there is no larger separation between high and low frequency limit for gas than there is for water saturation.

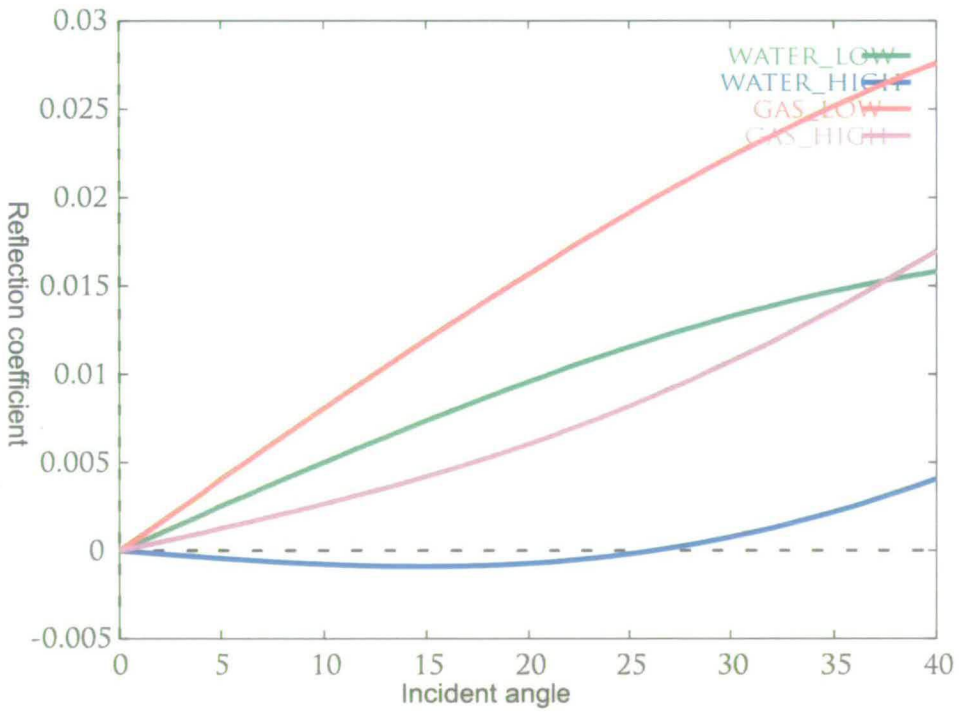

Figure 7.10: PS-wave reflection coefficients under both water and gas saturation cases in low (10hz) and high frequency (1e7hz) limits.

We applied similar techniques to frequency-dependent PS-synthetics, as we did to PP-wave synthetics. We obtain energy-balanced sections at low and high frequency limits for the gas saturation case only (Figure 7.11a and 7.11b). The section at the low frequency limit for the water case is balanced (Figure 7.12a), but at the high frequency limit the spectrum is not balanced (Figure 7.12b). This may be caused by the small reflection coefficient (blue curve in Figure 7.10) and the polarity reversal

(Figure 7.13) for the high frequency water-saturated case. Other finding is that dispersion at the gas saturation case (Figure 7.11d) occurs in a different frequency range (τ=5e-2) from the PP-wave case (τ=5e-3) in Figure 7.7c. Surprisingly, this gas-saturated attenuation occurs that is similar to the water-saturated dispersive case (Figure 7.12d), which maybe is a corresponding situation to that shown in Figure 7.10, there is a similar reflection coefficient separation between low and high frequency limits for gas case and for water case.

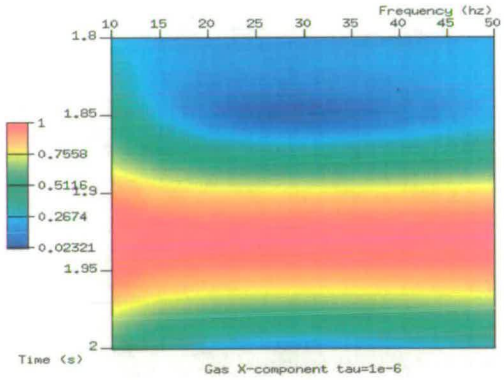

(a) low frequency limit

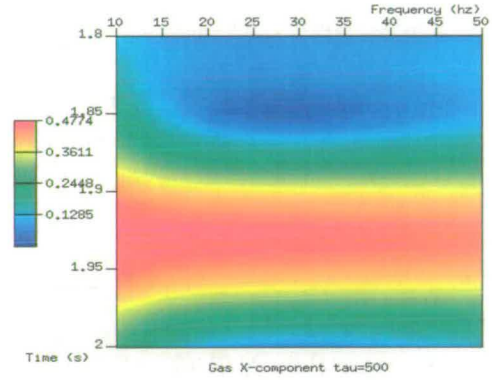

(b) high frequency limit

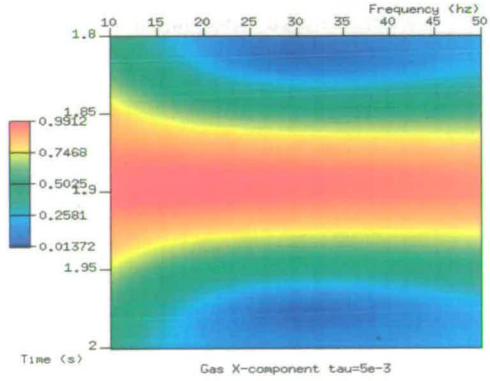

(c) dispersive frequency

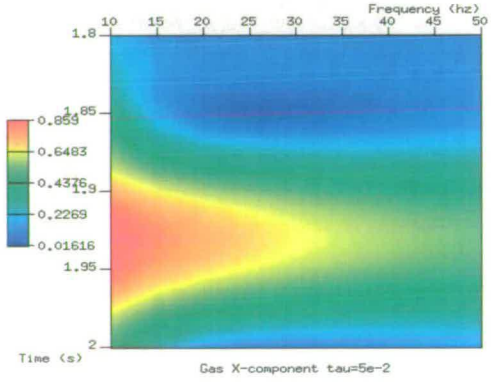

(d) dispersive frequency

Figure 7.11: Balanced spectra for PS-wave gas saturation at the different frequencies for the different time scales. All spectra were balanced by the low-frequency-limit gas case at each frequency. The first two graphs are for low and high frequency limit cases, which are well balanced. The last two graphs are for dispersive cases, which are not balanced any more.

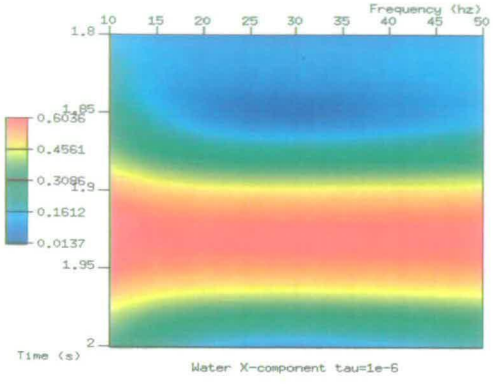

(a) low frequency limit

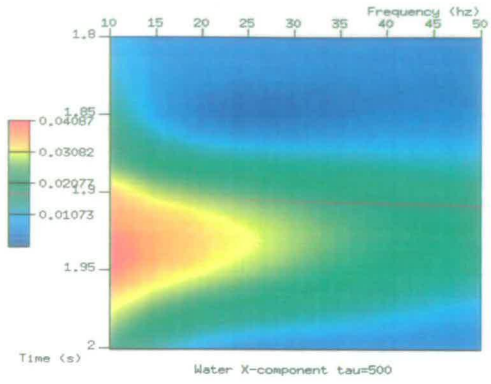

(b) high frequency limit

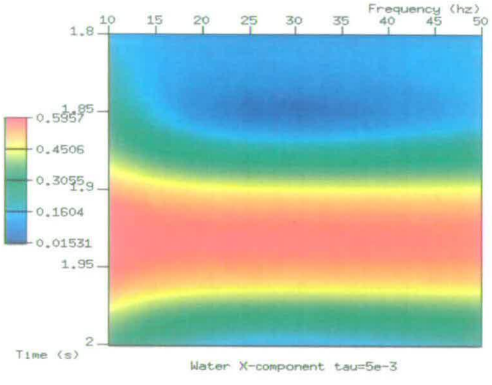

(c) dispersive frequency

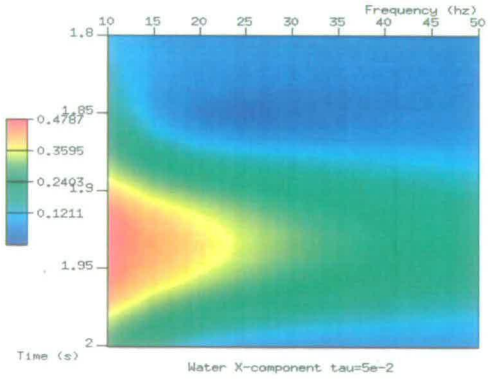

(d) dispersive frequency

Figure 7.12: As in Figure 7.11, but for a water-saturated case. All spectra were balanced by the low frequency limit gas case at each frequency. The unbalanced high frequency limit may result from the small reflection coefficient and the polarity reversal. Water saturated dispersive case shows a similar attenuation to gas saturated case.

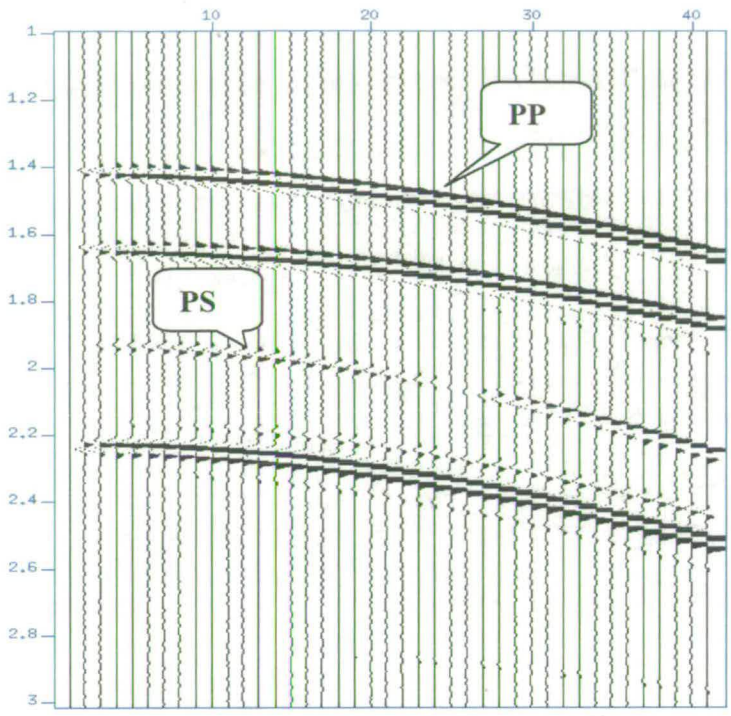

Figure 7.13: PS-wave synthetic for high frequency limit under water saturation

7.3.2 Example 2

In this example, I observe an evident difference in a gas reservoir wherein the energy shifts to the high frequency end in Daqing Oil field, North China. Figure 7.14 shows there is a dim reflection inside the gas reservoir (dashed line at 2.25s) compared to the surrounding areas, which indicates a Class I AVO. Amplitude spectral analysis (Figure 7.15) shows there is a higher dominant frequency in the gas reservoir. Figure 7.16 shows a systematic frequency-dependent anomaly from 15Hz to 30Hz after spectral balancing. The gas reservoir is indicated by a high frequency bright spot. This observation seems contradictory to the traditional understanding that the high frequency energy should be attenuated by transmission loss.

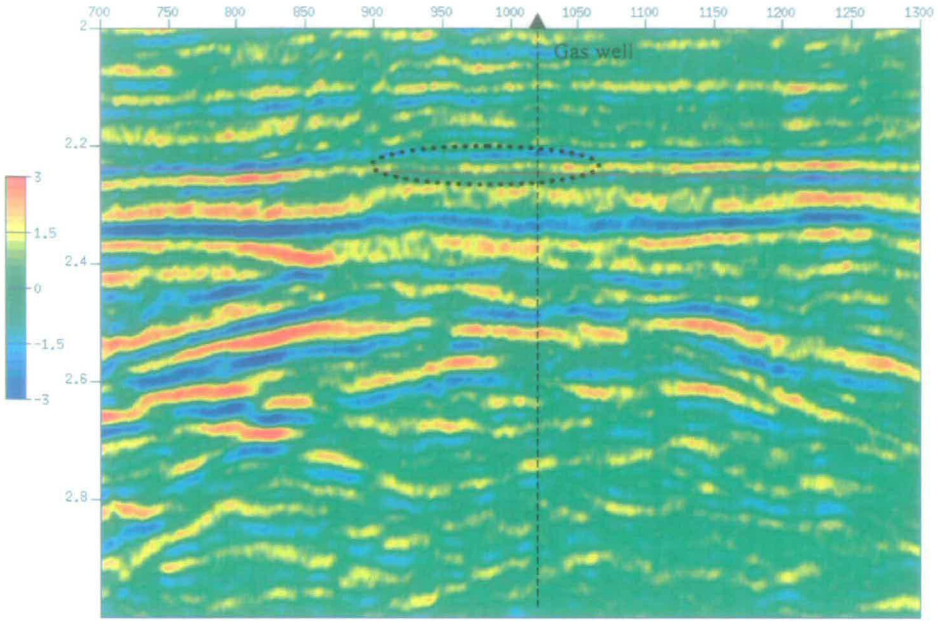

Figure 7.14: The stacked section showing a dim spot from the gas reservoir at 2.25s

However, this observation agrees with the theory of Chapman *et al.* (2006), as explained in section 7.2.1, and modelled in Figure 7.1a. In the case of Class I AVO (a low to high impedance interface), the gas-induced dispersion (Figure 7.1a) further increases the impedance contrast for high frequencies, which leads to a shift of reflection energy to the high frequencies.

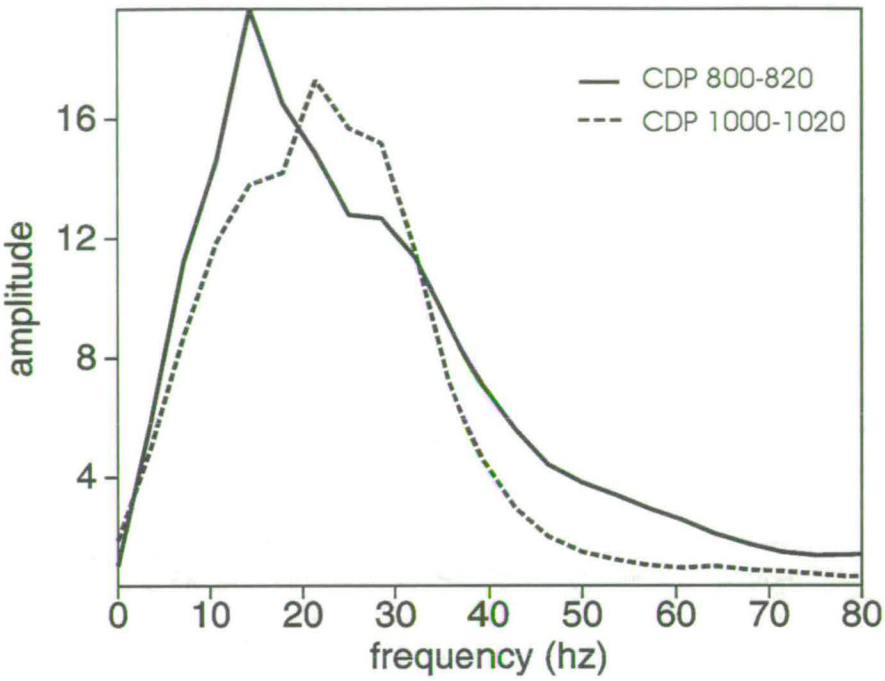

Figure 7.15: The amplitude spectra from inside (CDP 1000-1020) and outside (CDP800-820) gas reservoir.

Since the reservoir in Figure 7.14 is a thin-layer reservoir with interbedded sand/shale sequences, we will carry out full-wave synthetic modeling to model this response. We will consider both effects of gas-induced dispersion based on the theory of Chapman *et al.* (2006) and thin-layer tuning.

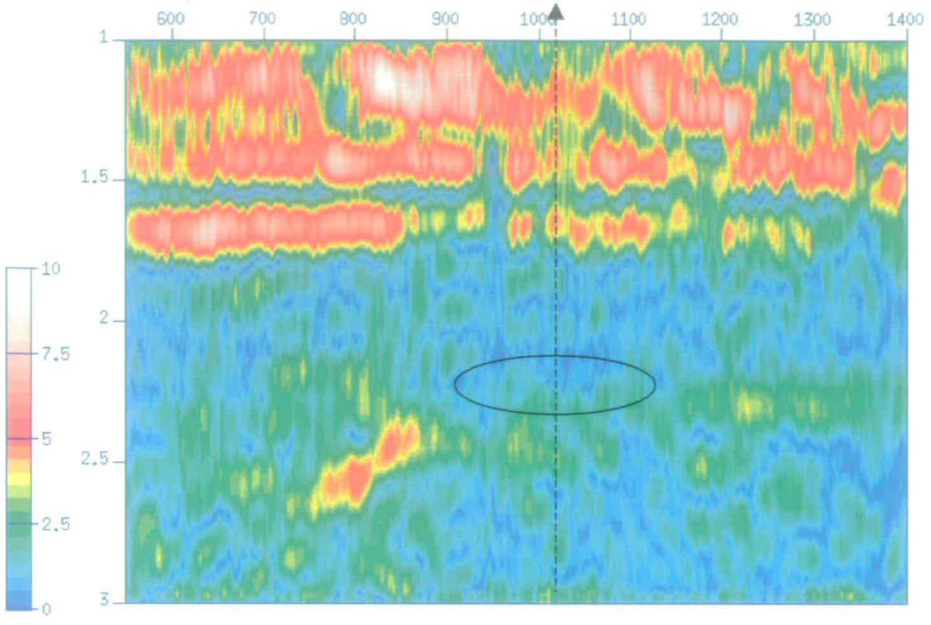

(a) iso-frequency section at 15Hz

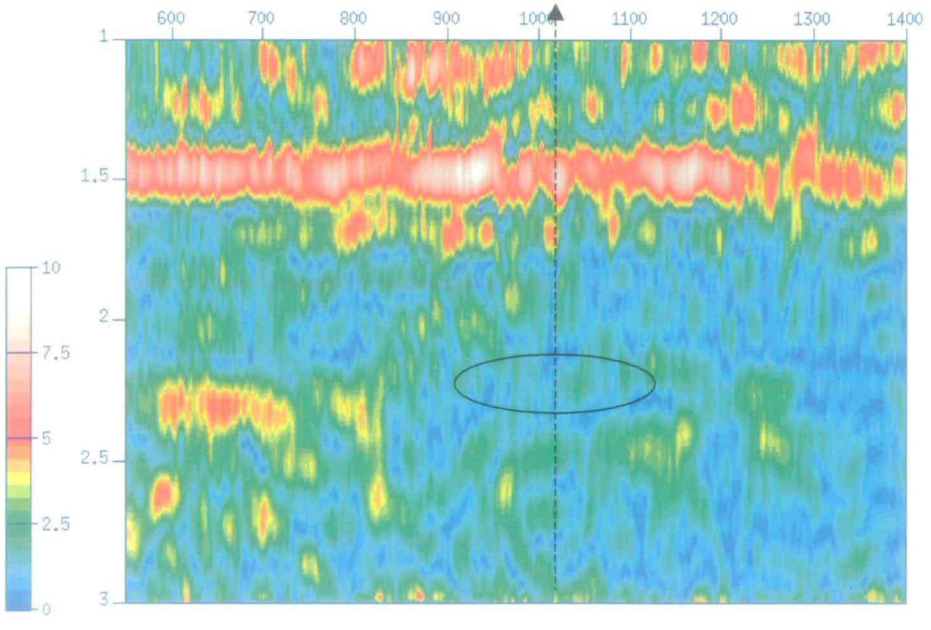

(b) iso-frequency section at 20Hz

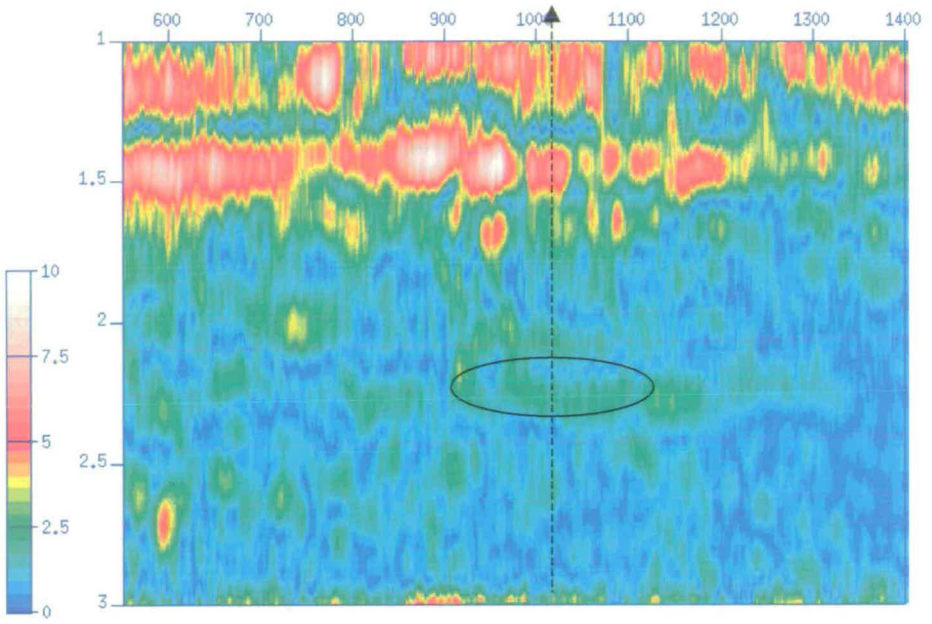

(c) iso-frequency section at 25Hz

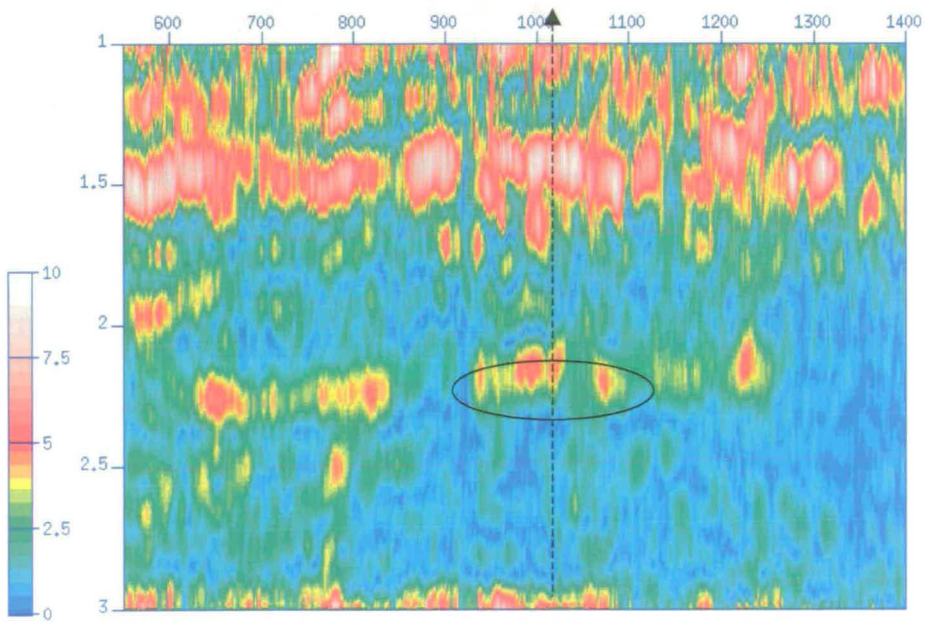

(d) iso-frequency section at 30Hz

Figure 7.16: Iso-frequency sections showing a systematic amplitude increase from 15Hz to 30Hz

7.4 Thick-layer model without tuning

Class I sands have high impedance contrast and a positive normal-incidence reflection coefficient at the top of the sand. The reflection magnitude decreases with offset, which causes a dimming effect. Due to the velocity dispersion for gas saturation between the low and high frequency limits, contrary to class III sands, the AVO behaviour of class I sand causes the reflection energy to shift from low frequency to high frequency end.

I first generate the frequency-dependent reflection coefficients for gas and water-saturated models to examine the frequency shifts. The velocity and density parameters of the gas sand and overlying shale are based on well logs and shown in Table 7.2. The reference frequency for these parameters is 10Hz. The overlying shale is assumed to be a pure elastic layer. The gas layer is designed to have dispersive properties. The porosity of the gas layer is 17%; the density under water replacement is 2.7 g/cc. The bulk modulus for gas is 400Mpa, and 4000Mpa for water.

Layer no. + lithology	Density (g/cc)	Vp (Km/s)	Vs (Km/s)	Thickness (Km)
1: reference layer for balancing	2.3	4.2	2.3	1
2: shale	2.4	4.3	2.5	1
3: sand	2.53(gas) 2.70(water)	5.15	3.18	0.4
4: shale	2.5	4.5	2.7	Halfspace

Table 7.2: The elastic parameters used for numerical modeling

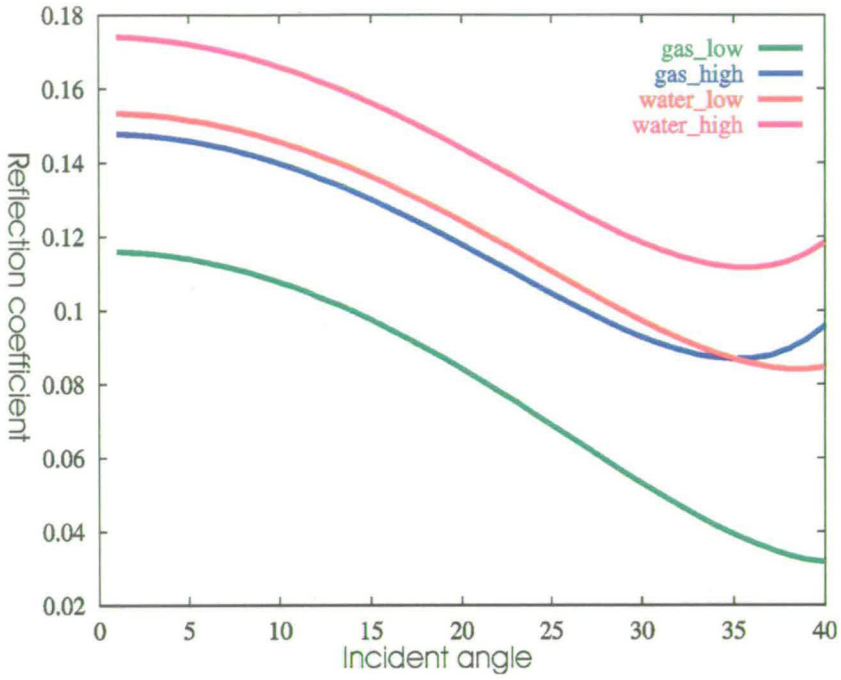

Figure 7.17: Frequency-dependent reflection coefficients in the low and high frequency limits for a Class I AVO sand in Table 7.2

Figure 7.17 shows the reflection coefficients under the low and high frequency limits for gas and water saturation. The Gassmann effect is displayed in that gas saturation has a lower reflection coefficient than the water saturation. Because P-wave velocity increases in both gas- and water-saturated layers from the low to high frequency limit, the positive reflection coefficient of normal incidence is greater in high frequency than in the low frequency. However, the reflection coefficients in the gas-saturated case move further apart between the low and high frequency limits than the water saturated case.

Now I use ANISEIS software package to generate the synthetic seismograms for a thick sand layer (400m) by the reflectivity method. The thickness of each layer is shown in Table 7.2. Only the sand layer has frequency-dependent velocities and attenuation, and the other layers are elastic. Such arrangement is for detecting the attenuation from the sand layer.

The wavelet used in the modeling is a 20Hz Ricker wavelet, and offsets range from 0 to 4000m at 100m interval. Figure 7.18 shows the seismograms with a time scale τ of 1e-6s (low frequency limit) and a τ of 1e-2s (dispersive case) for the gas-saturated model (see Appendix A for more detail). The reflections in the seismograms are: A, PP-reflection for the base reference layer; B, PS-reflection of the base reference layer; C, PP-reflection from the top sand layer; and D, PP-reflection of bottom the sand layer. E and F are PS-reflections of the top and bottom sand layer. As expected, the PP-reflection of top sand (C) increases amplitude in the dispersive case in Figure 7.18b as compared with the non-dispersive case in Figure 7.18a.

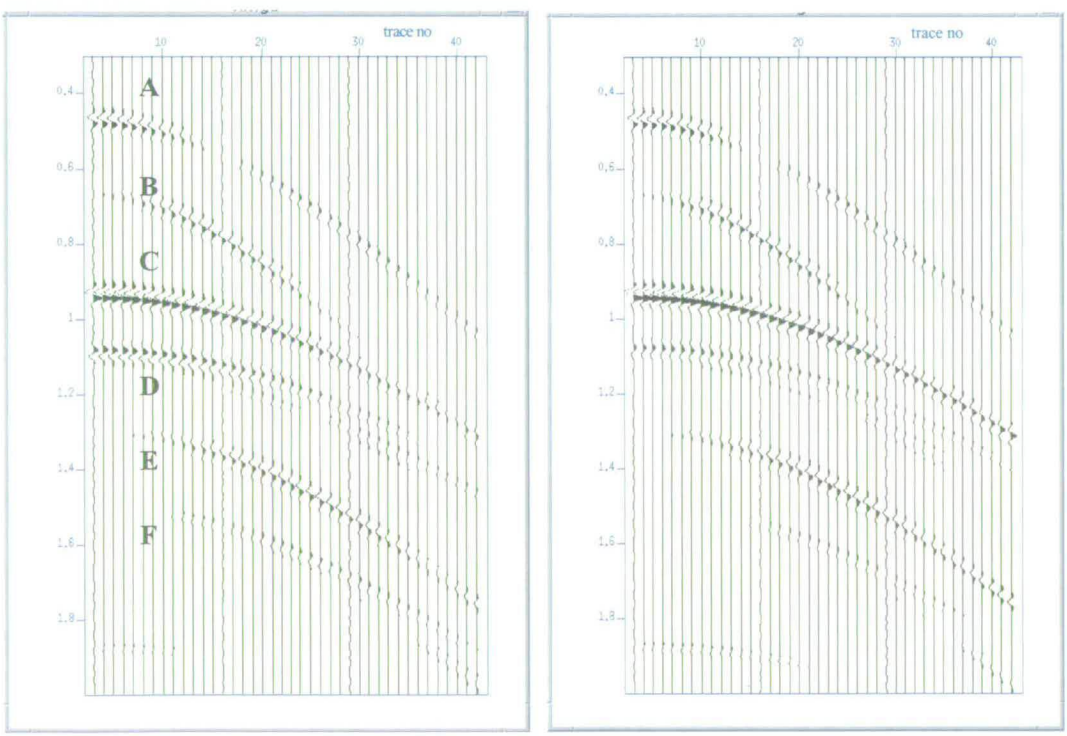

Figure 7.18: The synthetic seismograms for the thick gas saturation layer (without tuning effect) in Table 7.2 for the low frequency limit case (left, a) and the dispersive case (right, b)

Amplitude spectral analysis of the top PP reflection for offset 2000m is shown in Figure 7.19a. The amplitude in the dispersive case for both the gas and water-

saturated models increases as compared with the low frequency limit cases. The amplitude in the dispersive cases shifts towards the high frequency end for both gas and water saturated models (Figure 7.19b), whilst the gas-saturated case shows a greater shift than the water case, as expected from Figure 7.17.

I apply the spectral decomposition technique (Liu and Chapman, 2006) to the synthetic seismograms. To perform spectral balancing, here my preference is to equalize the average amplitudes between the various traces across a particular time window, or reference horizon. In this numerical model, a reference layer is given at the depth of 1km. By balancing the amplitude spectra of this pure elastic layer at different frequencies, the wavelet effect can be removed. This will then reveal the dispersion effect.

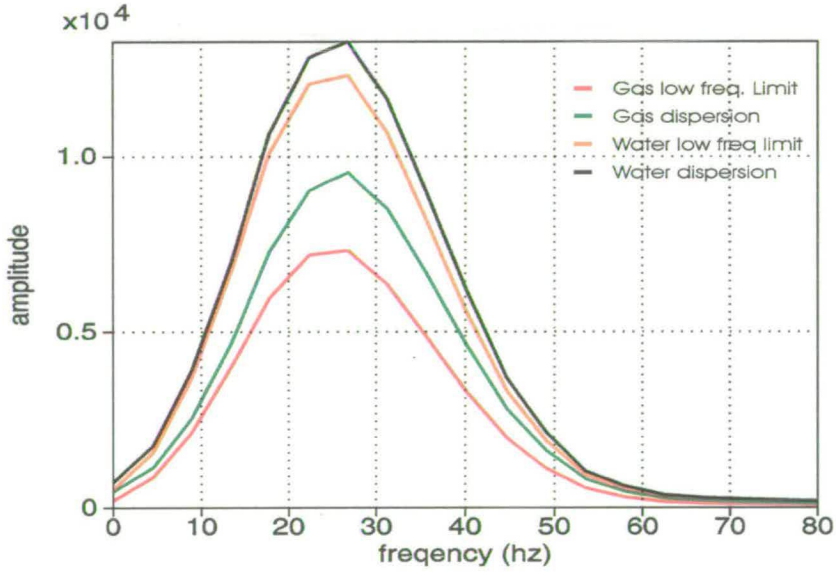

Figure 7.19a: Amplitude spectra for the PP-reflection from top gas- and water-saturated thick layers at offset 2000m. A shift to the high frequency appears in the dispersive cases, the gas-saturated case shows a greater shift than the water case.

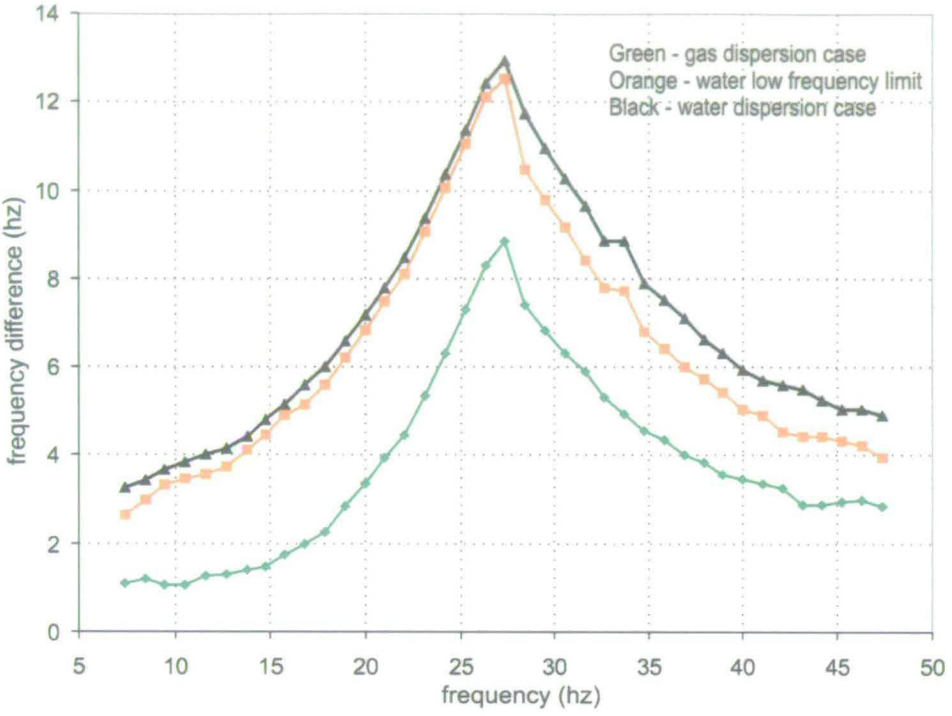

Figure 7.19b: Frequency differences at the same amplitude (Figure 7.19a) between the gas low frequency limit case and gas dispersion case (green curve), the gas low frequency limit case and water low frequency limit case (orange curve), the gas low frequency limit case and water dispersion case (black curve). The asymmetric frequency difference around the peak frequency axis (27Hz) indicates that there is a frequency shift at the high-frequency end, and the largest shift occurs in the gas dispersion case.

Figure 7.20 shows the balanced iso-frequency spectra of the gas-saturated model for the low frequency limit (the Gassmann case). The reference layer at 0.45s is balanced at each frequency. At the top sand layer (0.9s), the spectra of the PP-reflection show no frequency anomaly. We see unbalanced spectra at the base sand layer (1.1s), which indicates transmission attenuation in the thick sand.

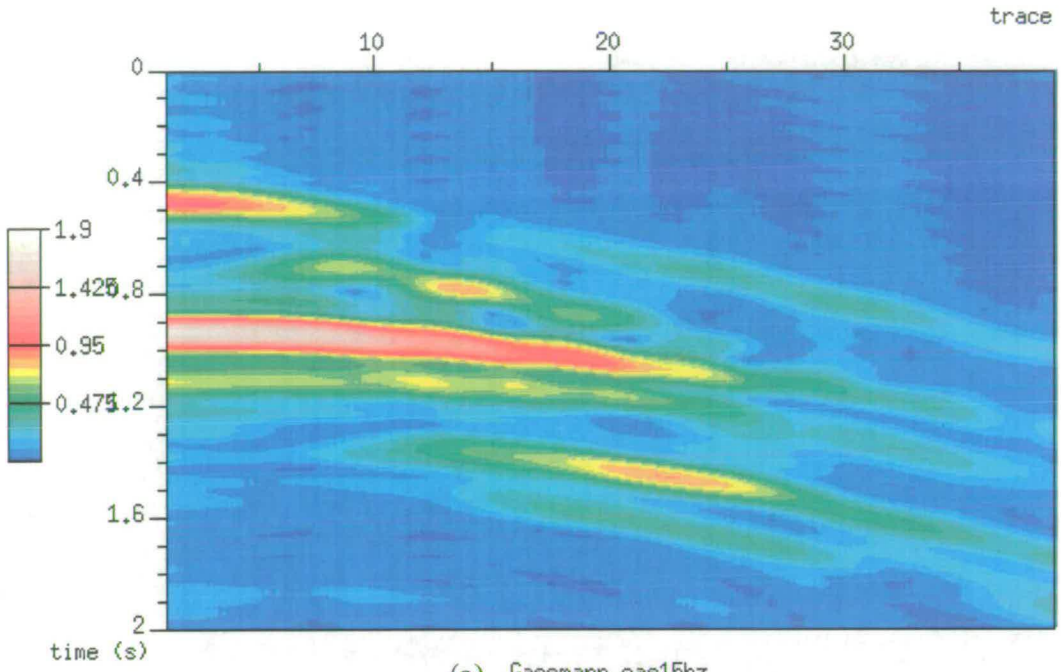

(a) Gassmann_gas15hz

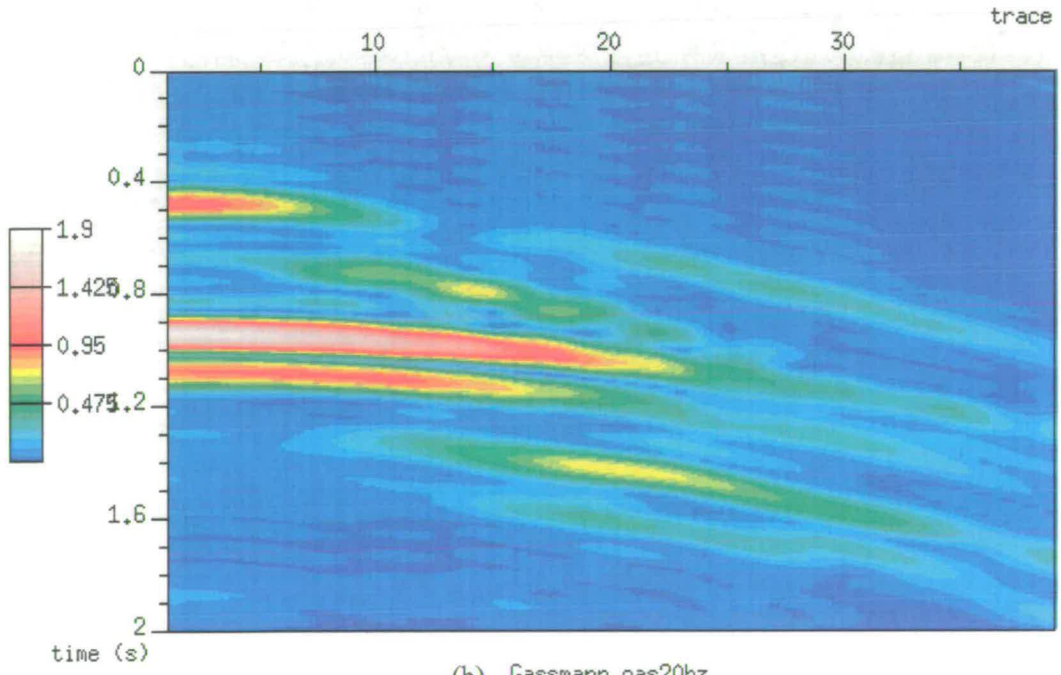

(b) Gassmann_gas20hz

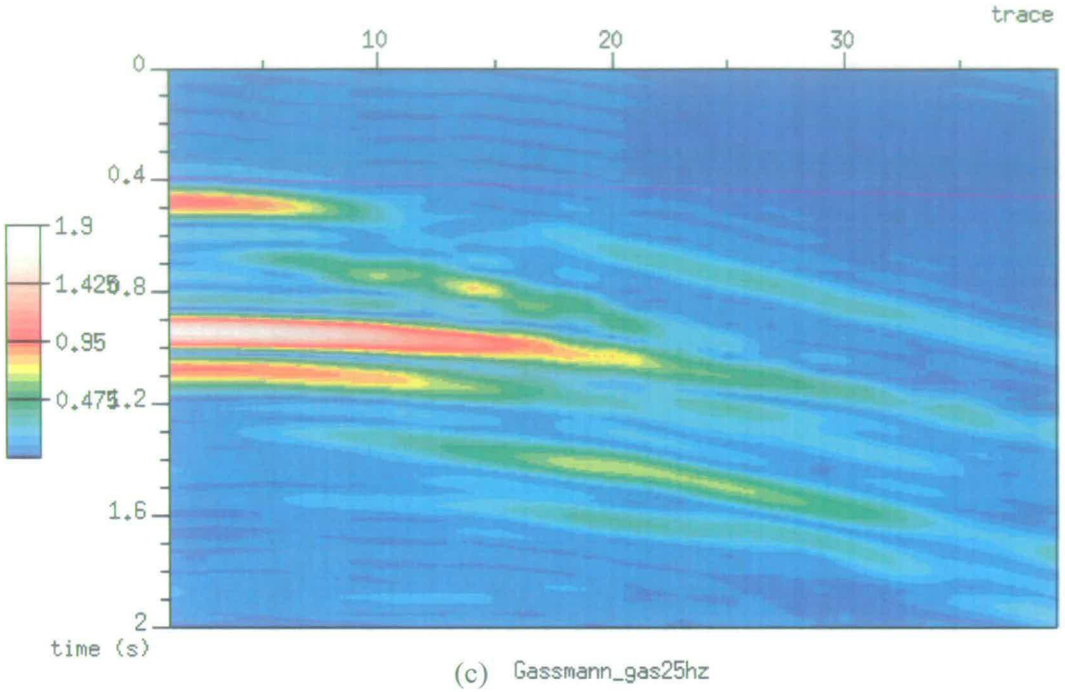

(c) Gassmann_gas25hz

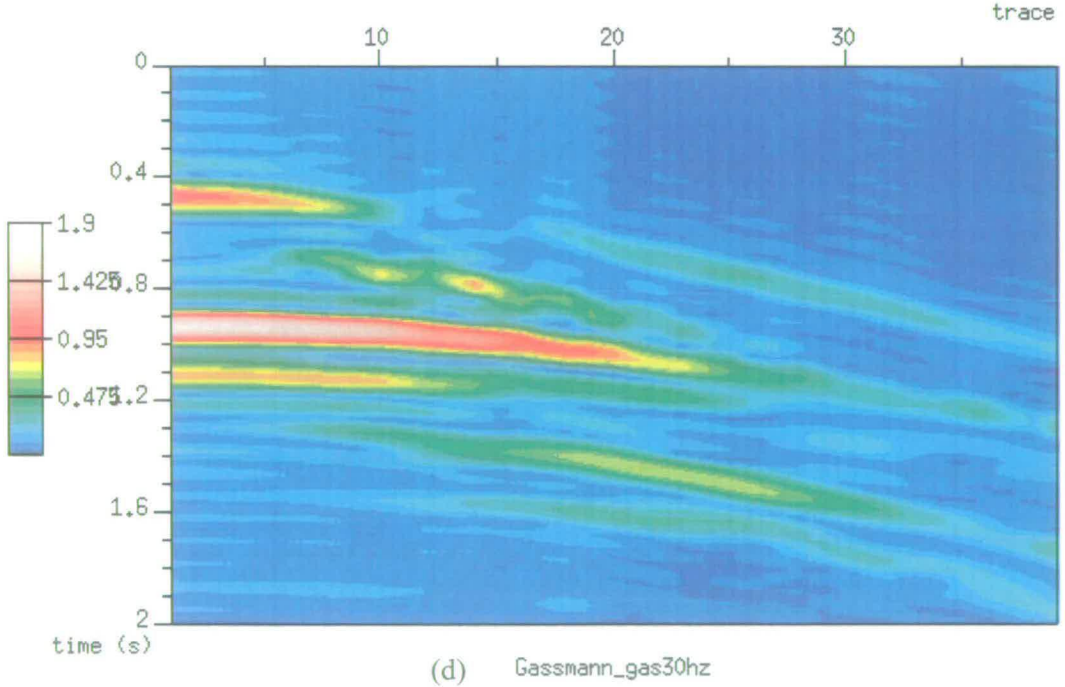

(d) Gassmann_gas30hz

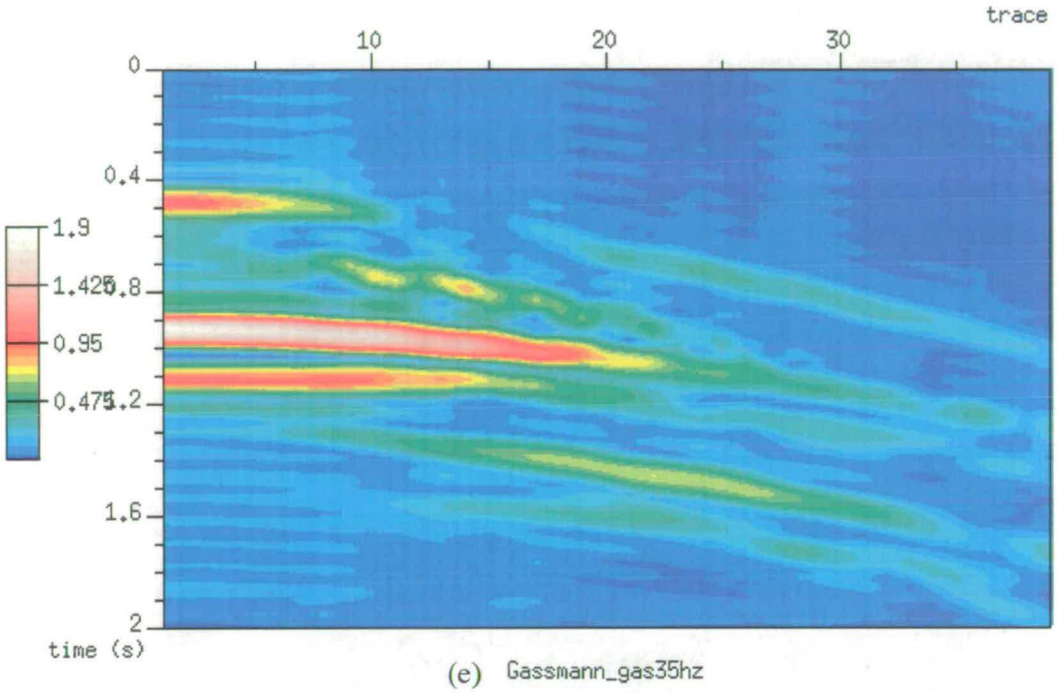

(e) Gassmann_gas35hz

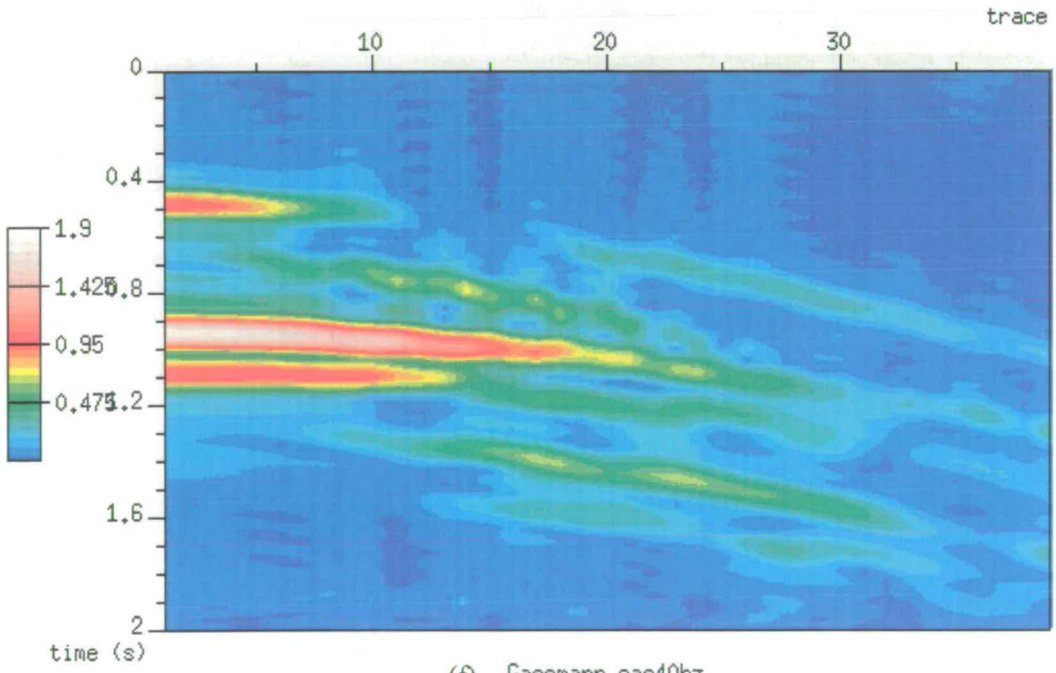

(f) Gassmann_gas40hz

Figure 7.20: Iso-frequency spectra from 15Hz to 40Hz for the gas-saturated thick layer in the low frequency limit case

The same analysis has been applied to three other cases: a dispersive gas saturated model, low frequency limit and dispersive water-saturated models, and iso-frequency spectra are produced. To aid our analysis of the frequency-dependent anomalies from amplitude spectra, I pick the maximum amplitudes of the top PP reflection from the normalized iso-frequency spectra, then average the picked amplitude into low frequency (15-25Hz) and high frequency (30-40Hz) bands. The amplitude curves are plotted in Figure 7.21 for gas-saturated model in the low frequency limit case and dispersive case. For the low frequency limit (Gassmann case), the amplitude curves of low and high frequency bands are very close, which is expected as from Figure 7.20, indicating no attenuation. In the dispersive case, the amplitudes become greater than the low frequency limit. The amplitude of the high frequency 30-40Hz band moves further away from the low frequency 15-25Hz band, which proves that attenuation appears in the model.

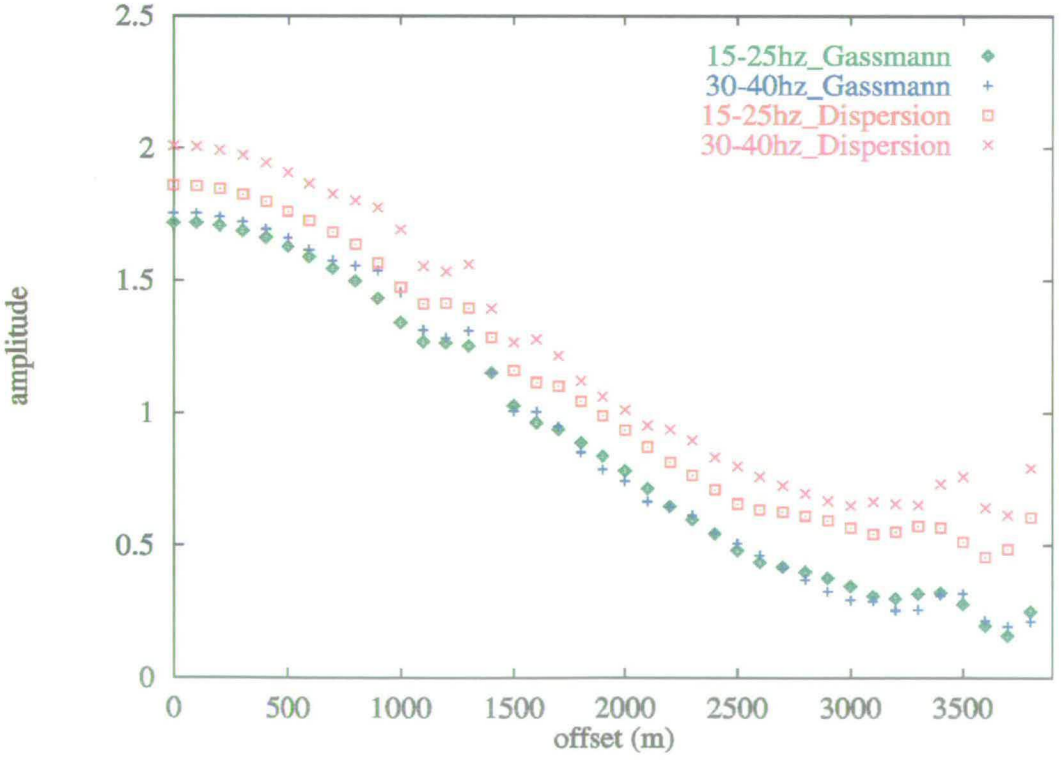

Figure 7.21: The picked amplitude values from the gas-saturated iso-frequency spectra are averaged into low frequency band (15-25Hz) and high frequency band (30-40Hz). Dispersive effect appears in the attenuation case.

Figure 7.22 shows the picked amplitude curves in the low and high frequency band for a water-saturated model. Similar amplitude values appear between low and high frequency band in the low frequency limit (Gassmann) case, which indicates no attenuation. As in the gas-saturated model with the dispersive case, the amplitude of the high frequency band in the water dispersive case has a shift, but this shift is smaller than in the gas-saturated model, which proves that the water-saturated model has a lower attenuation than gas-saturated model in the dispersion cases.

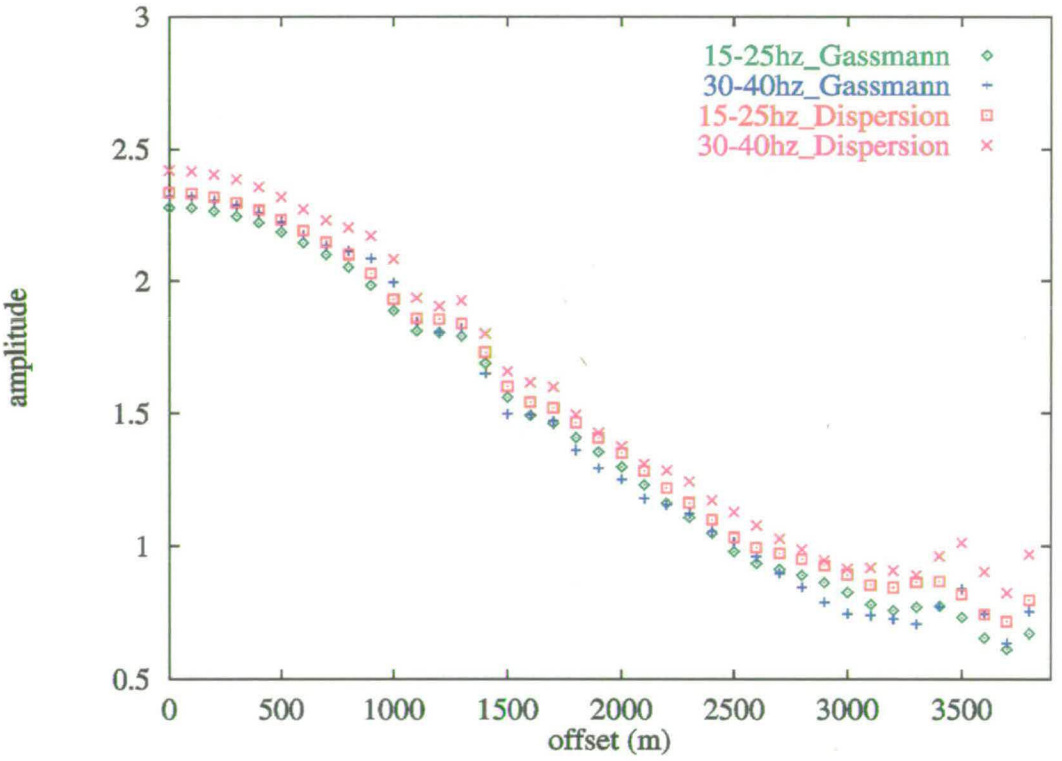

Figure 7.22: The same as Figure 7.21 but for the water-saturated case. Dispersive effect appears in the attenuation case, but less than the gas case.

7.5 Thin-layer model with tuning

Tuning is an important issue in the study area. Based on the above model and well logs, I reduce the thickness of the dispersive layer from 400m to 10m. Since the sand layer is only 10m thick, it is difficult to model this effect as being a traditional

attenuation mechanism. I use our dispersive modeling to explain the behaviour. Another five 10 meter thin layers are added in the model, and the parameters of the blocked model are shown in Figure 7.23. The multi-layered model has two 10m thick sand layers with dispersive properties. The other four interbedded 10m thick layers have pure elastic properties. Like the thick layer model, the overburden of 1km depth is used for spectral balancing. The geometry is the same as the thick layer case.

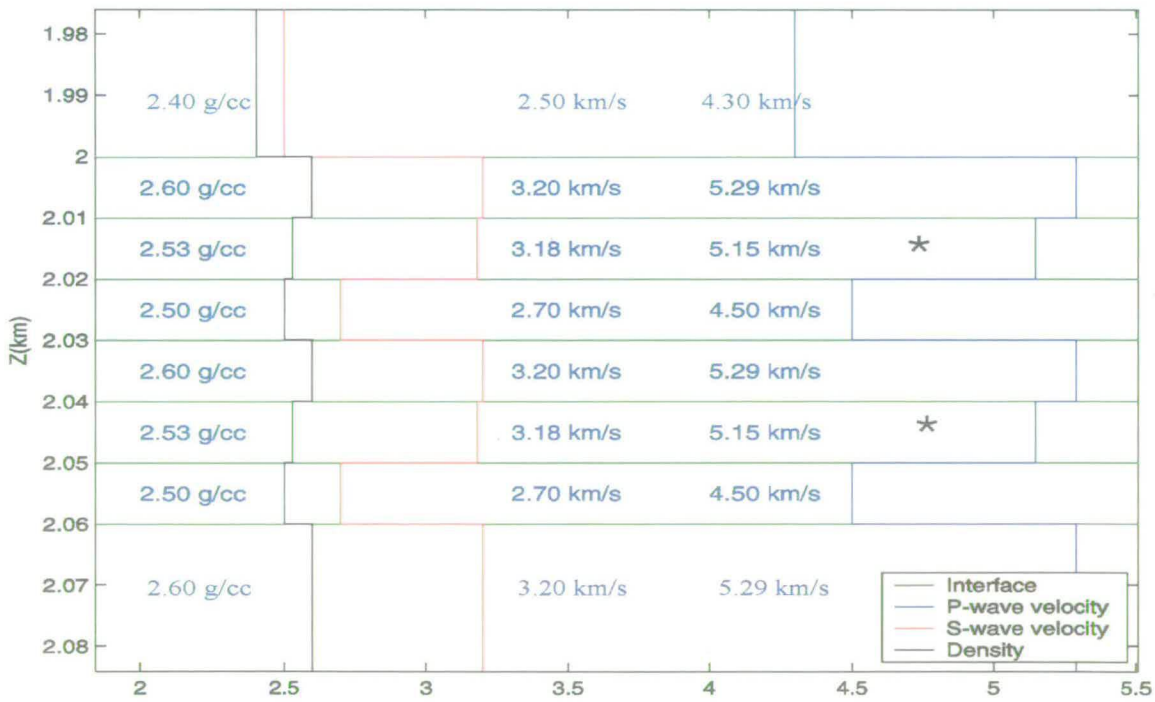

Figure 7.23: The parameters for the multi-thin layer model. The stars indicate the materials with frequency-dependent properties, and the other layers are pure elastic.

Figure 7.24 shows the synthetic seismograms for the multi-layered model with gas saturation for the low frequency limit (Figure 7.24a) and dispersive cases (Figure 7.24b). The reflection at 0.95s is a composite reflection from six thin layers. An amplitude increase can be seen in the dispersion case.

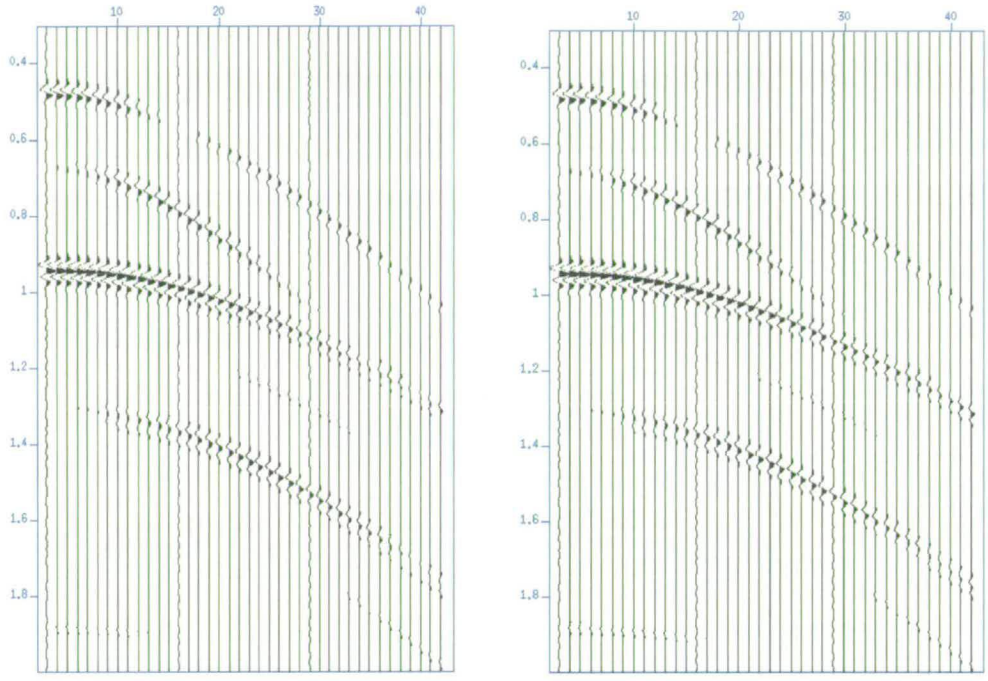

Figure 7.24: The synthetic seismograms for the multi-thin layered model with gas saturation in the low frequency limit case (left, a) and in the dispersion case (right, b)

The amplitude spectra for the multi-thin layers are shown in Figure 7.25. I overlay their spectra (solid line) upon the spectra of the thick layer (in dash line). Compared to the thick layer, a clear peak frequency shift towards higher frequencies appears in the multi-thin layered model for the gas-saturated cases (Figure7.25a), which does not appear to the water-saturated cases (Figure7.25b). This indicates that tuning is fluid-sensitive. Partyka *et al.* (1999) shows the amplitude spectrum interference pattern from a tuned reflection, which defines the relationship between acoustic properties from individual beds that comprise the reflection. However, for a 10m layer, far less than the tuning thickness (about 60m for 20Hz Ricker wavelet), and the seismic bandwidth is a narrow and below 100Hz, no periodic notches in the amplitude spectrum can be shown from the composite reflection of the thin layers.

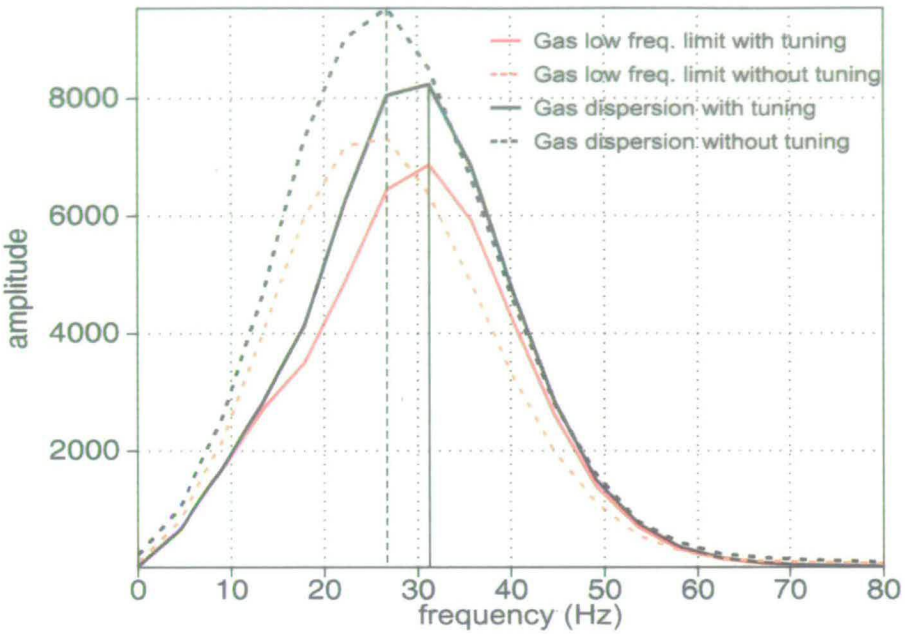

(a) gas saturation case

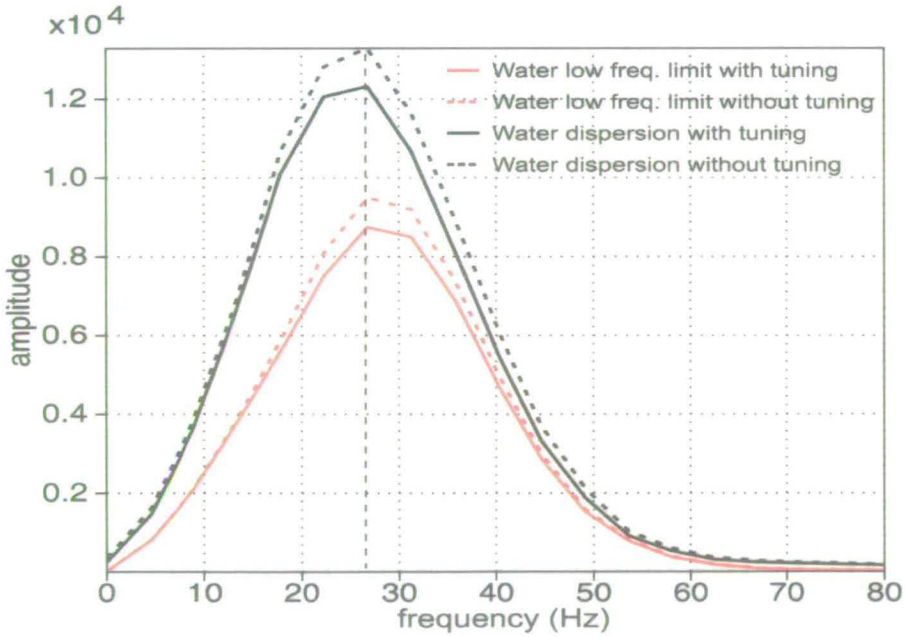

(b) water saturation case

Figure 7.25: Amplitude spectra for the gas and water-saturated multi-layered model at offset 2000m, in solid line, compared to the thick layer without tuning, in dash line. A higher dominant frequency by tuning is shown for the gas-saturated case, but not shown for water-saturated case.

After spectral decomposition and spectral balancing, I produce the iso-frequency sections for the thin layer model. Figure 7.26 shows the picked amplitude in the low and high frequency band for the gas-saturated tuning model for the low frequency limit (Gassmann) and dispersive cases, and Figure 7.27 for the water-saturated tuning model. We can see that tuning has a significant effect on energy distribution. In both the low frequency limit case and dispersive case, a significant amplitude increase appears in the high frequency band, which indicates that tuning boosts the high frequencies. Interestingly, a clear dispersion effect can still be seen in the gas-saturated model. The dispersive case has higher amplitude than the low frequency limit case, which does not happen to the water-saturated tuning model. We can also observe that the tuning effect decreases with offset. This is consistent with Bakke and Ursin (1998) who claim that the tuning effect on the amplitude is proportional to the inverse of the travel time.

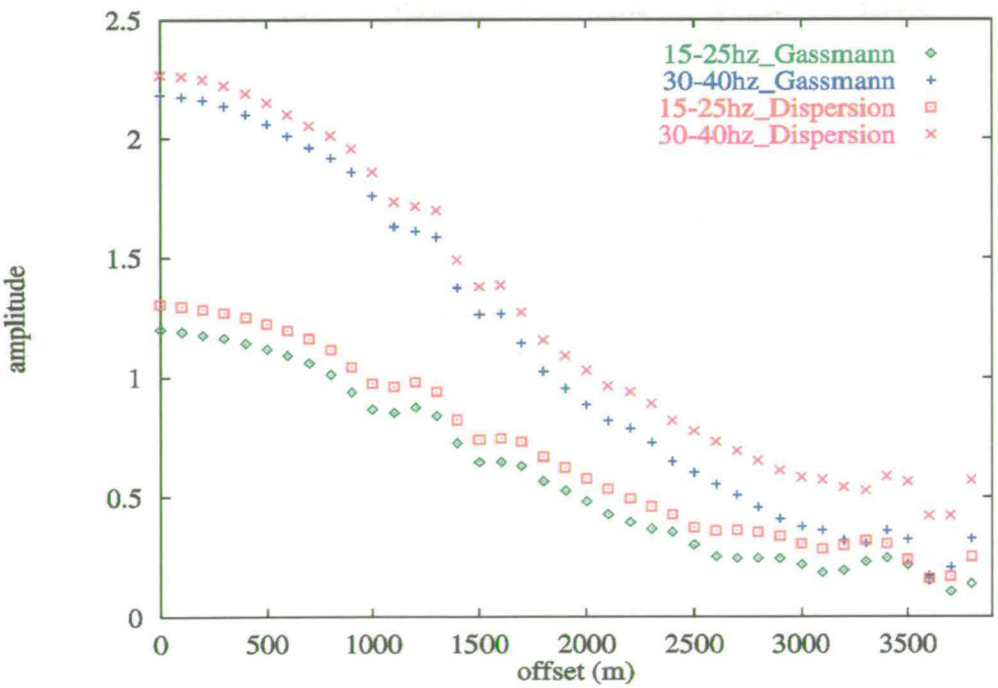

Figure 7.26: The picked amplitude values from the gas-saturated multi-thin layered model. Iso-frequency spectra are averaged into a low frequency band (15-25Hz) and a high frequency band (30-40Hz). Tuning boosts the high frequencies, but dispersion effect can still be seen in gas case.

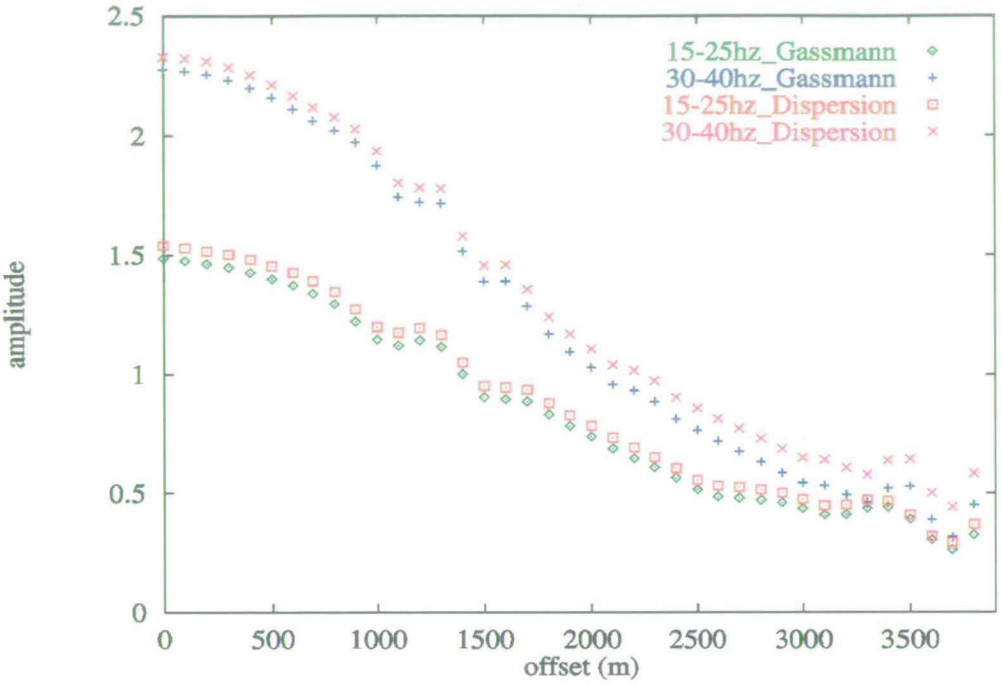

Figure 7.27: The same as Figure 7.26 but for the water-saturated case. Also tuning boosts the high frequencies, but the dispersive effect is reduced in the water-saturated case.

7.6 Discussion and conclusion

Numerical modeling has suggested that fluid-related dispersion may have a pronounced effect on AVO behaviour. It is a different matter to detect robustly such effects in field data or to demonstrate that the signatures from simple single layer models persist into more complicated multi-layer cases. This chapter has addressed these questions through numerical modeling and the analysis of field data.

In the first data example the gas saturation can be associated with a clear spectral signature, and the effect can actually be modelled as the low frequency effect in terms of a simple single layer model, provided we account for velocity dispersion. Nevertheless, we know that in practice we always deal with more complicated geological models. In particular, tuning is always present to a certain degree. Since our reservoir is only 10 m thick, the tuning effect is not sufficient to produce a significant spectral response for such thin reservoirs at seismic frequencies.

I have also analysed data from a known gas reservoir associated with a dim-spot on the seismic section. Following the approach set out in Chapman *et al.* (2006) and Odebeatu *et al.* (2006), I have carried out a thorough traditional AVO analysis and demonstrated that the dimming is consistent with Gassmann modeling. For such a case, the dispersive modeling predicts that the dimming should be accompanied by a shift of the reflection energy towards higher frequencies. Application of spectral decomposition and balancing reveals that such an effect is indeed visible.

Introducing dispersion into the synthetic models allows us to reproduce the observed effect. It is important to consider realistic velocity models, since in practice tuning will distort the spectral response. It is found that the introduction of tuning does indeed make the analysis difficult, but that the effect of dispersion can still be observed. Consequently, I conclude that the seismic response in the data is thus dominated by gas-related dispersion in the presence of tuning.

The interpretation of the spectral response of reflection data is fraught with difficulties. Ebrom (2004) has listed many mechanisms in which false spectral anomalies can be induced by processing techniques and other factors. For these reasons, in Chapter 8, I further verify our interpretation by analysing laboratory data that simulates the survey on a physical model constructed to correspond to Daqing area under consideration. The physical model is saturated with water, oil and gas respectively. I find that the characteristic dispersion effect discussed in this chapter is also seen in the data from the physical model when it is gas saturated. This supports the interpretation put forward in this chapter.

The velocity dispersion effect on converted PS-waves has also been modelled for a simple single layer model. The direct observations are the low frequency phenomena for both water and gas cases, which is consistent with PP-waves. However, both gas and water saturation demonstrate a similar attenuation. Unbalanced spectra for high frequency limit water saturated case may be due to the

small reflection coefficient and the polarity reversal. Further work on synthetic and real data is needed to confirm these findings.

Chapter 8: Application of frequency-dependent variations for fluid detection in thin-bedded sands

8.1 Introduction

Traditional P-wave AVO analysis has been very successful for characterizing gas deposits in sand reservoirs. The presence of gas lowers the P-wave velocity, and induces a Class III AVO response with a high to low impedance contrast (Castagna, 1993). In recent years, due to the improvement in acquisition technology, the bandwith of seismic data has significantly improved and this has made it possible to study the frequency-dependent variations in the seismic data. Castagna *et al.* (2003) showed that with Class III AVO, that the presence of gas will cause the seismic reflection energy to shift towards low frequencies and this is usually referred to as the low frequency gas shadow. Utilizing spectral decomposition, the low-frequency shadow can be isolated in the seismic data, and it becomes an important direct-hydrocarbon indicator. Ebrom (2004) gave a comprehensive analysis of the mechanisms of low-frequency effects in P-wave seismic data. He listed ten possible reasons for the presence of low-frequency shadows in stacked and pre-stacked data, of which gas-induced dispersion is a significant diagnostic feature of gas deposits. Since then the use of spectral decomposition for evaluating the low-frequency gas shadow has become more and more popular with the industry (Sinha *et al.*, 2005; Chapman *et al.*, 2005).

In contrast, the analysis of Class I AVO in a low-to-high impedance contrast is much more subtle and difficult compared with Class III AVO. As shown in Chapter 7, in this case, the presence of gas will cause the reflection energy to shift to the high-frequency end, forming a high frequency bright spot, instead of a low-frequency shadow. Further complications can arise in the case of thinly inter-

bedded sand and shale sequences due to tuning and wave interference. In order to understand the seismic response in such complicated situations, eleven-layer and fifteen-layer inter-bedded sand/shale physical models were built and acoustic seismic data were acquired in the laboratory for different pore fluids including water, oil and gas saturations. The physical modelling dataset consists of six 2D single-side spreading P-wave surveys, and six 2D fixed-offset surveys for the two physical models with three fluid saturations.

In this chapter, utilizing the spectral decomposition technique, I analyze this physical modelling dataset to evaluate the frequency dependent variation in the different fluid saturations. Our aim is to verify the findings in Chapter 7, and investigate if the abnormal high value of the dispersion and attenuation related to a gas deposit can be detected in the presence of a thin-layer tuning effect. Since the physical models are Class I AVO sands, they served as good examples for evaluating the high frequency effect predicted in Chapter 7.

8.2 The physical model

One of real data examples shown in Chapter 7 is from the Daqing oilfield in Northeast China, and the reservoir consists of inter-bedded thin sands and shale. The physical model is specially built for understanding the seismic response in such geological settings. Compared with numerical modelling, seismic physical modelling is closer to reality, particularly for simulating effects of layering, lithology and fluid saturations of the subsurface. Numerical modelling only reflects the rock physical model used for simulating the fluid-rock interactions, and does not necessarily represent the real physical situation.

Figure 8.1 shows the physical model used in the study, which consists of a thick overburden layer overlying several inter-bedded simulated sand/shale thin layers. The overburden is made of epoxy resin, of thickness 50.4mm and P-wave velocity

2440m/s. The inter-bedded thin layers are composed of two periodic thin layers (Figure 8.1). One layer is made of glass, simulating shale, and the other is made of SiO_2 and epoxy resin, compacted into thin layer, simulating sands. The average thickness of the glass layer is 1.22mm, velocity 2490m/s, and density 1.18g/cc. The sand layer is 1.434mm thick, porosity 17%, matrix P-velocity 3245m/s, bulk P-velocity 2580m/s when air-saturated, and density 1.69g/cc. For comparison, two thin-layer models are built: one has five sand layers and the other has seven. The total thickness of the inter-bedded layer is 19.8mm for the seven-sand-layer model. The horizontal dimensions of the physical model is 450mm long, and 300mm wide. Table 8.1 shows the scale ratios between real geology and the physical model, therefore the up-scaled depth of top inter-bedded thin layers is 706m, and the thickness of the 15 thin layers (seven sand layers) is 59.4m. The up-scaled model is 1.35km long and 0.9km wide. The ratio between the seismic wavelength and the individual thickness of the thin layers is greater than 10.

	Up-scaled model	Physical model
Velocity (1:1)	2500 (m/s)	2500 (m/s)
Frequency (1:3000)	35Hz	105kHz
Wavelength (λ) (3000:1)	50m	17mm
Sample rate (3000:1)	0.6ms	0.2 μs
Thin layer thickness (h)	< 5m	1-1.7mm
λ / h	>10	>10

Table 8.1: The scaling ratio used in the physical modelling study.

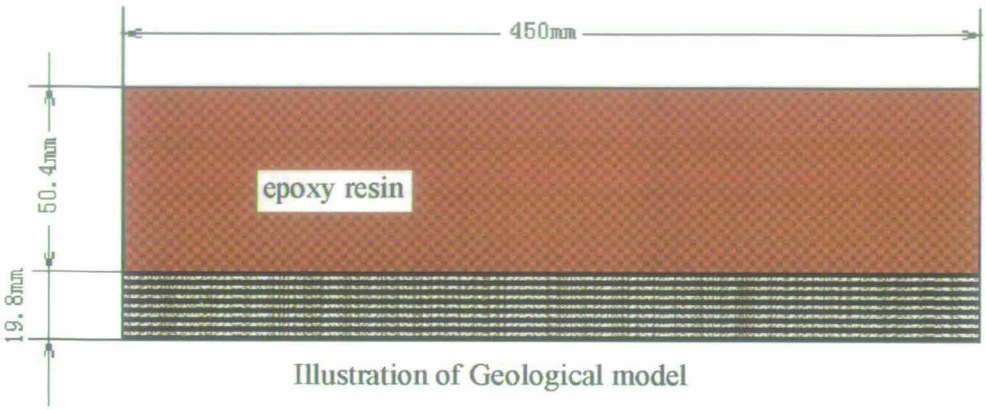

Illustration of Geological model

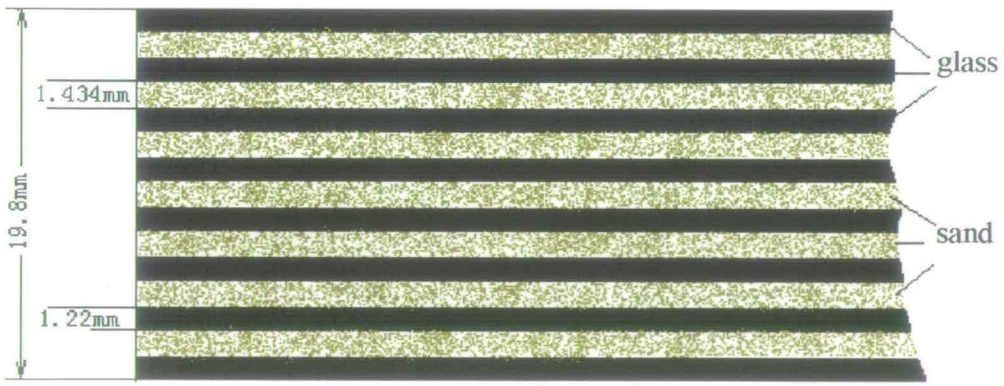

Enlargement illustration of interbedded thin layers

Figure 8.1: The physical model used in the study. Top panel shows the model structure consisting of an overburden layer overlaying a thin-layer reservoir. Bottom panel shows the internal structure of the thin-layer reservoir, consisting of two periodic shale/sand thin layers. The shale is simulated using glass, and the sand layer is simulated using coarse sand and resin. Here the reservoir contains seven sand layers.

8.3 Data acquisition and characteristics

A real dimension of the physical model was described in the previous section, and an up-scaled dimension will be used thereafter. The data are acquired in a water tank with a water-depth of 555m (Figure 8.2). First, a conventional single-side 2D geometry is used. The source and receivers are moved along the water surface. As shown in Figure 8.2, a total of 50 shots at 30m intervals have been acquired. There

are 80 receivers for each shot, and the offset ranges from 60m to 1008m with 12m interval. The sample rate is 0.6ms. Secondly, a fixed offset 2D survey is used. The offset is 90m and a total of 120 traces are acquired, which is treated as a zero-offset data.

During acquisition, the porous sand layer in the physical model is fully saturated with gas, water, and oil sequentially. This is repeated for both the seven-sand-layer and five-sand layer models. In this chapter I will process the 2D survey to produce a stacked section, and also evaluate the fixed-offset (90m) survey for seven-sand-layer model.

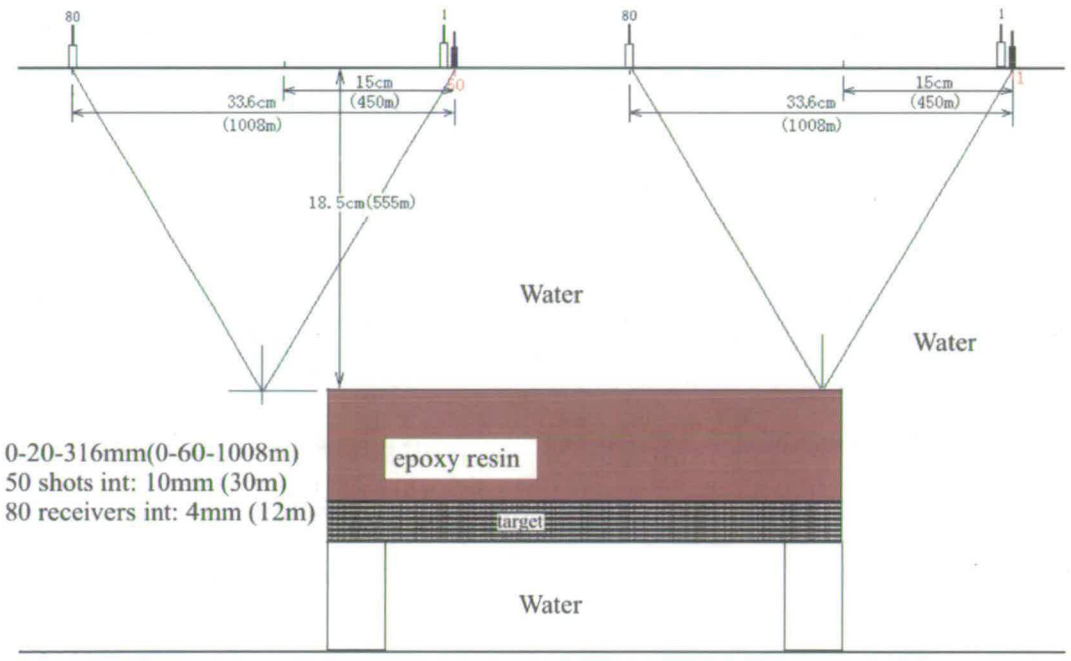

Figure 8.2: Acquisition geometry of the physical modelling experiment.

For classifying the AVO type, I generate a pure elastic model using similar parameters of the physical model. The parameter of the pure elastic numerical model is shown in Table 8.2. This model is composed of 11 thin layers, each 5 meters thick. The seismogram in Figure 8.3 shows the first event from the thin-layer reservoir is located at a depth of 650m. The seismogram shows the primary

reflections only, other effects such as multiples, geometry spreading, transmission losses, are not included. We can see that the amplitude decreases with offset. This indicates that the AVO response of the physical model is a Class I type, which is also confirmed by the CDP gathers of the physical-modelling data.

		Density (g/cc)	Vp (Km/s)	Vs (Km/s)	Thickness (m)
1	water	1	1.80	0.379	500
2	overburden	1.18	2.44	0.931	150
3	glass	1.18	2.49	0.974	5
4	sand	1.69	2.58	0.105	5
5	glass	1.18	2.49	0.974	5
6	sand	1.69	2.58	0.105	5
7	glass	1.18	2.49	0.974	5
8	sand	1.69	2.58	0.105	5
9	glass	1.18	2.49	0.974	5
10	sand	1.69	2.58	0.105	5
11	glass	1.18	2.49	0.974	5
12	sand	1.69	2.58	0.105	5
13	glass	1.18	2.49	0.974	5
14	water	1	1.80	0.379	195

Table 8.2: The elastic parameters of the numerical model.

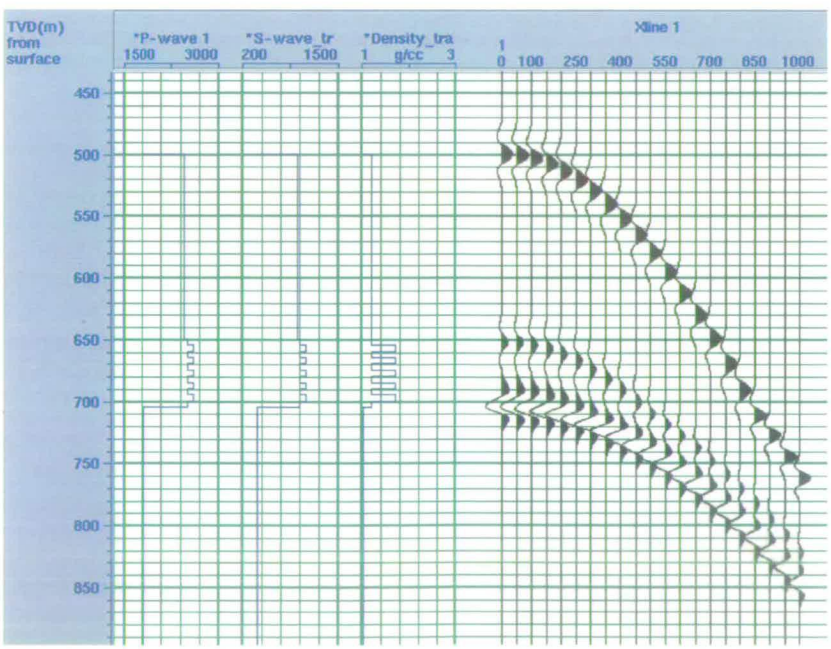

Figure 8.3: Illustration of the Class I AVO response by pure elastic-wave modelling (the amplitude decreases with offset at 650m, 35Hz Ricker wavelet)

8.4 Analysis of the 2D fixed-offset data

I start our analysis from the fixed offset 90m data, which is equivalent to zero-offset data. Figure 8.4 shows the seismic record of the seven-sand-layer model for the different fluid saturations (water, oil and gas). Note that the reflection events are not flat; the event (0.76s) in the water-saturated model tilts more than the other two cases. This variation is caused by some systematic errors in the model or acquisition system, since the model is isotropic in theory. However, this tilt can be easily corrected using a static correction method during processing, and will not affect our analysis of the amplitude response. As shown in Figure 8.4, a strong reflection appears at the bottom of the oil-saturated model, whilst the corresponding reflection is weak and scattered in the gas-saturated model.

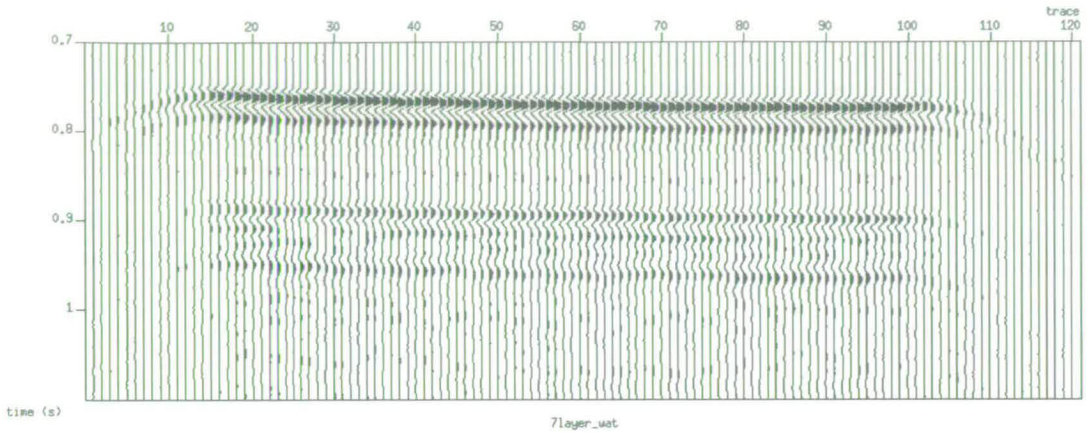

(a) water-saturated model

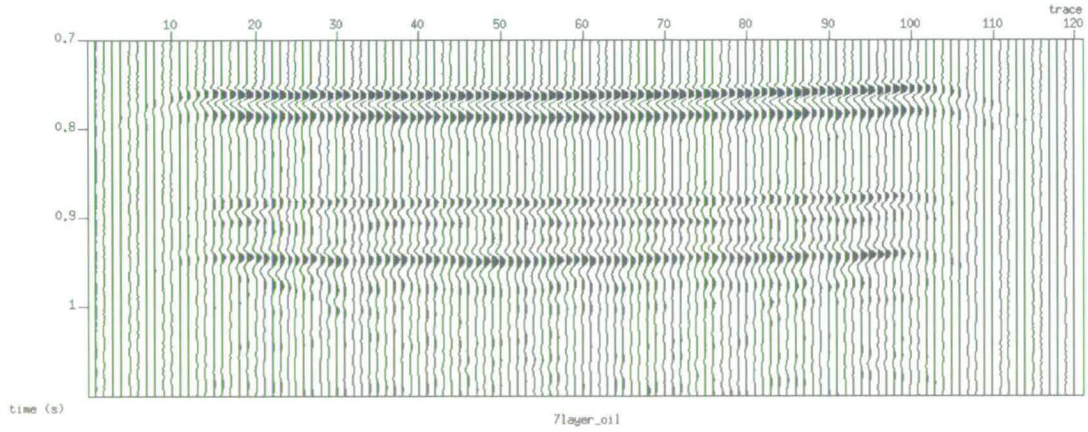

(b) oil-saturated model

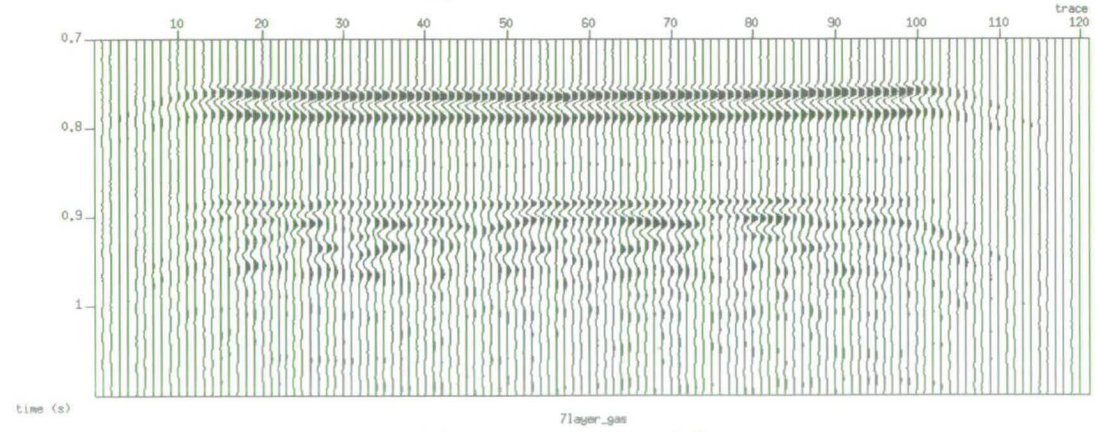

(c) gas-saturated model

Figure 8.4: The 2D fixed-offset (90m) data for (a) water-, (b) oil- and (c) gas-saturated model with seven sand layers. Note the tilt in the water-saturated case.

8.4.1 Analysis of amplitude spectra

Figure 8.5 shows the amplitude spectra of the reflection event from the water bottom (the top of the overburden layer) for the three different fluid saturations. The spectra appear to be similar for all three saturations, as expected. I average the amplitude spectra with a time window of 150ms between trace number 30 and 80 (see Figure 8.4), and plot them in Figure 8.6a. The spectral ratio are plotted in Figure 8.6b. This reflection is then used as a reference for spectrum balancing. Figure 8.7 shows the spectra of the reflection event from the thin-layer reservoir for the three fluid saturations of water, oil and gas. A decrease in the low frequency content can be observed in the gas-saturated model relative to other saturations. Again I average the amplitude spectra with a time window of 0.85s to 1s between trace number 30 and 80, and they are plotted in Figure 8.8a. Spectral ratios were formed by dividing oil and gas saturated average spectra by water saturated average spectrum (Figure 8.8b).

We can also see the presence of notches in the water- and oil-saturated models in Figure 8.8a, suggesting the presence of a tuning phenomenon in the thin beds. The notches appear at similar frequencies at the low-frequency ends for the oil- and water-saturated models. At the high frequency ends, a clear notch can only be observed in the oil-saturated data. Interestingly, there is no notch in the gas-saturated model. The tuning-induced notches are relevant to the fluid saturation. As expected, the amplitude of the gas-saturated model is lower than that of the oil-saturated model. However, the amplitude of the water-saturated model is not the highest in Figure 8.8a. This may possibly be explained by the fact that the water-saturated model is not sealed when put into the water tank, whilst the gas and oil-saturated models are sealed when put into the tank.

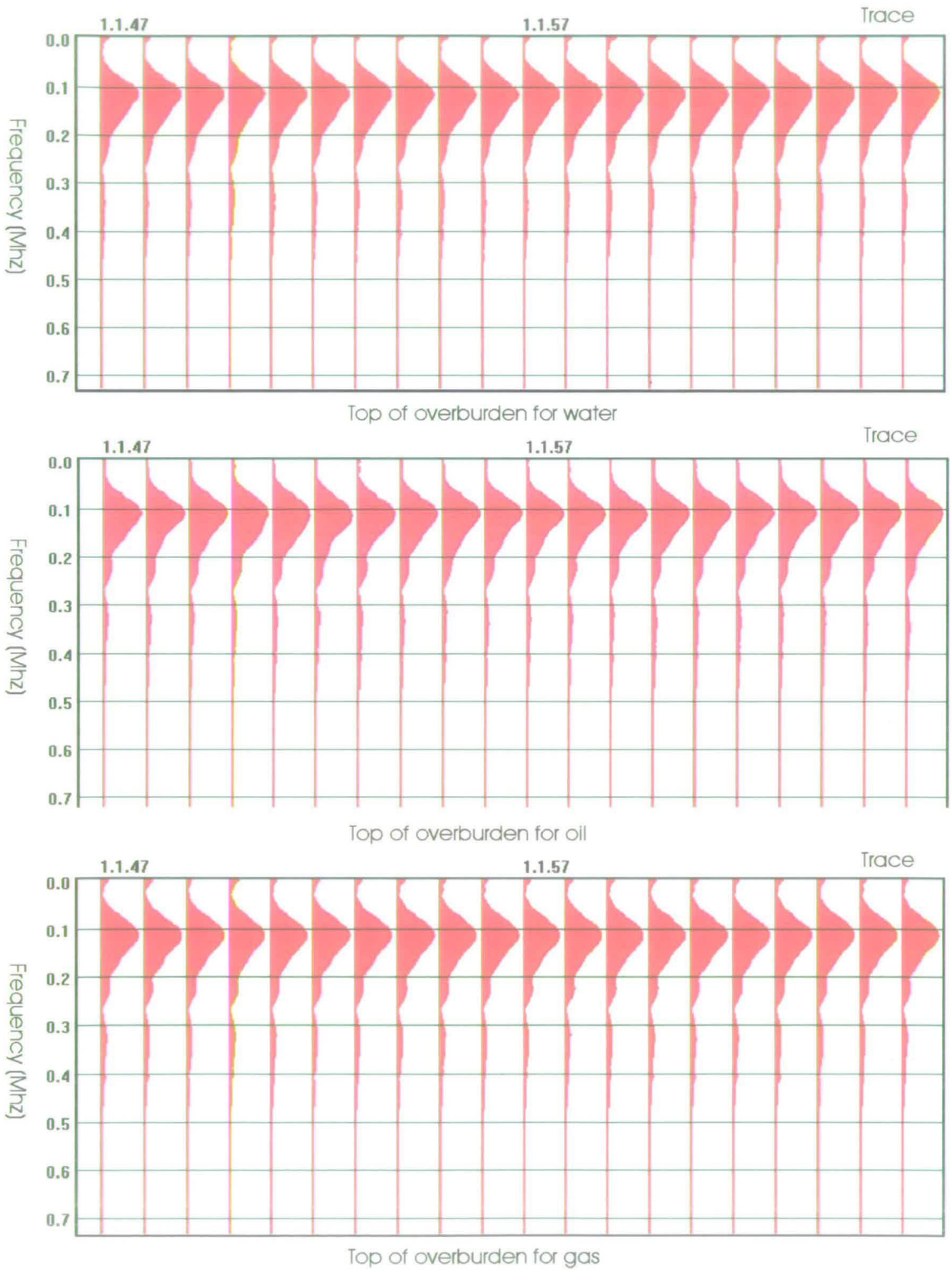

Figure 8.5: The amplitude spectra of the reflections from the water bottom (the top of the overburden) for the seven sand-layered model.

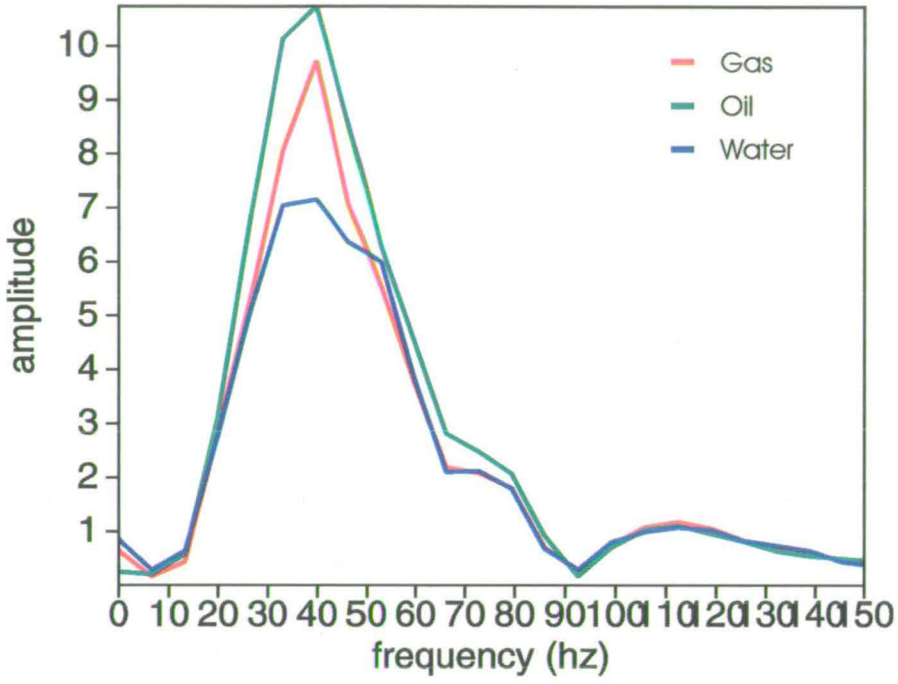

Figure 8.6a: The seven sand layers' average amplitude spectra for the top of the overburden between trace number 30 and 80, with a time window of 150ms, sample rate of 0.6ms.

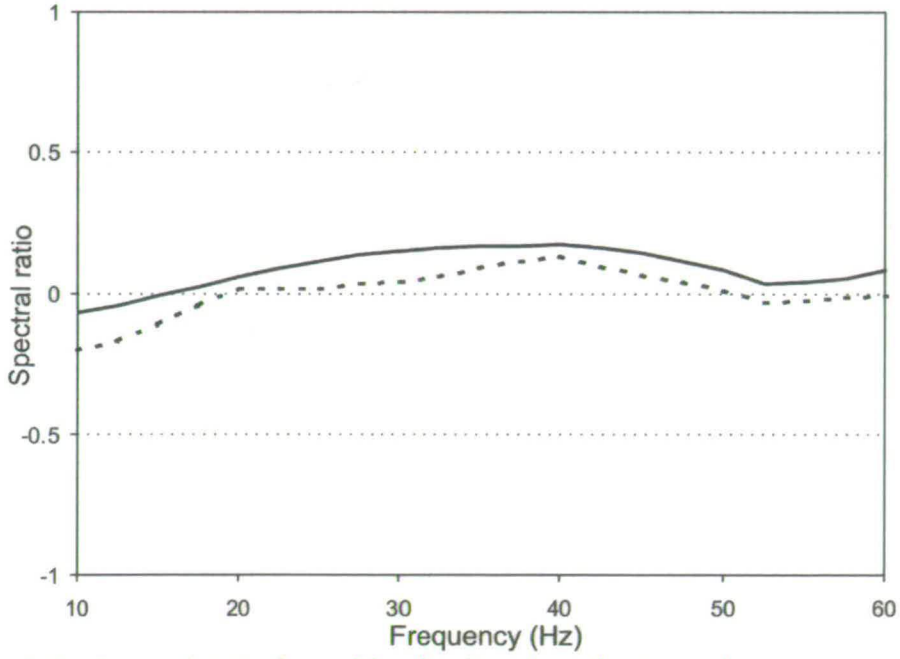

Figure 8.6b: Spectral ratio formed by dividing the oil saturated average spectrum by the water saturated average spectrum (solid line) and dividing the gas saturated average spectrum by the water saturated average spectrum (dot line).

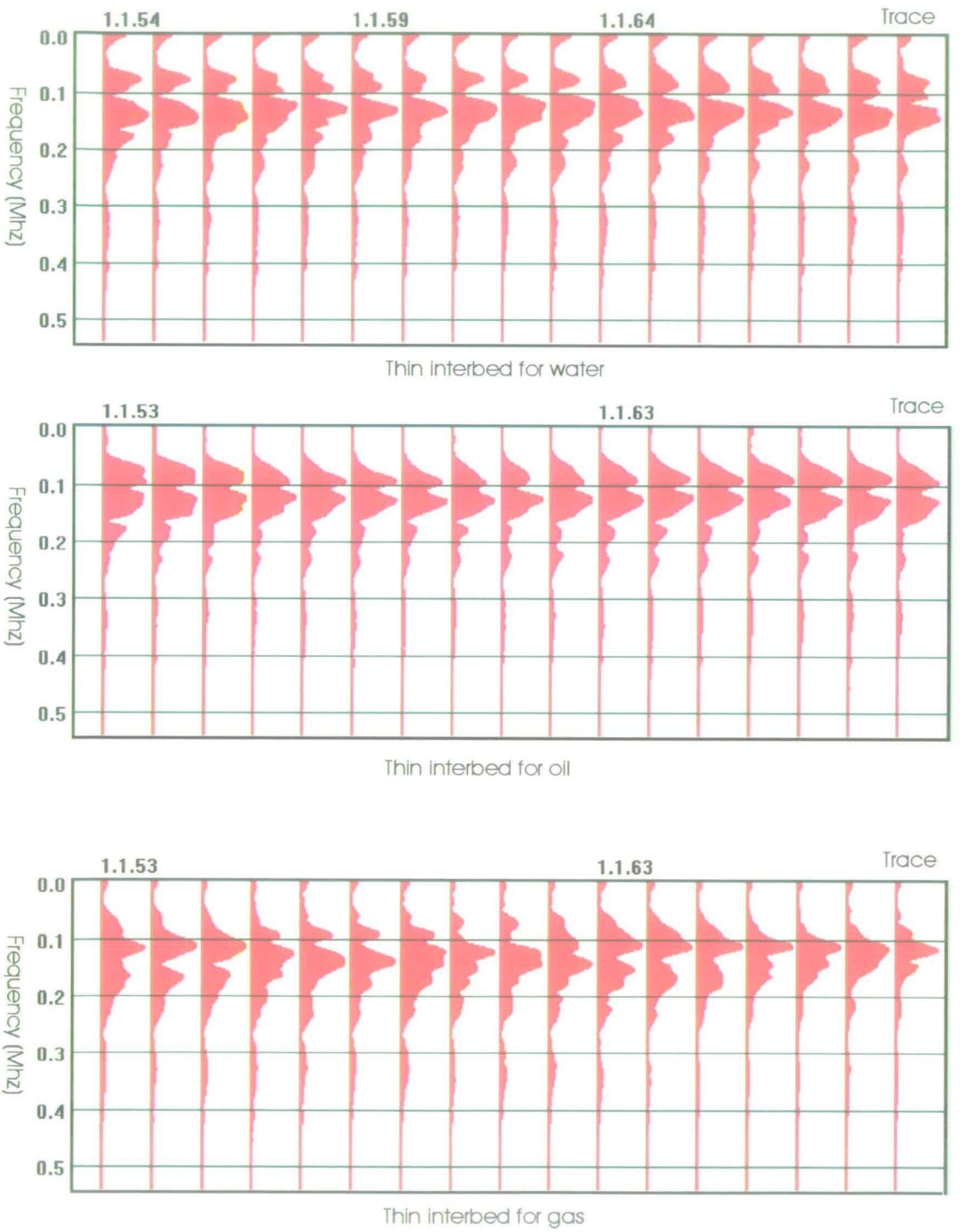

Figure 8.7: The amplitude spectra of the reflections from the thin-layered reservoir for the seven sand-layered model in Figure 8.4, for different fluid saturations. There is a reduction of amplitude in the low frequency part of the gas-saturated model.

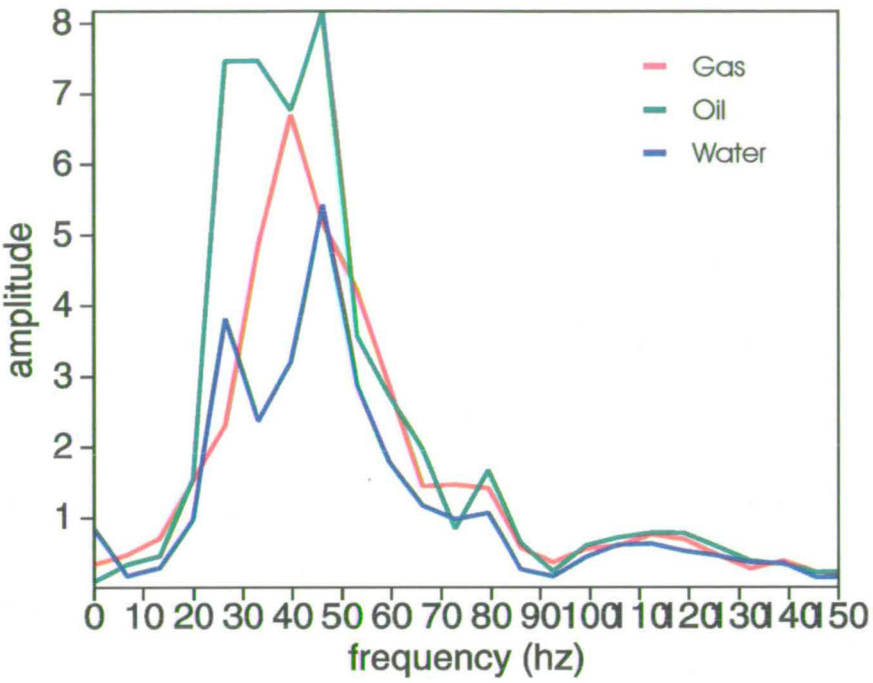

Figure 8.8a: The average amplitude spectra for the thin beds between trace number 30 and 80, with a time window of 150ms, and sample rate of 0.6ms.

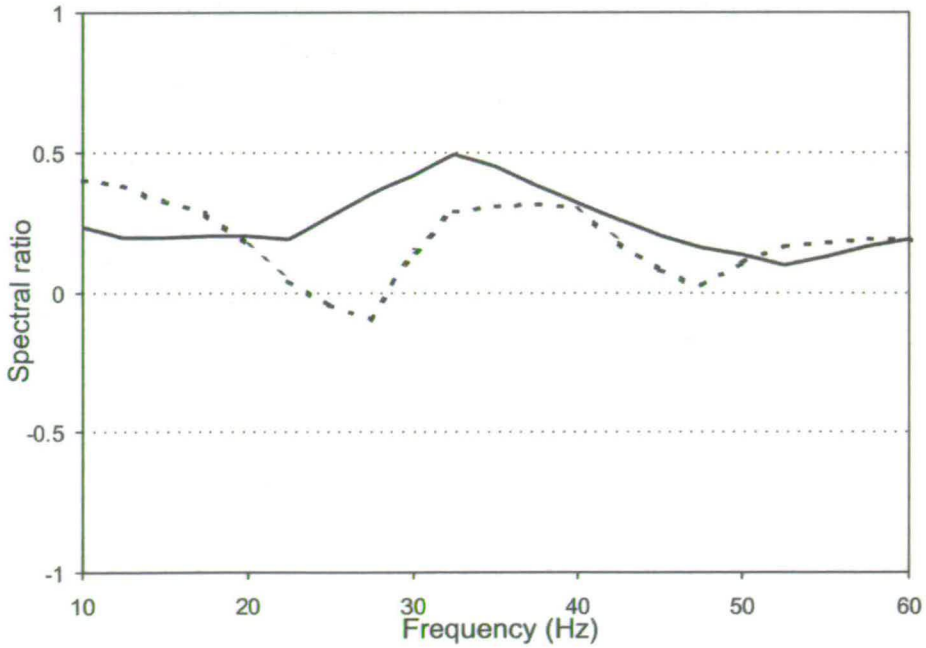

Figure 8.8b: Spectral ratio formed by dividing the oil saturated average spectrum by the water saturated average spectrum (solid line) and dividing the gas saturated average spectrum by the water saturated average spectrum (dot line).

8.4.2 Application of spectral decomposition

In this section, I apply the CWT spectral decomposition method (Liu, 2006) to the zero-offset data in Figures 8.4, in order to evaluate the frequency-dependent variations in the physical models. Figures 8.9 to 8.11 show the instantaneous spectra for the data in Figure 8.4 (the seven-sand-layer model) in the locations of Trace 40, 60 and 80, respectively. Spectral balancing has been applied to the data using the top of overburden layer (the water bottom) as the reference point. The iso-frequencies from 25Hz to 60Hz, at 5Hz intervals, are plotted together to display the frequency-dependent variations. The systematic amplitude increases, which are displayed in the gas-saturated model, indicate the high frequency effect, which does not appear in the water- and oil-saturated cases. The same procedure has been applied to trace 30 (Figure 8.12), where the amplitude is the weakest compared to the other locations. We can see still see systematic frequency variations in the gas-saturated case. This analysis also reveals that the model is not homogeneous, nor azimuthally isotropic, as expected. This may be resulted from the lateral variations in the model due to the compaction process. However, it does not invalidate our analysis of the frequency-dependent variations.

To examine this phenomenon across the section, I also generate iso-frequency sections for the data in Figure 8.4 for the three different fluid saturations, e.g. water, oil and gas, between trace numbers 20 to 80. The reflection energy in the iso-section at frequency 25Hz is very different for all three cases. Except for that, the reflection energy from 30Hz to 40Hz for the water- and oil-saturated models is similar and comparable with each other, and hence the figures are not shown here. Instead I focus on the gas-saturated case. As shown in Figure 8.13, in most of part of the section, the energy is very scattered. However, in the section from trace 55 to 65, there is a clear shift of energy to the high frequency end, forming high-frequency bright spots.

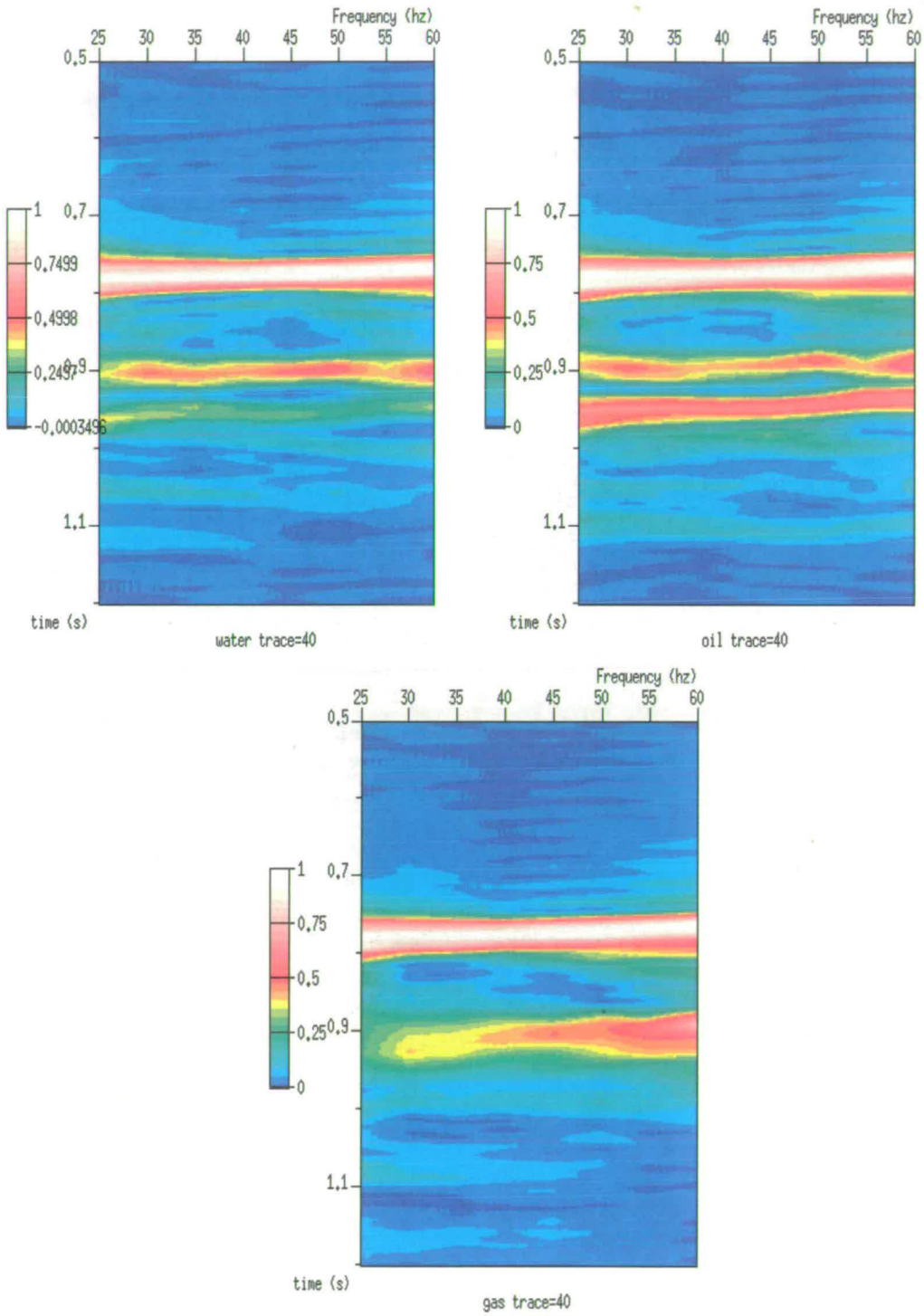

Figure 8.9: Instantaneous spectra for iso-frequency 25Hz to 60Hz, at 5Hz intervals, for the water-, oil-, and gas-saturated models with seven sand layers, in the location of trace 40. The high frequency effect (0.9s) is displayed in the gas-saturated model.

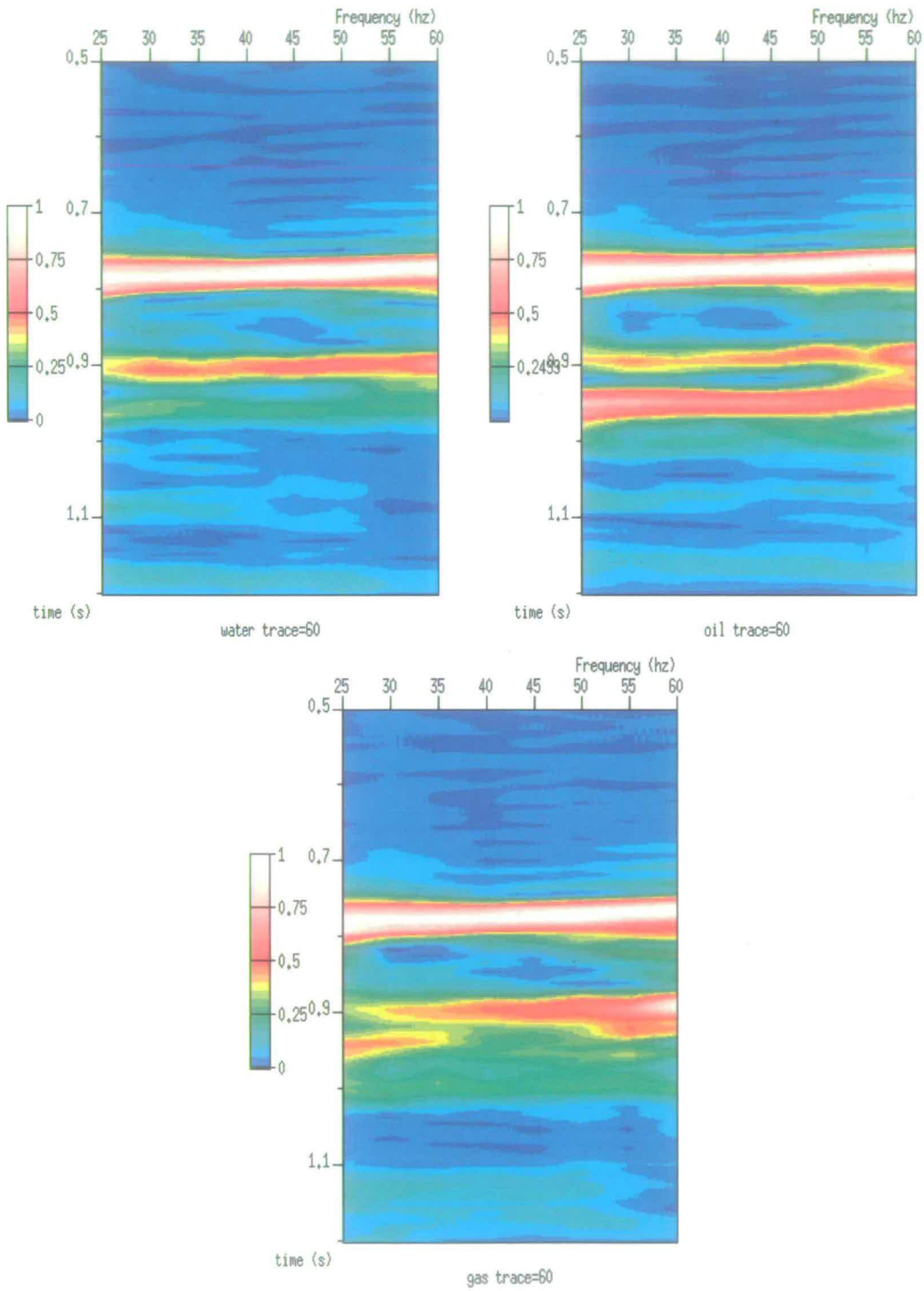

Figure 8.10: Instantaneous spectra for iso-frequency 25Hz to 60Hz, at 5Hz intervals, for the water-, oil-, and gas-saturated models with seven sand layers, in the location of trace 60. The high frequency effect (0.9s) is displayed in the gas-saturated model.

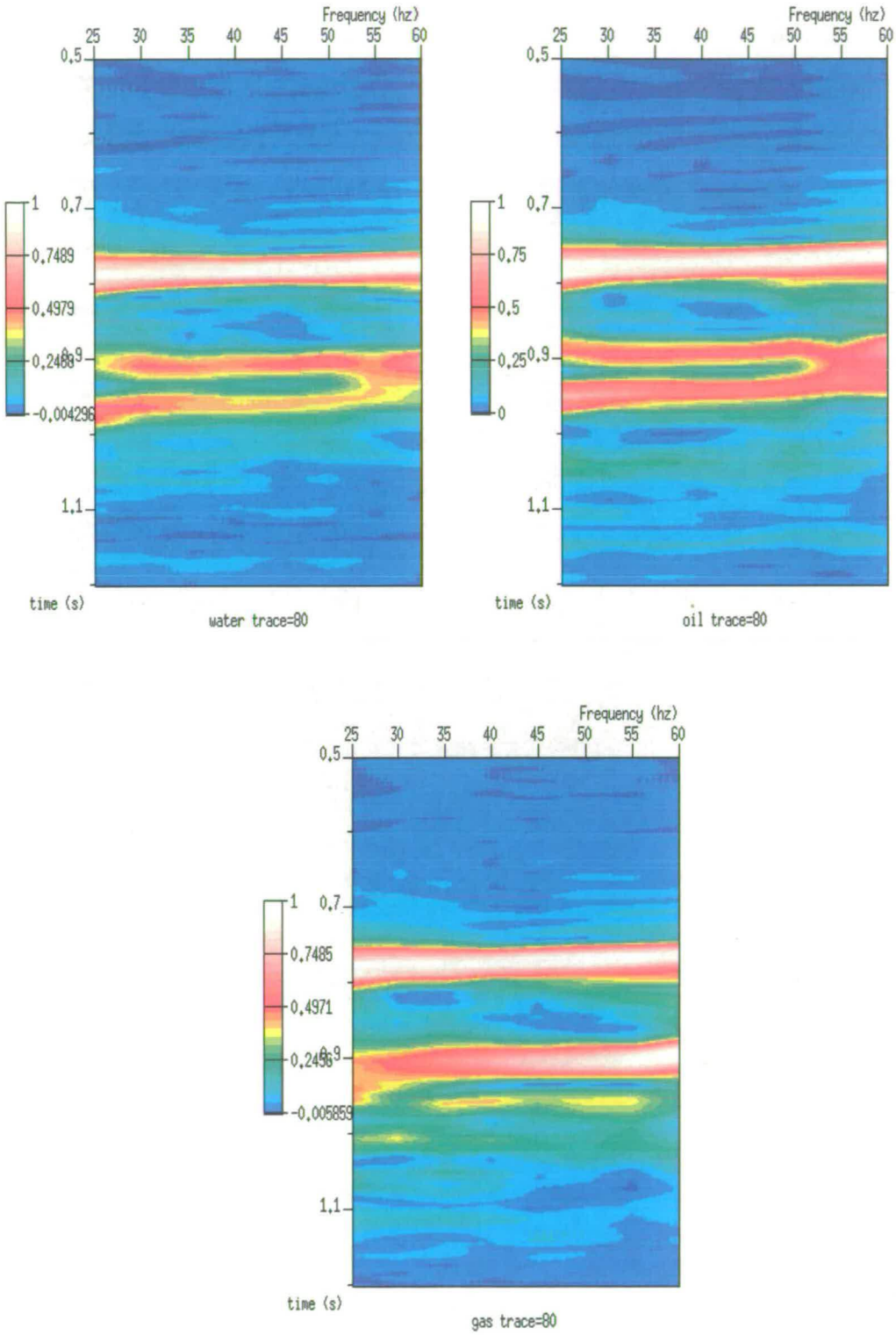

Figure 8.11: Instantaneous spectra for iso-frequency 25Hz to 60Hz, at 5Hz intervals, for the water-, oil-, and gas-saturated models with seven sand layers, in the location of trace 80. The high frequency effect (0.9s) is displayed in the gas-saturated model.

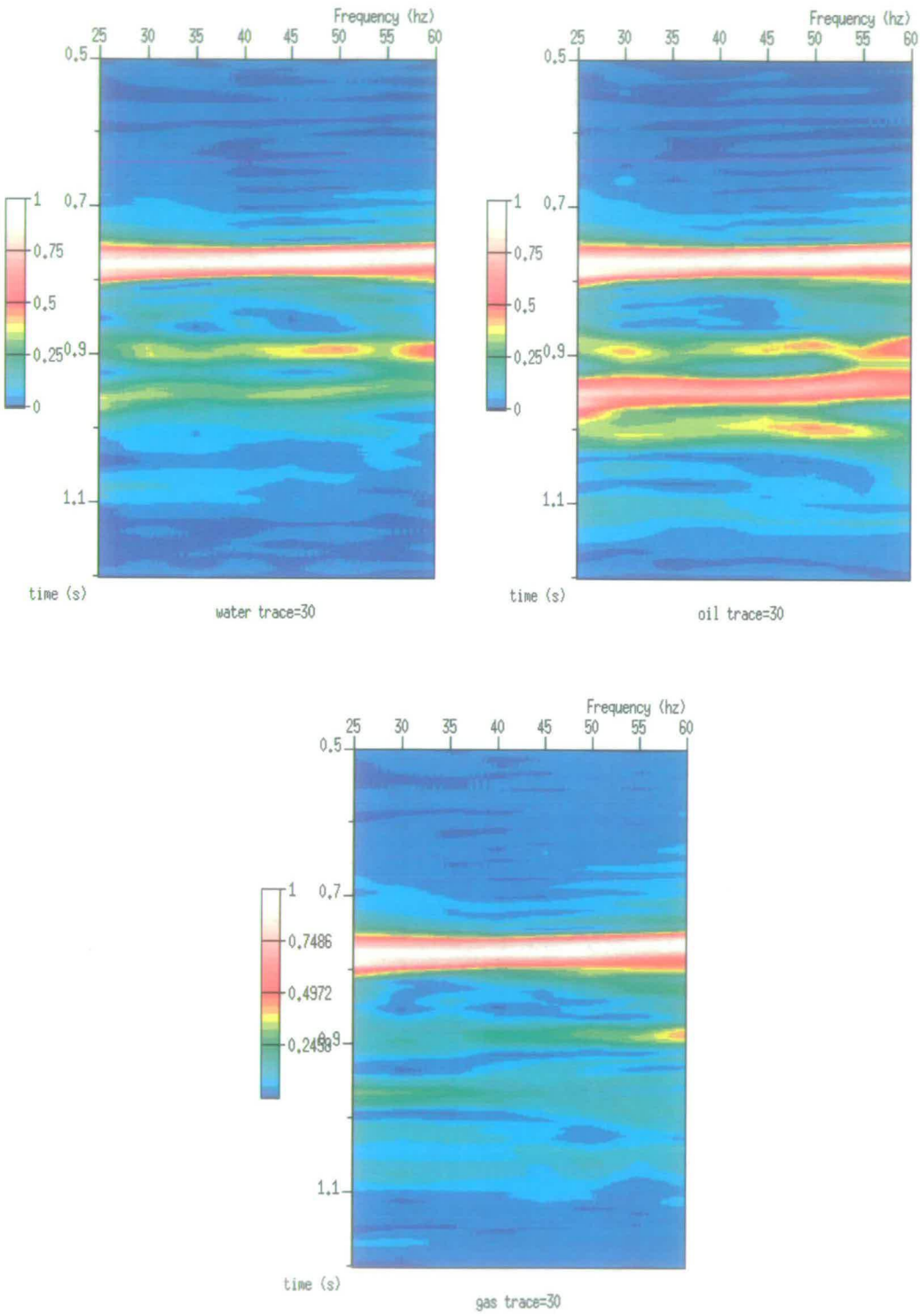

Figure 8.12: Instantaneous spectra for iso-frequency 25Hz to 60Hz, at 5Hz intervals, for the water-, oil-, and gas-saturated models with seven sand layers, in the location of trace 30. The small amplitude (0.9s) in this location indicates that the model is not completely homogeneous.

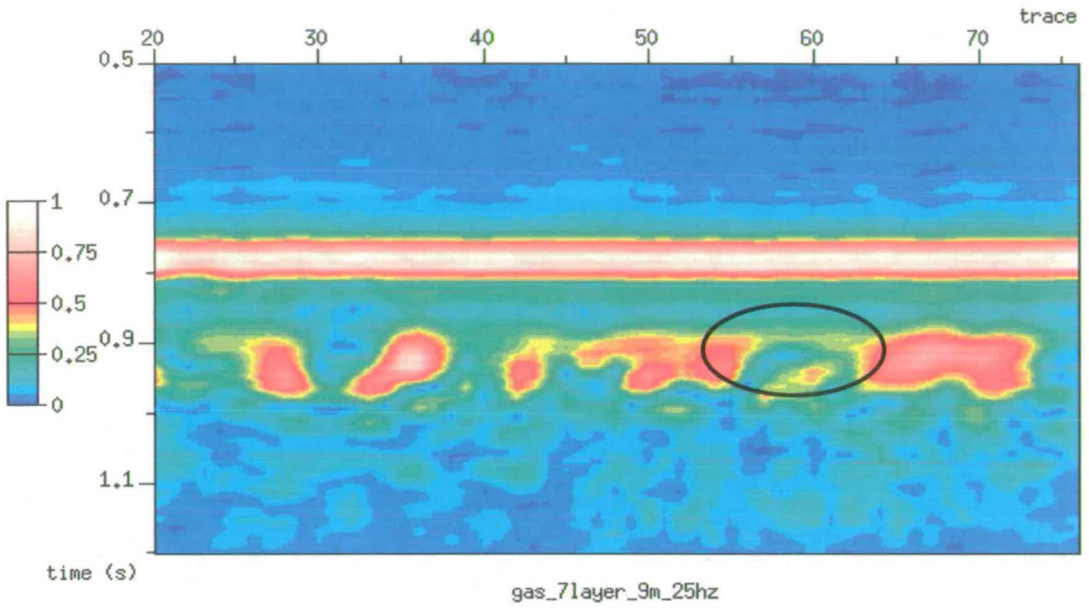

(a) iso-frequency 25Hz for zero-offset gas model

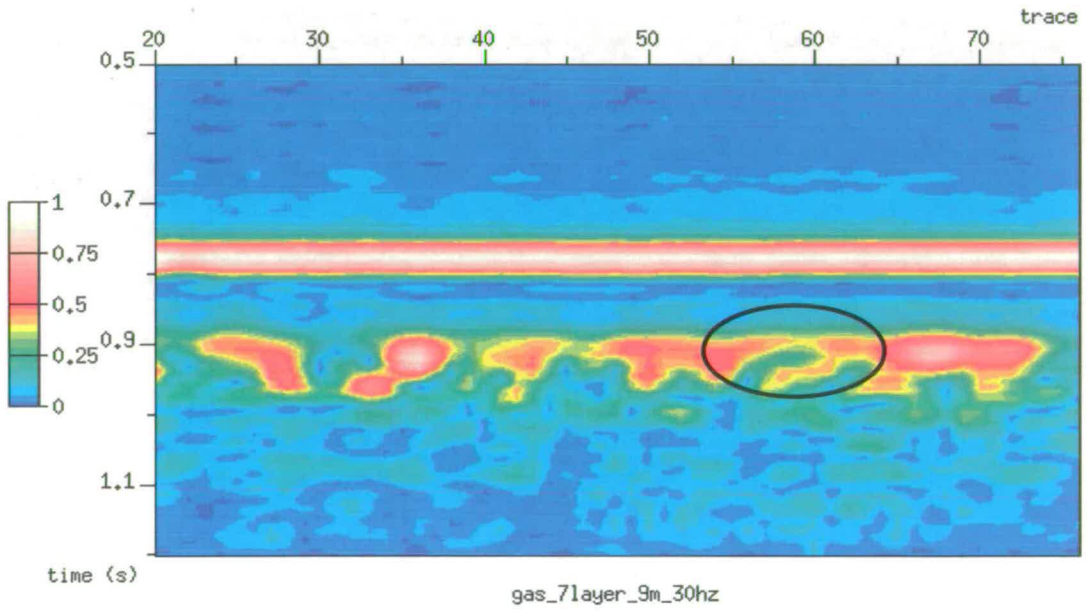

(b) iso-frequency 30Hz for zero-offset gas model

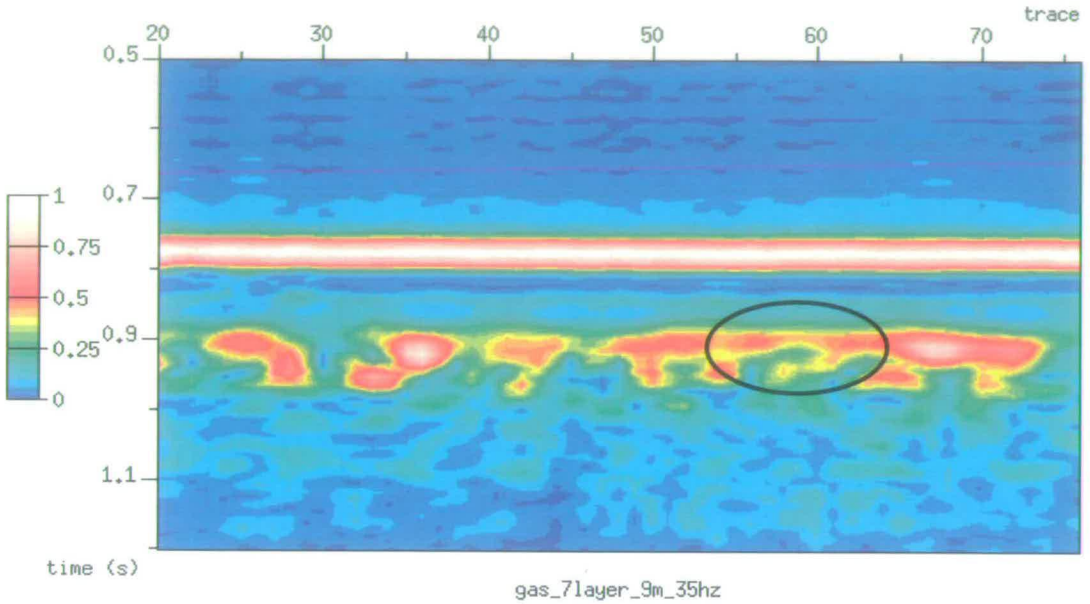

(c) iso-frequency 35Hz for zero-offset gas model

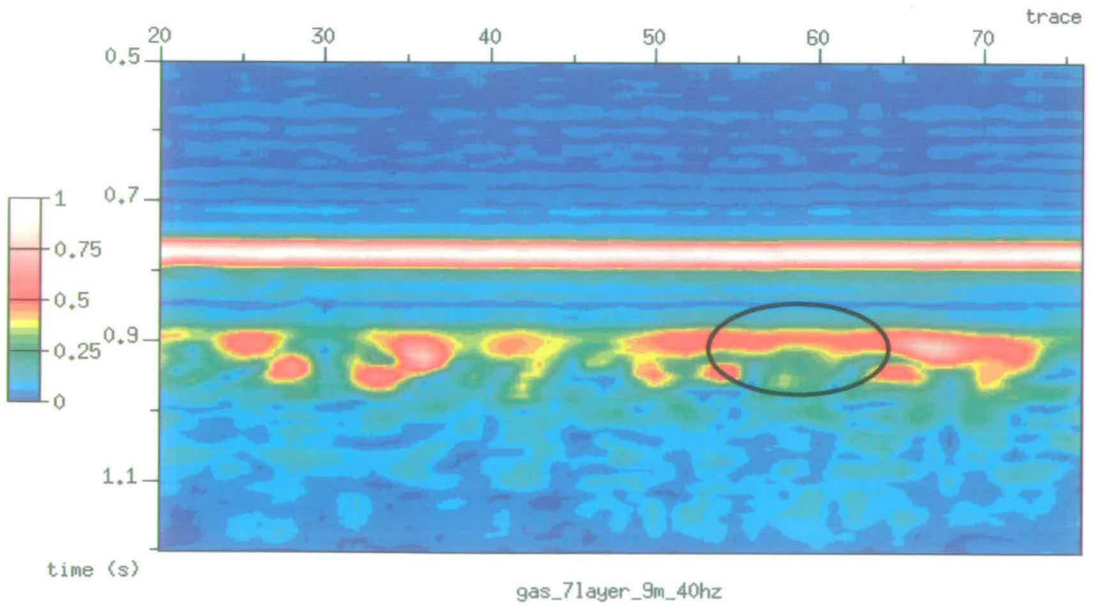

(d) iso-frequency 40Hz for zero-offset gas model

Figure 8.13: Iso-frequency sections for the gas-saturated model with seven sand layers in Figure 8.4c. A systematic increase appears in these frequencies from trace 55 to 65. Other parts of the section are more scattered.

To compensate for the lateral variations in the model due to the compaction process, I sum the traces between 30 and 80. For this, a static correction must be applied to the data to correct for the tilt present in Figures 8.4. Figure 8.14 shows the results of water-saturated models in Figures 8.4a, where we can see the events are properly aligned after applying a static correction. The corresponding results of spectral decomposition are shown in Figures 8.15. Similar in Figures 8.9-8.11, we can still see a systematic shift of energy to high frequencies in the gas-saturated models.

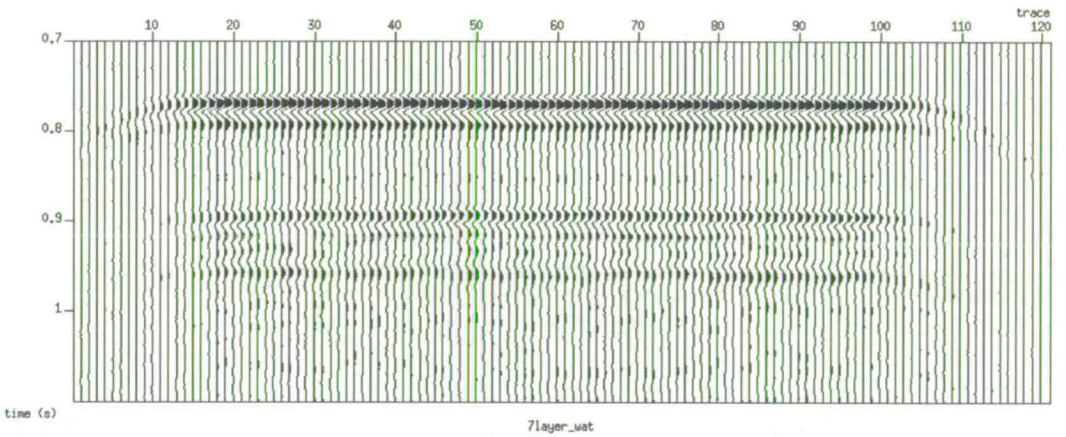

Figure 8.14: Application of the static correction for the water-saturated models in Figure 8.4a.

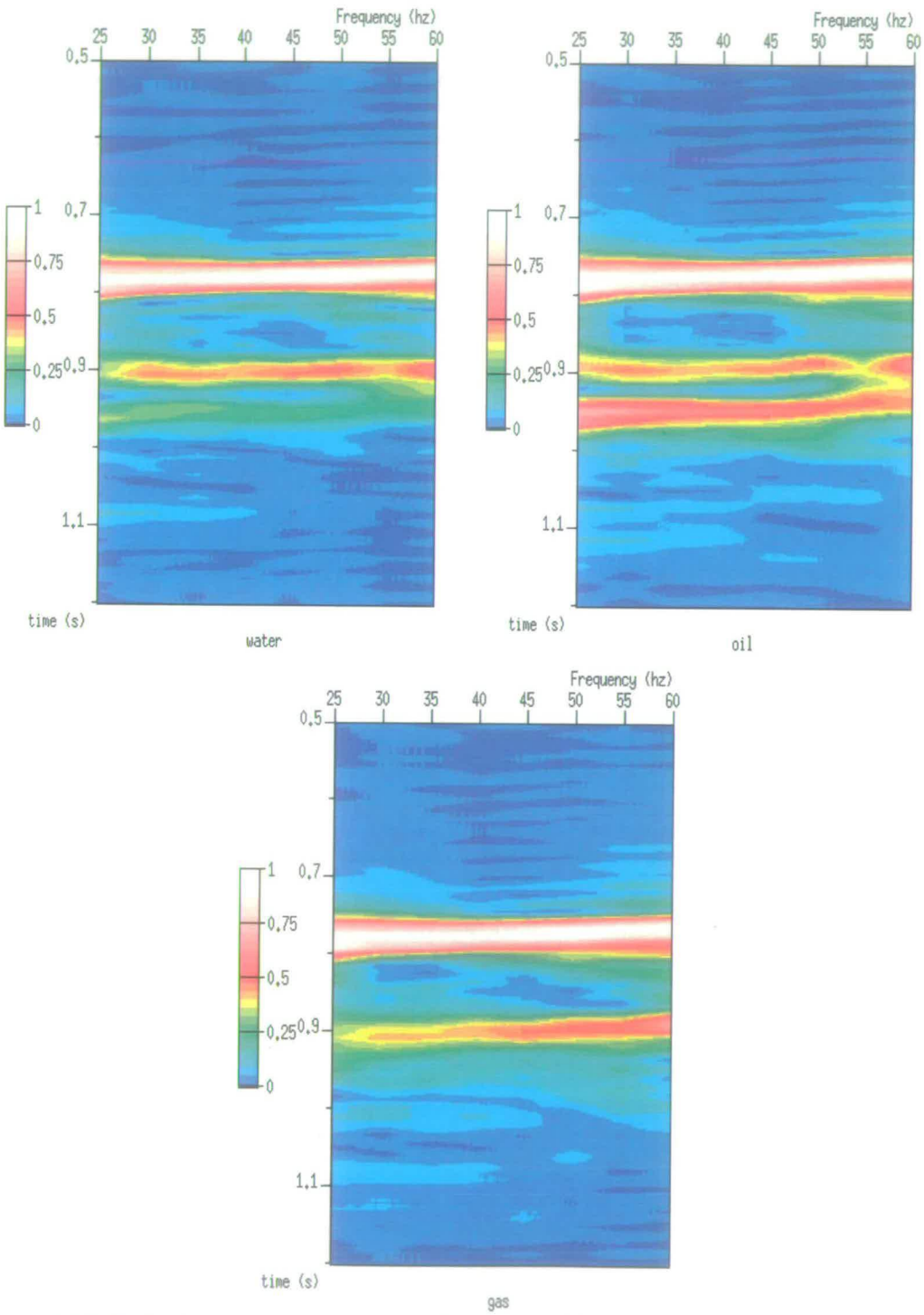

Figure 8.15: Instantaneous spectra for iso-frequency 25Hz to 60Hz, at 5Hz intervals, for the water-, oil-, and gas-saturated models with seven sand layers, for the summed fixed-offset traces. The high frequency effect is displayed in the gas-saturated model.

8.5 Analysis of the 2D Stacked data

Ebrom (2004) shows that low-frequency gas shadows can be induced by the stacking process, which is the stacking process is potentially harmful to high frequency content. This is because, if the prestack CDP gathers are not properly aligned, the stacking process will selectively suppress high frequencies and boost up the low frequencies by mis-stacking, or by emphasizing the larger offsets in the stack (NMO stretch effect). In our case, to examine if the stacking process will degrade the high-frequency bright spots, I process the 2D data using the conventional flow of static correction, velocity analysis, NMO correction and stack. Then the same analysis sequence as in the previous section was applied to the stacked data. The results are shown in Figures 8.16-8.19. Here, I show the three surveys for the seven-sand-layer model, corresponding to the fixed offset data in Figure 8.4.

As shown in Figure 8.16, the 2D stacked data also reveal some systematic variations in time. However, the waveforms seem to be very stable across the section. In general the reflections from gas-saturated reservoirs are more scattered than the other two cases, and this is similar to the fixed offset data in Figure 8.4.

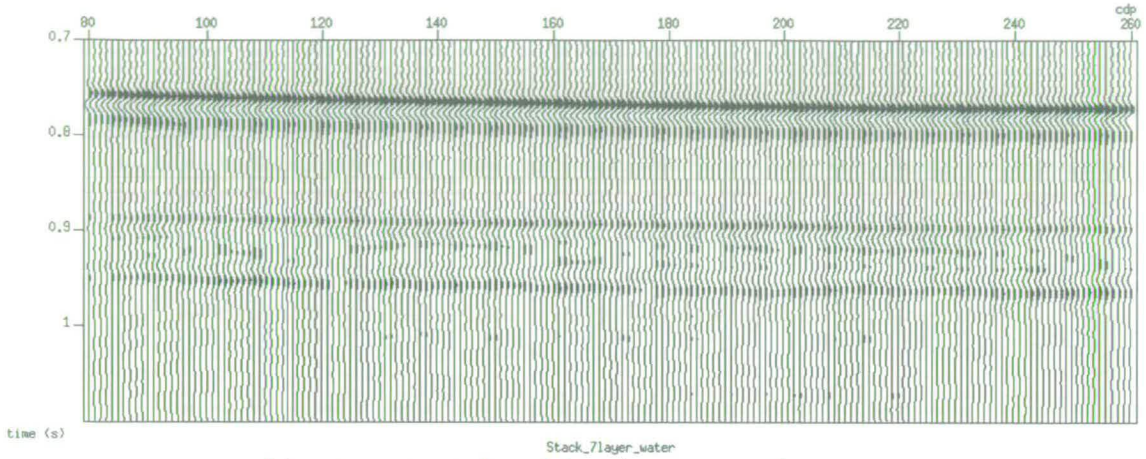

(a) water-saturated model with seven sand layers

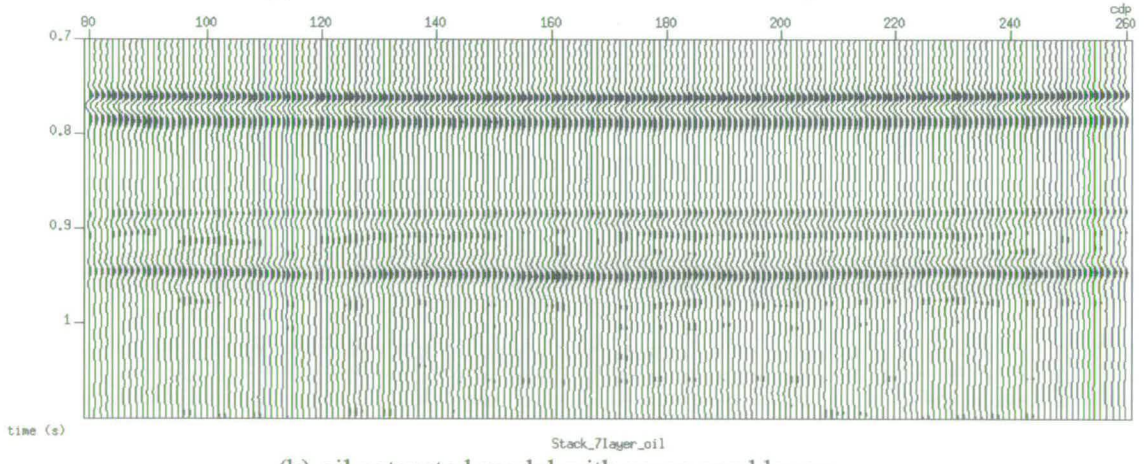

(b) oil-saturated model with seven sand layers

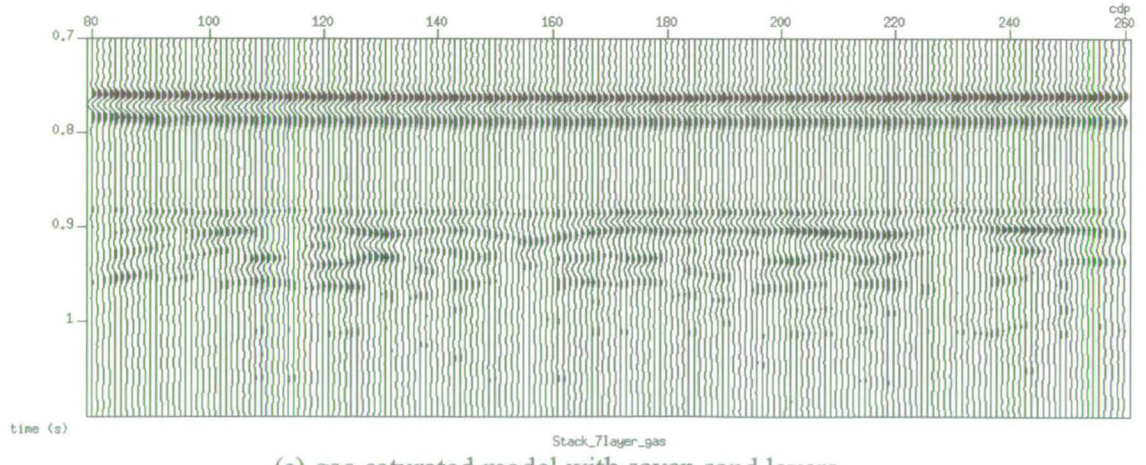

(c) gas-saturated model with seven sand layers

Figure 8.16: Stacked sections of the 2D survey for water-, oil- and gas-saturated models with seven sand layers.

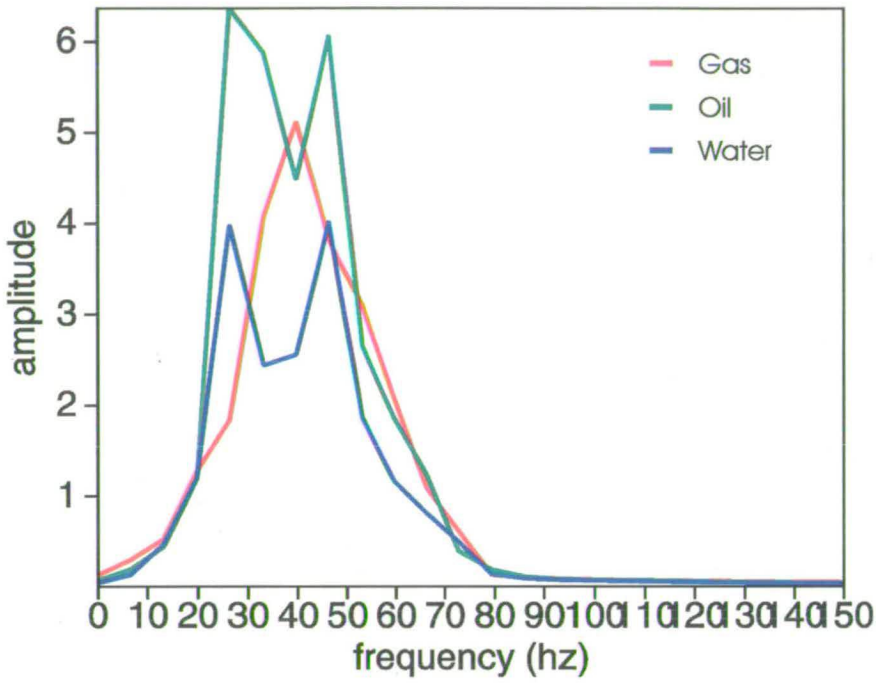

Figure 8.17a: The average amplitude spectra for the thin beds between CDP 120 and 240 in Figure 8.16, with a time window of 150ms, and sample rate of 0.6ms. A shift of energy to high frequencies appears in the gas-saturated model.

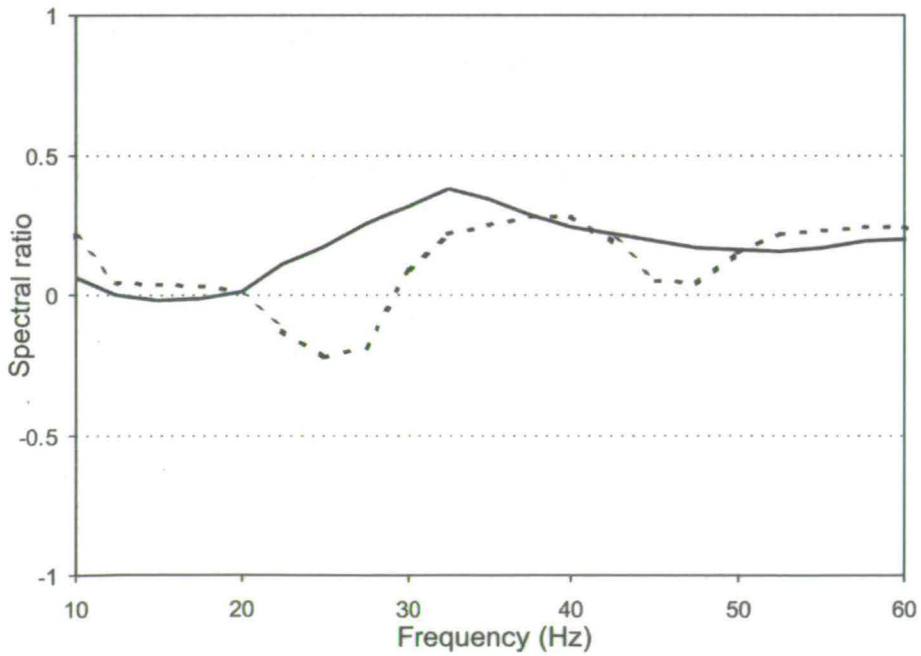

Figure 8.17b: Spectral ratio formed by dividing the oil saturated average spectrum by the water saturated average spectrum (solid line) and dividing the gas saturated average spectrum by the water saturated average spectrum (dot line).

Again I first apply the Fourier transform to see the amplitude spectra of the reflections from the thin beds. Figure 8.17a shows the average spectra from CDP 120 to 240, obtained using the same procedure as in Figure 8.8a. The overall characteristics are similar to Figure 8.8a, except that there is a reduction in the high-frequency amplitudes in both the water- and oil-saturated models. The gas-saturated model shows a shift of energy to the high frequencies (the red curve, Figure 8.17a). The spectral ratios were shown in Figure 8.17b.

The iso-frequency sections of the stacked data are very similar to the fixed offset data. The water-saturated model shows no consistent energy variations with frequency, and nor does the oil-saturated model. However, there is a bigger amplitude difference between the water- and oil saturated model, as shown in Figure 8.18. This again may be due to the fact that the water-saturated model is put into the water tank unsealed, whilst the oil-saturated model is sealed.

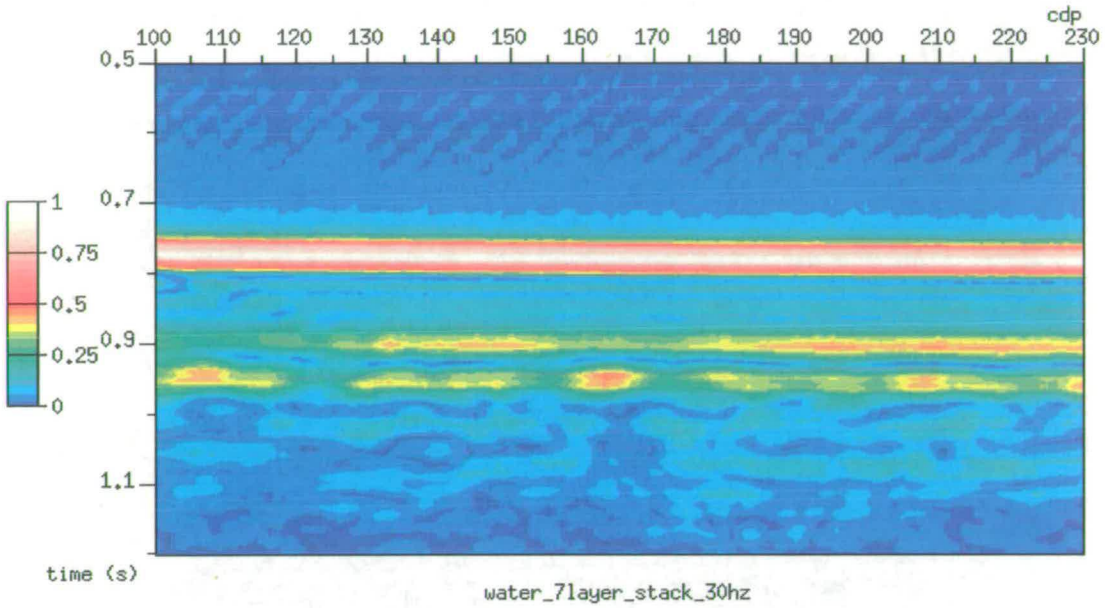

(a) iso-frequency 30Hz for stacked data of water-saturated model

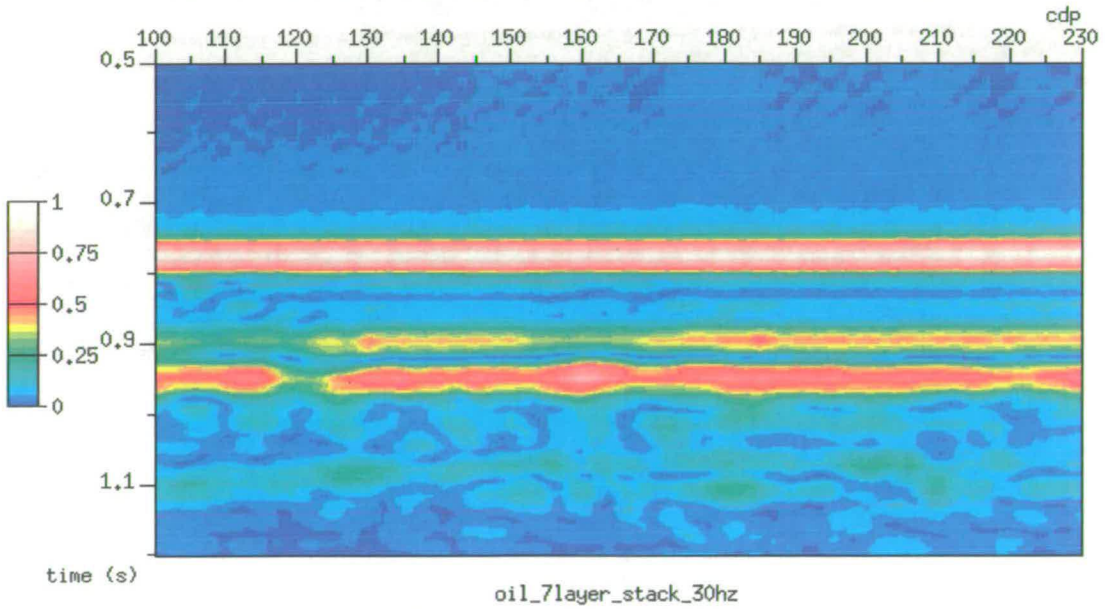

(b) iso-frequency 30Hz for stacked data of oil-saturated model

Figure 8.18: Comparison of the iso-frequency sections for water- and oil saturated models at 30Hz. There is a strong amplitude differences in the target between the two sections.

Figure 8.19 shows the iso-frequency sections of gas saturated model corresponding to Figure 8.13 of the fixed-offset data. I focus on CDP 180 to 200, which are

equivalent to traces 55 to 65, there is a strong increase from 25Hz to 40Hz. The high frequency effects are preserved in the stacked data.

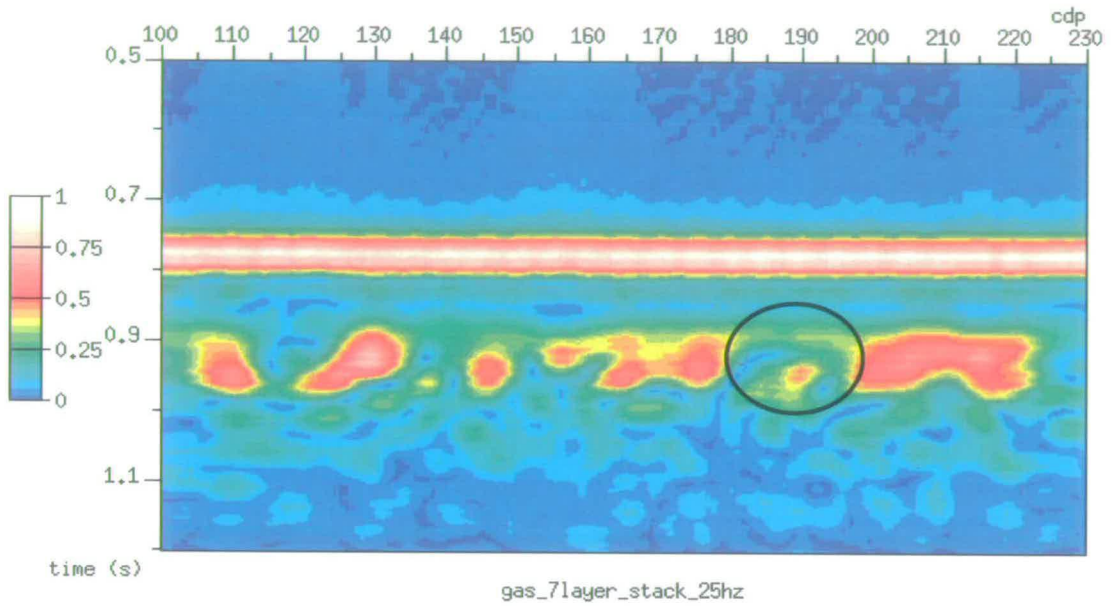

(a) iso-frequency 25Hz for stacked data of gas-saturated model

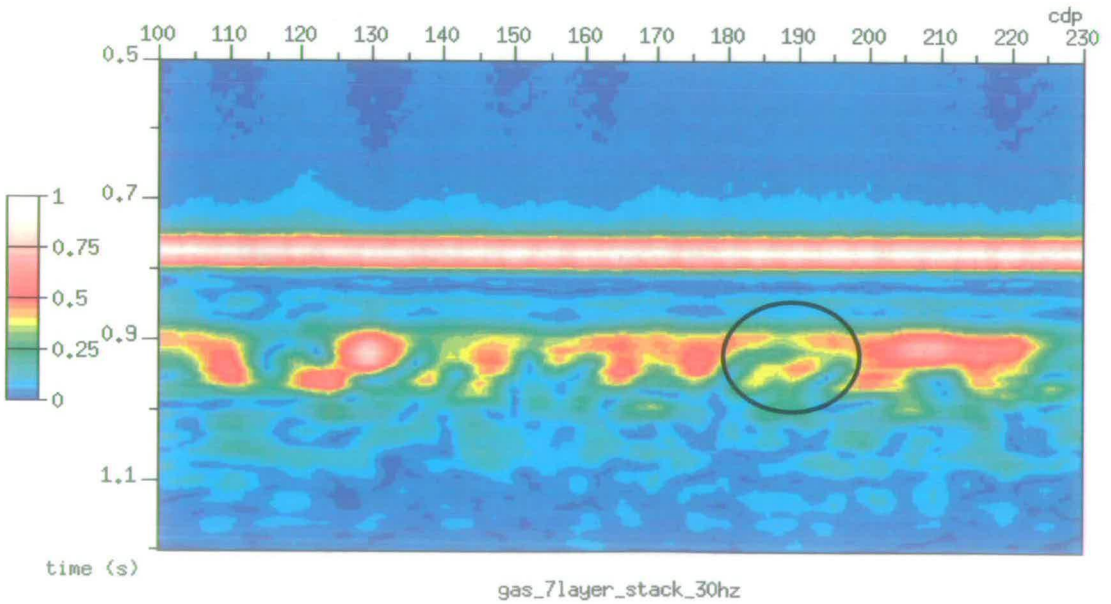

(b) iso-frequency 30Hz for stacked data of gas-saturated model

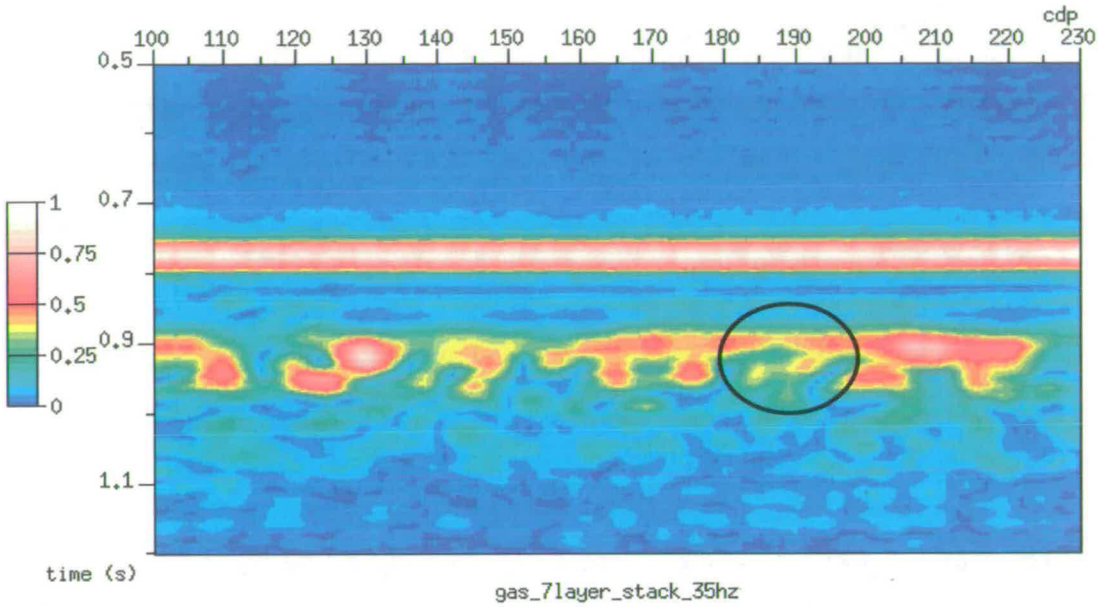

(c) iso-frequency 35Hz for stacked data of gas-saturated model

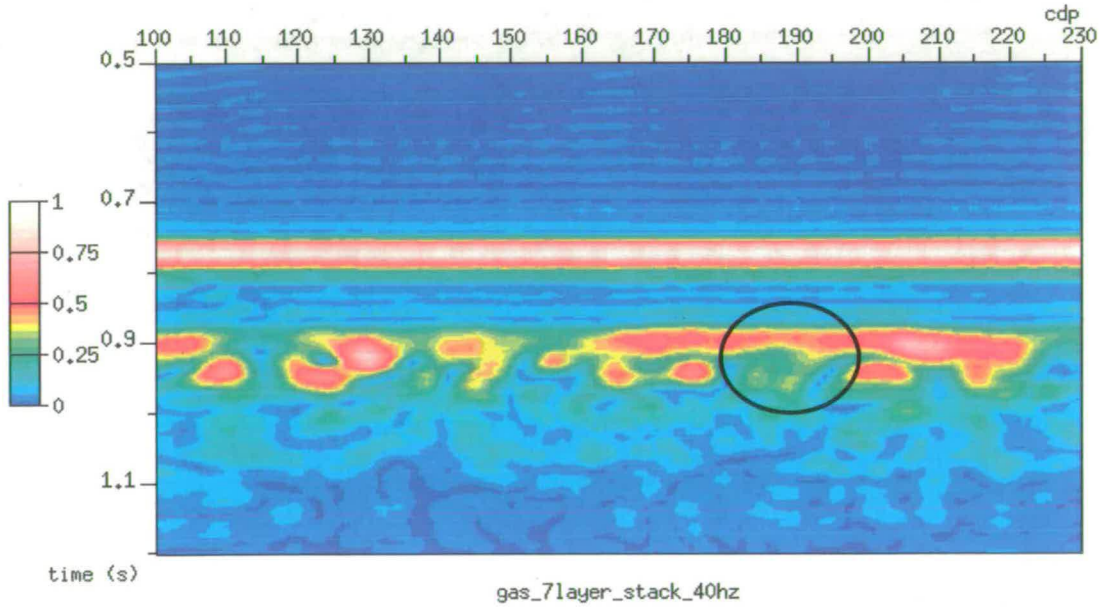

(d) iso-frequency 40Hz for stacked data of gas-saturated model

Figure 8.19: Iso-frequency sections for the data in Figure 8.16c, the gas-saturated model with seven sand layers. A systematic increase appears in these frequencies between CDPs 180-200.

8.6 Discussion and conclusion

It is readily understood that the bright spot AVO is rich in low frequencies, which has been shown by many previous workers. This is often associated with the standard Class III AVO response with a high-to-low impedance contact, and is referred to as the low-frequency gas shadow. It can be extracted from conventional P-wave seismic data using spectral decomposition. Chapman *et al.* (2005) have successfully modelled the low-frequency gas shadow using a multi-scale rock physics model that considers the dispersion effects. Chapman *et al.* (2005) provided the theoretical basis for our numerical modelling in Chapter 7, where I conclude that in the case of Class I AVO response with a low-to-high impedance contrast, the presence of gas will induce a high-frequency bright spot instead of a low-frequency shadow.

Analysis of Class I AVO anomalies is often more subtle and complicated than the traditional Class III AVO gas response. Class I AVO is often common in thin-layered reservoirs with inter-bedded sand/shale sequence, which further complicates AVO analysis. The prediction of a high-frequency bright spot offers a potential solution for gas detection in thin-layered sand reservoirs. To evaluate this further, I have analysed a physical-modelling data set that is specially designed for investigating fluid detection in thin-layered reservoirs. Through physical modelling, I have confirmed the numerical findings in Chapter 7.

The data used in the physical modelling were acquired under unchanged geological conditions and acquisition parameters, but different fluid saturation. The models were saturated with three different fluid types: water, oil and gas. The seismic physical modelling provides a realistic representation of the fluid-rock response, compared with numerical modelling.

Contrary to the numerical modelling, after spectral balancing, I find no systematic energy shift in the water and oil-saturated cases. The tuning effect does not make

the energy shift to the high frequency in water and oil-saturated models, whilst in numerical modelling, I have observed a strong energy shift to the high frequencies due to tuning. The analysis of the physical modelling data also reveals that there is a systematic shift of energy to the high frequencies in the gas-saturated case, which does agree with the numerical modelling (Figures 8.9 to 8.13).

Detailed analysis of the amplitude spectra for different fluid saturations for the physical models reveals that thin-layer tuning is also sensitive to fluid saturation (Figure 8.8a and Figure 8.17a). Therefore, I may conclude that the observed high-frequency bright spots in the gas-saturated model are a mixture of gas-dispersion effects and thin-layer tuning effects. Consequently, the presence of high-frequency bright spots is a valid indicator of gas deposits in a thin-layered reservoir with inter-bedded sand/shale sequences. This may provide a useful guide for the analysis of standard Class I AVO response in P-wave seismic data.

I observed that the spectral ratios did not show a high-frequency shift (Figure 8.8b and Figure 8.17b), possible because the amplitude of the water-saturated model is the lowest (Figure 8.8a and Figure 8.17a) contrary to what is expected. This may possibly be explained by the fact that the water-saturated model is not sealed when put into the water tank, whilst the gas and oil-saturated models are sealed when put into the tank.

Chapter 9: Conclusions

Multicomponent seismic has gained wide acceptance in the industry for imaging and reservoir characterization. However, there is still a long way to go before it becomes a mainstream technology. This thesis aims to tackle some of the bottlenecks in the interpretation and analysis of multicomponent seismic data. These include: (a) event correlation between PP-data and PS-data, (b) linking multicomponent seismic information to rock properties directly, (c) the effect of fluid-related dispersion on the AVO behaviours. Based on Li and Yuan's theory (2003), I developed a new approach for event correlation by converted-wave moveout analysis. I also developed algorithms for joint PP- and PS-waves inversion, tested the workflow through numerical modeling and applied them to field data. The issues of detecting fluid-related dispersion effect on thin-layer cases are also addressed. This chapter summarizes the main results and gives recommendations for future work.

9.1 Major conclusions from this thesis

9.1.1 Event correlation between PP- and PS-data

A new approach for event correlation is based on a modified two-parameter non-hyperbolic PS-wave traveltime equation, which shows better accuracy than three-parameter Thomsen's equation. The two-parameter equation is accurate for offset-depth ratio no less than 1.5. The accuracy increases with the decrease of vertical P- and S-velocity ratio γ_0.

The two parameters in the modified equation for multi-layered isotropic media are PS-wave stacking velocity V_{c2} and velocity ratio γ_{iso}. Based on this equation, an independent estimate of the P-wave stacking velocity V_{p2} from PS-wave moveout is obtained. These estimates of V_{p2} in T_{c0} time can then be compared to the V_{p2}

obtained from PP-wave moveout, thus the corresponding relationship between PP-wave vertical travel time T_{p0} and PS-wave time T_{c0} is established.

The reliability of the V_{p2} in T_{c0} time is mainly determined by the accuracy of the velocity ratio γ_{iso}. Because γ_{iso} mainly controls the moveout of the intermediate-far offsets, the offset-depth ratio in the semblance analysis is a key factor. The accuracy of the PS-wave travel time equation for intermediate-far offset is also important for resolving γ_{iso}. Based on the model study, for resolving γ_{iso} accurately (error less than 1%), the offset-depth ratio needs to be at least 1.5. The offset-depth ratio for an accurate γ_{iso} increases with depth. The model shows it is possible to perform a reliable correlation through the usage of γ_{iso} when the error by two-parameter PS-wave travel time equation is less 10ms at an offset-depth ratio of 2. The method assumes that the stacking velocities are monoclinally increasing with depth, and there is no velocity reversal.

Two-pass single scanning semblance analysis was applied to real data from the Ordos basin, which shows the result to be as accurate as double scanning semblance analysis.

9.1.2 Sensitivity of elastic parameters to rock properties

Seismic inversion has provided the potential to determine elastic parameters such as P and S-wave velocity, impedance, Poisson's ratio, and Lame's constants. Some parameters are more preferable to others in reservoir description due to their sensitivity to lithology and fluid contents, and the specific geology and geophysics conditions, such as weak impedance contrast and thin-layer tuning.

In the study area of the Ordos basin, laboratory measurement indicates that P-wave velocity of tight sand has no rapid drop at the low gas saturation (< 30%), which contradicts to what is expected from Biot-Gassmann theory. The reason for this needs to be examined. V_p/V_s ratio is more sensitive to gas saturation than P-wave

velocity. Lithology has a larger effect on V_p/V_s than fluid. Lame parameter $\lambda\rho$ and fluid factor ρf are more capable of detecting fluid than P-impedance and V_p/V_s ratio. $\mu\rho$ is sensitive to the lithology.

Traditional AVO intercept and gradient analysis can be undermined due to a small P-impedance and tuning effect. $\lambda\rho$ and $\mu\rho$ from PP-wave alone shows promise in fluid detection, however, this can be degraded by the accumulating errors from impedance inversion.

9.1.3 Elastic parameters estimation from Joint AVO inversion

Since typical acquisition geometry of PP-wave alone cannot yield reliable S-wave related information, combining PS-data into the inversion is beneficial for supporting gas sand detection.

Joint AVO inversion in this thesis makes full use of Aki-Richard's equations: the density effect is factored into the inversion without any assumptions. Two parameters are inverted for, which is more stable than a three-parameter inversion.

Model studies indicate that S-impedance inversion from PP-data alone has less accuracy than that from the PS-data alone. An offset-depth ratio of less than 1 is not enough for using PP-waves to invert S-impedance correctly. Joint inversion improves the S-impedance accuracy compared to PP-data alone, especially when noise is present in data. For P-impedance, PP-data alone and joint inversion lead to a similar result.

Synthetic data reveal that joint inversion of $\lambda\rho$ and λ reflectivity yield better results for gas detection compared to impedance reflectivity; λ reflectivity has the best of data quality since it has the same noise level as impedance. Since $\lambda\rho$ values are calculated from impedance, the noise may also be propagated in through the square of impedance.

CIP gathers for PP- and PS-data by PSTM are used in the joint inversion. Compared to CDP gathers, CIP gathers are more appropriate due to accurate reflection point positioning. For velocity background used in the inversion, the thesis confirms that a linear smoothed velocity-depth model can be used as successfully as the exact velocity model.

9.1.4 Offset dependent tuning effect on PP- and PS-wave AVO

Through a numerical model with two low P-wave velocity 10-meter thin layers embedded in a homogeneous high velocity thick layer, I conclude that the tuning effect has an adverse effect on both PP- and PS-wave AVO. The tuning effect makes both class II and class III PP-AVO anomalies eliminated. When two 10-meter thin layers have similar P-impedance, the tuning effect causes a dramatic amplitude change in both PP- and PS-waves. On the other hand, for the model of two 10-meter thin layers with a large P-impedance contrast, the tuning effect causes a small amplitude change on both PP- and PS-wave.

9.1.5 Frequency dependent AVO for fluid detection

Studies on field data, physical modelling data and numerical modelling have demonstrated that spectral decomposition techniques can be used to provide information on the saturating fluid. The spectral response to changing fluid is affected by fluid-sensitive tuning and the effect of dispersion on the reflection coefficient. The effect of attenuation during propagation can often be ignored in the case of a thin hydrocarbon layer, but modelling is necessary to understand the effects of tuning and dispersion. The accuracy of the velocity model is an important consideration in this case.

In the example showing the low frequency effect, we interpret the loss of high frequencies as being due to the frequency-dependent reflection coefficient, since the thickness of the hydrocarbon layer mitigates against tuning or attenuation being

the cause of the observed anomaly. In the example showing the high frequency effect, we see a clear spectral signature of gas saturation which appears consistently in our numerical, physical modelling and field data. The signature in the field data is most easily explained as a combination of fluid-sensitive tuning and dispersion, although we cannot confidently rule out the possibility that either effect is uniquely responsible. This highlights the main argument that careful modelling is necessary to understand the complex effect of different fluids on the spectral response and enable robust interpretation.

9.2 Future work recommendations

9.2.1 Elastic inversion using a full Zoeppritz equation

Linearized AVO inversion based on Aki-Richards approximations provides the meaningful physical parameters directly related to the rock properties, whilst full Zoeppritz equations link rock properties via complex algebra expressions. However, Zoeppritz equations are the fundamental relation between angle-dependent amplitude and rock parameters. The exact inversion from the full Zoeppritz equations is expected to provide more detailed links between amplitude and rock parameters. Few efforts have been made in AVO attribute exaction using full Zoeppritz equation inversion. The difficulty lies in transforming an irrational, fractional, and nonintegral equation into a rational and integral one (Krail, 2004).

9.2.2 Benchmark of fluid dispersion effect

In this thesis, a clear spectral signature of gas saturation appears consistently in the numerical, physical modelling and field data. However, we cannot recognize unique responsibility between fluid-sensitive tuning and dispersion. A careful physical modelling is necessary to understand the complex effect of different fluids on the spectral response and enable robust interpretation.

References

Aki, K. and Richards, P.G., 1980. Quantitative Seismology: Theory and methods. vol 1, W.H. Freeman & Co.

Alford, R.M., 1986. Shear data in the presence of azimuthal anisotropy. 56th Internat. Mtg. Soc. Expl. Geophys., Expanded Abstract, 476-479.

Alkhalifah, T. and Tsvankin, I., 1995. Velocity analysis for transversely isotropic media. Geophysics, 60, 1550-1566.

Audebert, F., Granger, P.Y., and Herrenshmidt, A., 1999. CCP-Scan technique: True common conversion point sorting and converted-wave velocity analysis solved by PP and PS pre-stack depth migration. 69th Internat. Mtg. Soc. Expl. Geophys., Expanded Abstract, 1186-1189.

Bagaini, C., Bale, R., Caprioli, P., and Ronen, S., 1999. Converted-wave binning analysis: in search of gamma. 69th Internat. Mtg. Soc. Expl. Geophys., Expanded Abstract, 703-706.

Bakke, N. E. and Ursin, B., 1998. Thin-bed AVO effects. Geophysical Prospecting, 46, 571-587.

Barkved, O., Bartman, B., Compani, B., Gaiser, J., Van Dok, R., Johns, T., Kristiansen, P., Probert, T., and Thompson, M. 2004. The many facets of multicomponent seismic data. Schlumberger Oilfield Review, summer, 42-56.

Barnola, A. and White, R., 2001. Gardner's relations and AVO inversion. First Break, 19, 607-611.

Behle, A. and Dohr, G., 1985. Converted waves in exploration seismics. in Dohr, G., Ed., Seismic shear-waves, Part B: Applications. Geophysical Press 15B, 178-223.

Berg, E., 1997. 4C-2D or 3D sea bed seismic methodology. Proceedings of IIR forum on acquisition, processing and interpretation of marine seismic data, 1274-1282.

Berlioux, A. and Lumley, D., 2001. Amplitude balancing for AVO analysis. Stanford Exploration Project, report 80, 1–356.

Bevc, D., 1997. Imaging Complex structure with semirecursive Kirchhoff migration. Geophysics, 62, 577-588.

Biot, M. A., 1941. General theory of three-dimensional consolidation. J. Appl. Physics, 12, 155–164.

Brown, S. and Korringa, J., 1975. On the dependence of the elastic properties of a porous rock on the compressibility of the pore fluid. Geophysics, 40, 608-616.

Caldwell, J., 1999. Marine multicomponent seismology. The Leading Edge, 18, 1274-1282.

Calvert, R., 2005. 4D technology: Where are we, and where are we going? Geophysical Prospecting, 53, 161–171.

Cambois, G., 2000. Can P-wave AVO be quantitative? The Leading Edge, 19, 1246-1251.

Castagna, J., 1993. AVO analysis-tutorial and review. SEG Investigations in Geophysics #8, "Offset-dependent reflectivity - theory and practice of AVO analysis", 3-36.

Castagna, J., Batzle, M.L., and Kan, T.K., 1993. Rock Physics-The link between rock properties and AVO response. SEG Investigations in Geophysics #8, "Offset-dependent reflectivity - theory and practice of AVO analysis", 135-171.

Castagna, J. and Swan, H., 1997. Principles of AVO crossplotting. The Leading Edge, 16, 337-342.

Castagna, J., Sun, S., and Siegfried, R., 2003. Instantaneous spectral analysis: Detection of low-frequency shadows associated with hydrocarbons. The Leading Edge, 22, 120-127.

Chan, W. and Stewart, R., 1997. Logarithmic correlation of P-P and P-S seismic data. Crewes reseach report, 9, 35(1-8).

Chapman, M., 2003. Frequency dependent anisotropy due to meso-scale fractures in the presence of equant porosity. Geophysical Prospecting, 51, 369-379.

Chapman, M., Liu, E., and Li, X., 2005. The influence of abnormally high reservoir attenuation on the AVO signature. The Leading Edge, 24, 1120-1125.

Chapman, M., Zatsepin, S.V., and Crampin, S., 2002. Derivation of a microstructural poroelastic model. Geophysical Journal International, 151, 427-451.

Chapman, M., Liu, E., and Li, X., 2006. The influence of fluid-sensitive dispersion and attenuation on AVO analysis. Geophysical Journal International, in press.

Chui, C., 1992. An introduction to wavelets. American academic press.

Chung, H. and Lawton, D.C., 1990. AVO analysis and complex attributes for a glauconitic gas sand bar. J. Can. Soc. Expl. Geophs. 26, 72-86.

Connolly, P., 1999. Elastic impedance. The Leading Edge, 18, 438-452.

Crampin, S., 1985. Evaluation of anisotropy by shear-wave splitting. Geophysics, 50, 142-152.

Dai, H., 2001. Parallel processing of prestack Kirchhoff time migration on a beowulf cluster. Edinburgh Anisotropy Project annual research report, 9, A46-61.

Dai, H. 2003. Interactive estimation of anisotropic parameters and velocities from PS converted waves. 73rd Internat. Mtg. Soc. Expl. Geophys., Expanded Abstract, 1577-1580.

Dai, H. and Li, X.-Y., 2001. Anisotropic migration and model building for Alba 4C data. 71st Internat. Mtg. Soc. Expl. Geophys., Expanded Abstract, 795-798.

Dai, H. and Li, X.-Y., 2003. Migration velocity analysis of C-wave using INMO-CIP gathers of PKTM: a case study from the Gulf of Mexico. 65th Annual International EAGE Meeting.

Dai, H., Li, X.-Y., and Mueller, M., 2000. Compensating for the effect of gas clouds by prestack migration: A case study from Valhall. 70th Internat. Mtg. Soc. Expl. Geophys., Expanded Abstract, 1047-1050.

Dellinger, J., Clarke, R., and Whitmore, D., 2002. P and C-wave depth imaging at Valhall field. FORCE Seminar, Stavanger: 4C/OBS data processing and interpretation – old myths, new insights.

De Tomasi, V., 1996. Prestack depth migration of target-converted PS-V Waves. 58th Annual International EAGE Meeting, P145.

Ebrom, D., 2004. The low-frequency gas shadow on seismic sections. The Leading Edge, 23, 772.

Fatti, J.L., Smith, G.C., Vail, P.J., Stauss, P.J., and Levitt, P.R., 1994. Detection of gas in sandstone reservoir using AVO analysis: A 3-D seismic case history using the geostack technique. Geophysics, 59, 1362-1376.

Fomel, S. and Backus, M., 2003. Multicomponent seismic data registration by least squares. 73rd Internat. Mtg. Soc. Expl. Geophys., Expanded Abstract, 781-784.

Fromm, G., Krey, T., and Wiest, B., 1985. Static and dynamic corrections. Seismic shear waves: Handbook of geophysical exploration. Vol. 15a. Geophysical Press. 191-225.

Gaiser, J., 1996. Multicomponent Vp/Vs correlation analysis. Geophysics, 61, 1137-1149.

Gaiser, J. 1999. Applications for vector coordinate systems of 3-D converted-wave data. The Leading Edge, 18, 1290-1300.

Gaiser, J. and Strudley, A., 2005. Acquisition and application of multicomponent vector wavefields: are they practical? First Break, 23, 61-67.

Gardner, G.H.F., Gardner, L.W., and Gregory, A.R., 1974. Formation velocity and density-the diagnostic basics for stratigraphic traps. Geophysics, 39, 770-780.

Gardner, G.H.F. and Harris, M.H., 1968. Velocity and attenuation of elastic waves in sand. Trans 9th Annual Log. Symp. PM1-M19.

Garotta, R., 2000. Shear waves from acquisition to interpretation. Soc. of Expl. Geophys, No. 3 in Distinguished Instructor Series.

Gassmann, F., 1951. Uber die Elastizitat poroser Medien:Vierteljahrsschrift der Naturforschenden Gesellschaft in Zurich, 96, 1–23.

Gibson, J., Watt, H., and Roche, S., 2003. Multicomponent seismic data acquisition-the economics revisited. CSEG Recorder, October, 16-21.

Gidlow, P. M., Smith, G. C., and Vail, P. J., 1992. Hydrocarbon detection using fluid factor traces: A case study: How useful is AVO analysis? Joint SEG/EAEG summer research workshop, Soekor, South Africa, Technical Program and Abstract, 78–89.

Goodway, B., Chen, T., and Downton, J., 1997. Improved AVO fluid detection and lithology discrimination using Lamè petrophysical parameters; "Lambda-Rho", "Mu-Rho", & "Lambda/Mu fluid stack", from P and S inversions. 67th Internat. Mtg. Soc. Expl. Geophys., Expanded Abstract, 183-186.

Goodway, B., 2001. AVO and Lamè constant for rock parameterization and fluid detection. CSEG Recorder, June, 39-60.

Goodway, B., 2002. Elastic-wave AVO methods. CSEG Annual convention abstracts.

Granli, J. R., Arntsen, B., Sollid, A., and Hilde, E., 1999. Imaging through gas-filled sediments using marine shear wave data. Geophysics, 64, 668-677.

Gray, D., Goodway, B., and Chen, T., 1999. Bridging the Gap: Using AVO to detect changes in fundamental elastic constants. CSEG Annual convention abstracts, 95-99.

Gray, F. D., 2002. Elastic inversion for lamè parameters. CSEG Annual convention abstracts.

Gray, D., 2003. P-S converted-wave AVO. CSEG Annual convention abstracts.

Gray, S., 1997. True-amplitude seismic migration: A comparison of three approaches. Geophysics, 62, 929-936.

Gregory, A.R., 1977. Aspects of rock physics from laboratory and log data that are important to seismic interpretation. AAPG memoir 26, 15-46.

Gresillaud, A., Suaudeau, E., and Granger, P.Y., 2003. C-wave imaging - Kirchhoff PSTM versus DMO. 65th Annual International EAGE Meeting.

He, D., Jia, A., and Xu, T., 2006. Reservoir Characterization of the Giant Sulige Gas Field, Ordos Basin, China. AAPG Search and Discovery Article #20035.

He, H., Zhou, H., and Fu, D., 2002. Multicomponent seismic exploration in Yinggehai Basin. The Leading Edge, 21, 914-920.

Hudson, J.A., Liu, E., and Crampin, S., 1996. The mechanical properties of materials with interconnected cracks and pores. Geophysical Journal International, 124, 105-112.

Jolly, R., 1956. Investigation of shear waves. Geophysics, 21, 905-938.

Kan, T. K., Batzle, M. L., and Gaiser, J., 1983. Attenuation measured from VSP, evidence of frequency dependent Q. 53rd Internat. Mtg. Soc. Expl. Geophys., Expanded Abstract.

Klimentos, T., 1995. Attenuation of P- and S-waves as a method of distinguishing gas and condensate from oil and water. Geophysics, 60, 447-458.

Kommedal, J., Ackers, M., Flostad, P., Gratacos, B., and Evans, R. 2002. Processing the Hod 3D multicomponent OBS survey, comparing parallel and orthogonal acquisition geometries. The Leading Edge, 21, 795-801.

Krail, P., 2004. Rock properties and amplitude versus angle. The Leading Edge, 23, 986-988.

Kristiansen, P. and Dok, P., 2003. Event registration and Vp/Vs correlation analysis in 4C processing. 73rd Internat. Mtg. Soc. Expl. Geophys., Expanded Abstract, 785-788.

Larsen, J., 1999. AVO inversion by simultaneous P-P and P-S Inversion, M.Sc. Thesis University of Calgary.

Lewis, S., Barkved, O., and Kjelstadli, R., 2003. Planning waterflood wells in a gas cloud. 73rd Internat. Mtg. Soc. Expl. Geophys., Expanded Abstract.

Li, G., Ziolkowski, A., Taylor, D., and Hall, G., 2002. An approach to determine subsurface structure using P-P and P-SV reflections. 64th Annual International EAGE Meeting, P006.

Li, X-Y., MacBeth, C., Lefeuvre, F., and Tabti, H., 1995. Integrated analysis of multicomponent VSP and surface data for fracture reservoir delineation in the Paris Basin. 57th Annual International EAGE Meeting, C036.

Li, X-Y., 1997. Fractural reservior delineating using multicomponent seismic data. Geophysical Prospecting, 54, 39-64.

Li, X-Y., Dai, H., Mueller, M., and Barkved, O., 2001. Compensating for the effects of gas clouds on C-wave imaging: A case study from Valhall. The Leading Edge, 20, 1022-1028.

Li, X-Y. and Yuan, J., 2001a. Accuracy and sensitivity analysis for estimating anisotropic parameters from 4C seismic data. 71st Internat. Mtg. Soc. Expl. Geophys., Expanded Abstract, 869-872.

Li, X-Y. and Yuan, J. 2001b. Converted-wave imaging in inhomogeneous, anisotropic media: Part I - Parameter estimation, 63rd Annual International EAGE Meeting, P109.

Li, X-Y., 2003. Converted-wave moveout analysis revisited: the search for a standard approach. 73rd Internat. Mtg. Soc. Expl. Geophys., Expanded Abstract, 805-808.

Li, X-Y. and Yuan, J., 2003. Converted-wave moveout and conversion-point equations in layered VTI media: theory and applications. Journal of Applied Geophysics, 54, 297-318.

Li, Y. and Gu, Y., 2004. Converted-wave exploration in Sulige gas field, China. 74th Internat. Mtg. Soc. Expl. Geophys., Expanded Abstract, VSP P1.3.

Liu, E., Chapman, M., Loizou, N., and Li, X., 2006. AVO analyses from four wells in the west of Shetland: Spectral decomposition. 68th Annual International EAGE Meeting.

Liu, E. and Chapman, M., 2006. Comparison of Spectral decomposition techniques for evaluating frequency-dependent variations in seismic data. Edinburgh Anisotropy Project annual report, Section C: Frequency-dependent anisotropy.

MacLeod, M., Hanson, R., Hadley, M., Reynolds, K., Lumley, D., McHugo, S., and Probert, A., 1999. The Alba field OBC Seismic survey. 61st Annual International EAGE Meeting.

Mancini, F., Li, X., Dai, H., and Pointer, T., 2005. Imaging Lomond field using C-wave anisotropic PSTM. The Leading Edge, 24, 614-620.

Margrave, G., Stewart, R., and Larsen, J., 2001. Joint PP and PS seismic inversion. The Leading Edge, 20, 1048-1052.

Masters, J., 1979. Deep basin gas trap, Western Canada. AAPG bulletin, 63, 152-181.

Mattocks, B., Li, J., and Roche,S., 2005. Converted-wave azimuthal anisotropy in a carbonate foreland basin. 75th Internat. Mtg. Soc. Expl. Geophys., Expanded Abstract.

Mavko, G., 2005. Expert Answers on Gassmann's equation. CSEG Recorder, May 8-12.

Mavko, G., Mukerji, T. and Dvorkin, J., 1998. The rock physics handbook: tools for seismic analysis in porous media. Cambridge University Press.

Mavko, G. and Nur, A., 1975. Melt squirt in the asthenosphere. J. geophys. Res., 80, 1444-1448.

Maxwell, P., 2001. Sensor improves image quality. Hart's E&P, September.

McCormack, M.D. and Tatham, R.H., 1991. Shear-waves and anisotropy in exploration seismology. SEG Special Publication.

Murphy,W., Reischer, A., and Hsu, K., 1993. Modulus decomposition of compressional and shear velocities in sand bodies. Geophysics, 58, 227-239.

Nahm, J. and Duhon, M., 2003. Interpretation and practical applications of 4C-3D seismic data, East Cameron gas fields, Gulf of Mexico. Multicomponent symposium, Houston.

Neidell, N.S. and Taner, M.T., 1971. Semblance and other coherency measures for multichannel data. Geophysics, 36, 482-497.

Nickel, M. and Sonneland, L., 2004. High resolution V_p-V_s ratio estimates from multi-component seismic data. 66th Annual International EAGE Meeting, E012.

Nolte, B., Bishop, K., and Sukup, D. 1999. Anisotropic prestack depth migration of Converted-wave data from the Gulf of Mexico. 69th Internat. Mtg. Soc. Expl. Geophys., Expanded Abstract,691-694.

Odebeatu, E., Zhang, J., Chapman, M., Liu, E., and Li, X., 2006. Application of spectral decomposition to detection of dispersion anomalies associated with gas saturation. The Leading Edge, 25, 206-210.

Ogiesoba, O. and Stewart, R., 2003. V_p/V_s from multicomponent seismic data and automatic PS to PP time mapping. 73rd Internat. Mtg. Soc. Expl. Geophys., Expanded Abstract, 789-792.

Ostrander, W.J., 1982. Plane wave reflection coefficient for gas sand at nonnormal angles of incidence. 52nd Internat. Mtg. Soc. Expl. Geophys., Expanded Abstract, 216-220.

Partyka, G., Gridley, J., and Lopez, J., 1999. Interpretational applications of spectral decomposition in reservoir characterization. The Leading Edge, 18, 353-360.

Peebler, R. and White, J., 2005. Full-wave seismic, digital acquisition systems setting -new standard for 3-D imaging. American Oil&Gas reporter, January.

Pickett, G. R., 1963. Acoustic character logs and their application in formation evaluation. J.Petr. Tech., 659-667.

Podolak, M., 2004. Development of C-wave onshore seismic survey in Poland. Presented at 5th Conference & Exposition on Petroleum Geophysics Hyderabad.

Pope, D., Kommedal, J., and Hansen, J., 2000. Using 3D 4C seismic to drill beneath the Lomond gas cloud. 62nd Annual International EAGE Meeting, L01.

Probert, T., Ronen, S., and Bryan, R., 2000. A case study of azimuthal anisotropy analysis from a N. Sea 3D 4C project. SEG/EAGE Summer Research Workshop, Boise, Idaho.

Probert, T. and Wells, S., 2000. The Gryphon 4C survey - processing and results. 62nd Annual International EAGE Meeting, L06.

Roche, S., Wagaman, M., and Watt, H., 2005. Anadarko Basin survey shows value of multicomponent acquisition. First Break, 23, February.

Russell, B., Hedlin, K., and Hilterman, F., 2003. Fluid-property discrimination with AVO: A Biot-Gassmann perspective. Geophysics, 68, 29-39.

Rutherford, S.R. and Williams, R.H., 1989. Amplitude-versus-offset variations in gas sands. Geophysics, 54, 680-688.

Shuey, R.T., 1985. A simplification of the Zoeppritz equations. Geophysics, 50, 609-614.

Sinha, S., Routh, P. S., Anno, P. D., and Castagna, J. P., 2005. Spectral decomposition of seismic data with continuous-wavelet transform. Geophysics, 70, 19-25.

Smith, G.C. and Gidlow, P.M., 1987. Weighted stacking for rock property estimation and detection of gas. Geophysical Prospecting, 35, 993-1014.

Spitz, S., Gratacos, B., Haggard, W., and Vuillermoz, C., 2000. Reservoir monitoring using multicompoinent seismic: Processing the Teal South 4D-4C. SEG/EAGE Summer Research Workshop, Boise, Idaho.

Stearn, J., Castoro, A., and Backhouse, R., 2001. Chestnut well planning using elastic impedance of 4C seismic data. 63rd Annual International EAGE Meeting, F14.

Stewart, R., 1994. The present and promise of P-S seismic exploration. Crewes Project Research Report, 6, Ch.1.

Stewart, R., Gaiser, J., Brown R., and Lawton, D., 2003. Converted-wave seismic exploration: Applications. Geophysics, 68, 40-57.

Taner, M.T. and Koehler, F., 1969. Velocity spectra-digital computer derivation and applications of velocity functions. Geophysics, 34, 859-881.

Taner, M.T., Koehler, F., and Sheriff, R.E., 1979. Complex seismic trace analysis. Geophysics, 44, 1041-1063.

Tatham, R., 2002. Future directions of multicomponent seismic methods in the marine environment. The Leading Edge, 21, 377-378.

Tatham, R., 2006. Successful Application of P- and S-wave seismic data. 76th Internat. Mtg. Soc. Expl. Geophys., Expanded Abstract.

Tessmer, G. and Behle, A., 1988. Common conversion point data-stacking technique for converted waves. Geophysical Prospecting, 36, 671-688.

Thompson, C., Helgesen, H. K., and Battie, J. E., 2000. 2D-4C seismic exploration data for risk reduction, Fles prospect, offshore Mid-Norway. SEG/EAGE Summer Research Workshop, Boise, Idaho.

Thomsen, L., 1990. Poisson was not a geophysicist. The Leading Edge, 9, 27-29.

Thomsen, L., 1999. Converted-wave reflection seismology over inhomogeneous, anisotropic media. Geophysics, 64, 678-690.

Thomsen, L., 2002. Understanding Seismic Anisotropy in Exploration and Exploitation. Soc. of Expl. Geophys, No. 5 in Distinguished Instructor Series.

Thomsen, L. A., Barkved, O. I., Kommedal, J. H., and Rosland, B., 1997. Converted-wave imaging of Valhall reservoir. 59th Annual International EAGE Meeting, B048.

Tian, L., Xia, Q., and Liu, C., 2004. The application of multiple component seismic exploration in BoHai Bay, P.R. China. 74th Internat. Mtg. Soc. Expl. Geophys., Expanded Abstract, 2565-2568.

Tsvankin, I. and Thomsen, L., 1994. Nonhyperbolic reflection moveout in anisotropic media. Geophysics, 59, 1290-1304.

van der Kolk, C.M., Guest, W.S., and Potters, J., 2001. The 3D shear experiment over Natih field in Oman: The effect of fracture-filling fluids on shear propagation. Geophysical Prospecting, 49, 179-197.

Verm, R. and Hilterman, F., 1995. Lithology color-coded seismic sections: The calibration of AVO crossplotting to rock properties. The Leading Edge, 14 ,847-853.

Vetri, L., Loinger, E., Gaiser, J., Grandi, A., and Lynn, H., 2003. 3D/4C Emilio: Azimuth processing and anisotropy analysis in a fractured carbonate reservoir. The Leading Edge, 22.675-679.

Wang, Z., 2000. Seismic and acoustic velocities in reservoir rocks, in Wang, Z., and Nur, A., Eds., Seismic and acoustic velocities in reservoir rocks. Soc. Expl. Geophys., 633.

Wei, X., Li, X-Y., Yang, O., and Songqun, S., 2003. Case study of using converted PS-waves to image gas reservoirs in the Ordos Basin, China. 73rd Internat. Mtg. Soc. Expl. Geophys., Expanded Abstract, 769-772.

Wei, X. and Liu, Y., 2002. The study of static correction in desert and loose terrain. 72nd Internat. Mtg. Soc. Expl. Geophys., Expanded Abstract,2249-2252.

Wyllie, M. R. J., Gregory, A. R., and Gardner, L. W., 1956. Elasticwave velocities in heterogeneous and porous media. Geophysics, 21,41-70.

Yuan, J., Li, X-Y. and Ziolkowski, A., 2001. Converted-wave moveout analysis in layered anisotropic media: a case study. 63rd Annual International EAGE Meeting, L027.

Zhang, Y., 1992. Stacking P-SV converted wave data with raypath velocity. 62nd Internat. Mtg. Soc. Expl. Geophys., Expanded abstract, 1214-1217.

Zhang, Y., 1996. Nonhyperbolic converted wave velocity analysis and normal moveout. 66th Internat. Mtg. Soc. Expl. Geophys., Expanded abstract, 1555-1558.

Appendix A

Calculation of the frequency dependent elastic tensor

Mark Chapman, Enru Liu, and Xiang-Yang Li

In this appendix we outline the procedure for calculating the frequency dependent elastic constants on which our modelling scheme depends. The equations are based on those of Chapman et al. (2002), under the simplifying assumption that we consider local ("squirt") flow rather than a combination of local and global flow. In this way we consider frequency dependent wave-induced exchange of fluid between cracks and pores as well as between cracks of different orientations. Cracks are considered to be oblate spheroids ("penny shaped") of low aspect ratio, and the pores are considered to be spherical. The calculations are based on those of Eshelby (1957).

The inputs to the model are the isotropic elastic moduli λ and μ, which in principle are associated with the rock without cracks or pores, the porosity ϕ , a time scale parameter τ , a crack density ε , the crack aspect ratio r and the fluid bulk modulus k_f . All other parameters being equal, ε controls the magnitude of dispersion and attenuation, while τ controls the frequency range over which that dispersion occurs. Theoretically, τ is proportional to fluid viscosity and inversely proportional to permeability, although there is also a scale dependence (Chapman, 2003). According to the model, variations in permeability should be modelled by changing the τ value.

To calculate the frequency dependent elastic tensor, we first define the pore- and crack-space compressibility parameters:

$$K_p = \frac{4\mu}{3\kappa_f}; \qquad \text{(A1)}$$

$$K_c = \frac{\pi\mu(\lambda+\mu)r}{\kappa_f(\lambda+2\mu)}. \qquad \text{(A2)}$$

We then define non-dimensional parameters:

$$\gamma = \frac{3\pi(\lambda+\mu)}{4(\lambda+2\mu)}\frac{(1+K_p)}{(1+K_c)}; \qquad \text{(A3)}$$

$$\gamma' = \gamma\frac{\lambda+2\mu}{3\lambda+2\mu}\frac{1}{1+K_p}; \qquad \text{(A4)}$$

and the frequency-dependent constants:

$$A(\omega) = \frac{(1+i\omega\gamma\tau)\dfrac{\lambda+2\mu}{(\lambda+\mu)}\left(\dfrac{16\varepsilon}{27\phi(1+K_p)}+\dfrac{(\lambda+\mu)}{3\lambda+2\mu}\right)+i\omega\tau\left(\dfrac{1}{3(1+K_c)}-\gamma'\right)}{1+i\omega\tau+(1+i\omega\gamma\tau)\dfrac{16\varepsilon(1+K_c)}{9\phi(1+K_p)}\dfrac{\lambda+2\mu}{(\lambda+\mu)}}; \qquad \text{(A5)}$$

$$B(\omega) = \frac{\dfrac{1}{3(1+K_c)}+\dfrac{9(1+K_p)}{16(1+K_c)}\dfrac{(\lambda+\mu)}{3\lambda+2\mu}+\dfrac{i\omega\tau}{1+i\omega\tau}\left(\gamma'-\dfrac{1}{3(1+K_c)}\right)}{\dfrac{9(1+K_p)}{16(1+K_c)}\dfrac{(\lambda+\mu)}{(\lambda+2\mu)}+\dfrac{1+i\omega\gamma\tau}{1+i\omega\tau}}. \qquad \text{(A6)}$$

The effective, frequency-dependent, bulk modulus is then given by:

$$\kappa_{eff} = \kappa - \varepsilon[\frac{4(3\lambda+2\mu)(\lambda+2\mu)}{\mu(\lambda+\mu)}\{1-3A(\omega)\} - 4\pi A(\omega)r]$$
$$-\phi[\frac{(3\lambda+2\mu)}{4\mu}\{\frac{\lambda+2\mu}{3\lambda+2\mu}+B(\omega)\}-3B(\omega)]. \qquad \text{(A7)}$$

The effective shear modulus is given by:

$$\mu_{eff} = \mu - \frac{16}{45}\varepsilon\frac{1}{1+K_c}\frac{\mu(\lambda+2\mu)}{3\lambda+4\mu}(K_c+\frac{1}{1+i\omega\tau}) - \frac{32}{45}\varepsilon\frac{\mu(\lambda+2\mu)}{3\lambda+4\mu} - \phi\frac{15\mu(\lambda+2\mu)}{9\lambda+14\mu}.$$

(A8)

Following O'Connell and Budiansky (1978), we define the Quality factor Q for P- and S-waves respectively as:

$$Q_p = \frac{-\mathrm{Re}(\kappa_{eff}+\frac{4}{3}\mu_{eff})}{\mathrm{Im}(\kappa_{eff}+\frac{4}{3}\mu_{eff})}; \qquad \text{(A9)}$$

$$Q_s = \frac{-\mathrm{Re}(\mu_{eff})}{\mathrm{Im}(\mu_{eff})}. \qquad \text{(A10)}$$

Appendix B

Publications

1. **Zhang, J.,** Chapman, M., Liu, E., Li, X-Y, Wang, S., and Liu, Z., 2007. *Fluid detection by spectral decomposition: lessons from numerical, physical modelling and field studies*, 69th Annual EAGE meeting, F18.

2. **Zhang, J.** and Fabio, M., 2006. *PP and PS joint inversion – a case study from west Africa*, 68th Annual EAGE meeting, P06.

3. Odebeatu, E., **Zhang, J.**, Chapman, M., Liu, E. and Li, X-Y, 2006. *Application of spectral decomposition to detection of dispersion anomalies associated with gas saturation*, The Leading Edge, Volume 25, Issue 2, 206-210.

4. **Zhang, J.** and Li, X.-Y., 2005. *AVO fluid discrimination with weak impedance contrast – a case study from the Ordos basin*, 67th Annual EAGE meeting, P035.

5. **Zhang, J.** and Li, X.-Y., 2004. *P-wave and converted wave event correlation by converted wave moveout analysis*, 66th Annual EAGE meeting, P025.

Fluid detection by spectral decomposition: lessons from numerical, physical modelling and field studies.

Jinghua Zhang, Mark Chapman, Enru Liu and Xiang-Yang Li, British Geological Survey; Shangxu Wang, China University of Petroleum; Zhenwu Liu, CNPC

Abstract

This paper investigates the use of spectral decomposition techniques to detect fluid saturation through studies on field data, physical modelling data and numerical modelling. The main mechanisms which control the spectral response are fluid-sensitive tuning, together with attenuation and dispersion for reflected waves. In many cases the direct transmission loss due to attenuation is less useful as a hydrocarbon indicator and may be ignored. In our examples, numerical modelling of the reflection response is able to predict the spectral response to changing fluid which is seen in the field and physical modelling data. Consequently we argue that with careful modelling it may be possible to interpret the spectral response in terms of fluid type.

Introduction

The interpretation of seismic data in terms of fluid saturation is a fundamental goal of geophysical exploration. Over the last twenty years it has come to be generally accepted that seismic amplitudes contain important information which can be related to fluid saturation. Most interpretations are based on Gassmann's theory and reflectivity modelling with the Zoeppritz equations.

Recent attention has focussed on the question of whether the frequency response of reflections can also be used to reveal fluid information through the application of spectral decomposition techniques (Ebrom, 2004; Castagna et al., 2003; Korneev et al, 2003; Zhao et al., 2006; Odebeatu et al., 2006). Hydrocarbon saturation is often associated with particularly high values of seismic attenuation, so it is tempting to associate apparent frequency anomalies with attenuation. Unfortunately many effects can be mistaken for attenuation, particularly processing artefacts and tuning phenomena.

In this study we apply spectral decomposition techniques to field and physical modelling data and attempt to interpret the results in terms of numerical modelling. We demonstrate that the seismic response is best explained as a combination of fluid-sensitive tuning and dispersion. This suggests that with careful modelling it should be possible to extract fluid information from the spectral response of seismic reflections.

Theory

In the case of reflection from a single interface, Gassmann's theory predicts that changing the fluid saturation in one of the layers will change the impedance contrast and therefore the amplitude of the reflection. This effect is independent of frequency. Reflections from a thin layer are typically composite events which result from the superposition of top and bottom reflections. In this case, fluid substitution will also change the traveltime within the thin layer, and this impacts on the interference between the two reflections. This effect does lead to a change in frequency, so we expect fluid substitution to be intrinsically frequency-dependent in multiple thin layers.

Attenuation and dispersion can also give rise to frequency-dependence of the reflection. Chapman et al. (2006) have presented a modelling framework which accounts for fluid-sensitive dispersion and attenuation. In this modelling, the introduction of gas results in a marked increase in attenuation, and associated dispersion. Attenuation leads to a loss of high frequencies during propagation. However, this transmission loss depends on having a thick layer to be effective and can often be ignored in most cases. Nevertheless, the existence of strong dispersion in a hydrocarbon saturated layer leads to frequency dependence of the impedance contrast at the interface and so makes the reflection coefficient frequency dependent. This tends to shift the reflections to higher or lower frequency markedly compared to the background trend, with the direction of the shift depending on the AVO class of the reflection. This reflection response does not depend on the thickness of the layer and is the main focus of our study. Chapman et al. (2006) demonstrated that the spectral response of the tuning and dispersion effects were often comparable in magnitude, and argued that both had to be taken into account to interpret seismic data properly. Odebeatu et al. (2006) introduced a technique for spectral balancing and differencing of frequency volumes which showed the spectral anomalies particularly clearly.

Example 1

The first example is land data from a gas reservoir in Northeast China. The targeted gas beds are thin and have a small P-wave velocity difference between the gas sand and the overlying shale, giving rise to a weak PP-wave reflection. AVO analysis suggested that the top of the reservoir was a class III interface, but that the reservoir reflection itself was a composite event whose amplitude declined with increasing angle of incidence. Based on log data, we created

an idealised multilayer model with a 10 m thick gas sand and 10 m thick shale layer encased in a half-space of higher impedance. This arrangement was able to effectively model the observed AVO behaviour within the reservoir.

Spectral decomposition of the stacked sections revealed that the high frequencies of the reflection had been attenuated. Modelling revealed that the gas saturated layer was too thin for us to explain the loss of high frequencies through either a tuning effect or attenuation during propagation (transmission loss). However the dispersion effect on the reflection coefficient was able to explain the data. The basis of the modelling was that the higher velocity in the gas sand at high frequency weakened the contrast in elastic impedance and therefore the reflection strength, while at low frequencies there was a significant contrast in the elastic properties. We concluded that the spectral anomaly in the data was most likely the result of excess dispersion in the reservoir layer.

Example 2

Our second example is once again taken from land data from West China. The target is a known gas reservoir which appears as a dim-spot on the seismic section. The reservoir itself consists of a succession of thin sand-shale layers.

The CNPC Key Geophysical Laboratory at the China University of Petroleum in Beijing carried out physical modelling to simulate reflection surveys over models relevant to the reservoir under consideration. The model consisted of a thick overburden layer overlying several inter-bedded sand/shale thin layers. The overburden is made of epoxy resin, of thickness 50.4mm and velocity 2440 m/s. The target consists of inter-bedded thin layers of glass, simulating shale, and a mixture of Silicon Dioxide and epoxy resin, simulating sands. The glass layers have an average thickness of 1.22mm, a velocity of 2490 m/s and a density of 1.18 g/cc. The sand layers are 1.4 mm thick, have a porosity of 17% and a P-wave velocity of 3245 m/s when saturated with air. Models with both 5 and 7 sand layers were constructed and tested, with the sand layers being saturated with water, oil and gas.

Since the velocities in the physical model were known, we were able to perform forward modelling with the reflectivity method to compute the expected responses of the model under gas, oil and water saturation. We performed the modelling first assuming elastic properties, and then introduced fluid-sensitive dispersion following the technique of Chapman et al. (2006). For the elastic modelling, we find that the collection of thin layers tends to act as a high pass filter, effectively attenuating the low frequencies through interference. This behaviour is strong for gas saturation, and rather less pronounced for water and oil saturation. Interestingly, when we introduce dispersion into the modelling we find, in agreement with Chapman et al. (2006), that for a reflection from a single layer the dimming in the gas-saturated case is associated with a shift towards high frequencies, since at low frequencies the reflection coefficient tends to be smaller. When we introduce dispersion into the multi-layer modelling we find that the two effects combine to give a very pronounced shift towards high frequencies.

For the physical modelling data we identify two reflections: the reflection from the top of the overburden and the reflection from the target. The amplitudes on the broadband stacked sections behave much as expected, with the gas saturated case having a dimmer reflection than the water and oil saturated cases. Following the method of Odebeatu et al. (2006), we take the reflection from the top of the overburden as the reference to be used for spectral balancing. After such spectral decomposition and balancing, we see that in the water and oil saturated cases the reflection strength from the target appears to be of a similar strength for all frequencies. This is not so in the gas saturated case, in which there is strong energy at high frequencies, but much lower amplitudes at low frequencies in the reflection from the target (Figure 1).

The same analysis technique was applied to the field data. We chose a reference horizon and carried out spectral decomposition and balancing. It is very clear that the reflection from the known gas reservoir zone, which appears to be dim on the broadband data, is rich in high frequencies (Figure 2). Indeed, on the high frequency sections the reservoir appears as a bright spot, but it is not visible on the low frequency sections. Thus we conclude that the spectral signature of gas saturation which was predicted from the numerical modelling and reproduced in the physical modelling data is also visible in the field data.

Conclusions

This paper has demonstrated that spectral decomposition techniques can be used to provide information on the saturating fluid. The spectral response to changing fluid is affected by fluid-sensitive tuning, the effect of dispersion on the reflection coefficient and attenuation during propagation through the dispersive zone. The effect of attenuation during propagation can often be ignored in the case of a thin hydrocarbon layer, but modelling is necessary to understand the effects of tuning and dispersion. The accuracy of the velocity model is an important consideration. In our first example, we interpret the loss of high frequencies to be due to the frequency-dependent reflection coefficient, since the thickness of the hydrocarbon layer mitigates against tuning or attenuation being the cause of the observed anomaly. In our second case we see a clear spectral signature of gas saturation which appears consistently in our numerical, physical modelling and field data. The signature in the field data is most easily explained as a combination of fluid-sensitive tuning and dispersion, although we cannot confidently rule out the possibility that either effect is uniquely responsible. This highlights our main argument that careful modelling is necessary to understand the complex effect of different fluids on the spectral response and enable robust interpretation.

Acknowledgements

We thank CNPC for permission to show the physical modeling and field data. This work is supported by the CNPC international collaboration programme through the Edinburgh Anisotropy Project (EAP) of the British Geological Survey (BGS) and the CNPC Key Geophysical Laboratory at the China University of Petroleum. The work is published with the approval of all project partners and the Executive Director of BGS.

References

Castagna, J.P., Sun, S. and Seigfried, R.W., 2003. Instantaneous spectral analysis: detection of low-frequency shadows associated with hydrocarbons. The Leading Edge, Vol. 22, No. 2, 120-1227.

Chapman, M., Liu, E. and Li, X-Y., 2006. The influence of fluid-sensitive dispersion and attenuation on AVO analysis. Geophysical Journal International, 167, 89-105.

Ebrom, D., 2004. The low-frequency gas shadow on seismic sections. The Leading Edge, Vol. 23, No. 8, p 772.

Korneev, V., Goloshubin, G., Daley, T. and Silin, D., 2004. Seismic low-frequency effects in monitoring fluid-saturated reservoirs. Geophysics, 69, 522-532.

Odebeatu, E., Zhang, Z., Chapman, M., Liu, E. and Li, X-Y., 2006. Application of spectral decomposition to detection of dispersion anomalies associated with gas saturation. The Leading Edge, Vol, 25, No. 2, 206-210.

Zhao, B., Johnston, D. and Gouvela, W., 2006. Spectral Decomposition of 4D Seismic Data. 76th Annual International Meeting, SEG, Expanded Abstracts.

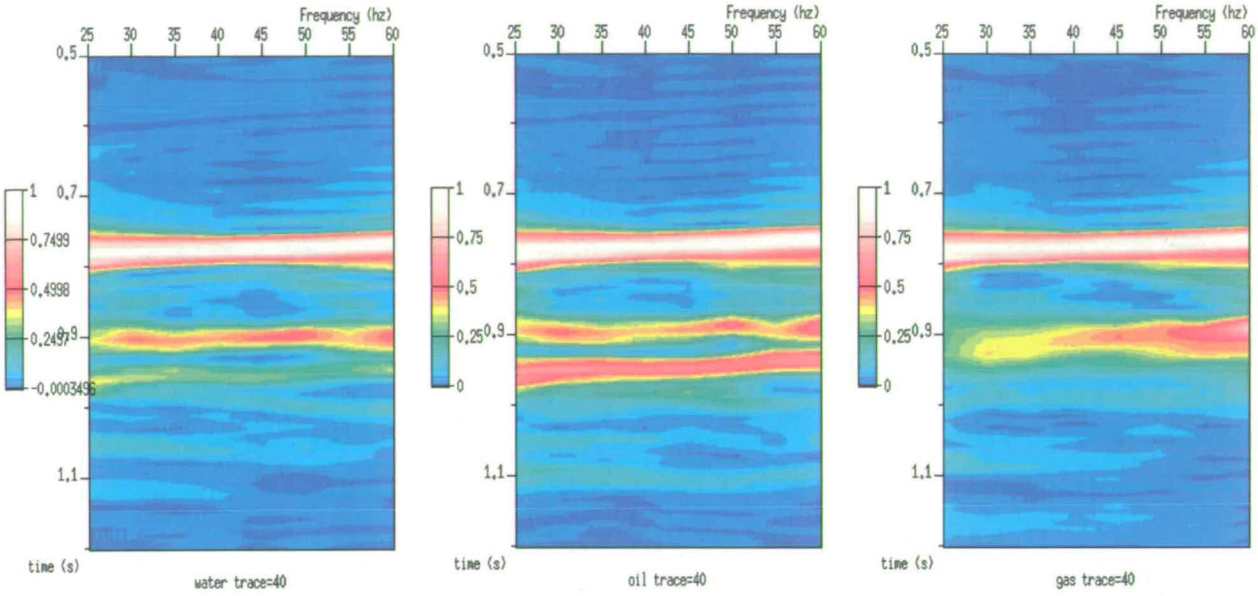

Figure 1: Spectral decomposition of physical modelling data for water (left), oil (center) and gas (right) saturation. Water bottom reflection (0.8s) is balanced in all cases. Note the strong shift of energy to higher frequencies in the lower reservoir reflection (0.9s) in the gas saturated case, which is absent for other saturations.

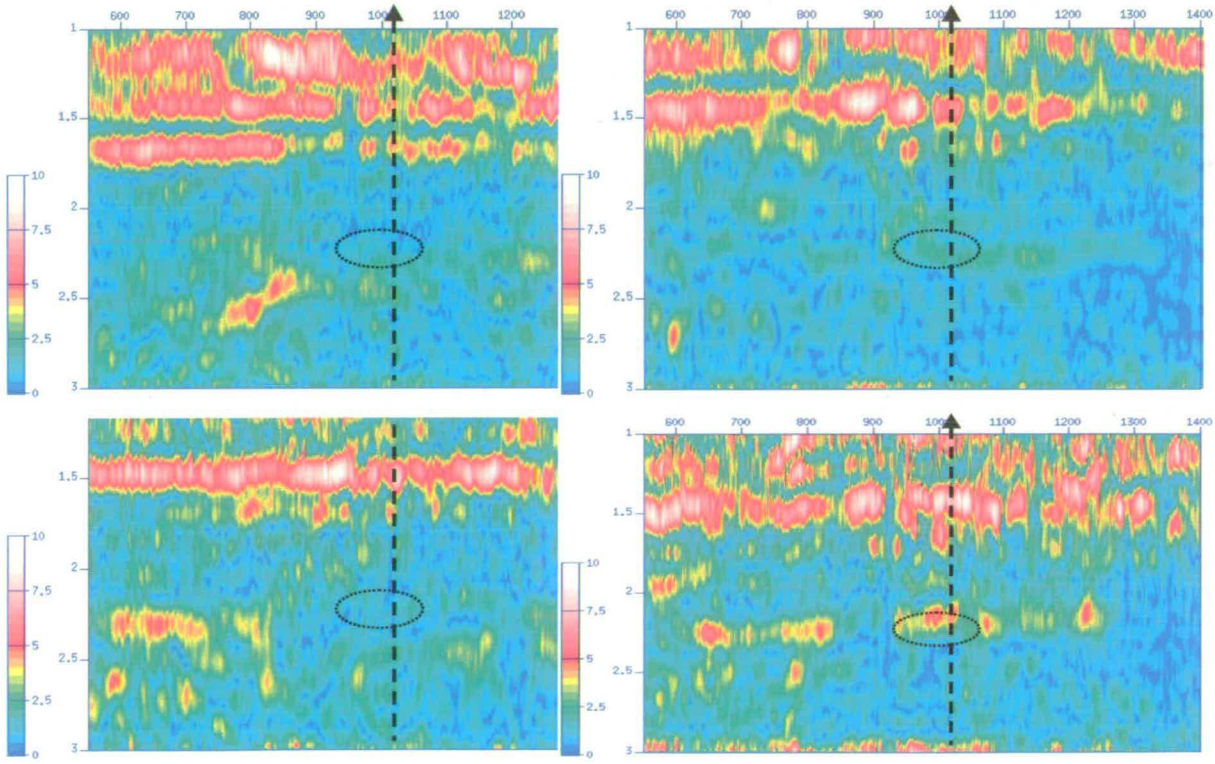

Figure 2: Balanced iso-frequency sections for 15 Hz (top left), 20 Hz (bottom left), 25 Hz (top right) and 30 Hz (bottom right) from field data. Note that the gas reservoir reflection (ringed) becomes progressively brighter as we move to higher frequency.

PP and PS joint inversion – a case study from West Africa

Jinghua Zhang[1] and Fabio Mancini[2]
[1]EAP, British Geological Survey, Murchison House, West Mains Road, Edinburgh EH9 3LA, UK
[2]Geoscience Research Centre, TOTAL E&P UK PLC, Crawpeel Road, Aberdeen AB12 3FG, UK

Abstract
We present results of a joint PP- and PS-wave AVO inversion from a multicomponent dataset acquired offshore West Africa. We compare these results with the output of the single, P-wave only, inversion. In both realistic synthetic examples and real data the joint inversion produces a better estimation of the shear impedance reflectivity and of the pseudo Poisson's ratio reflectivity compared with the single inversion.

Introduction
We used an AVO inversion based on the weighted stacking technique described by Smith and Gidlow (1987), and extended for converted waves by Stewart (1990). Examples of the application of this technique can be found in Margrave et al. (1998), on data from the Blackfoot field in Canada, and Zhang and Li (2005), on data from the Ordos Basin in China. The method works by least-square inversion of Aki-Richard's approximations to recover P- and S-impedance reflectivity ($\Delta Ip/Ip$, $\Delta Is/Is$) and pseudo Poisson's ratio reflectivity ($\Delta\sigma/\sigma$). The density is assumed to follow Gardner's relation ($\rho = k\alpha^{1/4}$). Using available log data we verified that this assumption is valid in our area of study.
The weighting parameters are angle-dependent. In single PP-wave inversion, the weights for $\Delta Is/Is$ distribute mainly in both the near and far offsets; while for $\Delta Ip/Ip$ the weights decrease with increasing offset. In joint inversion, although the near-offset PP-data and mid-offset PS-data have important weights for both $\Delta Is/Is$ and $\Delta Ip/Ip$ estimation, it's the mid-offset PS-data that have a larger impact on the estimation of $\Delta Is/Is$. Incident and reflection angles, time and spatial varying Vp/Vs ratio are calculated from ray tracing through a 1D velocity-depth model. The reservoir rocks in the study area derive from clastic deep-sea turbidites, mainly consisting of channel sands and basin floor fans. Porosity and permeability are generally good. The overall structure is relatively simple.

Data acquisition and processing
The acquisition was carried out by PGS using inline shooting, with swaths of two cables separated by 300 m. The shooting line separation was 50 m. with a shot interval of 50 m. The receiver interval was the conventional 25 m. Data quality was very good, both for P- and C-waves. Time processing via Pre-Stack Time Migration (PSTM) was carried out by CGG. For C-waves CGG took particular care of the estimation of the parameter γ_{eff}, responsible for the correct structural alignment in the positive and negative offset images (Thompsen, 1998), by performing repeated γ_{eff} scans.
The PZ and PS images for one inline are shown in Figure 1. The PS-waves are displayed in PP-time after event correlation. The correlation was guided by the well log and performed using Hampson-Russel ProMC software. The quality of the two migrated images is good, although we can notice a great difference in frequency content.

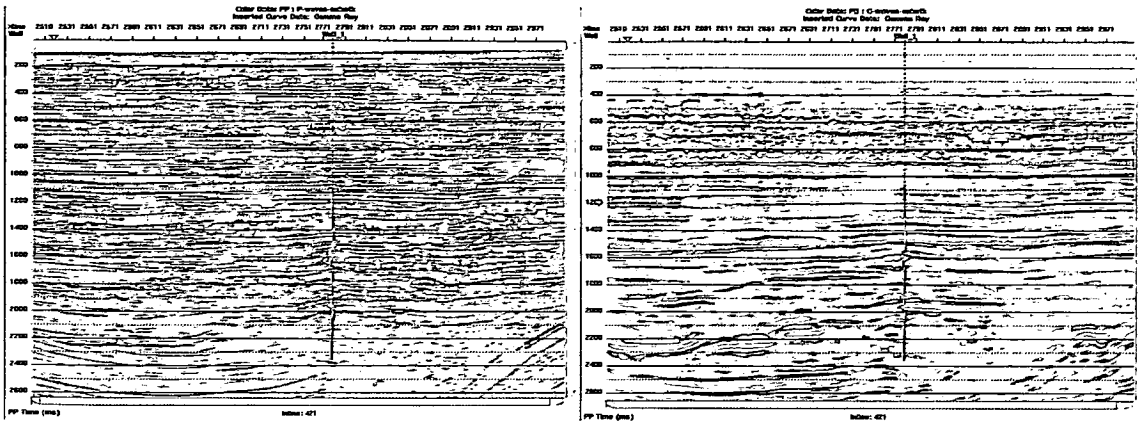

Figure 1: PZ image, left and PS image displayed in PP time, right.

Inversion results

Synthetics: We performed synthetic tests based on a geological model derived by blocking the logs from the available vertical well. Synthetic CDP and CCP (C-waves) gathers were calculated using Zoeppritz equations. As shown on the left of Figure 2, the response of the top of the reservoir, at 1.55 s., has inverse polarity for P and C-waves. This is confirmed by the real data shown on the right of Figure 2, where the main window is for PS-data and the inner window is for PP-data (after band-pass filter in order to make the two sections comparable).

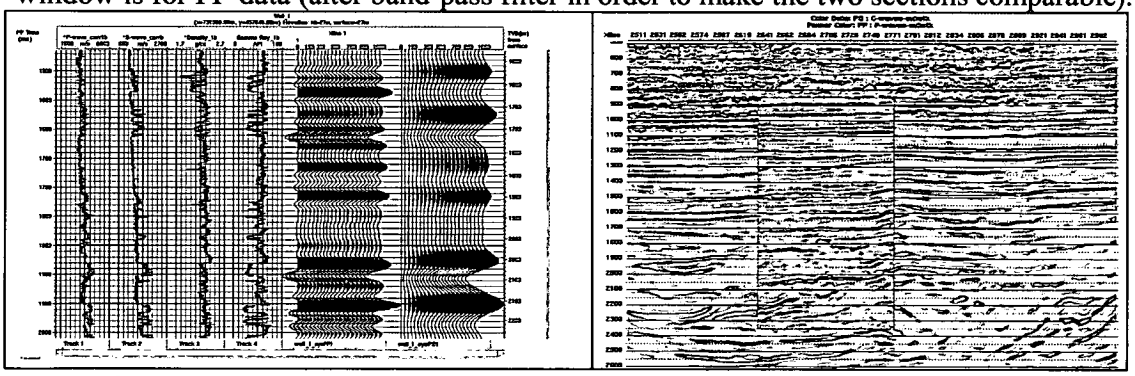

Figure 2: Blocked model from well logs and PP and PS synthetic gathers.

The easily recognizable structure of the area facilitated event registration, which can therefore be considered reliable, above all in the proximity of the well. On these synthetic gathers we tested single (PP-wave only) and joint inversion, with different ranges of offsets and different background velocity-depth models (the original well-derived model and its smoothed version). Results are summarized in Figure 3a, 3b, 3c, and 3d.

For each figure, the first two traces are the inversion results for data muted to an offset maximum of 2.5 km (the offset-to-depth ratio is still greater than one and the incidence angle is about 40°). The first of the two traces is for the original velocity-depth model; the second is for the smoothed model. The two traces in the middle of each figure are for the full offset, again with the two velocity models. The last trace on the right is the value derived from the well.

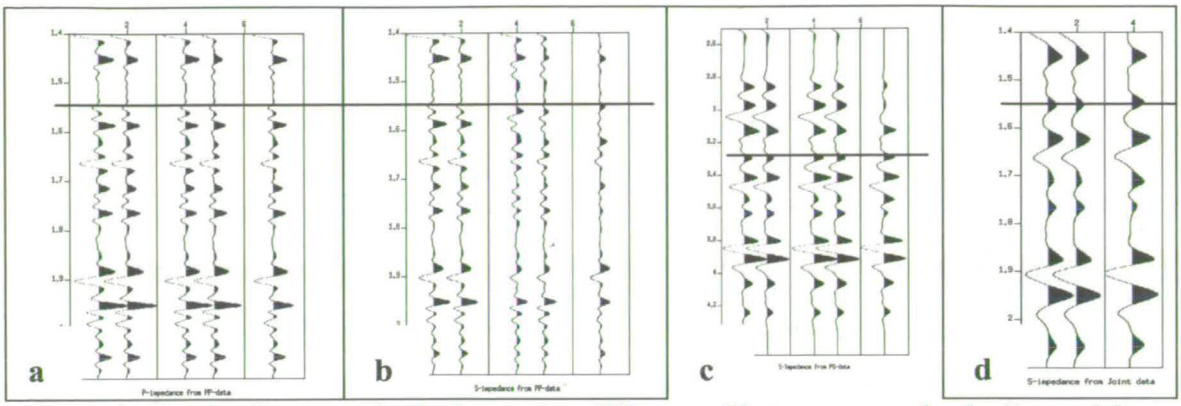

Figure 3: Results from synthetic data using different offset ranges and velocity models.

Figure 3a shows *ΔIp/Ip* from P-wave single inversion. The results do not change much for the different cases studied. Figure 3b shows *ΔIs/Is* from single inversion. In no case can we recover the top of the reservoir, which is the positive peak at 1.55 s. (black line). The inversion seems dominated by the *Ip* reflectivity. Apart from the top of the reservoir, the best result is given when using full offset (no residual NMO in the synthetics) and the smoothed velocity field. In Figure 3c we show *ΔIs/Is* from single inversion of C-wave data. The results are lower frequency as expected but the peak associated to the top reservoir is well recovered. Results with different offsets and velocity models do not show many differences. Finally in Figure 3d we report the results for *ΔIs/Is* from joint inversion for the full offset case. The top of the reservoir is again well recovered. The background velocity does not affect the results.

Real data: For the inversion of real data we used PSTM CIP gathers and the well derived smoothed velocity-depth model. In Figure 4 we show the *ΔIp/Ip* from P-wave single inversion (left) and from joint inversion (right). In this case the single inversion is better, since the joint inversion is contaminated by the lower frequency content of the PS dataset. In both cases the top reservoir is clearly inverted (black circle).

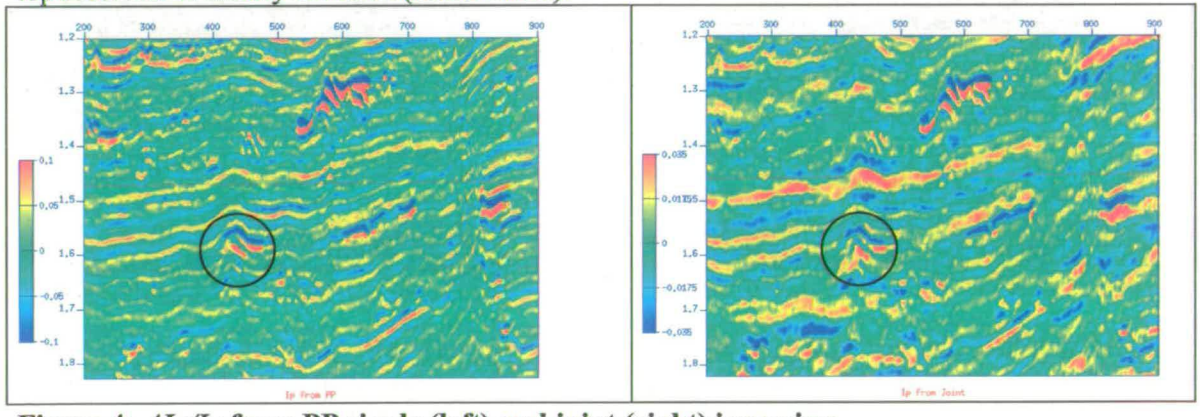

Figure 4: *ΔIp/Ip* from PP single (left) and joint (right) inversion.

Figure 5 shows the *ΔIs/Is*, again from single and joint inversion. For the S-impedance reflectivity we cannot correctly recover the top of the reservoir (positive peak) when we invert only P-waves. Again, as for the synthetics, the results seem dominated by the P-impedance reflectivity. We run more inversions incorporating further offsets, but with similar outcomes. When using both PP and PS data the inversion correctly recovers the top-reservoir. The image appears lower frequency due to the larger influence of C-waves on the *ΔIs/Is* inversion. This is also confirmed by looking at the weight distribution.

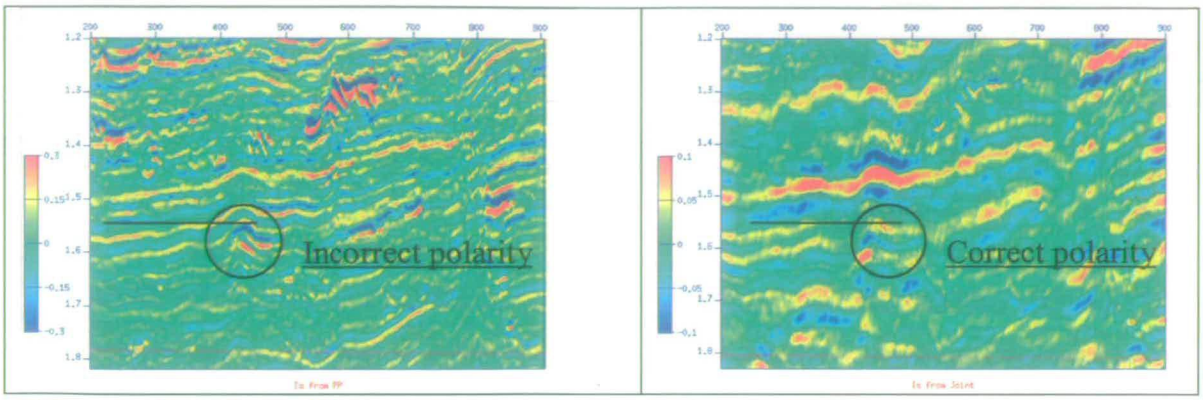

Figure 5: *ΔIs/Is* from PP single (left) and joint (right) inversion.

The most convincing proof of the benefits of introducing C-wave data in the inversion can be seen in the results of the pseudo Poisson's ratio reflectivity, $\Delta\sigma/\sigma$, given by *ΔIp/Ip* - *ΔIs/Is*. In Figure 6 we show the results from P-wave single inversion, on the left, and the results from joint inversion, on the right. While in both cases the anomaly at the reservoir is evident, in the case of joint inversion other anomalies stand out more clearly, above all at 1.3 s. This result should help to increase geophysicists' confidence during interpretation.

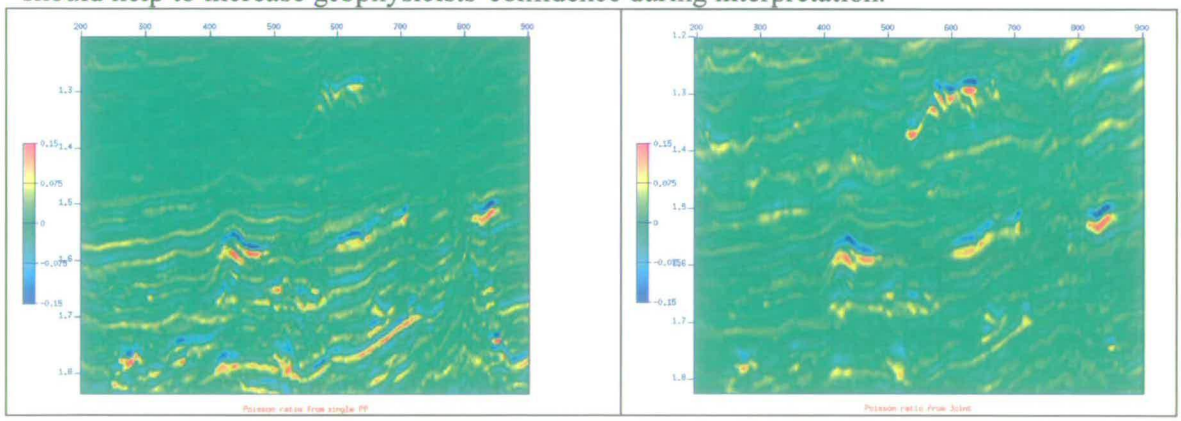

Figure 6: $\Delta\sigma/\sigma$ from PP single (left) and joint (right) inversion

Discussions and Conclusions

We showed results from single and joint inversion of a 4C dataset from West Africa. In this study we made some assumptions and approximations: we used a 1D background velocity-depth model for angle computation, we applied a second-order only NMO correction, we assumed the PSTM to be amplitude preserving and we used Gardner's relation for density estimation. Nevertheless the joint inversion was stable, also thanks to the good quality of the data. Also we did not try to correct for the footprints typically given by OBC acquisitions, since by working in inlines, given the polarized acquisition, we believe this should not be a major problem.

The results showed that we failed to correctly recover *ΔIs/Is* when only P-wave data were used, but we were successful when we introduced C-wave data into the inversion. The weight distribution shows that, in the joint inversion, the *ΔIs/Is* inversion is dominated by PS-wave mid-offset data. The results of the pseudo Poisson's ratio reflectivity also look greatly improved when both datasets were jointly inverted. Although these results are encouraging indeed, we always have to consider the main limitation of this inversion scheme, which is the need of event registration. This area was particularly favorable in that sense, since the main structural events are easily recognizable in both sections.

Acknowledgement

The authors would like to acknowledge TOTAL E&P UK PLC and the TOTAL subsidiary in West Africa and partners for permission to publish this paper. We also thank Remi Dartigalangue, Xiang-Yang Li and Henchang Dai for their help with this work.

References

Margrave, G.F., Stewart, R.R. and Larsen, J.A., 2001, Joint P-P and P-S inversion, The Leading Edge, 20, 1048-1052

Smith, G.C. and Gidlow, P.M., 1987, Weighted stacking for rock property estimation and detection of gas, Geophysical prospecting, 35, 993-1014

Stewart, R.R., 1990, Joint P and P-SV inversion: Crewes Research Report, 2, 112-115.

Zhang, J., Li, X.-Y., 2005, Joint PP- and PS-Wave AVO Inversion - Modelling and Case Studies From the Ordos Basin, EAP Research Report, 12, B1-1 - B1-45

Application of spectral decomposition to detection of dispersion anomalies associated with gas saturation

Emeka Odebeatu, Leeds University, U.K.
Jinghua Zhang, Mark Chapman, Enru Liu, and Xiang-Yang Li, Edinburgh Anisotropy Project, U.K.

For many years geophysicists have attempted to exploit attenuation measurements in exploration seismology, because attenuation is perhaps the seismic property most closely related to the saturating fluid. The routine application of such ideas has proven elusive, however, largely because of the difficulty experienced when we attempt to measure attenuation in reflection data. Recent developments in the application of spectral decomposition methods to seismic data have opened the possibility of making further progress in this direction.

It is certainly the case that a wide range of evidence suggests that hydrocarbon zones are associated with abnormally high values of seismic attenuation and, in view of the Kramers-Kronig relations, we might expect that this attenuation would be associated with significant velocity dispersion. Consideration of the "drift" between velocities measured in VSP and log data over thick sections of the earth's crust has suggested that velocity dispersion in seismic wave propagation is generally small, but this still leaves the possibility that certain zones, such as hydrocarbon reservoirs, exhibit significant magnitudes of velocity dispersion and attenuation. Consideration of indirect dispersion measurements, particularly the frequency dependence of shear-wave splitting and other anisotropic attributes, further suggests that this is the case.

It can be difficult to explain the link between fluid saturation and attenuation using poroelastic models; straightforward application of the Biot equations will lead to attenuation values which are far too small. A recent paper (Chapman et al., 2005) showed how to implement ideas from squirt-flow theory to model hydrocarbon-related attenuation anomalies. Abnormally high attenuation can be produced as result of gas saturation, but this attenuation must be accompanied by significant velocity dispersion in the reservoir layer. This leads naturally to the view of the reservoir as a "dispersion anomaly" and under these circumstances the reflection coefficient becomes strongly frequency dependent. Synthetic modeling suggests that this effect is rather important and would usually dominate the traditional effect of attenuation thought of as a continuous and cumulative loss of energy during propagation. The nature of the frequency response depends strongly on the AVO behavior at an interface.

The effect of the frequency-dependent reflection coefficient is essentially instantaneous in character. This makes modern instantaneous spectral analysis techniques the ideal tool for detecting such variations. Such an approach has a number of potential advantages over the traditional methods which rely on the comparison of the spectral properties of two windows separated in time, and which inevitably contain different combinations of events.

This article applies the spectral decomposition techniques to two field data sets in an attempt to detect the type of dispersion anomalies suggested by the modeling. Within the context of a standard AVO analysis, we find that reflections from the hydrocarbon-saturated zone appear to display systematic frequency anomalies. These anomalies can be reproduced with synthetic reflectivity modeling which is also consistent with the AVO analysis. In general, the study leads us to believe that the study of systematic frequency variations can potentially help provide additional information on fluid saturation.

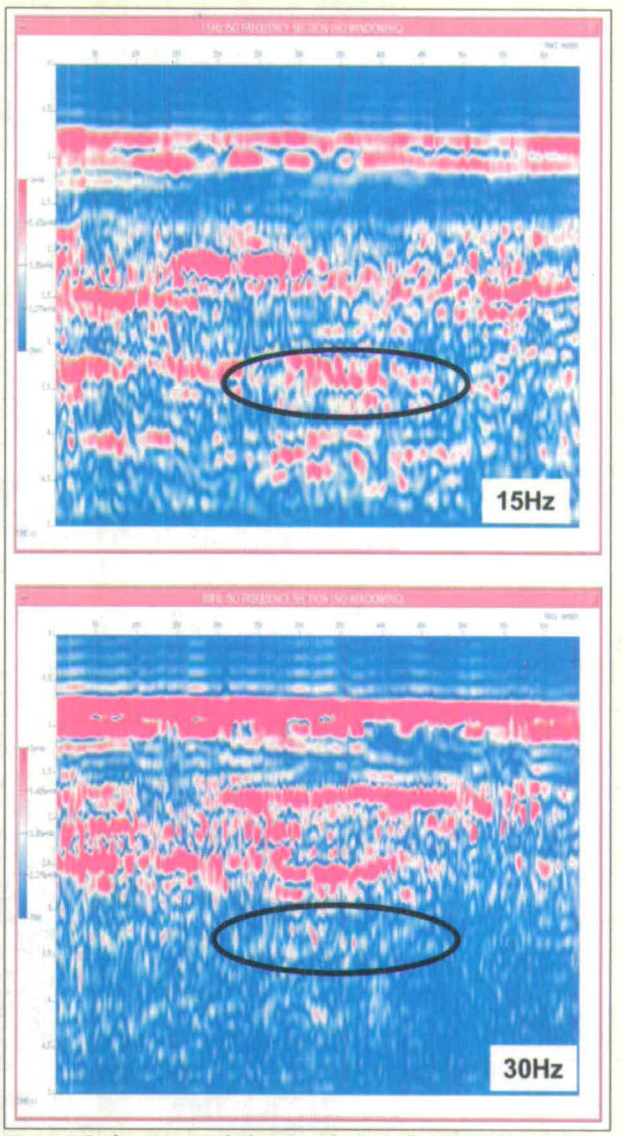

Figure 1. Isofrequency stacked sections for example 1 for 15 Hz and 30 Hz. The reservoir zone, indicated, is bright at the lower frequencies but cannot be observed on the higher frequency sections.

Spectral decomposition and balancing. Spectral decomposition techniques help us to understand scale and frequency-dependent phenomena, essentially by allowing us to study the data one frequency at a time. Specifically in this paper, given a trace $f(t)$, we form the Stockwell, or S-transform:

$$Sf(u,\omega)=\frac{1}{2\pi}\int_{-\infty}^{\infty} f(t)\frac{|\omega|}{\sqrt{2\pi}}e^{-\frac{(u-t)^2\omega^2}{8\pi^2}}e^{-i\omega t}dt,$$

which mean that, for each choice of frequency, we have a new trace corresponding to that particular frequency. With such a

concept and given a collection of traces we can form a "frequency gather," consisting of each trace's representation at the specified frequency. While such an arrangement may seem beguiling, it is very important to remember that perfect spectral decomposition is a logical impossibility on account of the Heisenberg uncertainty principle.

When we wish to compare the traces at different frequencies, we should expect to find markedly different amplitudes because neither the source nor the earth's reflectivity have white spectra. The procedure for compensating for these effects is to use spectral balancing. In our synthetic data, because we know the input wavelet, we can balance the different traces exactly, a step which is similar to deconvolution. In real data we attempt to equalize the average amplitudes between the various traces across a particular time window, or reference horizon. Our preference is to balance over a wide time window, because this makes local frequency anomalies particularly clear.

The main use of spectral decomposition has been in delineating tuning phenomena. Nevertheless, there have been suggestions that it can be used for direct hydrocarbon detection. This paper attempts to develop this aspect of the technique in conjunction with rock physics modeling.

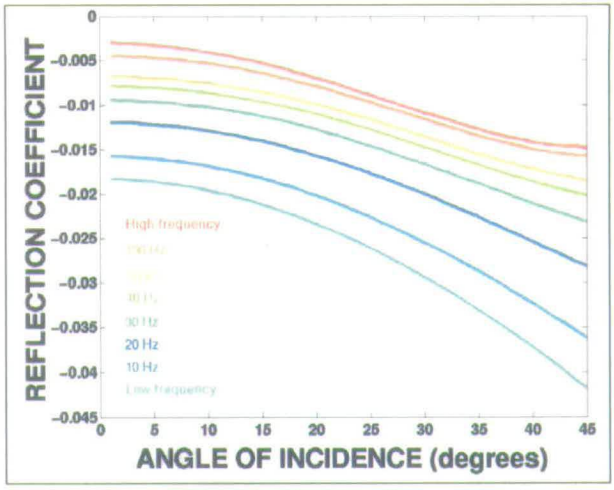

Figure 2. AVO curves for various frequencies for our first model, under gas saturation. The low-frequency curve corresponds to the traditional Gassmann case.

Example 1. Our first example is a 2D line of streamer data from a gas field in the North Sea. The main point of our approach is that interpretation has to begin with a standard AVO analysis. Such an analysis indicated that the data showed zones of strong class III AVO anomalies at the reservoir level; this was confirmed by gradient and intercept crossplotting as well as consideration of product, fluid-factor, and scaled Poisson ratio stacks.

Following the work of Castagna et al. (2003), we formed "isofrequency sections" from the stacked data. From these it is immediately apparent that significant frequency anomalies are associated with the class III AVO anomalies at the reservoir level. Figure 1 highlights such a region, which is bright on a 15-Hz section, but no bright spot is visible on the 30-Hz section. The effect was consistent for other frequencies; the reservoir was bright at low frequency, but did not stand out on the higher frequencies. This highlights the fact that in practice the concepts of amplitude and AVO anomalies are typically frequency-dependent phenomena.

We performed an extensive synthetic modeling study to determine if the frequency and AVO anomalies could be systematically related to gas saturation. We used a commercial reflectivity code (ANISEIS) which permits the use of materials with frequency-dependent velocities and attenuations. Our interest had three components; the simple Gassmann effect, the Gassmann effect with tuning, and the full dynamic modeling with attenuation and associated dispersion.

When we considered the simple single-layer case, it was

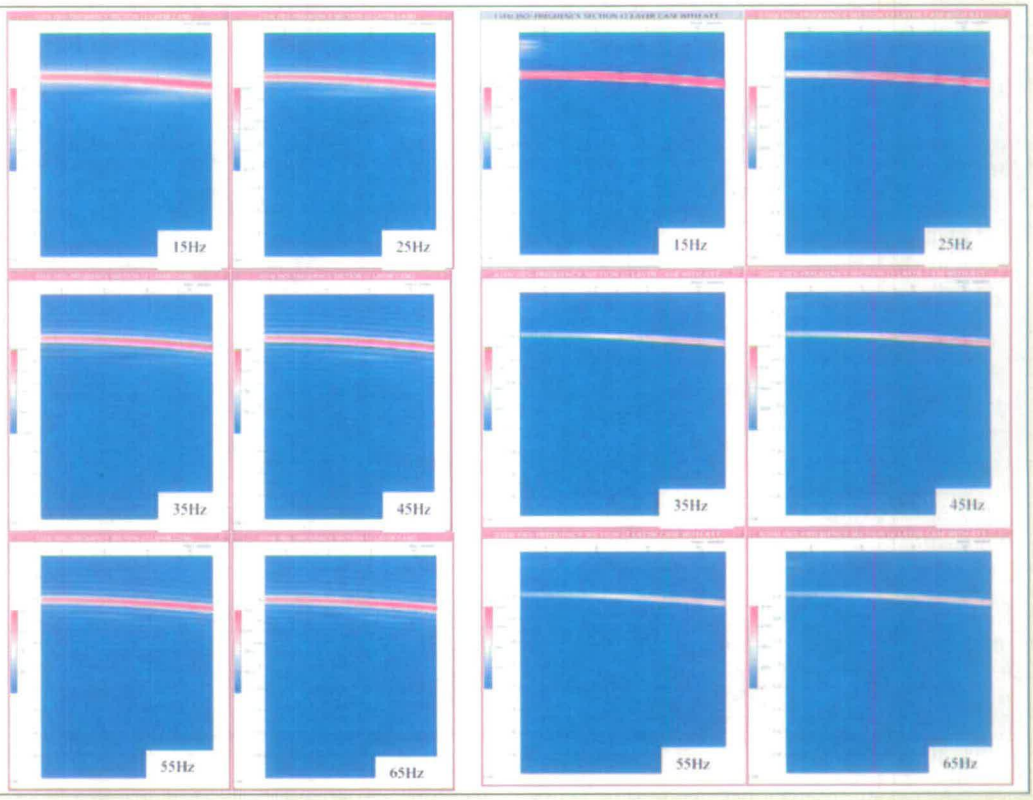

Figure 3. Reflections from the single interface for our model under gas saturation. Left diagrams are for the Gassmann case; right diagrams are the dispersive case. Spectral balancing based on the input wavelet has been carried out. For the Gassmann case, similar energy appears on each isofrequency section. In the dispersive case, the low-frequency sections have markedly more energy.

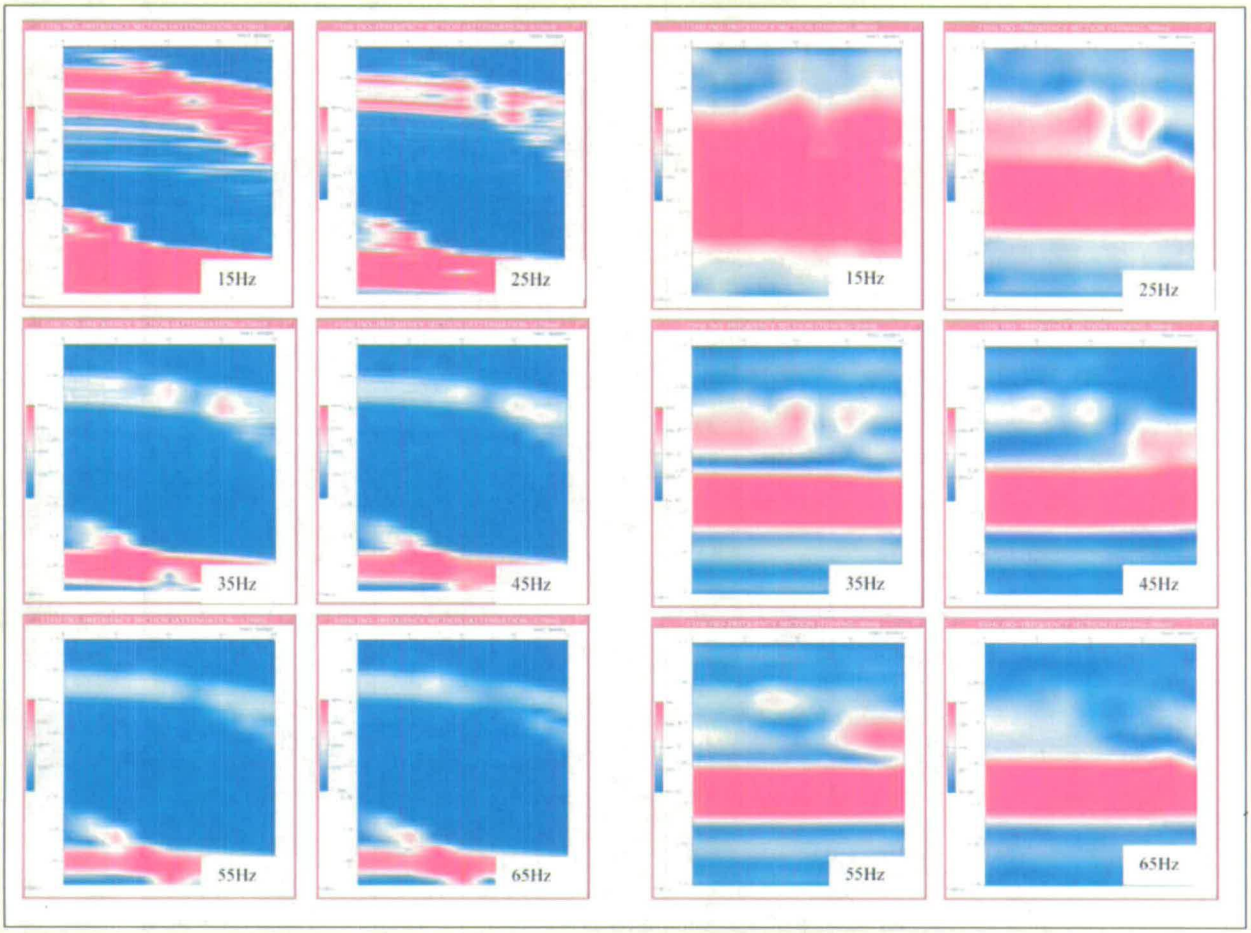

Figure 4. Isofrequency sections from the multilayer model. Left diagrams correspond to the dispersive case, but with a thick reservoir layer of 420 m for which no tuning occurs. Right diagrams are for the Gassmann case, but with a thin reservoir of 90 m which is close to the tuning thickness. Spectral balancing has been applied in both cases, but the lower-frequency sections appear brighter.

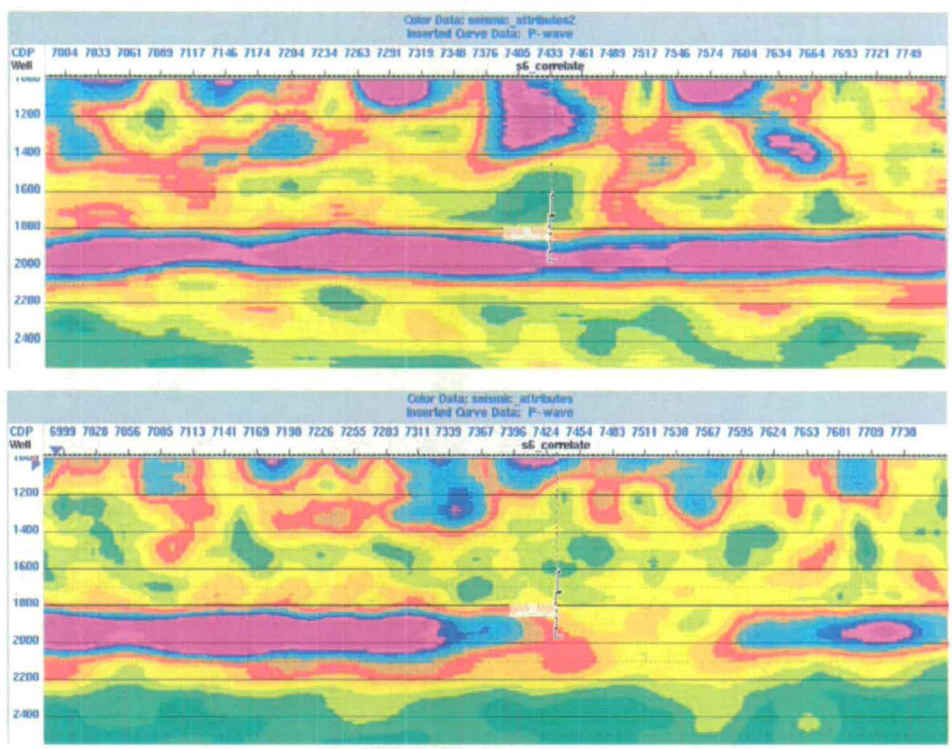

Figure 5. PP stacked sections from example 2, band-passed into low- (top) and high- (bottom) frequency sections. Note how the reservoir level (around 2 s) appears dim in the high-frequency section but not in the low-frequency section.

easy to model the standard AVO attributes with Gassmann, under straightforward assumptions. We performed spectral decomposition to produce balanced isofrequency sections. As might be expected, these sections showed similar energy in each isofrequency section, and so we could not model the effect seen in the data with a simple one-layer model. When we introduced dispersion into the reservoir layer, however, the frequency dependence of the reflection implied that the isofrequency sections were no longer balanced, and the low frequencies appear to have much more energy. Figure 2 shows the gas-saturated reflection coefficients for a range of frequencies for the model while Figure 3 shows a comparison between the balanced isofrequency sections for the single-layer case, assuming both the purely elastic case (left) and the case with a dispersive reservoir layer (right).

In practice we know that we never deal with reflections from single layers; tuning and multiples are always important issues. To address these issues, we formed a blocked model with 10 layers from velocity data from the field in question. We also varied the thickness of the reservoir layer to simulate tuning phenomena, and we did this both for the simple Gassmann modeling as well as the modeling with dispersion. In general we found that the dispersion effect is still strong even in the multilayer case, but, for certain reservoir layer thicknesses, tuning can give a similar effect to that arising from the dynamic modeling. Figure 4 shows a comparison for the multilayer case between a dispersive reservoir layer without tuning and an elastic reservoir layer with tuning. We conclude that without detailed information on the velocity model it can be difficult to distinguish between the effects of dispersion and tuning.

Example 2. We applied similar ideas to a gas field from Ordos Basin, onshore China. The potential reservoirs in the area are primarily in the fluvial sandstone in the Permian. The subsurface has a flat-layered structure with gas reservoirs typically below 3000 m. The targeted gas beds are thin and have a small P-wave velocity difference between the gas sand and the overlaid shale, giving rise to a weak amplitude on the

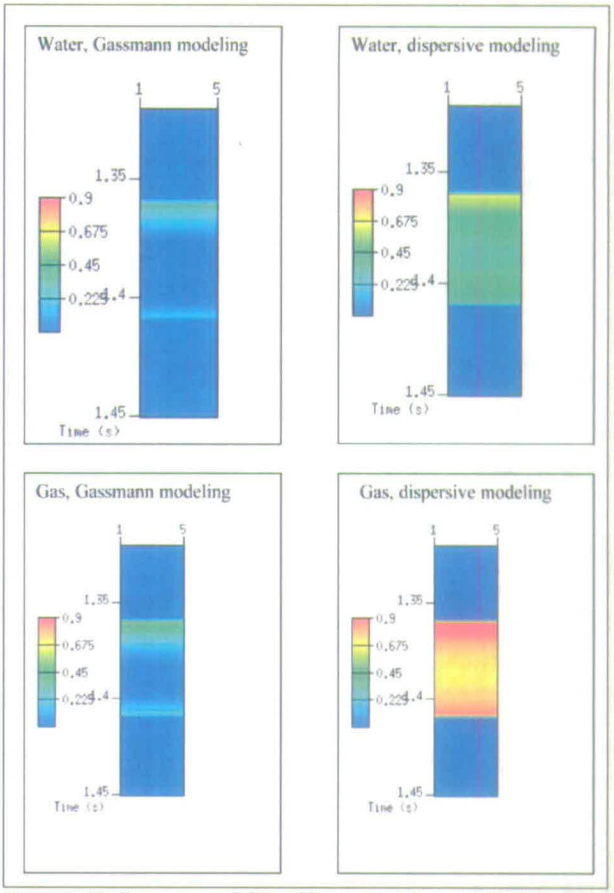

Figure 6. "Difference traces" formed by stacking the synthetic data, performing spectral decomposition, consistent spectral balancing, and subtracting the 30-Hz trace from the 15-Hz trace. The reservoir layer is 10-m thick, and we consider water and gas saturation in both the dispersive and Gassmann cases. Note that the Gassmann modeling gives small absolute values, but that gas saturation is associated with a strong positive amplitude when we perform dispersive modeling.

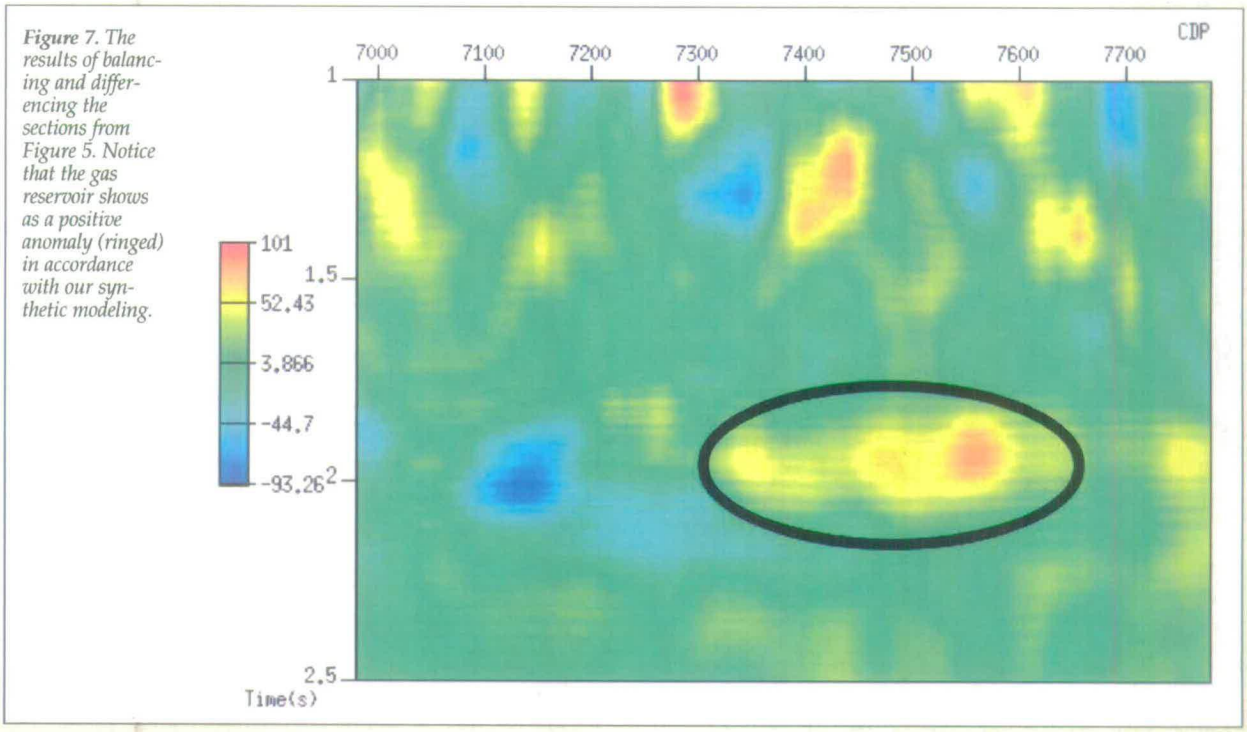

Figure 7. The results of balancing and differencing the sections from Figure 5. Notice that the gas reservoir shows as a positive anomaly (ringed) in accordance with our synthetic modeling.

PP-wave reflection.

Standard AVO analysis suggested that the top of the reservoir was in principle a class III interface, but that the reservoir reflection itself was a composite event, which led to an apparent negative reflection coefficient whose absolute amplitude declined with increasing angle of incidence, resembling the behavior of a class IV interface. Based on log data, we created an idealized multilayer model, with a 10-m thick gas sand and 10-m thick shale layer encased in a half space of higher impedance. This arrangement was able to effectively model the observed AVO behavior within the reservoir.

Application of spectral decomposition techniques to the stacked field data revealed an unexpected anomaly. Figure 5 shows the results of filtering the final stack into low- and high-frequency bands. It is clear that in the high-frequency section the reservoir appears as a low-amplitude anomaly, but this is not the case in the low-frequency section. Because the reservoir is only 10-m thick, it proved difficult to model this effect as being due either to a traditional attenuation mechanism or fluid-related changes in the tuning-thickness. To explain the behavior, we turned to our dispersive modeling.

As before we ran two sets of models, the standard elastic Gassmann case as well as the dispersive modeling, and found that as expected, for a class III interface, the gas saturation was associated with a systematic boost to the low frequencies relative to the high frequencies in the dispersive case. To illustrate this point we ran four models corresponding to water and gas saturation for both Gassmann and the dispersive case, stacked the data, formed isofrequency traces, and performed consistent spectral balancing on each trace. We then subtracted the resulting 30-Hz trace from the 15-Hz trace, and windowed around the main arrival to compensate for the different time durations of the signals. The results are illustrated in Figure 6. For each Gassmann trace there is little residual energy, implying that the traces were well balanced. In the dispersive case there was residual energy for both saturations, but it was much stronger in the gas-saturated case. A similar procedure was carried out on the data shown in Figure 5. The two sections were balanced and a difference was taken; Figure 7 shows the result. As can be seen, in the vicinity of the reservoir we have a response very similar to the gas response we saw in our synthetics.

Discussion. In this paper we have applied the spectral decomposition techniques to reflection data from hydrocarbon-saturated zones. Sharp changes in the spectral behavior associated with gas saturation have been noted elsewhere; the novelty of this paper lies in the attempt to model the behavior in terms of well-defined poroelastic effects. The understanding of such effects builds on the standard AVO analysis, since our interpretation is within the extended Rutherford-Williams classification outlined by Chapman et al. (2005). We emphasize that our work is an adjunct to the standard AVO methodology; we do not believe that it is possible to robustly interpret the spectral response in the absence of a thorough AVO analysis.

In our data examples, the gas saturation can be associated with a clear spectral signature, and the effect can actually be modeled in terms of a simple single-layer model, provided we account for velocity dispersion. Nevertheless, we know that in practice we always deal with more complicated geologic models. In particular, tuning is always present to a certain degree. When we perform fluid substitution with Gassmann in such a thin-layer case, we change the velocity and hence the effective tuning thickness. This provides a natural explanation as to why gas-saturated zones should appear as spectral anomalies. In our first example, we cannot discriminate whether the observed spectral anomaly is caused by tuning or dispersion, but in the second example the reservoir is only 10-m thick, and the tuning effect is not sufficient to produce a significant spectral response for such thin reservoirs at seismic frequencies.

Paradoxically, the fact that spectral anomalies often occur for such very thin reservoirs has often been cited as a reason why attenuation cannot be the responsible mechanism, because it was thought that attenuation, being primarily a propagation phenomenon, could only accumulate a significant impact for waves traveling over longer distances. Our emphasis on the frequency-dependent reflection coefficient arising from the attenuation-related dispersion anomaly provides an explanation to this point. The framework also answers another common argument against attenuation mechanisms being responsible for spectral anomalies which is that the high frequencies are commonly observed to return for reflections from below the reservoir, which would be impossible if we viewed attenuation as a simple cumulative loss during transmission mechanism. This phenomenon is reproduced in our synthetics. The deeper reflections occur at interfaces which are not associated with a strong attenuation and dispersion contrast and so are governed by a relatively frequency independent reflection coefficient. The spectral properties of such reflections therefore are those of the background trend, with the energy loss associated with passing twice through the attenuating layer being generally only a secondary effect.

Unfortunately, many processing and other artifacts can give rise to spectral anomalies which correlate with gas saturation, as has been eloquently pointed out by Ebrom (2004), and we are consequently conscious of the danger in overinterpreting such observed features. The purpose of this paper is simply to show that it is in fact possible to quantitatively model observed spectral anomalies in seismic data associated with gas saturation in terms of dispersion. Whether in fact velocity dispersion is the true cause of the spectral anomalies must be considered an open question; but nevertheless if the success of the modeling is maintained in other data sets, then it may be possible to develop an extension of the current AVO methodology which will include consideration of the dispersion effect and might give better access to fluid-saturation information.

Suggested reading. "Instantaneous spectral analysis: Detection of low-frequency shadows associated with hydrocarbons" by Castagna et al. (*TLE*, 2003). "Direct detection of oil and gas fields based on seismic inelasticity effect" by Rapoport et al. (*TLE*, 2004). "The influence of abnormally high reservoir attenuation on the AVO signature" by Chapman et al. (*TLE*, 2005). "Application of spectral decomposition to gas basins in Mexico" by Burnett et al. (*TLE*, 2003). "The low-frequency gas shadow on seismic sections" by Ebrom (*TLE*, 2004). TLE

Acknowledgments: Emeka Odebeatu was sponsored throughout this research by the Shell Centenary Scholarship Fund, and the work was carried out at the Edinburgh Anisotropy Project (EAP) as part of the course MSc in Exploration Geophysics at Leeds University, UK. This work is presented with the permission of the executive director of the British Geological Survey (NERC) and is supported by the sponsors of the EAP: BG, BGP, BP, Chevron, CNPC, ConocoPhillips, Eni-Agip, ExxonMobil, GX Technology, Hydro, Kerr-McGee, Landmark, Marathon, PetroChina, PDVSA, Schlumberger, Shell, Total, and Veritas DGC. Our particular gratitude to David Taylor of Macroc Ltd., for his help with the computation of synthetic seismograms in the ANISEIS software package. For information on ANISEIS contact macroc@blueyonder.co.uk. All other calculations were carried out using the EAP's rock unix (RU) software package.

Corresponding author: mhch@bgs.ac.uk

Z-99 AVO FLUID DISCRIMINATION WITH WEAK IMPEDANCE CONTRAST – A CASE STUDY FROM THE ORDOS BASIN

JINGHUA ZHANG[1, 2] AND XIANG-YANG LI[1]

[1]*British Geological Survey, Murchison House, West Mains Road, Edinburgh EH9 3LA, UK*

[2] *University of Edinburgh*

Summary

The paper presents a case study from the Ordos Basin, where the weak impedance contrast between the overlying shale and the gas layer in the Lower Permian formation makes it difficult to separate gas sands from the surrounding rocks using traditional AVO intercept and gradient analysis. Laboratory data show an enhanced sensitivity to pore fluid and lithology from Lame and density parameters $\lambda\rho$ and $\mu\rho$, which are then applied to real data to map the gas sands in the basin.

Introduction

As a seismic lithology analysis tool, the amplitude versus offset (AVO) method has been applied in the petroleum industry over the last 20 years. Rutherford et al (1989) define three AVO types of gas sands based on the zero offset reflection coefficient at the top of the gas sand. Castagna et al (1997) further develop the intercept-versus-gradient crossplot method for identification of fluid anomalies.

Due to the small impedance contrast between the overlying layer and the gas layer, the Type II gas sands have near zero value of zero-offset amplitude; the reflection magnitude may increase or decrease with the offset, and may reverse the polarity. In this case, AVO anomaly is hard to be determined using the intercept-versus-gradient crossplot method.

Goodway et al (1997) and Russell et al (2003) show an enhanced sensitivity to pore fluid from Lame's moduli and extract the lambda-mu-rho ($\lambda\rho$ and $\mu\rho$) from P- and S- wave impedance. We apply the method to this area, where by the post-stack impedance inversion and AVO analysis it is difficult to separate gas sand from the shale due to the weak impedance contrast between them.

Baisc Biot-Gassmann theory

Given an initial P-wave velocity V_{p0} (and optional density ρ_0) of a rock for known porosity ϕ_0, water saturation S_{w0}, the P-wave and S-wave velocities at different porosities ϕ and water saturation S_w can be obtained if the densities and the bulk modulus of water (ρ_w and K_w), hydrocarbon (ρ_{hc},and K_{hc}) and matrix (ρ_m and K_m), and the dry rock Poisson's ratio (σ_{dry}), bulk modulus (K_{dry}) and shear modulus (μ_{dry}) are known. Gregory (1977) points out that for most dry rocks and unconsolidated sands, σ_{dry} is about 0.1 and is independent of pressure. The calculated P-wave velocity is not very sensitive to the value of σ_{dry}. Assuming that the porous rock contains only one type of solid with a homogeneous mineral modulus and that the pore space is statistically isotropic, the P-wave velocity can be written in the low-frequency Gassmann's (1951) formulation as,

$$V_p = \sqrt{\frac{K_{dry} + \frac{4}{3}\mu_{dry} + \frac{(1 - K_{dry}/K_m)^2}{(1 - \phi - K_{dry}/K_m)/K_m + \phi/K_f}}{\rho_b}} \qquad (1),$$

where ρ_b is the bulk density of the rock and K_f is the bulk modulus of the fluid.
The dry rock bulk modulus K_{dry} and shear modulus μ_{dry} satisfy,

$$K_{dry} = 1/(\phi/K_p + 1/K_m) \qquad (2),$$

and $$\mu_{dry} = \frac{3(1-2\sigma_{dry})}{2(1+\sigma_{dry})} K_{dry} \qquad (3),$$

μ_{dry} is not affected by the pore fluid, and one has

$$\mu_{dry} = \mu \qquad (4).$$

K_f satisfies that the equation

$$K_f = 1/(S_w/K_w + (1-S_w)/K_{hc}) \qquad (5)$$

K_p is the bulk modulus of pore space, and is introduced for calculating K_{dry} at new porosity values.

$$K_p = \phi_0/(1/K_{dry0} - 1/K_m), \qquad (6),$$

where K_{dry0} is the initial bulk modulus of the dry rock, which can be obtained with the following equation using Gregory's (1977) formulation:

$$y = 1 - K_{dry0}/K_m, \qquad (7)$$

$$S = 3(1-\sigma_{dry})/(1+\sigma_{dry}), \qquad (8) \text{ and}$$

$$y^2(S-1) + y\left(\phi_0 S(K_m/K_f - 1) - S + \rho_0 V_{p0}^2/K_m\right) - \phi_0(S - \rho_0 V_{p0}^2/K_m)(K_m/K_f - 1) = 0. \qquad (9)$$

The S-wave velocity is not affected by the pore fluid and can be written as:

$$V_s = \left(\frac{\mu}{\rho_b}\right)^{\frac{1}{2}}, \qquad (10)$$

The bulk modulus K and Lame parameter λ for the fluid-saturated rock have the following relation:

$$\lambda = K - \frac{2}{3}\mu, \qquad (11)$$

From equations (1), (10) and (11), $\lambda\rho$ and $\mu\rho$ have the following relations with the P- and S-wave impedance I_p (ρV_p) and I_s (ρV_s):

$$\lambda\rho = I_p^2 - 2I_s^2 \qquad (12) \quad \text{and} \quad \mu\rho = I_s^2 \qquad (13)$$

Rock sample analysis

The study area is situated in the western part of the Ordos Basin, China. The subsurface structure is flat-layered with the gas reservoir below 3000m. Potential reservoirs in the area are primarily fluvial sandstone in the Permian formation. Table 1 shows the physical parameters of the gas sand and shale from the acoustic and density log data of a gas-producing well. Average changes in σ, $\lambda\rho$ and $\mu\rho$ are larger than those in V_p, V_s, V_p/V_s and impedance. The small average changes in velocity and impedance show that by velocity and impedance analysis it is difficult to distinguish gas sand from the shale. The sensitivity increases in Possion's ratio σ, $\lambda\rho$ and $\mu\rho$.

	V_p	V_s	ρ	Ip	Is	V_p/V_s	σ	$\lambda\rho$	$\mu\rho$	λ/μ
Shale	4367	2509	2.38	10393	5971	1.74	0.25	36.7	35.7	1.03
GasSand	4202	2562	2.44	10252	6251	1.64	0.20	26.8	39.1	0.68
Ave %	3.9	2.1	2.5	1.4	4.5	6.1	25	37	10	51

Table 1: Rock properties from a gas-producing well, showing relative large change in $\lambda\rho$ and $\mu\rho$ (Vp, Vs in m/s, ρ in g/cc, λ and μ in Gpa.)

Different types of core samples from 15 wells including gas sands, water sands, and shaly sands from the Lower Permian formation were measured to get V_p, V_s and density data under different gas saturations (0%, 35%, 65% and100%). These data have been used to calculate V_p/V_s ratio and lambda-mu-rho. Figure 1 shows the lithology and fluid effect using $\lambda\rho$ and $\mu\rho$. For the porous sand samples with 100% gas saturation, $\lambda\rho$ values are less than 33 Gpa × g/cm^3 and are less than the $\mu\rho$ values. The $\lambda\rho$ value increases with decreasing gas saturation. $\lambda\rho$ values for shaly sand are generally larger than those of the porous sand with the same gas saturation. Tight sand has the higher $\mu\rho$ values, and the shaly gas sand has the same $\mu\rho$ value range as the porous sand.

Well-log data analysis

Using the well log data (Figure 2a) and the fluid replacement modeling equations 1 to 10, AVO synthetics using Aki and Richards's approximations were built for wet sand and gas sand models as

shown in Figures 2b and 2c. In Figure 2d, the flat gradient causes blank reflections at the target top and base (around 1790ms) for the gas model in the Intercept-gradient section, and no AVO anomaly can be seen in this section.

We convert the V_p, V_s, and density logs to $\lambda\rho$ and $\mu\rho$ curves (Figure 3a) and crossplot them in Figure 3b. As expected, the $\lambda\rho$ values of the gas layer shown in the pink zone Z1 decrease and can be separated with the surrounding rocks. The $\mu\rho$ values of the gas layer increase compared with the overlaid shale (green Z4). This makes sense because the sand matrix has a higher value of shear modulus than the shale matrix. The tight sands (orange Z3) have the highest $\mu\rho$-values, and the shaly sands (blue Z3) have similar $\mu\rho$ values to the gas sand.

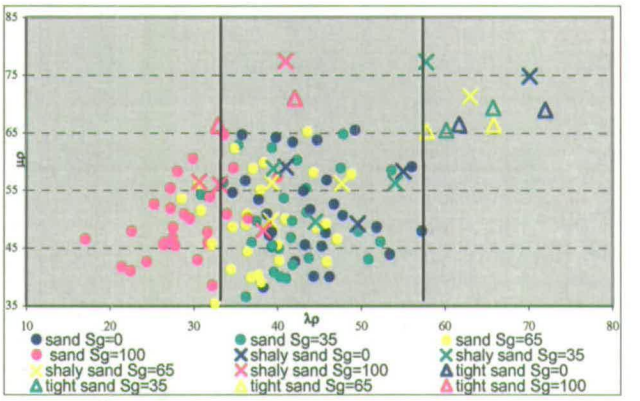

Figure 1: $\lambda\rho$ (Incompressibility × Density) versus $\mu\rho$ (Rigidity × Density) for porous sand, shaly sand and tight sand under gas saturation 0%, 35%, 65% and 100%. High gas-saturated sand can be separated from mid-to-low gas-saturated sand by $\lambda\rho$, and tight sand by higher $\mu\rho$.

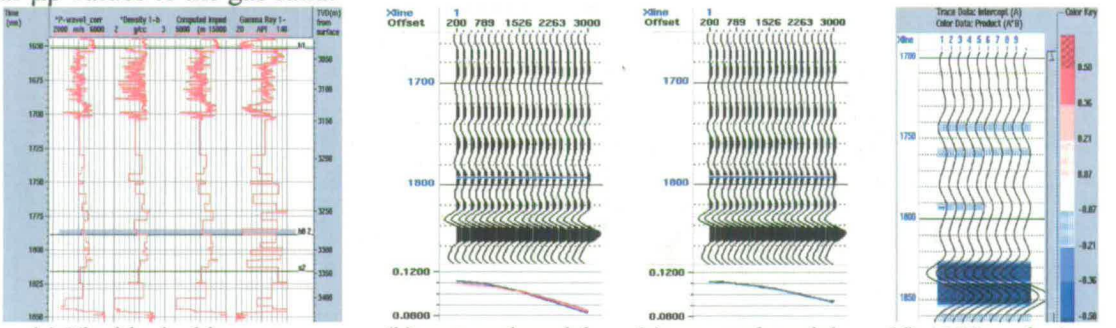

(a) The blocked log curves (b) wet sand model (c) gas sand model (d) AVO analysis

Figure 2: (a) From left to right are: P-wave velocity, density, P-wave impedance and Gamma Ray logs. Gas layer is shown in the grey square. (b) AVO synthetic for wet sand model (c) AVO synthetic for gas sand model. The bottom graphs of (b) and (c) show the picked amplitudes (blue curve) of the target base with gradient analysis (red curve). The trend of the picked amplitudes value of the target base becomes flat for gas sand model. (d) Intercept-gradient analysis: intercept is shown in black traces, the product of the intercept and gradient is shown in colour. The first 5 traces are for the wet sand and the last 5 traces for the gas model, and no AVO anomaly can be seen in this section for the gas model.

Seismic data analysis

A model-based impedance inversion was used to invert the reflectivity R_{p0} and R_{s0} from the AVO data to P- and S- wave impedance, I_p and I_s. Figure 4 show the P- and S-wave impedance inversion sections. There is an impedance drop below horizon 2 in the P-wave section due to the contrast between the low impedance shale/gas sand and the overlying high impedance tight sand. The inserted curve is the Gamma Ray log. The S-wave impedance drops below horizon 2 because the overlaid tight sand has a higher shear modulus value.

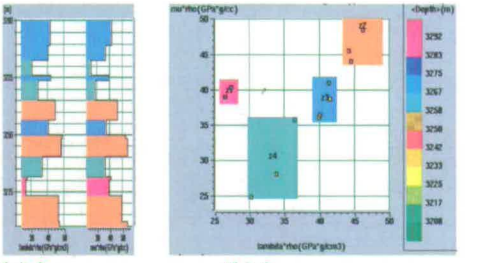

(a) $\lambda\rho$ $\mu\rho$ (b) $\lambda\rho$ versus $\mu\rho$

Figure 3: (a) the calculated log curves of $\lambda\rho$ and $\mu\rho$ from Figure 2a for 3200-3300m. (b) Crossplot of $\lambda\rho$ versus $\mu\rho$, z1 stands for gas sand, z2 for tight sand, z3 for shaly sand and z4 for shale.

Figure 5 shows the $\lambda\rho$ and $\mu\rho$ section computed from the P- and S-wave impedance shown in Figure 4. The $\lambda\rho$ section shows a decrease in the gas filled layer. The $\mu\rho$ section shows an increase in the gas filled layer, which can be understood since the shear modulus of the sand matrix is higher than that of the shale matrix. Figure 6 shows a crossplot between $\lambda\rho$ and $\mu\rho$ section from horizon 2 to the coal horizon. We can see a low value $\lambda\rho$ and medium value $\mu\rho$ zone in pink color, where the $\lambda\rho$ value is less than the $\mu\rho$ value. The pink zone can be interpreted as the gas zone, and the higher value $\lambda\rho$ zone as non-gas zone. Accordingly, the pink area is plotted on the seismic section in Figure 7, and the gas zone is shown as expected.

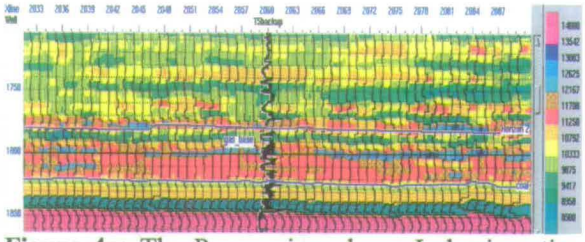

Figure 4a: The P-wave impedance I_p, by inverting the R_p estimates. Horizon 2 is picked near the top of the gas layer. The inserted curve is the Gamma Ray log.

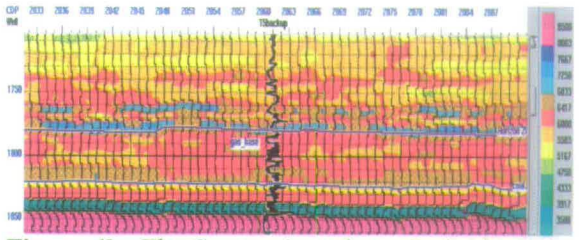

Figure 4b: The S-wave impedance I_s, by inverting the R_s estimates. Horizon 2 is picked near the top of the gas layer. The inserted curve is the Gamma Ray log.

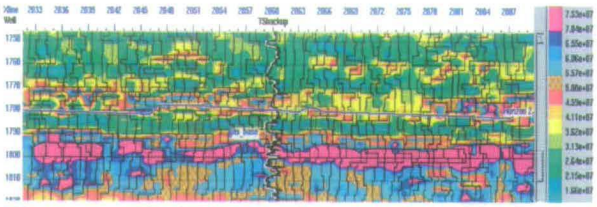

Figure 5a: The $\lambda\rho$ section by combining the I_p and I_s inversions of Figure 4

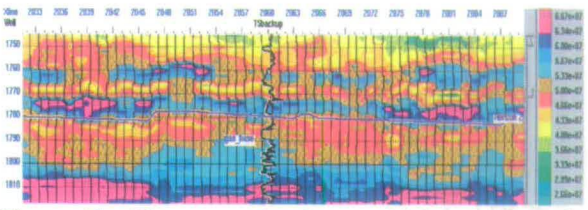

Figure 5b: The $\mu\rho$ section by combining the I_p and I_s inversions of Figure 4

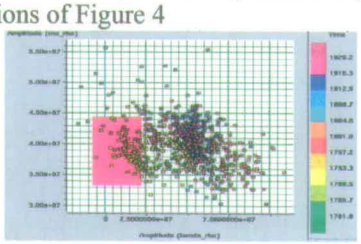

Figure 6: A crossplot between $\lambda\rho$ and $\mu\rho$ section of Figure 5 from horizon 2 to the coal horizon

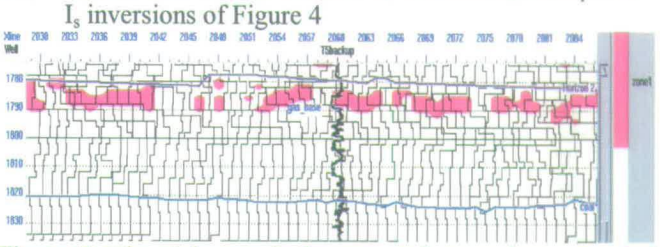

Figure 7: The pink zone is the gas sand area where expected. The inserted curve is the Gamma Ray log

Conclusions

The small P-wave impedance contrast between gas sand and shale makes it difficult to separate gas filled sand from the shale in this area. Traditional AVO intercept and gradient analysis cannot determine the AVO anomaly due to a Type II AVO for gas sand in the studying area. The Ordos laboratory core data indicate that Lame moduli and density parameters are sensitive to the variation of fluid content and can be used to separate gas sands from shaly and tight sands in this area. $\lambda\rho$ can be a direct indicator for gas saturation, $\mu\rho$ has less ambiguity in lithology. The real data confirm the laboratory analysis and show that the $\lambda\rho$ value has an improved sensitivity over impedance for the gas sand.

Acknowledgement

The authors thank PetroChina for permission to show the data. This work is supported by the Edinburgh Anisotropy Project (EAP) of the British Geological Survey, and is published with the approval of the Executive Director of BGS and the EAP sponsors.

Reference

Biot, M. A., 1941, General theory of three-dimensional consolidation:J. Appl. Physics, 12, 155–164

Castagna, J., and Swan, H., 1997 Principles of AVO crossplotting, The leading edge Apr, P337-342

Gassmann, F., 1951, Uber die Elastizitat poroser Medien:Vierteljahrsschrift der Naturforschenden Gesellschaft in Zurich, 96, 1–23

Goodway, B., Chen, T., and Downton, J., 1997, Improved AVO fluid detection and lithology discrimination using Lamé petrophysical parameters; "Lambda-Rho", "Mu-Rho", & "Lambda/Mu fluid stack", from P and S inversions: 67th Annual International SEG Meeting, P183-186

Gregory, A.R., 1977, Aspects of rock physics from laboratory and log data that are important to seismic interpretation, AAPG memoir 26 P15-46

Russell, B., Hedlin, K., and Hilterman, F. 2003 Fluid-property discrimination with AVO: A Biot-Gassmann perspective *Geophysics*, V68, P29–39

Rutherford S.R. and Williams R.H. 1989 Amplitude-versus-offset variations in gas sands Geophysics Vol54 No6 P.680-688

Z-99 P-WAVE AND CONVERTED WAVE EVENT CORRELATION BY CONVERTED WAVE MOVEOUT ANALYSIS

JINGHUA ZHANG[1, 2] AND XIANG-YANG LI[1]

[1]*British Geological Survey, Murchison House, West Mains Road, Edinburgh EH9 3LA, UK*

[2] *University of Edinburgh*

Summary

A reliable correlation between the P-wave and converted-wave (C-wave) events is critical for multicomponent data processing and interpretation. Recent studies show that the C-wave moveout in layered isotropic media can be determined by two parameters: the C-wave stacking velocity V_{c2} and velocity ratio γ_{iso}. Based on this theory, it is possible to obtain an independent estimate of the P-wave stacking velocity V_{p2} as a function of C-wave vertical travel time T_{c0} from C-wave reflection moveout. These estimates of V_{p2} in T_{c0} can then be compared to the V_{p2} obtained from P-wave reflection moveout in order to establish the corresponding relationship between P-wave vertical travel time T_{p0} and C-wave time T_{c0}. Velocity ratio γ_{iso} is a key parameter that determinates the reliability of V_{p2} in T_{c0}. Semblance analysis is performed to resolve C-wave stacking velocity V_{c2} and γ_{iso}. An analysis of a layered model shows that a reliable correlation can be achieved for layered media. Field 4C data from Ordos Basin, China, are used to illustrate the application.

Introduction

Acquisition and processing of multicomponent data make it possible to carry out P-wave and C-wave analysis simultaneously. However, joint P- and C-wave methods require a good match between the P- and C-wave sections (Goodway, 2002), and P- and C-wave correlation is also a major issue in processing and interpretation (Gaiser, 1996).

Several methods (e.g. Garotta, 1985; Behle and Dohr, 1985; Gaiser, 1996) were presented to calculate velocity ratio V_p/V_s from multicomponent data to perform P- and C- wave correlation. Li et al. (1999) devised a method to determine V_p/V_s from C-wave moveout data. This method is further developed here for performing P- and C-event correlation by using the revised two-parameter C-wave moveout equation in Li (2003).

Method

The revised C-wave traveltime equation for isotropic multi-layered media given by Li (2003) shows that C-wave NMO moveout is controlled by two parameters V_{c2} and γ_{iso}.

$$t_c^2 = t_{c0}^2 + \frac{x^2}{V_{c2}^2} - \frac{(\gamma_{iso}-1)}{\gamma_{iso} V_{c2}^2} \times \frac{(\gamma_{iso}-1)x^4}{4t_{c0}^2 V_{c2}^2 + (\gamma_{iso}-1)x^2} \qquad (1)$$

$$\gamma_{iso} = V_{p2}^2 / V_{c2}^2 \qquad (2)$$

where γ_{iso} is the velocity ratio between squared P- and C-wave stacking velocities. Equation (1) is accurate for offsets up to twice the reflection depth. Equation (2) indicates that V_{p2} in T_{c0} can be obtained independently from C-wave moveout data if V_{c2} and γ_{iso} can be resolved reliably. Semblance analysis can be used to obtain V_{c2} and γ_{iso}. If we minimize the errors between V_{p2} in T_{c0} and V_{p2} in T_{p0}

obtained by P-wave moveout analysis, and compare the respective travel times of the P-wave velocity in T_{c0} and T_{p0}, the correlation between P- and C-wave events can then be established.

Model study

Synthetic data (Figure 1) calculated for an eight-layer model (Table1) have been generated to test the method. The C-wave travel times calculated by equation (1) are shown as red curves in Figure 1. Traces are muted when offsets are larger than twice the reflection depth. Figure 1 confirms that equation (1) is accurate for offsets at least twice the reflection depth.

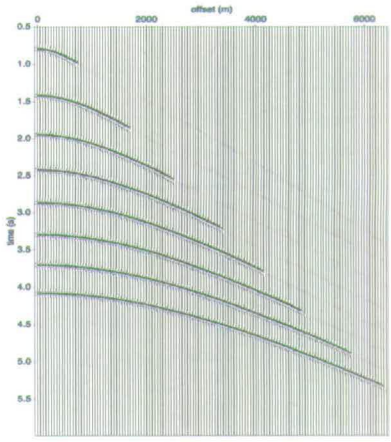

Figure1: Synthetic gather calculated for the layered model in Table 1. Traces are muted when offsets are larger than twice the reflection depth. The red curves are travel times calculated with equation (1).

	Z_k (m)	V_{pk} (m/s)	V_{sk} (m/s)	T_{p0} (s)	T_{c0} (s)	γ_0	V_{c2} (m/s)	γ_{iso}	γ^*_{iso}	V_{p2} (m/s)	V^*_{p2} (m/s)
1	400	2000	667	0.400	0.800	3.00	1155	3.00	2.84	2000	1946
2	400	2300	885	0.748	1.426	2.81	1281	2.80	2.76	2144	2128
3	400	2500	1087	1.068	1.954	2.66	1390	2.64	2.65	2257	2263
4	400	2600	1238	1.376	2.431	2.53	1478	2.50	2.52	2338	2346
5	400	2700	1350	1.671	2.875	2.44	1552	2.40	2.39	2406	2399
6	400	2800	1417	1.958	3.300	2.37	1615	2.34	2.36	2468	2481
7	400	2900	1515	2.233	3.702	2.32	1674	2.28	2.30	2525	2539
8	400	3000	1613	2.500	4.083	2.27	1730	2.22	2.26	2581	2600

Table 1: Modelling parameters to examine the accuracy of the calculated P- wave stacking velocity by C-wave moveout analysis in the isotropic media. V_{pk} and V_{sk} are interval velocities for P- and S-waves, γ_0 is vertical velocity ratio and $\gamma_0 = 2T_{c0}/T_{p0} - 1$. γ^*_{iso} is the obtained value from C-wave semblance analysis. V^*_{p2} is the P-wave velocity calculated from equation (2).

Based on equation (1), a double-scanning semblance analysis can be used to resolve V_{c2} and γ_{iso} from C-wave data alone (Figure 2). The offsets used in the analysis are restricted to $x/z \leq 2.0$. The obtained γ_{iso} values are shown in Table 1 as γ^*_{iso}. The errors for resolved γ_{iso} for all events are less than 2% (except the shallowest layer). Figure 2 shows that semblance analysis provides sufficient accuracy for resolving V_{c2} and γ_{iso}. Based on equation (2), P-wave stacking velocity V_{p2} can be obtained in the C-wave vertical travel time T_{c0} (shown as V^*_{p2} in Table 1). All events (except the shallowest layer) have errors less than 1% for V_{p2}. V_{p2} in T_{c0} time can be compared with the V_{p2} in T_{p0} as shown in Figure 3. Except the shallowest event, all events show a good one-to-one

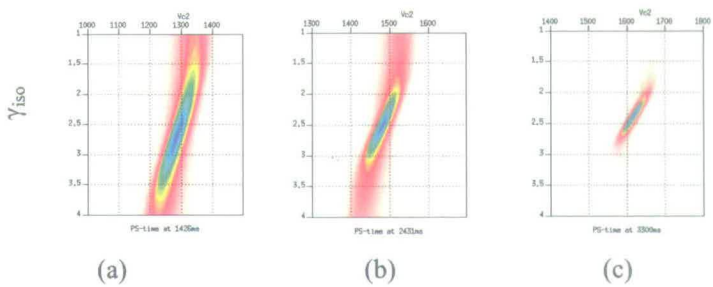

Figure 2: Double-scanning results for V_{c2} and γ_{iso}. The picked values of γ_{iso} are shown in Table 1 (γ^*_{iso}). (a), (b) and (c) correspond to the events 2,4 and 6, respectively, in Figure 1.

correspondence in terms of V_{p2}. The marked correlation indicates the minimum difference between the values of V_{p2} in T_{c0} and those in T_{p0}.

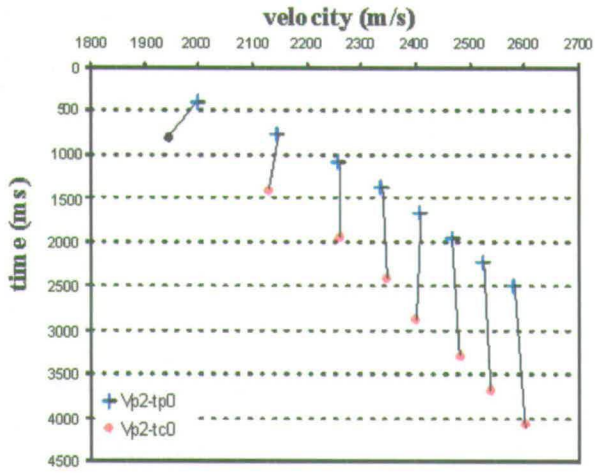

Figure 3: Correlation of the velocity picks. The blue crosses are V_{p2} in P-wave vertical travel time T_{p0} and the red dots are V_{p2} in C-wave vertical travel time T_{c0}. T_{p0} and T_{c0} are listed in Table 1.

Application to the Ordos 4C data

The Ordos 4C data (Li et al., 2002) are acquired over a horizontal stratigraphy, which is desirable for this study. A remarkable flat coal layer (around 2.0s in P-wave time) is distributed across the region and provides a good calibration point to examine the accuracy of the application in real data. Two passes of single-scanning semblance analysis have been used to determine V_{c2} and γ_{iso}. Examples of single-scanning results are shown in Figure 4. The P-wave velocity spectra in T_{C0} and T_{P0} times (Figures 5a and 5b, respectively) provide a good correlation among the three events in Table 2. For these three events, their V_{p2} in T_{c0} matches those in T_{p0} very closely. The resulted vertical velocity ratios (γ_0) are 1.97, 1.96 and 1.86, respectively. The compressed C-wave section using these values of γ_0 also matches the P-wave section very well, confirming the analysis (Figure 6).

T_{c0} (ms)	V_{c2} (m/s)	γ_{iso}	V^*_{p2} (m/s)	T_{p0} (ms)	V_{p2} (m/s)	γ_0
700	2050	2.00	2899	472	2929	1.97
1266	2440	1.85	3319	855	3324	1.96
2865	2970	1.80	3984	2007	3968	1.86

Table 2: Results from the Ordos 4C data showing the comparison of obtained V^*_{p2} in T_{c0} from C-wave moveout data with V_{p2} in T_{p0} from P-wave data

Discussion and Conclusions

Synthetic and real data examples show C-wave semblance analysis can be used to resolve V_{c2} and γ_{iso} in layered media. P-wave stacking velocity can then be obtained independently in the C-wave travel time domain. The reliability of this V_{p2} is mainly determined by the accuracy of the stacking velocity ratio γ_{iso}. The method can be used as a good reference for P- and C-wave correlation.

Acknowledgement

The authors thank PetroChina for permission to show the data. This work is supported by the Edinburgh Anisotropy Project (EAP) of the British Geological Survey, and is published with the approval of the Executive Director of BGS and the EAP sponsors.

Reference

Behle, A. and Dohr, G., 1985. Converted waves in exploration seismics, in Dohr, G., Ed., Seismic shear-waves, Part B: Applications. Geophysical Press 15B, 178-223.

Gaiser, J.E., 1996. Multicomponent Vp/Vs correlation analysis. Geophysics 61, 1137-1149.

Garotta, R., 1985 Observation of shear wave and correlation with P events, in Dohr, G., Ed., Seismic shear-waves, Part B: Applications. Geophysical Press 15B, 1-86.

Goodway, B. 2002 Elastic-wave AVO methods CSEG Annual convention abstracts

Li X-Y 2003 Converted-wave moveout analysis revisited: the search for a standard approach, 73rd Annual International SEG Meeting, 805-808.

Li,X-Y.,Yuan,J., Ziolkowski, A. and Strijbos, F. 1999 Estimating Vp/Vs ratio from converted waves: a 4C case example, 61st Annual EAGE meeting P066.

Li,X_Y., Wei, X. and Liu, E. 2002 Integrated analysis of seismic response of gas reservoirs in Ordos Basin, 64th Annual EAGE meeting, P255

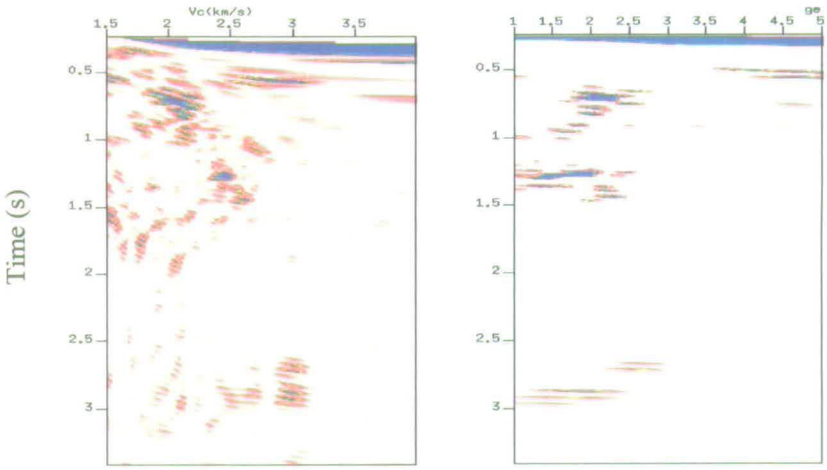

Figure 4: Single-scanning results for V_{c2} and γ_{iso} in the Ordos 4C data.

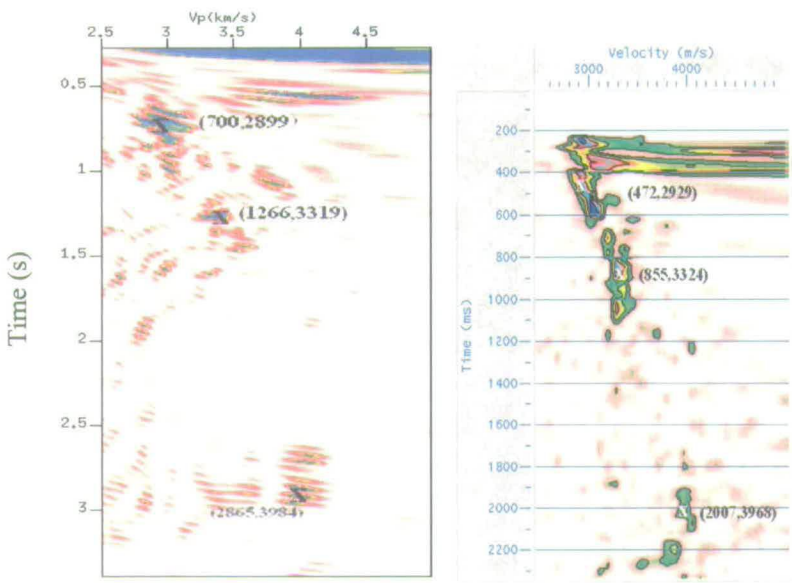

Figure 5: Comparison of (a) V_{p2} spectra obtained from C-wave moveout data in Figure 4 with (b) V_{p2} spectra from P-wave moveout data. The vertical time is T_{c0} in (a), but T_{p0} in (b). The crosses indicated the correlated velocity points with their corresponding coordinates in bracket (time, velocity).

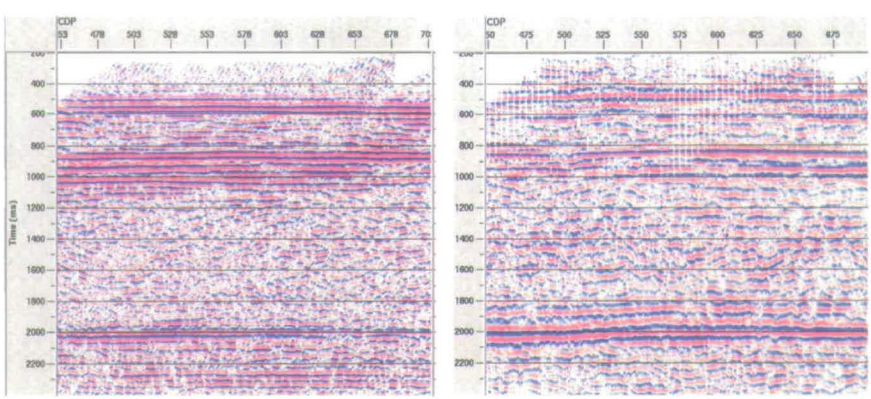

Figure 6: Final processed sections of P-wave (a) and C-wave (b). Both sections are displayed in P-wave vertical time.